



THE HONG KONG
POLYTECHNIC UNIVERSITY

香港理工大學

Pao Yue-kong Library

包玉剛圖書館

Copyright Undertaking

This thesis is protected by copyright, with all rights reserved.

By reading and using the thesis, the reader understands and agrees to the following terms:

1. The reader will abide by the rules and legal ordinances governing copyright regarding the use of the thesis.
2. The reader will use the thesis for the purpose of research or private study only and not for distribution or further reproduction or any other purpose.
3. The reader agrees to indemnify and hold the University harmless from and against any loss, damage, cost, liability or expenses arising from copyright infringement or unauthorized usage.

IMPORTANT

If you have reasons to believe that any materials in this thesis are deemed not suitable to be distributed in this form, or a copyright owner having difficulty with the material being included in our database, please contact lbsys@polyu.edu.hk providing details. The Library will look into your claim and consider taking remedial action upon receipt of the written requests.

**ACTIVE CONTROL OF
FLOW-INDUCED ACOUSTIC
RESONANCE THROUGH SURFACE
PERTURBATION**

LU ZHENBO

Ph.D

The Hong Kong Polytechnic University

2011

The Hong Kong Polytechnic University



Department of Mechanical Engineering

**Active Control of Flow-induced Acoustic
Resonance through Surface Perturbation**

LU Zhenbo

September 2011

CERTIFICATE OF ORIGINALITY

I hereby declare that this thesis is my own work and that, to the best of my knowledge and belief, it reproduces no material previously published or written, nor material that has been accepted for the award of any other degree or diploma, except where due acknowledgement has been made in the text.

_____ (Signature)

LU ZHENBO _____ (Name of student)

Abstract

Vortex shedding after a bluff body in the cross flow creates alternating lift and drag forces on the rear surface of the body, which can cause serious structural vibrations, and considerable acoustic noise particularly due to the acoustic resonance with a downstream cavity. This phenomenon can be classified as a type of flow-structure-sound (FSS) interaction. FSS is a very complex and challenging research area, which is relevant to a large variety of applications in mechanical, civil and environmental engineering. One aspect awaiting technological breakthrough is the development of innovative technologies for stabilizing flow and suppressing flow-induced vibration vortex-induced noise at the same time. This issue motivated the present research, in which the active control of flow-induced acoustic resonance has been experimentally investigated by using a novel surface perturbation technique. Seven interrelated subtopics are addressed in the present thesis. Major conclusions are:

- 1) The vortex shedding from a semi-circular leading edge test model and its associated acoustic resonance was controlled by utilizing a novel surface perturbation technique in the open-loop control scheme. It was observed that the control performances were repeatable and reliable. A reduction of sound pressure level (SPL) of about 16.3dB in the duct and 21.3dB in the cavity was achieved by using the optimal control parameters.

- 2) During the generation of the trailing edge vortex shedding for the semi-circular leading edge test model, a pressure pulse was generated and feedback to the leading edge shear layer to influence the formation of the next vortex shedding.

The surface perturbation technique generates a small local perturbation in the space between leading edge shear layer and trailing edge, which disturbs the pressure pulse. The change of the pressure pulse alters the generation of next vortex shedding that can lead to a reduction in the vortex shedding strength. This mechanism is referred to as ‘Pressure Disturbance Mechanism’. Furthermore, the surface perturbation technique changed the geometry of the up surface of test model and shifted the shear layer which was attached to the surface. The shift disturbed the shear layers around the test model, and thus resulted in a clear disturbance on the formation of the trailing edge vortices, leading to a significant reduction in the vortex strength in the wake of the model.

3) A frequency shift phenomenon was observed in both open-loop and closed-loop control scheme, and its effect on suppressing acoustical resonance inside the cavity was discussed. A formula was derived to predict this frequency shift in the effective control region. It was shown that the applied perturbation brings about a small increase in the effective height of the control plate, resulting in a frequency shift. If the shedding frequency shift exceeded the resonance bandwidth of the downstream acoustic cavity, the sound reduction inside the cavity would be larger than that in the duct. This phenomenon along gave a rise to a further sound pressure reduction of 5 dB for open-loop control and 4.4dB for the closed-loop control inside the acoustic cavity, respectively.

4) Closed-loop tests were proposed for a semi-circular leading edge test model, along with a down-sampling control algorithm. It was observed that the closed-loop control could achieve a better control performance than that of the open-loop control. At the optimum control voltage and control phase delay, a noise reduction of 17.5 dB in the duct and 22.6 dB inside the cavity was obtained. In particular, the phase delay

of control actuation could be optimally tuned so that the strength of vortex shedding energy could be minimized effectively, leading to a satisfactory noise reduction in the duct and cavity. This process was evident from the spectral phase shift results, where the vortex traveling time has been delayed at downstream of the test model.

5) For the square leading edge test model, the developed surface perturbation technique was also effective. However, the control mechanism was found to be different from that of the semi-circular leading edge test model. The path of the leading edge vortex shedding started from the leading edge and then propagated downstream. The vertical velocity generated by the perturbation played the key role in the vortex strength reduction. More significant reductions can be achieved when the velocity disturbance was near the propagation path of the vortex shedding.

6) The control strategies for two primary leading edge geometries have been investigated. The optimal control strategy for the semi-circular leading edge test model consists in arranging the perturbation at the position where the pressure pulse was the smallest. This way, the targeted noise reduction can be achieved by using perturbation within a relatively small area at a low control voltage. While for the square leading edge test model, the optimal control strategy requires applying the perturbation near the propagation path of the LEVS for achieving sufficient vortex strength abatement.

7) The energy distribution at vortex shedding frequency along the up surface of test model measured by the hot wire was used to identify the existence of the pressure pulse for the semi-circular leading edge test model. It was found that the pressure pulse had strong directivity characteristics; therefore, a small disturbance generated by the surface perturbation can change the direction of the pressure pulse and then influence the generation the vortex shedding.

List of Publications

Refereed Journal Papers

1. Zhenbo Lu, and Li Cheng, ‘Active control of flow-induced acoustic resonance through surface perturbation’, *AIAA Journal*, (Submitted)
2. Z. B. Lu, D. Halim and L. Cheng, ‘Closed-loop control of flow-induced acoustic resonance inside downstream cavities in a flow duct’, *Journal of the Acoustical Society of America*, (Submitted)
3. Zhenbo Lu, Li Cheng and Dunant Halim, ‘Control strategies for the vortex-induced acoustic resonance inside a downstream cavity from a bluff body with various leading edges ’, *AIAA Journal*, (in preparation)

Refereed International Conference Papers

1. Zhenbo Lu, Dunant Halim and Li Cheng, ‘Active Closed-loop Control of Vortex-Induced Acoustic Resonance inside a Downstream Cavity in a Duct’, 5th ECCOMAS Thematic Conference on Smart Structures and Materials SMART'11, Saarbrücken, Germany, July 6– 8, 2011
2. Z. B. Lu, L. Cheng, D. Halim, ‘Active control of flow-induced acoustic resonance through surface perturbation’, Inter noise 2010, Lisbon, Portugal, 2010

3. Zhenbo Lu, Li Cheng, 'Active manipulation of flow-induced acoustic resonance', International Symposium on Active Control of Sound and Vibration 2009, Ottawa, Canada, 2009 August 20-22
4. K.F. Yu, R.C.K. Leung, Z. B. Lu and L. Cheng, 'A Numerical Study of Wall Effect on Separated Flow past a Rectangular Bluff Body with Semi-Circular Leading Edge', Int. Conf. on Jets, Wakes and Separated Flows, ICJWSF-2010, Sept. 27-30, 2010, Cincinnati, Ohio USA

Acknowledgements

First and foremost, I owe my deepest gratitude to my supervisor, Prof. Li CHENG, who has provided me with the most valuable guidance in every stage of my postgraduate study. No matter what difficulties I have met, he never hesitated to give me his strongest support, which really means a lot to me. His unassuming, meticulous and rigorous scholarship enlightens me a lot in the development of my future career. At the same time, I would also express my great appreciation to Dr. Dunant Halim, who discussed the experiment with me and helped me to revise the whole thesis.

I also appreciate Prof. Xiaodong Jing and Prof. Xiaofeng Sun who were my previous supervisors when I studied in Beijing University of Aeronautics and Astronautics (BUAA). They contributed a lot to cultivate my fundamental and experimental abilities in the past.

During my study in the Department of Mechanical Engineering, the Hong Kong Polytechnic University, I was very lucky to work with many nice people, to whom my sincere gratitude is given. Particular thanks go to Dr. Deyu Li, Dr. Su Zhang, Mr. Yang Cheng, Mr. Shenzhen Feng, Dr. Chao Zhou, Dr. Yang Liu and Mrs. Xiaonan Wang who have provided me with valuable assistance in the whole process of my study.

Last but not least, I would like to thank my wife, my parents and my daughter for their greatest support all the time. It is their self-giving love that encourages me eternally.

Table of contents

Abstract	I
List of Publications	IV
Acknowledgment	VI
Table of contents	VII
List of the Figures	X
List of the Tables	XVII
Nomenclature	XVIII
1. Introduction	1
1.1 Background	1
1.2 Literature Review	2
1.2.1 The vortex shedding process	2
1.2.2 Vortex shedding mechanism for a single bluff body.....	6
1.2.3 Flow-induced acoustic resonances in duct	19
1.2.4 Control method	25
1.3 Motivations and Objectives.....	30
1.4 Outline of the thesis.....	32
2. The surface perturbation technique and experimental set-up	34
2.1 Introduction	34
2.2 A low-order model for vortex shedding behind a vibrating bluff body	35
2.3 Experimental setup	39
2.4 The surface perturbation technique	41
2.4.1 The principle of the surface perturbation technique	41
2.4.2 The piezoelectric effect.....	42
2.4.3 THUNDER actuator and its installation	43
2.5 The designs of test models and downstream cavities.....	48
2.5.1 The perturbation module and its characteristic.....	48
2.5.2 Test models.....	55
2.5.3 Downstream cavities.....	59

2.6 Platform and control strategy	62
2.6.1 Measurement system	62
2.6.2 dSPACE system and Simulink	65
2.6.3 Open-loop and closed-loop control strategies	65
2.7 Flow characteristics	68
2.8 Conclusions	70
3. Active open-loop control of flow-induced acoustic resonance	72
3.1 Introduction	72
3.2 Optimal control parameters for open-loop control	72
3.3 Control performance of open-loop control	75
3.4 Vortex strength abatement mechanism	80
3.4.1 The types of vortex shedding	80
3.4.2 Pressure disturbance mechanism	82
3.4.3 Shear layer shifts mechanism	87
3.5 Frequency shift phenomena	93
3.6 Effects on downstream cavity resonance	99
3.6.1 The resonance of downstream cavities	99
3.6.2 Resonance bandwidth and acoustic resonance effect	101
3.7 Conclusions	103
4. Downsampling theory and implement in real time control system	106
4.1 Introduction	106
4.2 Limitations of the open-loop control	107
4.3 Possibilities for applying closed-loop control strategy	109
4.4 Downsampling theory and its implementation	112
4.4.1 Nyquist–Shannon sampling theorem and the aliasing phenomenon	112
4.4.2 Downsampling theory	117
4.4.3 The implementation of downsampling theory	122
4.5 Conclusions	128
5. Closed-loop control for the flow-induced acoustic resonance	129
5.1 Introduction	129
5.2 The signal processing in closed-loop control	130
5.2.1 The selection of the single feedback signal	130
5.2.2 The application of downsampling program in closed-loop control	132

5.2.3	The normalization program	135
5.2.4	Modified PID controller	138
5.3	Optimal control voltage and phase delay	140
5.4	The control performance of closed-loop control	142
5.5	The analysis of fluid-sound interaction	147
5.6	Vortex strength abasement mechanism for closed-loop control	153
5.7	Vortex shedding frequency shift in the closed-loop control	155
5.8	Effects on cavity resonance in closed-loop control	158
5.9	The combination of different feedback signals	160
5.10	Conclusions	161
6.	The investigation of control strategy	164
6.1	Introduction	164
6.2	Vortex types and their characteristic for various leading edges.....	165
6.2.1	Vortex type for semi-circular leading edge	165
6.2.2	Vortex type for the square leading edge	168
6.3	Control performance of square leading edge test model	170
6.3.1	Optimal control parameters	171
6.3.2	The control performance of closed-loop control	173
6.3.3	The frequency shift and its analysis.....	178
6.3.4	Vortex abasement mechanism for a square leading edge test model	178
6.4	Effective perturbation position for various leading edges.....	180
6.4.1	The semi-circular leading edge.....	180
6.4.2	The square leading edge	183
6.5	The verification of pressure pulse	186
6.5.1	The existence of the pressure pulse	187
6.5.2	The directivity characteristic of the pressure pulse	189
6.6	The implementation of control strategy	193
6.7	Conclusions	194
7.	Conclusions	195
7.1	General conclusions	195
7.2	Recommendations	200
8.	Reference.....	202

List of the Figures

Figure 1-1 Boundary layer for a flat plate.....	3
Figure 1-2 Reynolds number dependence of drag coefficient for circular cylinder [20]	4
Figure 1-3 Cylinder pressure distributions for different Re [21].....	4
Figure 1-4 Classes of vortex formation (strouhal number and vortex types) observed with increasing elongation of different prismatic bodies: Class I leading-edge vortex shedding; Class II impinging leading edge vortices; Class III trailing-edge vortex shedding [29]	6
Figure 1-5 Vortex-formation model showing entrainment flows (Gerrard [30])	7
Figure 1-6 Visualization of the flow in a bluff-body wake [6].....	8
Figure 1-7 Motion of boundary layers during the vortex formation process (after Gerrard [30] and Lucas and Turner [32])......	9
Figure 1-8 Stages in vortex shedding for a single bluff body [33]	10
Figure 1-9 A single bluff body with square leading edge.....	11
Figure 1-10 Vortex patterns for a square leading edge bluff body.....	12
Figure 1-11 Patterns of flow around (a) a circular cylinder at $Re=100$ (Batchelor [34]) and (b) rectangular plate at $Re= 200$ (Bearman [35]).	13
Figure 1-12 Flow visualization for a plate with $c/t = 2.0$ at $Re \approx 800$: (a) anti-symmetric mode and (b) symmetrical mode. [42].....	15
Figure 1-13 Flow visualization at $Re \approx 600$ for a plate with $c/t = 3.6$ [42].....	16
Figure 1-14 Flow visualization for a plate with $c/t = 10.0$, $Re \approx 600$. [42]	17
Figure 1-15 Sketches of the vortical flow structures for flow past a semi-circular leading edge plate and a square leading edge bluff body.	18
Figure 1-16 vortex shedding from a plate with $c/t=16$ and $t=12.1\text{mm}$ [28].	18
Figure 1-17 Schematic of the plate in a duct leading to acoustic resonance.	21
Figure 1-18 Variation of vortex shedding frequency and SPL at the P-mode frequency with flow velocity [60].....	23
Figure 1-19 Coherence of signals from the hot wire and the probe microphone located above the mid-chord position of the plate; flow velocity = 12 m/s; SPL = 93 dB [60].	24
Figure 1-20 the sketch of the duct containing cavities.....	25

Figure 2-1 The schematic of the vibrating semi-circular leading edge bluff body in the flow stream. a) Without vibration, the vortex shedding frequency is f_s ; b) With vibration, the frequency of the signal is f_v and amplitude A .	36
Figure 2-2 A generic system of two nonlinearly coupled oscillators at mode-locked state in phase space and Poincaré section [110].	37
Figure 2-3 Sketch of the wind tunnel system.	40
Figure 2-4 The surface perturbation technique: (a) The strong vortex-induced noise; (b) The effect of a small local surface perturbation.	42
Figure 2-5 Dipole alignment in piezoelectric material.	43
Figure 2-6 Description of THUNDER actuators: (a) THUNDER construction; (b) A photo of THUNDER; (c) A typical deformation versus applied voltage.	45
Figure 2-7 Mounting method of the THUNDER actuator. (a) Simply supported mounting and displacement measurements; (b) Cantilever mounting and displacement measurements.	47
Figure 2-8 Vibration characteristic of the single THUNDER at various control frequencies. The control voltage is set to 140V: (a) Vibration velocity; (b) Displacement.	48
Figure 2-9 The installation of the THUNDER actuator by using cantilever mounting method (a) Side view; (b) Top view.	50
Figure 2-10 The placement of THUNDER actuators in the perturbation module. (a) Placement type P-A; (b) Placement type P-B	51
Figure 2-11 The perturbation module (a) Installation of the perturbation module; (b) Top view of the perturbation module; (c) Side view of the perturbation module.	52
Figure 2-12 The photo of perturbation module.	53
Figure 2-13 Vibration characteristic of the perturbation module at various control frequencies. The control voltage was set to 140V	54
Figure 2-14 Characteristic of the perturbation module at $f_p = 30\text{Hz}$, $V_{rms} = 160\text{V}$ a) Time-domain; b) Frequency domain.	54
Figure 2-15 The leading edge and trailing edge modules.	55
Figure 2-16 The process for combining semi-circular leading edge test model.	56
Figure 2-17 The process for combining square leading edge test model.	57
Figure 2-18 Peak values measured in the duct by microphone 1 at the shedding frequency f_s for different length of the bluff bodies, (a) Square leading edge; (b) Semi-circular leading edge.	58
Figure 2-19 The dimension limitation in the room of acoustic wind tunnel.	60

Figure 2-20 The characteristic of cavity at different width of cavity: (a) $B=20\text{mm}$; (b) $B=70\text{mm}$, $U = 8.2\text{m/s}$ and the shedding frequency of the bluff body installed in the duct is 78Hz	62
Figure 2-21 Sensing configurations, the control and measurement systems.....	64
Figure 2-22 The experimental set-up system.....	64
Figure 2-23 Open-loop control process.....	66
Figure 2-24 The closed-loop control process.....	68
Figure 2-25 Velocity profile inside the duct, measured by a single boundary hot-wire probe at $x=-275\text{mm}$, $U_{\infty} = 8.2\text{m/s}$	69
Figure 2-26 Flow distribution, measured at $x = 34\text{mm}$, C1 test model, $U_{\infty} = 8.2\text{m/s}$	70
Figure 3-1 The surface perturbation process used in active open-loop control.	74
Figure 3-2 The control performance for different control voltages in open-loop control.	75
Figure 3-3 Control performance of open-loop control in sound field, flow speed is $U=8.2\text{m/s}$ ($\text{Re}=5980$). (a) SPL measured by Mic.1; (b) SPL measured by Mic.2.....	77
Figure 3-4 Time-domain results for the control performance in sound field, the signals are filtered by a 5Hz-band filter. (a) Without control: measured in the duct; (b) With control: measured in the duct; (c) Without control: measured inside the cavity; (d) With control: measured inside the cavity.....	78
Figure 3-5 Control performance in flow field, flow speed is 8.2m/s ($\text{Re}=5980$). The hot wire 2 was located at $x = 34\text{mm}$ and $y = 8.25\text{mm}$	79
Figure 3-6 Time-domain results for the control performance in sound field, measured by hot-wire 2 located at $x = 34\text{mm}$ and $y = 8.25\text{mm}$. the signals are filtered by a 5Hz-band filter. (a) Without control; (b) With control.	80
Figure 3-7 Phase relationship between hot-wire 1 and hot-wire 2 along $y=11\text{mm}$. Hot-wire 1 was located at $x=0\text{mm}$ and $y=11\text{mm}$, hot-wire 2 was move along the $y=11\text{mm}$ at different x positions.	82
Figure 3-8 Schematic of feedback loops of vortex shedding for semi-circular leading edge bluff body.	85
Figure 3-9 Illustration of pressure disturbance mechanism.	86
Figure 3-10 Motion of boundary layers during the trailing edge vortex formation process and the schematic for applying small local perturbation.	88
Figure 3-11 The shear layer shifts mechanism.	90
Figure 3-12 Cross-flow distribution of mean streamwise flow velocity and Reynolds stresses at x/t , open-loop control. (a) \bar{U} , (b) \bar{u}^2 , (c) \bar{v}^2 , (d) \bar{uv} . $U_{\infty} = 8.2\text{m/s}$	93

Figure 3-13 the shift of shedding frequency at various maximum displacement d_{pm} of the vibration plate, $f_p = 30\text{Hz}$, measured by Mic.1.....	94
Figure 3-14 The schematic of effective displacement of the vibration plate.....	96
Figure 3-15 The effective perturbation displacement of the vibration plate, $f_p = 30\text{Hz}$	96
Figure 3-16 The prediction process of the frequency shift Δf_{sp}	98
Figure 3-17 Downstream cavity resonance, $L = 487\text{mm}$, $d = 100\text{mm}$, $U = 8.2\text{m/s}$	100
Figure 3-18 Sound pressure level at f_s at various flow velocities, without control.	102
Figure 3-19 The control effect on $SPL_{m2} - SPL_{m1}$ at f_s at various flow velocities, $f_p = 30\text{Hz}$ and $V_p = 160\text{V}$	102
Figure 4-1 The possible methods for applying closed-loop control.	112
Figure 4-2 Spectrum of a band-limited signal as a function of frequency.....	113
Figure 4-3 Spectrum of a properly sampled bandlimited signal (solid line) and images (dashed line) that do not overlap. A low-pass filter can remove the images and leave the original spectrum, thus recovering the original signal from the samples.	115
Figure 4-4 Spectrum of an insufficiently sampled band-limited signal (solid line) $U(f)$ is overlap with the images (dashed line).	116
Figure 4-5 Schematic of the downsampling theory.	119
Figure 4-6 The typical process for applying the downsampling theory.	121
Figure 4-7 The characteristic of the original signal. (a) Time-domain; (b) Frequency-domain.	122
Figure 4-8 The comparison result by using Zero-Order Hold (ZOH) module to change the sample frequency of the signal. (a) Time-domain; (b) Frequency-domain.	124
Figure 4-9 The results of using the Rate Transition module. (a) Time-domain; (b) Frequency-domain.	125
Figure 4-10 The comparison of transition signal with output signal. (a) Time-domain; (b) Frequency-domain.....	126
Figure 4-11 The comparison of the original signal with the output signal. (a) Time-domain; (b) Frequency-domain.....	127
Figure 4-12 The downsampling algorithm for closed-loop control.....	127
Figure 5-1 The comparison of the spectrum between the signal measured by hot wire 1 and measured by hot wire 2.	131

Figure 5-2 The comparison of the spectrum between the signal measured by hot wire 2 and measured by Mic.1	131
Figure 5-3 The comparison of the spectrum between the signal measured by hot wire 2 and measured by Mic.2	132
Figure 5-4 The feedback signal and its spectrum. (a) Time-domain; (b) Frequency-domain.	133
Figure 5-5 The original signal and its spectrum. (a) Time-domain; (b) Frequency-domain.	134
Figure 5-6 The downsampling algorithm for closed-loop control.....	135
Figure 5-7 A typical feedback signal obtained from hot wire 2. (a) Without control; (b) With control, the control voltage is 150V which is measured before input into the test model.....	136
Figure 5-8 The spectrum of a typical feedback signal obtained from hot wire 2.	136
Figure 5-9 The process of normalization program.....	138
Figure 5-10 The process of signal processing.....	140
Figure 5-11 The control effect for different control voltages. The control signal was from hot wire 2 which was located at $x=35.5\text{mm}$, $y=11\text{mm}$	142
Figure 5-12. The closed-loop control performance for varying phases. The feedback signal was obtained from the hot-wire 2 located at $x=35.5\text{mm}$, $y=11\text{mm}$. the control voltage is 155V.	142
Figure 5-13 The best control performance in frequency-domain. (a) Measured in the duct; (b) Measured inside the cavity.....	143
Figure 5-14 The best control performance in frequency-domain. (a) Measured by hot wire 1 at $x=0\text{mm}$, $y=11\text{mm}$; (b) Measured by hot-wire 2 at $x=34\text{mm}$; $y=11\text{mm}$;	144
Figure 5-15. Time-domain results for the control performance in sound field; the signals are filtered by a 5Hz-band filter. a) Without control, measured in the duct; b) With control, measured in the duct; c) Without control, measured inside the cavity; d) With control, measured inside the cavity.....	145
Figure 5-16. Time-domain results for the control performance in flow field; the signals are filtered by a 5Hz-band filter. a) Without control, measured by hot wire 1 at $x=0\text{mm}$, $y=11\text{mm}$; b) With control, measured by hot wire 1 at $x=0\text{mm}$, $y=11\text{mm}$; c) Without control, measured by hot wire 2 at $x=34\text{mm}$, $y=11\text{mm}$; d) With control, measured by hot wire 2 at $x=34\text{mm}$, $y=11\text{mm}$	146
Figure 5-17 The spectral coherence and spectral phase at the vortex shedding frequency between u_1 and u_2 for closed-loop control. Here, u_1 was measured by hot-wire 1 which was located at $x=0\text{mm}$, $y=11\text{mm}$. u_2 was measured by hot-wire 2 which was located at $x=34\text{mm}$, $y=11\text{mm}$. The feedback signal was obtained from hot-wire 2 for closed-loop control. (a) Spectral coherence; (b) Spectral phase.....	148

Figure 5-18 The spectral coherence and spectral phase at the vortex shedding frequency between m_1 and m_2 for closed-loop control. Here, m_1 was the sound pressure measured in the duct. m_2 was the sound pressure measured inside the cavity. The feedback signal was obtained from hot-wire 2 for closed-loop control.	150
Figure 5-19 The spectral coherence and spectral phase at the vortex shedding frequency between m_1 and u_2 for closed-loop control. Here, m_1 was the sound pressure measured in the duct. u_2 was measured by hot-wire 2 which was located at $x=34mm, y=11 mm$. The feedback signal was obtained from hot-wire 2 for closed-loop control.....	151
Figure 5-20 The spectral coherence and spectral phase at the vortex shedding frequency between m_2 and u_2 for closed-loop control. Here, m_2 was the sound pressure measured inside the cavity. U_2 was measured by hot-wire 2 which was located at $x=34mm, y=11 mm$. The feedback signal was obtained from hot-wire 2 for closed-loop control.....	152
Figure 5-21. The spectral phase between u_1 and u_2 at the vortex shedding frequency. Here, u_1 was measured by hot-wire 1 which was located at $x=0 mm, y=11 mm$. u_2 was measured by hot-wire 2 which was moved along $y=11 mm$. The feedback signal was obtained from hot-wire 1 for closed-loop control.....	155
Figure 5-22 The shift in the vortex shedding frequency at various maximum displacements d_{pm} of the test model.	157
Figure 5-23 The effective perturbation displacement of the vibration plate.....	157
Figure 5-24 Sound pressure level at f_s at various flow velocities, without control.	159
Figure 5-25 The control effect on $SPL_{m_2} - SPL_{m_1}$ at f_s at various flow velocities.	159
Figure 5-26 The control effect measured by Mic.1 for combination of different feedback signals.	161
Figure 6-1 Phase relationship between hot-wire 1 and hot-wire 2 along $y=11mm$ for C-1 test model. Hot-wire 1 was located at $x=0mm$ and $y=11mm$, hot-wire 2 was move along the $y=11mm$ at different x positions.....	166
Figure 6-2 The strength of vortex shedding distribution along $y=11mm$ for C-1 test model. hot-wire 2 was moved along the $y=11mm$ at different x positions.....	167
Figure 6-3 Diagram of the vortex type for short square leading edge test model and the measured points.....	168
Figure 6-4 Phase relationship between hot-wire 1 and hot-wire 2 along $y=11mm$ for S-1 test model. Hot-wire 1 was located at $x=0mm$ and $y=11mm$, hot-wire 2 was move along the $y=11mm$ at different x positions.....	169

Figure 6-5 The strength of vortex shedding distribution along $y=11\text{mm}$ for S-1 test model. hot-wire 2 was moved along the $y=11\text{mm}$ at different x positions.....	170
Figure 6-6 The control performance of different control voltages, open-loop control.	171
Figure 6-7 The control effect for different control voltages. The control signal was from hot wire 2 which was located at $x=30.0\text{mm}$, $y=11\text{mm}$	172
Figure 6-8. The closed-loop control performance for varying phases. The feedback signal was obtained from the hot-wire 2 located at $x=30.0\text{mm}$, $y=11\text{mm}$. the control voltage is 155V	173
Figure 6-9 The best control performance in frequency-domain. (a) Measured in the duct; (b) Measured inside the cavity.	174
Figure 6-10 The best control performance in frequency-domain. (a) Measured by hot wire 1 at $x=0\text{mm}$, $y=11\text{mm}$; (b) Measured by hot-wire 2 at $x=30\text{mm}$; $y=11\text{mm}$	175
Figure 6-11. Time-domain results for the control performance in sound field; the signals are filtered by a 5Hz -band filter. a) Without control, measured in the duct; b) With control, measured in the duct; c) Without control, measured inside the cavity; d) With control, measured inside the cavity.	176
Figure 6-12. Time-domain results for the control performance in flow field; the signals are filtered by a 5Hz -band filter. a) Without control, measured by hot wire 1 at $x=0\text{mm}$, $y=11\text{mm}$; b) With control, measured by hot wire 1 at $x=0\text{mm}$, $y=11\text{mm}$; c) Without control, measured by hot wire 2 at $x=30\text{mm}$, $y=11\text{mm}$; d) With control, measured by hot wire 2 at $x=30\text{mm}$, $y=11\text{mm}$	177
Figure 6-13 The maximum perturbation displacement of the vibration plate.	178
Figure 6-14 The illustration of the abasement mechanism for short square leading edge test model.....	180
Figure 6-15 The sketch of the 3mm -vibration-plate semi-circular leading edge test model (a) C-3-1; (b) C-3-2.....	181
Figure 6-16 The control performance of different perturbation positions for semi-circular leading edge test model.....	182
Figure 6-17 The sketch of the 3mm -vibration-plate square leading edge test model (a) S-2-1; (b) S-2-2.	184
Figure 6-18 The control performance of different perturbation positions for square leading edge test model.....	184
Figure 6-19 The maximum magnitudes of E_{u_2} measured by hot wire 2 between the leading edge and trailing edge.	188
Figure 6-20 The sketch of the ‘modified two microphones method’, tube A is used to measure the pressure pulse from the trailing edge to leading edge.	191

Figure 6-21 The comparison of the reduction between tube A and tube B. tube A is used to measure the pressure pulse from the trailing edge to leading edge..... 192
Figure 6-22 The sketch for changing the direction of the pressure pulse..... 193

List of the Tables

Table 2-1 The list of test models used in experiment59
Table 2-2 The list of downstream cavities62

Nomenclature

General Symbols

Re	Reynolds number
ν	Kinematic viscosity
μ	Dynamic viscosity of the fluid
ρ	Density of the fluid
l	Characteristic length
S_t	Strouhal number
f_s	Vortex shedding frequency
t	Thickness of the bluff body
U	Mean flow velocity along x direction
V	Mean flow velocity along y direction
c	The length of the bluff body
ω	Characteristic frequency
F	The force fluctuation on the body.
C	Sound speed
L	The depth of the cavity
d	The height of the duct
dB	Decibels
Ω	The bare winding number
Ω'	The dressed winding number
θ	Angular coordinate

f_p	Control frequency
V_p	Control voltage
B	The width of the cavity in the stream-wise direction
H	The width of the cavity in the vertical direction relative to the stream-wise flow
f_a	The resonance frequency of the cavities
ϕ	Phase of the signal
SPL_{m1}	The sound pressure level (SPL) at shedding frequency f_s measured in the duct
SPL_{m2}	The sound pressure level (SPL) at shedding frequency f_s measured in the cavities
$\phi_{u_1 u_2}$	Spectral phase $\phi_{u_1 u_2}$ between signal u_1 and u_2
d_{pm}	The maximum displacement of the vibration plate
\bar{d}_p	The equivalent increase in the thickness of the vibration plate
Δf_{sp}	The frequency shift
$2B_{NS}$	The sampling frequency
$U_0(f)$	Original spectrum
E_u	Power spectra density

Abbreviations

SPL	Sound pressure level
THUNDER	THin layer composite UNimorph Driver and sEnsoR
FSS	Flow-structure-sound
PZT	Piezo-electric transducer
LEVS	Leading-edge vortex shedding
TEVS	Trailing-edge vortex shedding
ILEV	Impinging leading edge vortex
Mic.1	The microphone installed in the duct
Mic.2	The microphone installed inside the cavity
PID	Proportional–integral–derivative

1. Introduction

1.1 Background

Bluff bodies are utilized in many branches of engineering, such as aeronautics, mechanical, chemical and civil engineering. When subjected to airstreams at lower Reynolds numbers (the ratio between the inertia force and the friction force acting on the fluid), the flow over a bluff body is highly viscous, and the force exerted on the bluff body is mainly attributed to skin friction. However, when the Reynolds number exceeds a critical value, the so-called vortex shedding phenomenon occurs in the wake, resulting in alternating lift and drag forces on the rear surface of the body. Such alternating lift and drag forces can cause the oscillation of the bluff body. In general, vortex shedding can potentially cause serious structural vibrations, considerable acoustic noise particularly due to acoustic resonance, significant increases in the mean drag and lift fluctuations. A lot of efforts have been concentrated on this particular fluid-structure interaction (see, e.g., Bishop & Hassan [1], Tanida et al [2], Griffin & Ramberg[3], Davies[4], Sarpkaya [5], Bearman [6], Ongoren & Rockwell [7] and Williamson & Roshko[8]).

In some other engineering applications such as mixing, combustion or heat transfer, such vortex shedding phenomena actually need to be enhanced in order to achieve a better performance. However in most cases, vortex shedding from bluff bodies needs to be impaired to reduce drag of vehicles, flow induced vibration and noise (among many studies, see *e.g.* Roshko [9-10], Monkewitz [11], Schumm et al. [12], Roussopoulos and Monkewitz [13]). Vortex-induced structural vibration should be suppressed in the cases of long-span bridges, tall buildings and towers, electric power transmission, heating ventilations and cooling systems. This is because the

excessive vibration may cause significant structural deformations or even damages to the engineering structures in the long run. Famous examples of catastrophic failures caused by vortex-induced vibration include the collapse of the Tacoma Narrows Bridge due to a sustained steady wind producing vortex shedding at the bridge resonance frequency over a long period of time and the damage of piling during the construction of an oil terminal on the Humber estuary of England in 1960s [3]. These serious accidents demonstrate the necessity of reducing the occurrence of resonance and synchronization of structures in the flow. Therefore, the control of vortex shedding behind bluff bodies is a subject of continued high interest and a considerable practical importance. There have been a considerable amount of research that focus on developing methodologies on how such vortex-induced structural vibration can be reduced (Ware& Shah[14], Yamane& Orita[15], Guerout & Fisher [16] and Pettigrew& Taylor[17]).

1.2 Literature Review

1.2.1 The vortex shedding process

When considering the effect of viscosity in the system, the vortex shedding process can be explained. In general, a viscous fluid satisfies a no-slip condition of its particles on the surface of a body immersed in the flow. Even if the viscosity is very low this condition will hold but its influence on the flow regime will be confined to a small region: the boundary layer along the surface of the body. Within this boundary layer the velocity of the fluid changes from zero on the surface to the free-stream velocity of the flow as shown in Figure 1-1 for a flat plate.

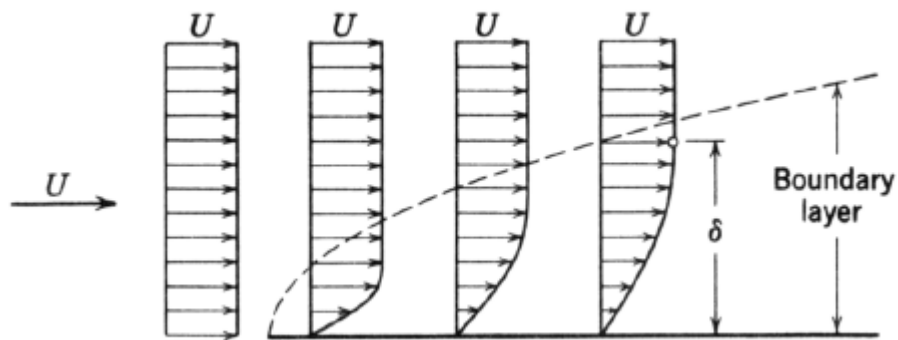


Figure 1-1 Boundary layer for a flat plate

Whilst the free stream is pulling the boundary layer forward the skin friction at the solid wall is retarding it. At surfaces with high curvature there can also be an adverse pressure gradient adding to the retarding action, which may cause the flow to be interrupted entirely and the boundary layer may detach from the wall. This phenomenon is called separation. Concerning the adverse pressure gradient, streamlined bodies can still experience the separation if the angle between free stream and surface is large enough. The viscosity and free stream velocity have an important influence and they can be described by the so-called Reynolds number

$$\text{Re} = \frac{Ul}{\nu} \quad (1)$$

where $\nu = \frac{\mu}{\rho}$, which is the kinematic viscosity, μ is the dynamic viscosity of the fluid, ρ is the density of the fluid and l the characteristic length. For example, a great variety of changes in the nature of the flow occur with an increasing Reynolds number when the flow past a circular cylinder. The dependence of drag coefficient and pressure distribution on it is shown in Figure 1-2 and Figure 1-3.

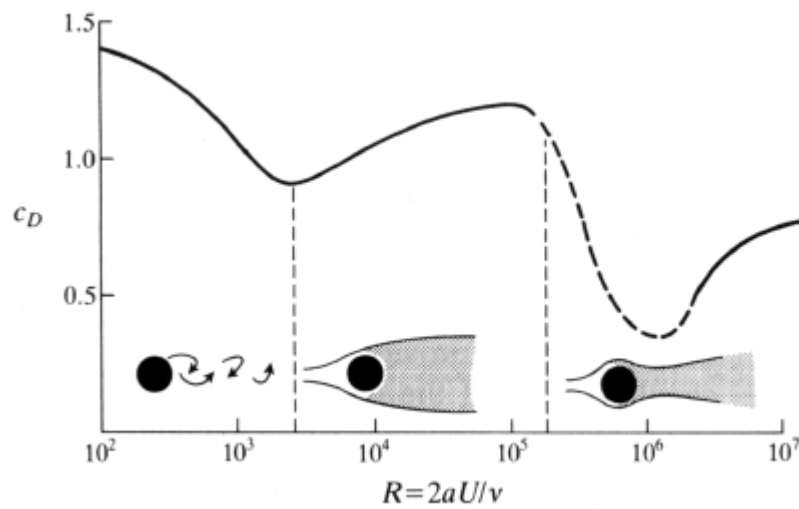


Figure 1-2 Reynolds number dependence of drag coefficient for circular cylinder [20]

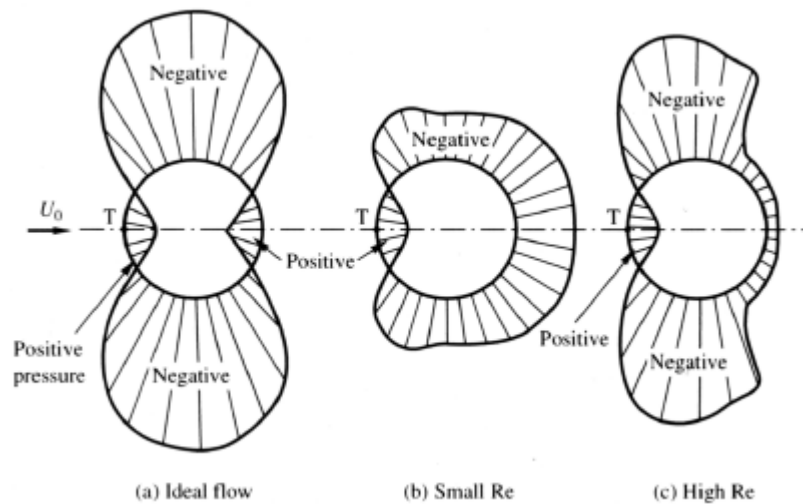


Figure 1-3 Cylinder pressure distributions for different Re [21]

At a very low Reynolds number (below 0.5), the inertia effects are negligible and the flow pattern is very similar to that for laminar flow, the pressure recovery being nearly complete. This means, that the pressure drag is also negligible and effective drag on the body is entirely due to skin friction. At an increased Reynolds number, approximately between 2 and 30, separation of the boundary layer occurs at two points at the back of the cylinder. Symmetrical eddies are formed which rotate in opposite direction. They remain fixed and the flow closes behind them. Further increase of the Reynolds number elongates the fixed vortices, which then begin to oscillate until they break away at a Reynolds number of around 90. The breaking

away occurs alternately from one and the other side, and then eddy travels downstream. This process is intensified with further increase of Reynolds number while the shedding of vortices from alternate sides of the cylinder is regular. This leads to the formation of the characteristic wake which is known as vortex street or Kármán vortex street. The eddying motion is periodic both in space and time. The pressure drag at this stage is already larger than the profile drag. Having passed a transition range where the regularity of shedding decreases, above a Reynolds number of 300 vortex shedding is irregular. However, there still is a predominant frequency but the amplitude appears to be random. At very high levels of Reynolds number from about 3×10^5 the separation point moves rearward on the cylinder. The drag coefficient decreases appreciably. The flow in the wake becomes so turbulent that the vortex street pattern is no longer recognizable.

Generally, the process of vortex shedding and its dependence on the Reynolds number is highly complex which makes analytical as well as numerical treatment very challenging. A comprehensive overview of the vortex shedding phenomenon and its different modes has been presented by Zdravkovich [22]. Since the vortex shedding exerts a fluctuating force on the body, which is of particular interest when the body can be excited to oscillations, Strouhal [23] defined a dimensionless shedding frequency, the Strouhal number, to characterize this process

$$St = \frac{ft}{U} \quad (2)$$

where f is the shedding frequency, and t is the thickness of the bluff body. For circular cylinders the formula can be applied when $250 < Re < 2 \times 10^5$.

Parkinson [24] stressed that the most important physical parameters of a two-dimensional body exhibiting vortex-induced oscillations are the size and shape of its after body which is the part of the cross-section downstream of the separation

points. For vortex-induced or galloping type excitation the pressure loading occurs principally on the after body surface. Accordingly, a body with a very short after body, e.g. a semicircular cylinder with the flat face downstream, will only be weakly excited. On the contrary, the same cylinder mounted the other way round can experience considerable oscillations under the same conditions [25]. Figure 1-4 shows a compilation by Deniz and Staubli [26], which compares results obtained in investigations on the effect of body geometry on the vortex shedding process. In Figure 1-4, c is the length of the bluff body and t is the thickness of the bluff body. A comprehensive set of data regarding the influence of the angle of attack on vortex formation can also be found in [27] and [28].

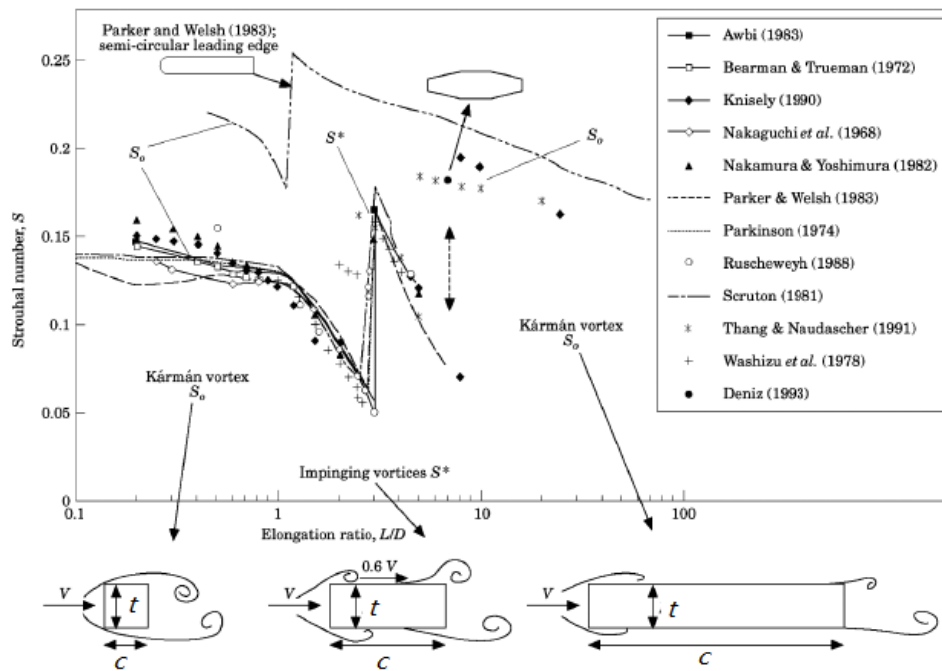


Figure 1-4 Classes of vortex formation (strouhal number and vortex types) observed with increasing elongation of different prismatic bodies: Class I leading-edge vortex shedding; Class II impinging leading edge vortices; Class III trailing-edge vortex shedding [29]

1.2.2 Vortex shedding mechanism for a single bluff body

When a bluff body is placed in a fluid stream, it can generate separated flow over a substantial proportion of the surface. On sharp-edged bluff body, separation is fixed

at the salient edge, whereas on bluff body with continuous surface curvature the location of separation depends both on the shape of the body and the state of the boundary layer. At low Reynolds numbers, when separation first occurs, the flow around the bluff body remains stable, but as the Reynolds number is increased to a critical value, these instabilities can lead to the vortex shedding. Until now, there is no complete theoretical solution to the problem of vortex shedding. Gerrard [30] has given an extremely useful physical description of the mechanics of the vortex-formation region. A key factor in the formation of a vortex-street wave is the mutual interaction between the two separating shear layers. It is postulated that a vortex continues to grow, fed by circulation from its connected shear layer, until it is strong enough to draw the opposing shear layer cross the near wake. The process of vortices which oppositely signed, in sufficient concentration, cut off further supply of circulation to the growing vortex, which is then shed and moves off downstream. Gerrard's vortex-formation model can be illustrated as Figure 1-5, which indicates several entrainment flow processes.

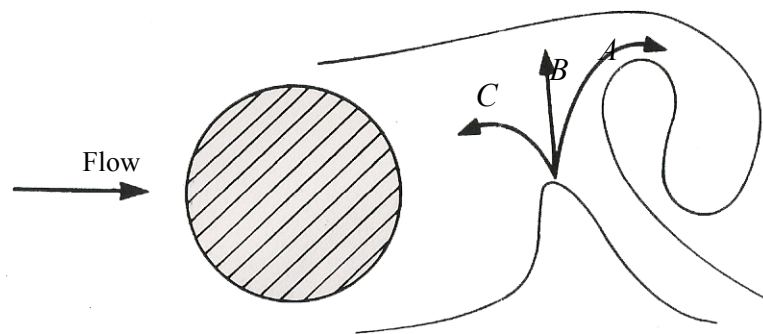


Figure 1-5 Vortex-formation model showing entrainment flows (Gerrard [30])

In this model, entrainment flows (flow A, B and C) play an important role in vortex formation. Entrained flow A is engulfed into the growing vortex while flow B finds its way into the developing shear layer. The near wake region between the base of the body and the growing vortex oscillates in size, and further flow C, is temporarily

entrained into it. Entrained flow A, which contains some fluid with oppositely signed vortices to that in the growing vortex, is the largest of the three flows. The photograph in Figure 1-6 shows smoke filaments around a bluff body, and the interaction between two shear layers and the vortex forming on the opposite side of the wake is clearly seen.

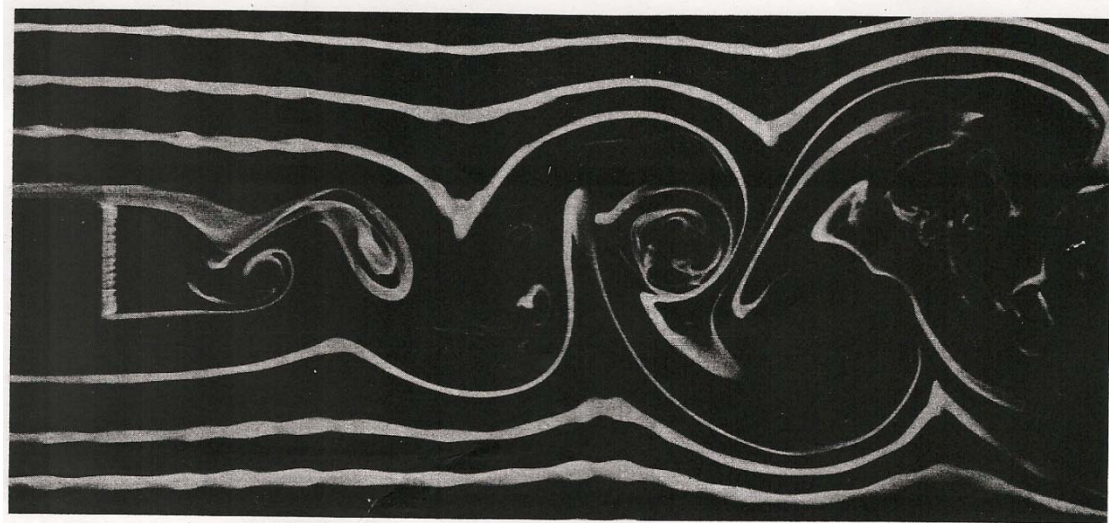


Figure 1-6 Visualization of the flow in a bluff-body wake [6]

The interaction process of shear layer interaction is extremely well illustrated in the numerical calculations of Abernathy & Kronauer [31]. They represented two parallel shear layers of opposing signs by rows of point vortices. The rows were disturbed and calculation proceeded until clouds of vortices resembling a vortex street were formed. Although these calculations may not have been carried out with the utmost mathematical rigor, they represent a very important step forward in the understanding of the mechanism of vortex shedding. They have shown that it is the presence of two shear layers, rather than the bluff body itself, that is primarily responsible for vortex shedding.

Lucas and Turner [32] further presented the motion of boundary layers during the vortex formation process in detail and proved this model by using different bluff body geometries, as shown in Figure 1-7. Just downstream of the rear surface of the bluff

body there is a vortex formation region. Here, two shear layers SL_1 and SL_2 alternately roll up to form the vortices in the wake. The process involves three flows:

- 1) Flow A from shear layer SL_1 on the opposite side of the wake is entrained into the growing vortex V_1 created from shear layer SL_1 .
- 2) Flow B from shear layer SL_2 moves across the wake and is entrained by the shear layer SL_1 upstream of V_1 , this causes detachment of V_1 .
- 3) Flow C from shear layer SL_2 is induced back into the formation region, by the action of the growing vortex V_1 , ready to initiate production of the next vortex V_2 on the opposite side of the wake. The strength of the vortices will be determined by the relative magnitudes of flows A, B and C. Normally C should be maximum, A minimum, with B just sufficient to ensure effective detachment of the growing vortex [32].

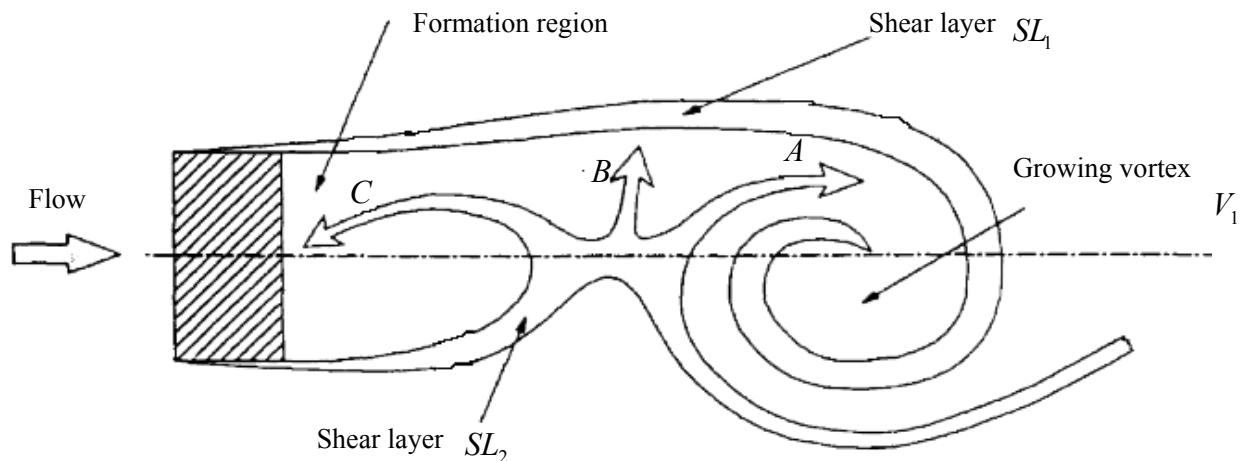


Figure 1-7 Motion of boundary layers during the vortex formation process (after Gerrad [30] and Lucas and Turner [32]).

The six stages of the vortex shedding for a single bluff body in a half cycle are as follows Figure 1-8:

Stage (a), the flow at rear of body reverses anticlockwise to clockwise. Flow of RH boundary layers moving into the RH vortex is about to stop as it becomes

detached. Anticlockwise vortex is about to move downwards to form the left-hand (LH) vortex.

Stage (b), clockwise vortex is starting to form on right, i.e. C flow. LH boundary layers flow into LH vortex. RH layers starting to move left, i.e. B flow starting.

Stage (c), as for (b) with clockwise vortex continuing to develop, RH layers moving further left as the B flow develops.

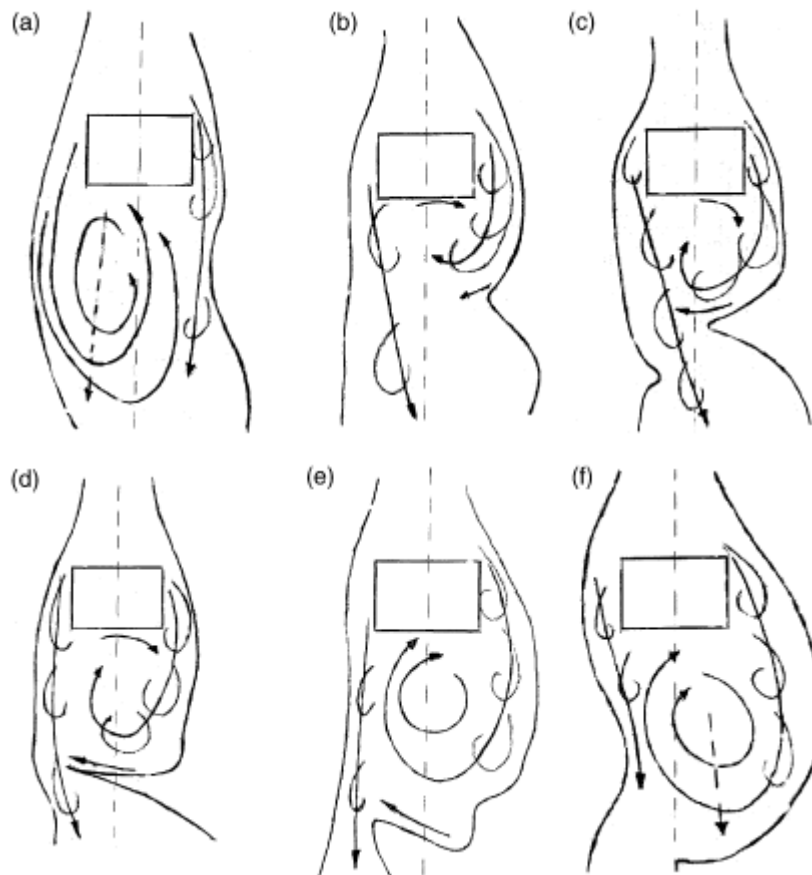


Figure 1-8 Stages in vortex shedding for a single bluff body [33]

Stage (d), as for (c) with a clockwise vortex (C flow) develops further, also RH layers moving further to left (B flow). LH layers still move into the LH vortex.

Stage (e), as for (d), LH layers still moving into LH vortex but RH layers moving left (B flow) are about to cut off this flow of off.

Stage (f), flow of LH layers into LH vortex stopping as LH vortex is detached. Clockwise vortex is about to move downwards to form RH vortex.

At very low Reynolds number, typically $Re = \frac{Ut}{\nu} < 50$ (where U is free stream velocity, t the plate thickness and ν the kinematic viscosity of the fluid), the flow over a rectangular plate is completely laminar and the flow separation does not occur. At slightly higher Reynolds numbers, $50 < Re < 100$, the flow remains attached to the leading edges and side faces of the plate but separates at the trailing corners, giving rise to vortex shedding and the formation of a von Karman vortex street in the wake. However, at all higher Reynolds numbers the flow is dominated by separation of shear layers at the salient points of the body, the leading and trailing corners. Even though the separation points are fixed, the flow regime established is still significantly dependent on the Reynolds number. The Reynolds number and the chord-to-thickness ratio c/t of the plate are the two most important parameters that determine the flow characteristics, when c is the length of the bluff body and t is the thickness of the bluff body.

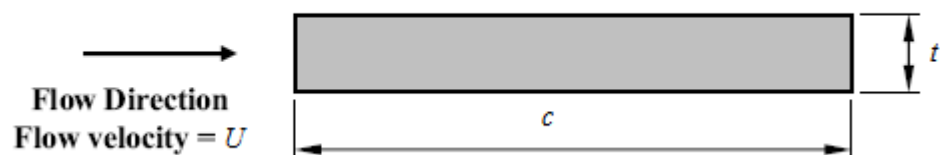


Figure 1-9 A single bluff body with square leading edge.

Following flow separation from a leading corner of a long plate, the separated shear layer reattaches to the side surface of the plate, forming a closed leading-edge-separation bubble as shown in Figure 1-10a. The separation bubble is generally not steady, but fluctuates in length between S_{max} and S_{min} as indicated in the Figure 1-9. On a ‘short’ plate reattachment may or may not occur. For a sufficiently long plate the fluctuating shear layer reattaches intermittently on the plate (Figure 1-10b) and for a very short plate no reattachment occurs (Figure 1-10c). In

addition to the nature of the leading-edge separation, the flow regime established is influenced by the growth of instabilities in the separated shear layers and the characteristics of vortex shedding from the trailing edges of plate. All of these phenomena may be affected by the nature of incident flow, particularly the level of free-stream turbulence.

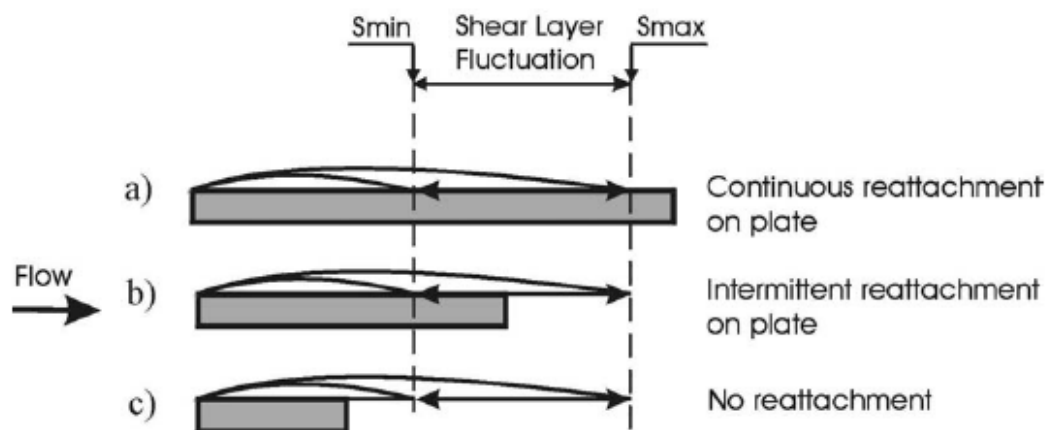


Figure 1-10 Vortex patterns for a square leading edge bluff body.

When a laminar shear layer separates from the leading edge of a bluff body, it may be subject to several types of instability. One is related to transition from laminar to turbulent flow. Another is related to vortex formation, which may involve a Kelvin-Helmholtz instability or, in the presence of a salient edge (such as the trailing edge of a single plate), an impinging-shear-layer instability. The source of both laminar-to turbulent transition and vortex formation can be seen as instability waves in the visualized flow patterns presented by Nakamura, Ohya and Tsuruta [21].

In the case of two-dimensional flow over short plates (i.e. plates with short stream wise chord length, or more specifically small chord-to-thickness ratio c/t) the two shear layers (of oppositely-signed vortices) separating from the leading corners do not reattach to the stream wise side faces but interact downstream of the plate. A flow of

this type shows strong similarities to the most extensively investigated bluff-body flow, namely that around a circular cylinder. An example of the similarity can be seen in Figure 1-11 which shows the flow patterns for a circular cylinder and a very short plate at similar Reynolds numbers.

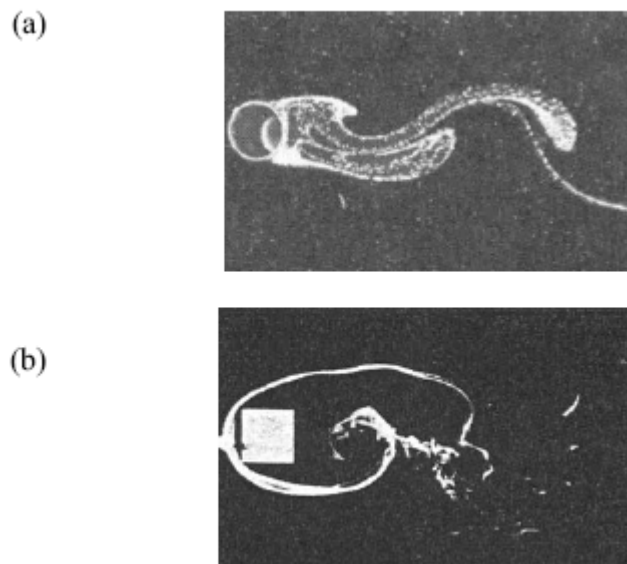


Figure 1-11 Patterns of flow around (a) a circular cylinder at $Re=100$ (Batchelor [34]) and (b) rectangular plate at $Re=200$ (Bearman [35]).

Details of the behavior of separated shear layers in the flow over circular cylinders, obtained in such investigations as those of Roshko [36] and Rockwell [37,38], can be expected to give a good indication of the behavior of the shear layers separating from the leading corners of short rectangular plates in particular the dependence on Reynolds number of the development of turbulent flow from instability of the laminar free-shear-layer and the development of vortices as a result of Kelvin-Helmholtz instability. The experimental findings of the cylinder investigations are broadly in agreement, although the Reynolds numbers which characterize various flow regimes differ somewhat according to individual free-stream flow conditions.

On long plates the separated leading-edge shear layers reattach to the side faces to

form leading-edge-separation bubbles. The bubbles on the upper and lower surfaces appear to have no significant influence on each other. Each separated shear layer is subject to laminar-turbulent and Kelvin-Helmholtz instability: transition to turbulence and vortex formation may still occur, but vortices formed in each shear layer now all have the same sense of rotation (although opposite senses in top and bottom shear layers). There is also a similarity to circular cylinders with a splitter plate located downstream (Unal and Rockwell [38]), free mixing layers, or the separated shear layer behind a backward facing step (Eaton and Johnston [39]). In these flows, in contrast to the short rectangular plate flows, pairing of the small-scale instabilities does take place and a sub harmonic of the transition wave appears in velocity spectra.

Depending on c/t , the turbulent boundary layers can either roll into a regular vortex street in the wake of the plate without reattachment or with intermittent reattachment on the plate ('short' plates), or permanently reattach to form a separation bubble on the plate stream wise surface ('long' plates). For the short plates there is a critical value of $c/t \approx 0.6$ below which the plate does not interact with the separated shear layer (Bearman and Trueman [41]). Using wake frequencies from peaks in the velocity fluctuation spectra measured by hot-wire sensors, Parker and Welsh [40] identify four different flow regimes, depending on chord-to-thickness ratio.

For $c/t \leq 3.2$, flow separation occurs at the leading edge of the plate and never reattaches. The shedding is an interaction generated at the leading and trailing edges of the plates and of the shear layers to form a vortex street. The separated shear layers roll up to form a vortex street downstream of the trailing edge of the plate without reattachment to it, there is a strong correspondence between the Strouhal numbers of the velocity fluctuations and the Strouhal numbers of frequency peaks observed in acoustic spectra. This leads to the conclusion that the vortex formation in the

separated shear layer is the main cause of noise radiation. The level of acoustic radiation reaches its maximum value at c/t corresponding to longer plates within this range. The anti-symmetric vortex street, which is a characteristic flow pattern for this regime, can occasionally, for a duration of a few shedding cycles, switch into a symmetric shedding mode, at least for $Re \leq 1300$. Figure 1-12a shows the flow around a plate with $c/t = 2$ at $Re \approx 800$, with separated shear layers forming a regular von Karman vortex street. However such anti-symmetric vortex shedding occasionally switches into symmetrical shedding as shown in Figure 1-12b.

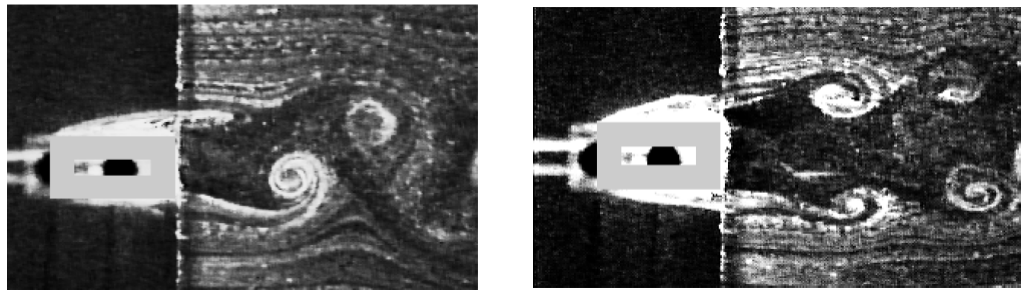


Figure 1-12 Flow visualization for a plate with $c/t = 2.0$ at $Re \approx 800$: (a) anti-symmetric mode and (b) symmetrical mode. [42]

For $3.2 < c/t \leq 7.6$, intermittent reattachment of the shear layers separated from the leading edge of the plate occurs on the stream wise surfaces. The separated shear layers reattach intermittently to the stream wise plate surfaces, vortex formation in the shear layer is the dominant cause of noise radiation for the smaller chord-to-thickness ratios. As the chord-to-thickness ratio is increased, the vortex shedding becomes weaker and the magnitude of the radiated noise drops as it apparently becomes dominated by complex three-dimensional effects. The radiation is also influenced by the low-frequency components associated with a variation in the impingement location of successive vortices. A typical flow pattern at $Re \approx 600$ is shown in Figure 1-13 for a plate with $c/t = 3.6$. In this case the separated shear layers reattach intermittently on the stream wise surfaces of the plates, as is indicated by hydrogen

bubbles swept downstream from a wire located just downstream of the plate's trailing edge (top stream wise surface in Figure 1-13). The shear layers from both sides of the plates merge downstream of the trailing edges and form Karman Vortex Street. The peaks are distinct and accompanied by harmonics for the lower values of c/t , but become smaller and less distinct as c/t is increased. The weakening of the characteristic peaks with the increase of c/t may indicate that as the time during which the separated shear layer is reattached to the plate increases the vortex formation in the layer becomes weaker and less regular and the flow becomes dominated by complex, three-dimensional flow fluctuations in the separated shear layers, as reported in previous investigations such as Kiya and Sasaki [43].

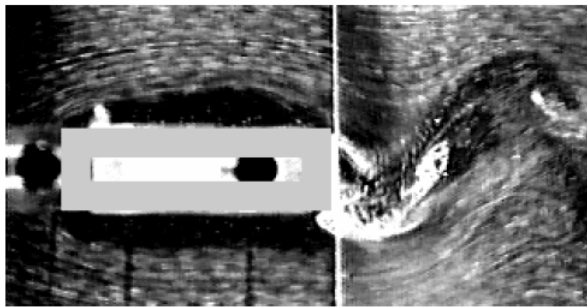


Figure 1-13 Flow visualization at $Re \approx 600$ for a plate with $c/t = 3.6$ [42]

For $7.6 < c/t < 16$, permanent reattachment of the shear layer occurs, but no dominant spectral peak is detectable. The shear layer are always reattached upstream of the trailing edge and form a separation bubble which grows and divides in a random manner. This generates a boundary layer with discrete concentrations of vortices which move along the plate surface towards the vortex street formation region. The vortices are distributed randomly throughout the boundary layers and consequently produce irregular vortex shedding and no clear regular vortex street. The separated shear layer reattaches to the stream wise plate surfaces forming a permanent separation bubble, the only vortex shedding with a detectable discrete

frequency appears to occur at the trailing edge of the plate. This trailing-edge vortex shedding is weak and irregular, especially for the plates with the smaller chord-to-thickness ratios. It contributes to the noise radiation, but sound power level of the spectral peak corresponding to the shedding is relatively low. Figure 1-14 shows flow in Regime 5 around a plate with $c/t = 10$ at $Re \approx 600$ where the shear layers separate at the leading edges and reattach on the plate stream wise surfaces, forming permanent separation bubbles. The streak lines visible in the Figure 1-6 never reach the plate surface, with the mean separation/reattachment streamline located under the streak lines. The reattached flow separates at the trailing edges of the plate, forming a periodic vortex street.

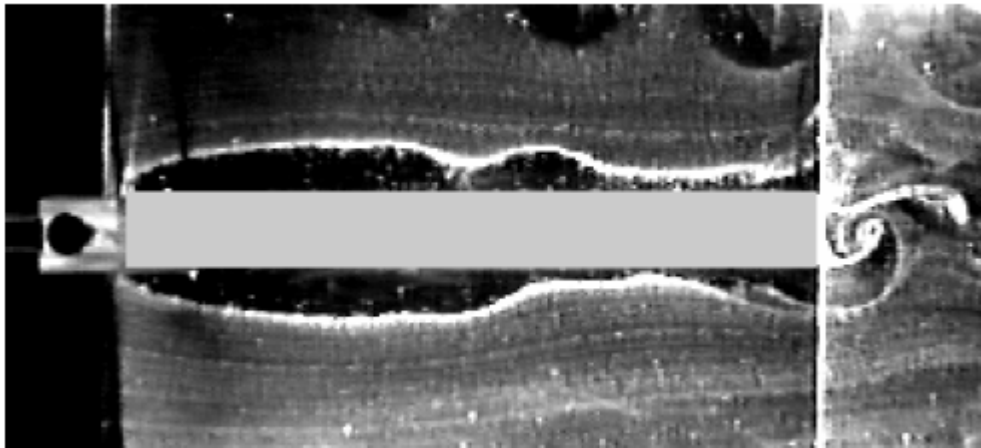


Figure 1-14 Flow visualization for a plate with $c/t = 10.0$, $Re \approx 600$. [42]

For $c/t \geq 16$, reattachment occurs and the spectra show a broad spectral peak that becomes sharper as c/t increases. The separation bubbles fluctuate in length in the same manner as described in $7.6 < c/t < 16$, but the vortices, which are distributed randomly in the boundary layers, diffuse before reaching the trailing edge. The characteristics of the boundary layers on each side of the plate approach those of the fully developed turbulent state and interact to form a regular vortex street not directly related to the formation of leading edge separation bubbles.

The flow over a single plate with a semi-circular leading edge and a square trailing edge is characterized by attached flow over the leading edge and separation of the boundary layer at the trailing edge, followed by regular vortex street formation downstream of the plate. A sketch of the flow structures for flow past a semi-circular leading edge plate and a square leading edge bluff body is shown as Figure 1-15. There is only trailing edge shedding when flow pasts a semi-circular leading edge bluff body.

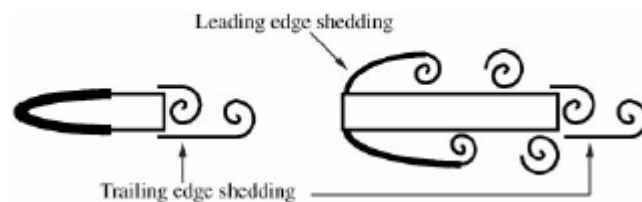


Figure 1-15 Sketches of the vortical flow structures for flow past a semi-circular leading edge plate and a square leading edge bluff body.

The results for plates with semi-circular leading edges show that only two regimes can be identified, separated by a jump in Strouhal number when c/t is approximately 1.20. Flow visualization showed that at $c/t=1.16$, the flow separated from the curved surface and did not reattach, the two shear layer interacting directly to form the vortices behind the plate in the same way as for the shorter, square leading edge plates. The following figure show the result of vortex shedding from a plate with $c/t=16$ and $t=12.1\text{mm}$. It showed the vortices forming very close to the trailing edge and there was only trailing edge vortex shedding.

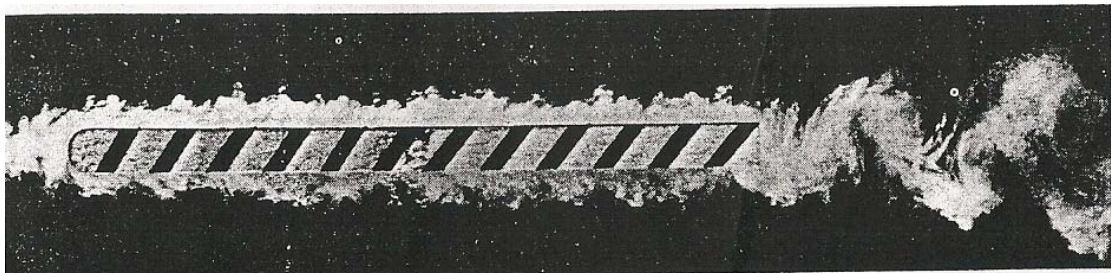


Figure 1-16 vortex shedding from a plate with $c/t=16$ and $t=12.1\text{mm}$ [28].

The theoretical analysis of aerodynamic noise radiation carried out by Lighthill [44, 45] shows that a field of aerodynamic quadrupoles constitutes the main source of acoustic radiation from a free turbulent flow. Lighthill's result for the acoustic power W of quadrupole radiation from a free turbulent flow is

$$W \propto \frac{\rho U^8 L^2}{a^5} \quad (3)$$

where ρ is the fluid density, L a characteristic length of the body, U the flow velocity and a is the speed of sound in the fluid. In contrast, Curle's [46] extension of Lighthill's theory to turbulent flow over rigid objects shows that, if an object is small compared with the wavelength of the radiated sound, it can be treated as a dipole sound source and that the radiated acoustic power is proportional to the square of the force generated by the interaction between the fluid and the object, and the square of a characteristic frequency. This leads to:

$$W \propto \frac{\omega^2 F^2}{\rho a^3} \propto \frac{\rho U^6 L^2}{a^3} \quad (4)$$

where ω is a characteristic frequency ($\sim U/L$), and F is the force fluctuation on the body. Experimental investigations aimed, either directly or indirectly, at testing Curle's theory have been made by Etkin, Korbacher and Keefe [47].

1.2.3 Flow-induced acoustic resonances in duct

It has been found in both experimental [48,49] and numerical studies [50,51] that shedding from both sides of the bluff body are out of phase and locked to a single frequency. The Strouhal number based on chord shows a stepwise increase with an increasing aspect ratio. This is a result of a feedback loop driven by vortices shed from the leading edge which later pass the trailing edge and generate a pressure pulse which in turn propagates upstream to lock further leading-edge shedding. More recent

work [52] has shown the presence of strong vortices forming at the trailing edge between the passing of leading-edge vortices and it has been proposed that the trailing-edge shedding plays a significant role in controlling the details of the feedback loop. As an example, a plate is placed in a duct as shown the sketch in Figure 1-17. The plate is placed centrally along streamwise axis parallel to the mean flow direction. Initially the flow is not locked and many frequencies may be present. If any of these frequencies match the natural frequency of the duct, the acoustic mode in the duct is excited and resonance occurs. If the flow system is receptive to this frequency, the flow will become locked and thus complete feedback loop, sustaining the resonance. Although it is possible to excite numerous acoustic modes in the duct, this study is only concerned with the first β -mode (as defined in [53]). This consists of a single standing wave in the cross flow direction. This field has a pressure node at the centre of the duct and an acoustic particle velocity node at the top and bottom surfaces of the duct. Earlier experiments by Welsh & Gibson [54] found two resonance ranges at $0.10 < S_r < 0.12$ and $0.18 < S_r < 0.21$ for a plate with an aspect ratio of $c/t = 5$. These different resonances were excited by slowly increasing the flow velocity until the flow field became locked to the resonant acoustic field. If the plate had an aerodynamic leading edge, there was only one resonant range [55] because there is no leading edge shedding and the flow at the trailing edge is receptive only over a narrow frequency range. Later experiments [56] for plates in the range of $0.5 < c/t < 16$ found that while certain aspect ratios displayed multiple resonant ranges, these also showed a stepwise increase with aspect ratio.

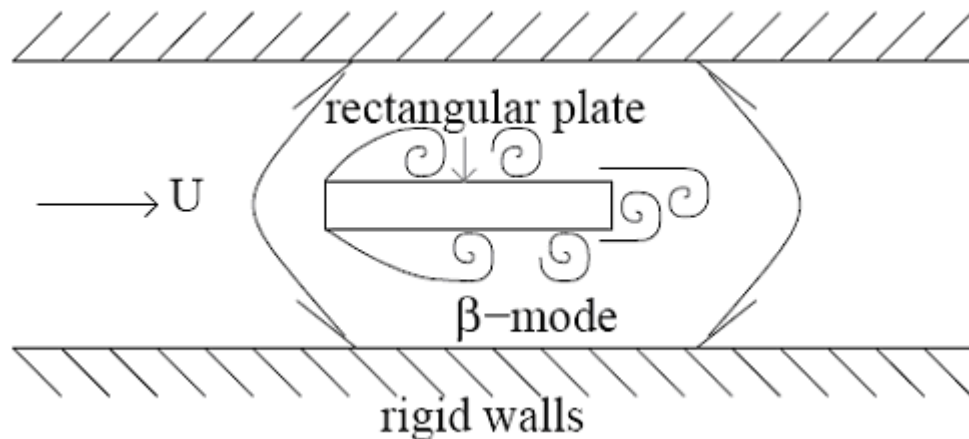


Figure 1-17 Schematic of the plate in a duct leading to acoustic resonance.

A similar phenomenon may occur if an acoustic cavity is present in the downstream. In that case, the acoustic resonance can be classified into self-induced and vortex-induced resonances. The former is excited by vortices shed from the orifice leading edge over the cavity, and often occurs in landing gears, weapon bays in aircrafts, and open cavities in moving vehicles. The latter is caused by vortex shedding from a bluff body in cross flows and is frequently seen in tube or plate bundles of heat exchangers and boilers, cascades of compressor blades and radial diffusers. Flow-induced acoustic resonance may induce acoustic pressure amplitude sufficiently high to cause very serious noise or vibration problems [57].

Strouhal [58] showed that sound is produced when air flows around a body. Although he thought the sound was generated by friction, it is associated with periodic shedding of vortices. Howe's theory [59] quantified the association. In a confined space, such as a duct, the sound generated is reflected back and can become very loud. The sound pressure level (SPL) produced by the flow around a plate with a semi-circular leading edge (Welsh *et al.*[55]) can reach 160 dB. In this case, the resonance occurs over a range of flow velocity where the natural Strouhal shedding frequency is close to the frequency of the appropriate acoustic mode in the space.

Parker P-mode (Parker [53]) is the simplest acoustic mode for a plate in a duct.

When the velocity of air flowing past a plate with a semi-circular leading edge in a duct is increasing, the vortex shedding frequency from the trailing edge is proportional to flow velocity (Constant Strouhal number) until it approaches the P-mode acoustic frequency. Figure 1-18 shows the variation of the vortex shedding frequency and the SPL, at the frequency of the resonant acoustic β -mode. The major peak in SPL is due to locked shedding from the trailing edge, and has been described by Welsh et al [55]. Between 6 m/s and 15 m/s there are seven peaks in the SPL. The sound frequency at each peak is that of the P-mode (606Hz to 619Hz) which is much higher than the corresponding vortex shedding frequency shown in Figure 1-18. The disparity in frequency means that the vortex street is unlikely to be the source of sound. Stokes and Welsh [55] showed that for a plate with a square leading edge, P-mode resonances were generated over several ranges of flow velocity. The source of the sound was the stream of vortices shed from the leading edge separation bubble. These vortices moved along the plate and past the trailing edge where they exchanged energy with the sound field. The direction of the exchange depends on the phase of the acoustic cycle at which each vortex arrives at the trailing edge. This is primarily determined by the time taken for the vortices to traverse the length of the plate, and this in turn depends on the flow velocity. There are many possible time intervals, differing by a discrete number of sound cycles. And each corresponds to a different flow velocity range in which resonance is possible. Water droplets placed near the semi-circular leading edge of the plate used in the experiments described here show the existence of a small leading edge separation bubble. It is hypothesized that the sound field causes small vortices to shed from this bubble at the sound frequency, just as it does from larger bubbles on plates with square leading edges. These vortices would then enter the boundary layer and move along the plate past the trailing edge

where they act as a sound source before merging into the larger vortices observed in the vortex street. Evidence for this hypothesis is given in Figure 1-19. At the P-mode frequency, there is high coherence (0.98) between the probe microphone signal and the signal from the hot wire located above the mid-chord position of the plate. This means that the hot wire signal is associated in both frequency and phase with the sound field. However the velocity perturbation measured is much greater than the acoustic velocities anywhere in the region. Therefore, the coherence of the hot wire signal and the microphone response is attributed to the velocity fluctuations induced by passing vortices, whose release has been triggered by the sound field.

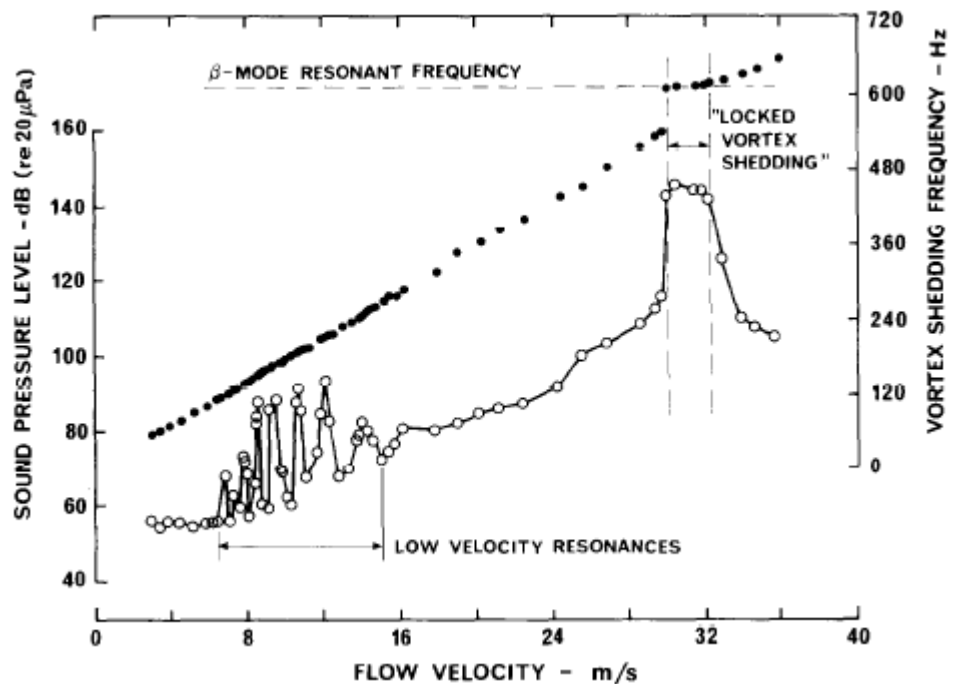


Figure 1-18 Variation of vortex shedding frequency and SPL at the P-mode frequency with flow velocity [60]

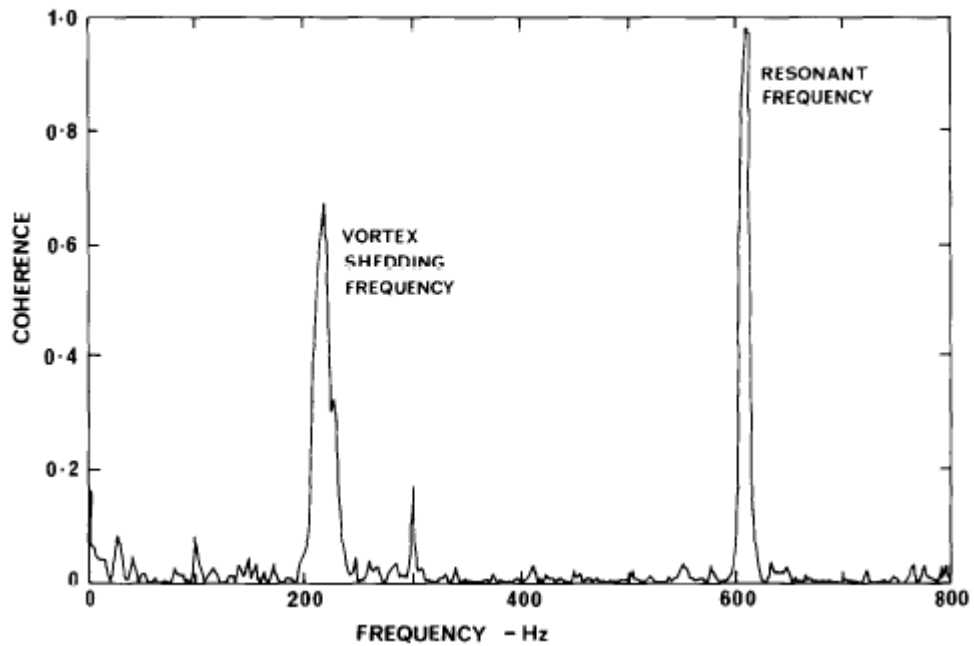


Figure 1-19 Coherence of signals from the hot wire and the probe microphone located above the mid-chord position of the plate; flow velocity = 12 m/s; SPL = 93 dB [60].

Flow-excited acoustic resonance of duct that contains cavities of bluff bodies is a design concern in many engineering applications (Figure 1-20), such as tube bundles of heat exchangers and boilers (Blevins and Bressler[61]; Oengoren and Ziada[62]), cascades of compressor blades (Parker and Pryce[63]) and guide turning vanes in ducts and radial diffusers (Ziada et al.[64]). When these resonances are excited, the resulting acoustic pressure may exceed the dynamic pressure of the mean flow in the duct. This can be sufficiently high to cause acute noise and or vibration problems in diverse industrial equipment. The resonance occurs when the vortex shedding frequency f_s approaches that of first acoustic mode of the cavity. As the acoustic mode is excited by the dipole-like source of vortex shedding (Curle[46]), the resulting sound field of the resonant acoustic mode enhances the process of vortex shedding.

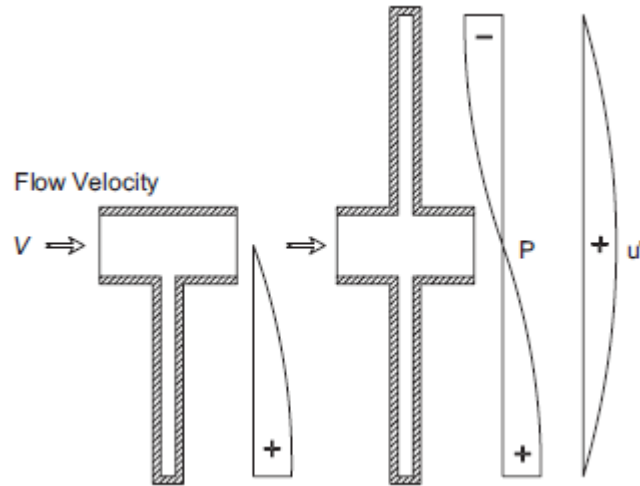


Figure 1-20 the sketch of the duct containing cavities

Ziada and Shine (1999) and Graf and Ziada (1992) demonstrated that for piping systems with long side-branches ($L_{1,2}/d \gg 1.0$) and large diameter ratios ($t/d \approx 1.0$), L is the length of the cavity and d is the height of the duct, the resonance frequencies of the coaxial side-branch modes can be accurately predicted based on the length between the ends of the side-branches and the speed of sound. The piping system can use the standard relationship used for long coaxial branches

$$f_{\lambda/2} = \frac{C(2n-1)}{2L} \quad (5)$$

Where L is the total length of the side-branches including the diameter of the main duct ($L_1 + L_2 + d$) and n is the acoustic mode number.

1.2.4 Control method

Fundamentally, the bluff body excitation amplitude is controlled by the flow velocity, fluid and flow properties, dimensions and geometry of the body, damping and also on the orientation of the body to the flow direction. Hence, in general, by controlling one or more of these factors, the flow induced oscillations could be influenced. But, in situations where some of these factors could not be controlled or

unpredictable (for example, tall buildings exposed to extreme wind flows) or in situations where these factors are set at certain values to achieve certain other engineering objectives, other controlling measures have to be adopted. Two factors are centrally important in the vortex formation and shedding [18], (a) the shear layers should roll up to form vortices of sufficient strength; (b) the shear layers should interact closely with each other. If any one of these factors (or both of them) is disabled or disrupted, then, it would prevent proper roll up of shear layers and thus, the vortex shedding phenomenon which would ultimately suppress the vortex-induced vibrations.

Basically, vortex-induced vibrations could be controlled using passive and active control [67]. Gad-el-Hak [68] classifies recent bluff-body flow controls into three groups (passive, active open-loop, and active closed-loop controls, respectively) for cases of actuator(s) without power input, actuator(s) with power input but no sensor, and sensor(s) and actuator(s) with power input.

Typical examples using passive methods include surface modifications with roughness [69], dimple [70, 71], helical wire [72], longitudinal groove [73], splitter plate [74], and small secondary control cylinder [75]. Among these passive methods, geometric modification in the spanwise direction near the separation point has been recognized as an effective control method. Although these techniques require no energy input, their effect has no relationship with flow or acoustic source and thus their performances are limited.

Active control methods involve the input of energies via actuators to bring about desirable effect on shear flow and subsequent the flow-acoustic system, using either independent external disturbance (the active open-loop control), or feedback-signal controlled system (active closed-loop control). In both cases, one of the key points to

ensure a successful control is that actuators used should create significant effects on physical parameters to be controlled. There are many active open-loop control examples, such as rotary, streamwise, and transverse oscillations of a bluff body; inflow oscillation; electromagnetic forcing; steady blowing/suction; time-periodic blowing/suction; distributed forcing; and a synthetic jet; [76-86]. Sarno and Franke [87] successfully used the active open-loop control to suppress shear layer oscillations in a cavity through a 45° steady or pulsating flow injection to the flow at the cavity leading edge, resulting in a reduction of 10 dB in the sound pressure level (SPL) at the occurrence of the acoustic resonance.

Controls using either passive or open-loop method cannot always lead to ideal performance for the control signal is not directly related to the response of the fluid field or body vibration. This problem can be solved by using active closed-loop methods; the input signal to the actuators for controlling is continuously adjusted based on the corresponding feedback signals acquired by sensors. Berger [88] first introduced the single-sensor feedback control by actuating a bimorph cylinder with signals from a hot-wire sensor located in the wake, reporting the possibility of suppressing vortex shedding behind a bluff body. Ffowcs Williams & Zhao [89] performed a feedback control of vortex shedding at $Re = 400$ with a loudspeaker based on the velocity phase information measured at a point in the wake and showed that velocity fluctuations at the nominal vortex shedding frequency were reduced. Park et al. [90] conducted a numerical simulation on a similar feedback approach by using a pair of blowing/suction slots on a cylinder and a single feedback sensor located in the wake, they showed that control results are sensitive to the feedback sensor location. Huang and Weaver [91] and Ziada *et al* [92] measured the fluctuating acoustic pressure inside the cavity, mounted on the wall of a tunnel, by a microphone

for feedback signals. The feedback signals were then amplified and phase-shifted by a controller to drive the loudspeakers at the entrance of the tunnel and at the upstream corner of the cavity, respectively. In this way, the shear layer oscillation across the cavity was attenuated by the acoustic excitation and thus the SPL under resonance was effectively reduced by 15 dB. In addition, Cattafesta *et al.* [93-95] and Kook *et al* [96] used an oscillating flap hinged near the cavity leading edge to disturb the shear layer separation. The action of the flap was controlled by a closed-loop controller with the feedback signals from the fluctuating acoustic pressure measured by a microphone within the cavity. As a result, the attenuation in SPL by 20 dB was reported in both of the two papers when the acoustic resonance occurred.

Cheng *et al* [97] developed a novel perturbation technique to control both vortex shedding and structural vibration. The essence of the technique was to generate a controllable transverse motion of a structural surface using embedded piezo-ceramic actuators to alter fluid-structure interactions. The perturbed action to flow was based on an advanced piezoceramic THUNDER (THin layer composite UNimorph Driver and sEnsoR) [98] actuator. THUNDER could provide large displacement and load capacity, smaller dimensions, more reliability, strength and flexibility than other traditional actuators. In addition, its operation, unlike loudspeakers used in most other work, would not generate any noise.

Zhang [99] experimentally studied an open-loop control of fluid-structure interaction by using the proposed perturbation technique. Three THUNDER actuators, embedded underneath the surface of the cylinder, and produced a periodic perturbation on the cylinder surface and thus the fluid field, which altered the interactions between synchronizing cylinder motions and vortex shedding. Subsequently, both vortex shedding and its induced cylinder vibration were modified

simultaneously.

In order to improve the control performance obtained in the open-loop control and reveal the underlying physics of flow-structure interaction under external perturbation; Zhang *et al.* [100-103] developed a closed-loop control system based on a PID controller, including a resonant flow structure coupling on a flexible-supported rigid cylinder[100-101], a resonant flow-structure coupling on a fix-supported flexible cylinder [102], and a non-resonant coupling on a fix supported flexible cylinder.[103]. Three piezoelectric ceramic actuators were used to perturb the upper surface of the cylinder. They considered three control schemes using different feedback signals, such as the streamwise velocity signal (PID-u control), flow-induced structural oscillation signal (PID-Y control), and a combination of both signals (PID-Yu control). The feedback control based on PID-Yu showed the best result and led to an almost complete suppression of vortex shedding. This technique has recently been successfully applied to the control of noise caused by blade-vortex interaction (BVI) [104] and the control of airfoil aerodynamics [105]. Piezoceramic actuators are lighter and smaller than other actuation devices such as loudspeakers and electromagnetic actuators. Owing to its special design, the actuator presently used requires a relatively low energy input to generate appreciably large displacements. Typically, without any loading, it can vibrate at a maximum displacement of about 2 mm and a frequency up to 2 kHz.

Zhang *et al.* [106] further proposed an active open-loop control to the control of vortex-induced acoustic resonance, comprised an upstream structure as vortex generator and a downstream acoustic cavity as noise amplifier. Piezoelectric actuators are embedded into the structure to generate control action to the flow. Experiments target the occurrence of acoustic resonance when the vortex shedding frequency

coincides with first acoustic resonance of the duct. It was found that the induced transverse vibrations were effective to reduce the acoustic resonance. The cavity sound pressure level (SPL) at resonance was reduced by 8.2 dB in presence of actuation. Zhang's work mainly focused on flow-induced vibration. Though the flow-induced acoustic resonance phenomenon was investigated by using the open-loop control, apart from the apparent performance of the control, the underlying physical mechanism behind the control action still remained unknown. Furthermore, the sound reduction was interpreted as a direct consequence of the vortex strength impairment, the reason behind which, however, could not be fully explained either. Therefore, the primary objective of the present work is to provide a comprehensive assessment on the efficiency of the technique using an improved actuator configuration, and more importantly, provide experimental evidences for further explanation on the control mechanism of the perturbation technique in attenuating flow-induced sound.

1.3 Motivations and Objectives

The problem of flow-structure-sound (FSS) interaction is a very complex and challenging research area relevant to a large variety of applications in mechanical, civil and environmental engineering. Previous literature review shows that tireless effort of researchers and significant progresses have been made in the past few decades. But new ideas and breakthroughs are still much needed to provide practical solutions to various engineering problems.

Most existing work has focused on a separate control of either flow field or structural vibration. A few papers which aim at controlling the structural vibration in a cross flow, considered the flow only as a disturbance, rather than a control target. In fact, a simultaneous control of both flow and its structural vibration would probably

be more effective. So, one aspect awaiting technological breakthrough is the development of innovative technologies for the dual purpose of stabilizing flow and suppressing flow-induced vibration, and then to reduce the vortex-induced noise.

Details of the mechanism under the application of control action on the vortex shedding have not yet been comprehensively investigated. In particular, detailed analyses are still needed for a number of phenomena, including the study of the motions of boundary shear layers and the entrainment flows; and the change of vortex strength and vortex shedding frequency under the control application.

Flow-induced acoustic resonance may generate sufficiently high acoustic pressure amplitudes that may cause serious noise or vibration problems. Control of vortex-induced acoustic resonance, however, has been scarcely reported in the literature, apart from a few papers reporting numerical simulations of the phenomenon. The present thesis will further develop an active closed-loop control system for minimizing the strength of vortex-induced acoustic resonance. The controller was implemented via a DSPACE rapid control prototyping system, which utilized feedback signals from sensor measurements and generated control actions to the piezo-driver for actuating THUNDERS. Hot wires and microphones were used either separately or simultaneously as feedback signals. A series of tests and analyses were then performed for the dual process of assessing the performance of the developed technique in suppressing vortex-induced noise and of providing guidelines for choosing the best control strategy.

In conclusion, the main objective of this work is to develop an active closed-loop control system for suppressing flow-induced acoustic resonance. In the pursuit of this objective, the following specific issues are aimed in this work:

- 1) To develop an active control methodology to control the vortex-induced noise

by using piezoelectric actuator-based perturbation technique, applied to different shapes of bluff bodies.

- 2) To carry out a systematic experiment to investigate the controllability of the system and the physical mechanism of surface-perturbation control action for different leading edge test models.
- 3) To understand the mechanism of vortex shedding strength reduction and quantify the control effect for better physical understanding and find an optimal control strategy for different types of the test models.

1.4 Outline of the thesis

This thesis is organized in seven chapters.

Chapter 1 introduces the background of the present work. Previous related works are reviewed and the motivation and objectives of the present investigation are presented.

In Chapter 2, the experimental condition is introduced and quantified, in which the flow field in the present system is measured and analyzed. The characteristics of the test model used to implement the perturbation technique are described.

The open-loop control is experimentally investigated in Chapter 3. The control performance is shown and the preliminary mechanism is analyzed. The equation for the shedding frequency shift is developed and its effect on the cavity resonance is discussed.

In order to improve control performance, in comparison with other previous work in open-loop control, the present thesis includes comprehensive analyses on closed-loop control implementation. To take the advantage of the unique characteristics of actuators used in the test model, a down-sampling theory is proposed in the present experiment. Details of the closed-loop control implementation

are discussed in Chapter 4.

Further in Chapter 5, a method to improve the performance of open-loop control is proposed by using the closed-loop control utilizing the down-sampling theory. The best control performance is shown and the physics mechanism behind the open-loop control and closed-loop control is further analyzed.

The control strategy of various leading edges is investigated in Chapter 6. Differences between square and semi-circular leading edges are investigated together with the corresponding control mechanisms. In order to understand the effect of different perturbation positions on vortex shedding control, the present work implements surface perturbations at different locations over a test model and investigate the control mechanism.

Finally, the conclusions drawn from the work are summarized in Chapter 7.

2. The surface perturbation technique and experimental set-up

2.1 Introduction

The nonlinear dynamics of vortex shedding behind the bluff body had been the focus of increased attention in recent years. In these investigations, it was found that certain features of the vortex shedding behind the vibrating bluff body could be predicted by a low-dimensional iterative model [107-110]. In their work, the circle map, a standard universal model describing systems with two coupled oscillators, was used to study a cylinder wake subjected to an imposed oscillation of controlled amplitude and frequency. Although in the present study, the test model was a semi-circular leading edge bluff body or square leading edge bluff body, which is different from the cylinder, the method that Olinger [110] used in developing the low-order model for vortex shedding behind vibrating cylinder could be used to develop the low-order model for vortex shedding behind vibrating semi-circular leading edge or square leading edge bluff body.

Based on this low-order model, the surface perturbation technique, developed by Cheng et al [97], could be used and interpreted to actively control vortex shedding, flow-induced acoustic resonance and structural vibration. The technique was primarily used to generate a controllable transverse motion on a structural surface using embedded piezo-ceramic actuators to alter the fluid-structure interaction.

The main aim of this chapter is to introduce the low-order model and the surface

perturbation technique. The low-order model for vortex shedding behind the vibrating bluff body is first developed, and then the principle of the surface perturbation technique, piezoelectric effect and THUNDER actuators will be described. The design of test models based on the surface perturbation technique will be then introduced. Finally, the design of downstream cavities and the preparation for the experimental set-up, including the control platform will be discussed.

2.2 A low-order model for vortex shedding behind a vibrating bluff body

In Figure 2-1, a semi-circular leading edge bluff body is put in airflow stream. The frequency of the vortex shedding behind a rigid bluff body is denoted by f_s . Suppose that a periodic excitation $C(t) = A \sin(2\pi f_v t)$ is used to vibrate the bluff body where, f_v is the signal frequency and A is the signal amplitude. The displacement of the bluff body is denoted by d_v . Due to the interaction between the vortex shedding and the vibrating body, the frequency of vortex shedding is changed to f'_s . Here, the displacement of bluff body is normalized and represented as $K = \frac{d_v}{t}$, where t is the thickness of the bluff body. Two parameters are defined: the bare winding number:

$$\Omega = \frac{f_v}{f_s}, \quad (2-1)$$

and the dressed winding number:

$$\Omega' = \frac{f_v}{f'_s}. \quad (2-2)$$

The bare winding number Ω can be thought of as an uncoupled frequency ratio in the absence of perturbation, while the dressed winding number Ω' is the coupled frequency ratio when perturbation is applied.

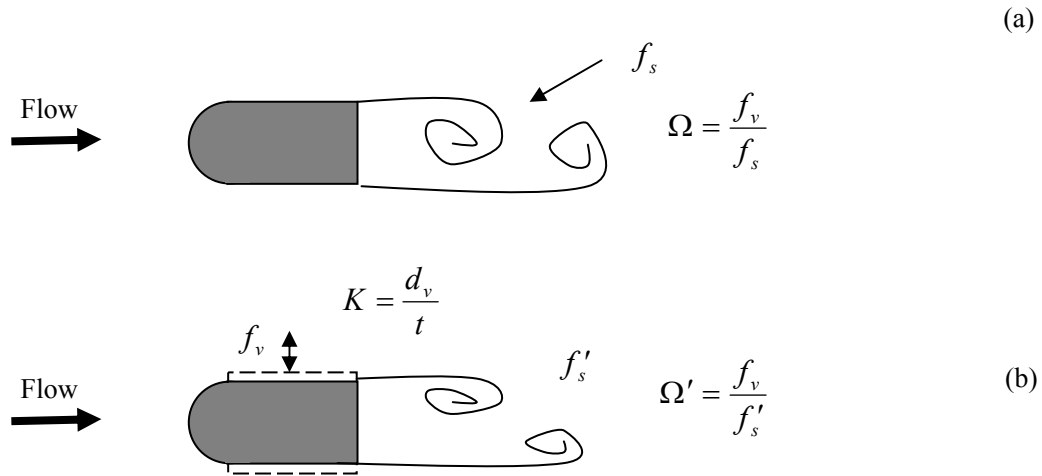


Figure 2-1 The schematic of the vibrating semi-circular leading edge bluff body in the flow stream. a) Without vibration, the vortex shedding frequency is f_s ; b) With vibration, the frequency of the signal is f_v and amplitude A .

In Figure 2-1, when the bluff body vibrates, the body acts as an oscillator. The vibration influences the vortex shedding behind the body. At the same time, the vortex shedding also induces vibration in the flow field, so it acts as another oscillator. These two types of non-linearly coupled oscillators moves in the phase space on a two-dimensional torus T^2 , which is the product of limit cycles of each of the two oscillators [110] as shown in Figure 2-2. The major and minor circumferences of the torus are each traversed at frequencies f_v and f'_s respectively. Different types of orbits on this attractor are studied for investigating the dynamical behavior of a physical system. When the dressed winding number $\Omega' = \frac{f_v}{f'_s}$ is a rational number, the orbit is in the Mode-locked states. In this state, the two-dimensional torus closes upon itself, which means that it is a periodic motion.

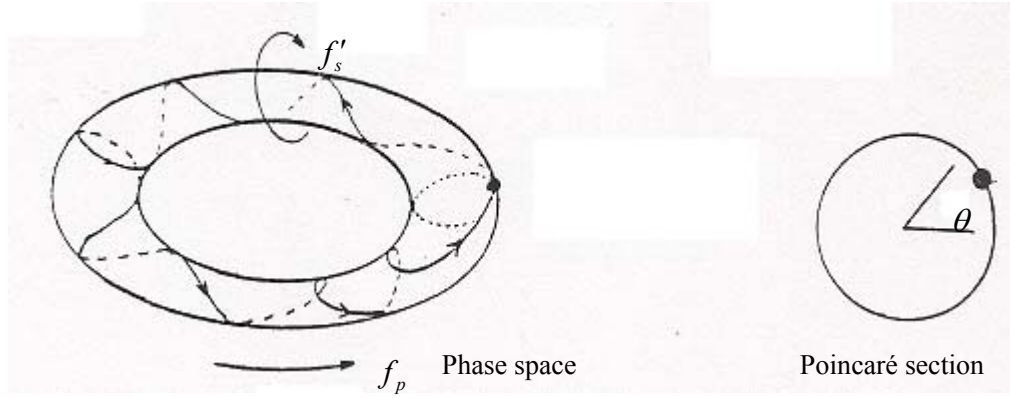


Figure 2-2 A generic system of two nonlinearly coupled oscillators at mode-locked state in phase space and Poincaré section [110].

A cross section of the torus, obtained by cutting the torus with a plane surface, can be used to study the coupled oscillators while still retaining all the essential dynamical information. In general, the torus is not a plane but all orbits should cross it transversally. A Poincaré section can be extracted from the trajectory of a system simply by sampling the trajectory at time intervals separated by one of the two frequencies in the system, f_p and f_s , as these two frequencies represent the frequency of passage around the major and minor circumferences of the two-dimensional torus. The dynamics of the system is then reduced to the investigation of the Poincaré section. Poincaré section is also shown in Figure 2-2. The angular coordinate θ (radians) parameterizes the angular rotation on the Poincaré section. The study of the dynamics system is accomplished by building a return map of the circle onto itself. A return map is a functional relationship between the angular coordinate at the n -th crossing of the Poincaré section, θ_n , and the angular crossing at the $(n+1)$ -st crossing θ_{n+1} :

$$\theta_{n+1} = f(\theta_n). \quad (2-3)$$

In general, a second order differential equation

$$\theta'' = f(\theta, \theta') \quad (2-4)$$

can be used to describe a general system with a periodically excited nonlinear

oscillator. This function can be recast into a system of two first-order differential equations in the variables θ and θ' . Bohr [111] and Bak [112] developed a method to construct a return map between values of θ and θ' . Equation 2-4 became

$$\theta_{n+1} = g_1(\theta_n, g_2(\theta_n)) \quad (2-5)$$

where the functions g_i are periodic in θ . Equation 2-5 is a one-dimensional map of the circle onto itself. A general form of equation 2-5 which is known as the sine circle map [113-121] is most often studied:

$$f(\theta) = \theta_{n+1} = \theta_n + \Omega - \frac{K}{2\pi} \sin(2\pi\theta_n) \quad (2-6)$$

where $\Omega = f_v/f_s$ represents the average angular shift around the Poincaré section in the absence of forcing. The parameter K is analogous to the external forcing imposed on the system d_v/t . When $\Omega = 0$ and $K = 0$, it means there is not external excitation, the angular Poincaré section in does not change. When there is external excitation, $\Omega > 0$ or $K > 0$, the angular Poincaré section in changes due to the external frequency or displacement.

A low-order model for vortex shedding behind the vibrating bluff body is developed. In Equation 2-6, one can conclude that the vortex shedding behind the bluff body can be controlled by imposing vibration on the bluff body. Though Equation 2-6 cannot predict the exact strength or shedding frequency change on vortex shedding when an external oscillators are introduced to the system, it shows that the vortex shedding can be influenced by controlled parameters $\Omega = f_v/f_s$ and $K = d_v/t$, which are relative to the amplitude and frequency of external vibration. In principle the external vibration could be imposed in several ways, for example through acoustic excitation, a perturbation or a time varying mean flow. In the present experiment, a perturbation at a controlled amplitude and frequency in the transverse

direction of the up surface of the bluff body is used.

The low-order model for vortex shedding behind the vibrating bluff body indicates that the vortex shedding behind the bluff body can be controlled by using external controllable vibration or perturbation. However, this model cannot predict the exact change of both the frequency and energy associated with the vortex shedding under the influence of external oscillators. The model is only a qualitative model for determining the relationship between two coupled oscillators.

2.3 Experimental setup

A closed circuit acoustic wind tunnel was used to carry out the experiments in the present thesis [Figure 2-3]. The flow in the wind tunnel was generated by a fan and an embedded control system could be use to adjust the flow velocity with an accuracy of about 0.1m/s. The wind tunnel had a parabolic contraction at the inlet to improve the uniformity of the flow velocity profile, and reduce boundary layer thickness. A flat-walled diffuser, with a half angle of 14° , was used downstream of the working section to increase pressure recovery. The maximum flow velocity was 50 m/s with a turbulence intensity of less than 0.1% in the upstream section. The background noise of the tunnel was low since the motor and fan noise was mostly absorbed by acoustic lining.

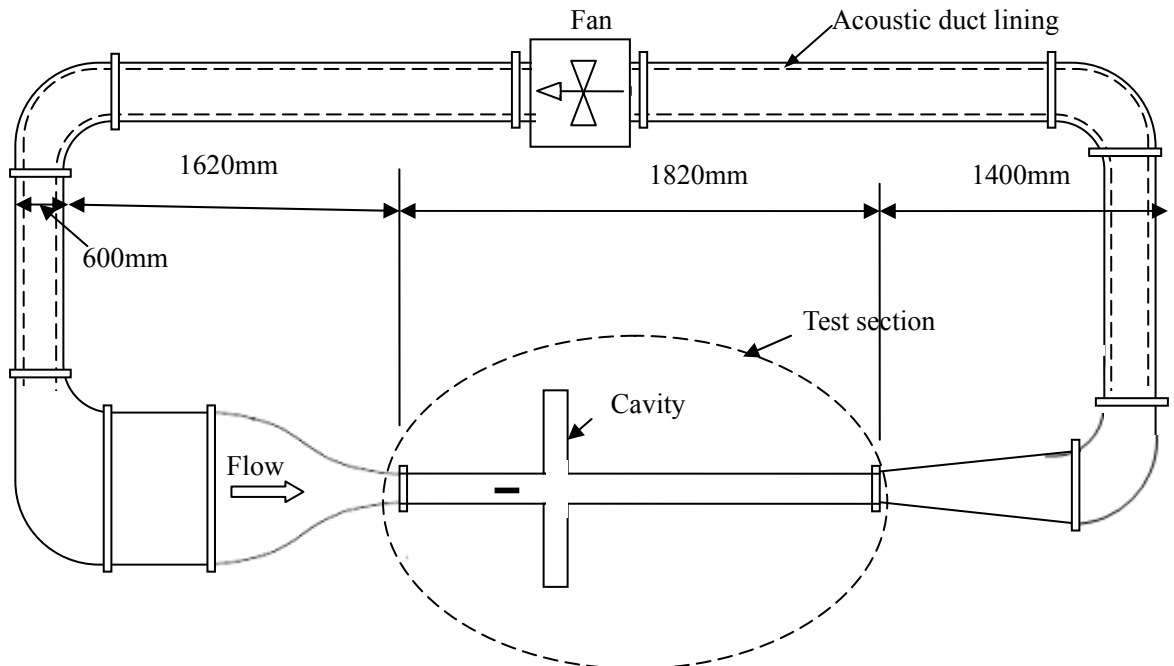


Figure 2-3 Sketch of the wind tunnel system.

In the working section of the wind tunnel system shown in Figure 2-3, a 1.82-m-long duct which had square test section of $100\text{ mm} \times 100\text{ mm}$ was installed, and the thickness of the duct wall was 10mm. The resonance frequency of the duct system was estimated to be 1700Hz. Since the vortex shedding frequency of interest was below 200Hz, the vortex shedding in the duct could not excite the resonance of the duct system.

A test model with either semi-circular leading edge or square leading edge was used as a vortex generator. Design detail of the model will be given later. The test model was placed on both side walls of the test section and located about 0.4 m downstream of the exit plane of the tunnel contraction. The origin of coordinates was located at the leading edge of the test model.

Two identical downstream cavities with square cross sections were located downstream of the plate, symmetrical to the streamwise flow line. The two downstream cavities acted as side-branch acoustic resonators. The distance between the trailing edge of the plate and the downstream wall of the cavities was about $10.0t$,

t was the thickness of the test model. This distance ensured an effective resonant fluid-acoustic interaction in the near vortex shedding of the test model inside the downstream cavities.

2.4 The surface perturbation technique

2.4.1 The principle of the surface perturbation technique

When a bluff body is placed in a fluid stream in a duct, separated flow can be generated over a substantial proportion of the surface, yielding a vortex shedding process. The shedding of vortices from alternate sides of the cylinder becomes regular when the Reynolds number is sufficiently large. Such a vortex shedding phenomenon is called the Kármán vortex street, which can generate strong vortex-induced noise in the duct as depicted in [Figure 2-4(a)].

Based on the low-order model for vortex shedding behind vibrating bluff body developed in Section 2.2, small local perturbation techniques can be implemented on the surface of bluff body in order to alter the vortex shedding behind the body. Previous work has indicated that local perturbations might significantly influence the nature of fluid–structure interaction or the vortex-induced structural vibration [107-113]. Based on this understanding, Cheng *et. al* developed a novel perturbation technique which was conceived to provide a possible control of both flow-induced acoustic resonance and structural vibration. When a small local perturbation was imposed on the structural surface of the bluff body such as using PZT actuators [Figure 2-4(b)], it was found that the vortex shedding could be altered and then consequently the vortex-induced noise was reduced.

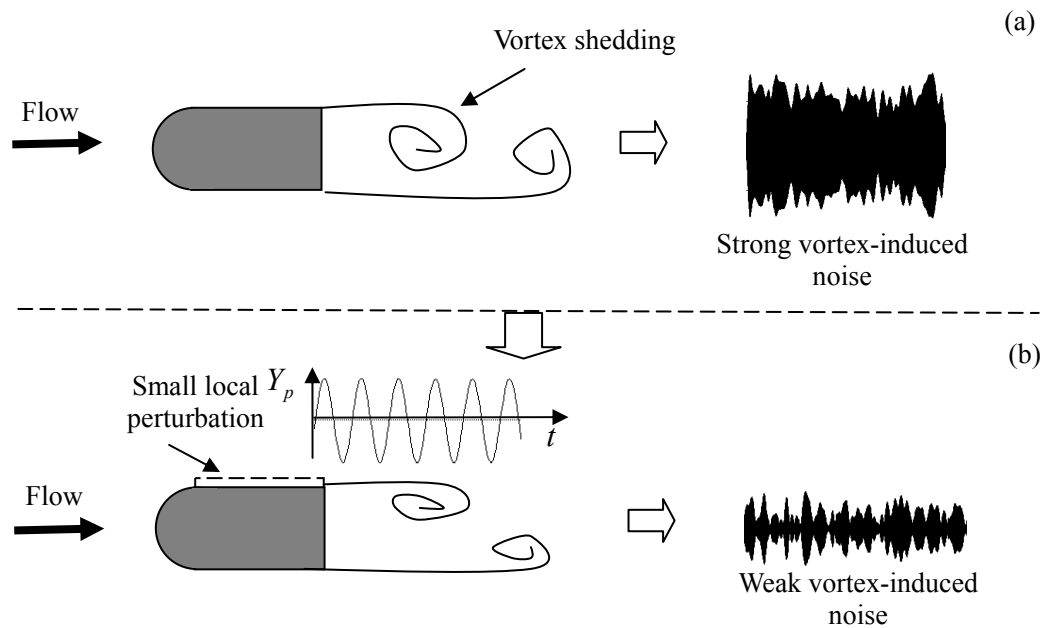


Figure 2-4 The surface perturbation technique: (a) The strong vortex-induced noise; (b) The effect of a small local surface perturbation.

2.4.2 The piezoelectric effect

The piezoelectric effect was discovered by Jacques and Pierre Curie in 1880. Piezoelectric effect describes a phenomenon that occurs in a certain class of naturally occurring crystalline materials such as quartz, Rochelle salt and tourmaline. When an electrical charge (voltage) is applied to them, these materials change their geometry or dimensions. Conversely, when mechanical pressure is applied to them, they produce an electrical charge (voltage). However, these natural materials only exhibit minor piezoelectric behavior, leading to a development of piezoelectric ceramics with improved piezoelectric properties. These types of materials are often made of polycrystalline ferroelectric materials such as BaTiO₃ and Lead Zirconate Titanate (PZT).

The piezoceramic material is composed of randomly oriented crystals or grains. The material is isotropic and it does not exhibit any piezoelectric effect when no electric field (poling) is applied because the domain dipoles are randomly oriented.

When electric field poling is applied across the material, the dipoles will tend to align themselves parallel to the direction of the electric field, so that the material will have a permanent residual polarization. The material is then considered to be anisotropic because of the increased number of aligned dipoles. After the poling process, the material has a residual polarization, which means the domains will proportionally increase their alignment with an applied voltage. The result is a change of the geometric dimensions (expansion, contraction) of the PZT material with an applied voltage. [Figure 2-5]

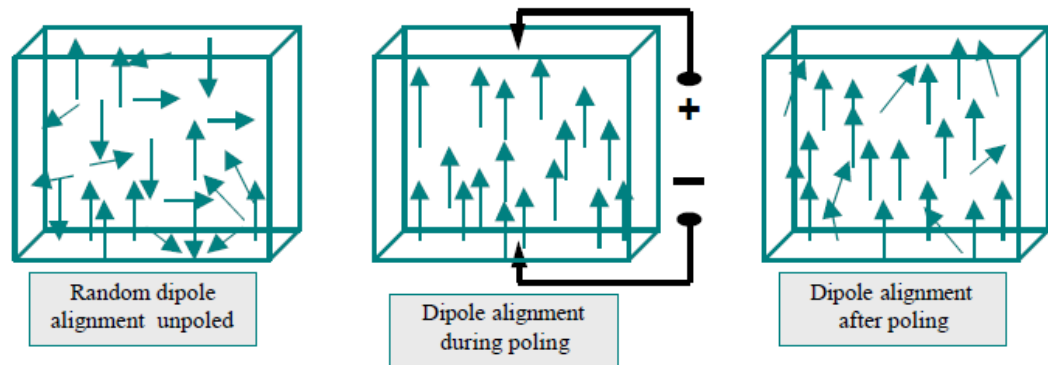


Figure 2-5 Dipole alignment in piezoelectric material. (Refer to: technique document of THUNDER actuators).

2.4.3 THUNDER actuator and its installation

THUNDER actuators were used in the present study for create controllable perturbation over the structural surface. THUNDER, developed by NASA Langley research center in 1996, is a ‘smart’ piezoceramic-based element. It is most commonly used in actuators, sensors, and acoustic sound generators. THUNDER is a unique, extremely rugged and highly adaptable member of the ‘smart’ materials group of products. THUNDER is a ferroelectric device made of multiple layers of material, typically stainless steel, aluminum and PZT piezoceramic. All the individual material layers are held together in a ‘sandwich-like’ package using a NASA patented high temperature polyimide adhesive called LaRCTTM-SI. The bonding strength of the

adhesive induces a ‘pre-stress or pre-load’ in the device and enables THUNDER to have exceptional ruggedness and performance capability. THUNDER is a layered composite in which individual materials are layered on top of each other to form a ‘sandwich’, In a ‘standard’ THUNDER configuration found in Figure 2-6(a), the bottom layer is stainless steel followed by an adhesive, usually a NASA invention and trademarked material called LaRC™-SI, PZT, more LaRC™-SI and finally an aluminum layer on top. The entire assembly is placed into an autoclave for processing. During the autoclave cycle the ‘sandwich’ is heated and squeezed, allowed to cook and then cooled to room temperature. During the cool down cycle, the different individual materials' thermal coefficients of expansion rates begin to work against one another. However, the strength of the adhesive bond holds everything together. The result is a ‘pre-stress’ internal to the individual layers that results in the characteristic bend or curvature of the final product. [Figure 2-6(a)]

2. The surface perturbation technique and experimental set-up

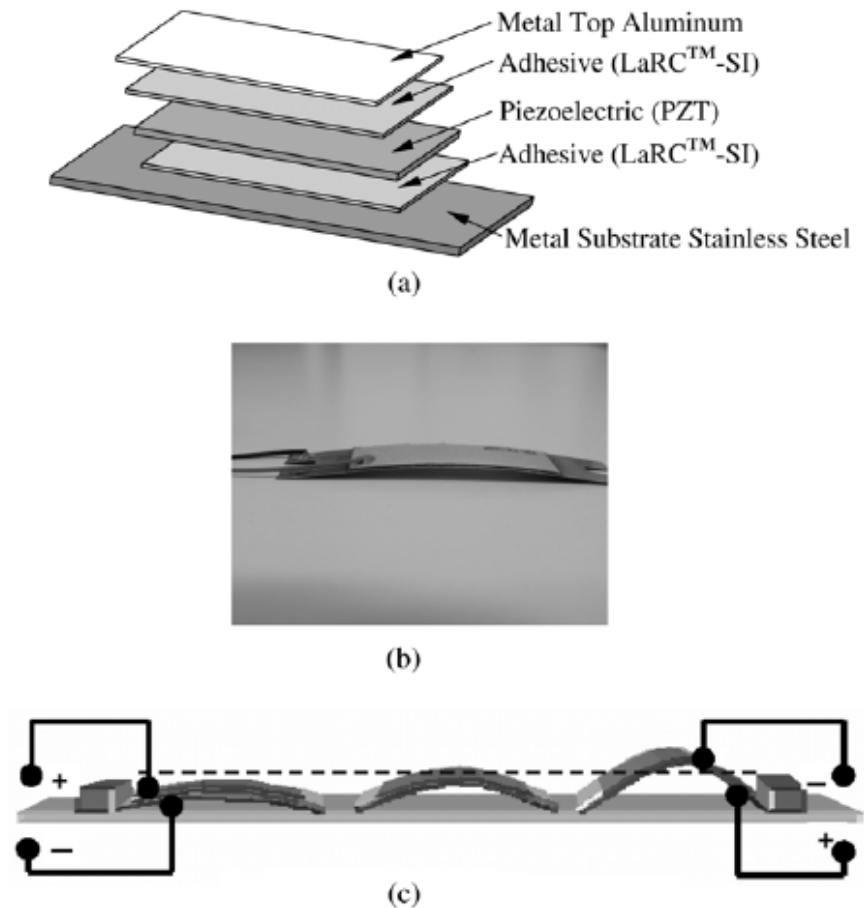


Figure 2-6 Description of THUNDER actuators: (a) THUNDER construction; (b) A photo of THUNDER; (c) A typical deformation versus applied voltage. (Refer to: technique document of THUNDER actuators).

When zero voltage is present at the electrodes of a standard THUNDER device, the piezoceramic material is in a pre-stressed compressive state. At the same time, the substrate is actually in a tensile state as described previously. When positive voltage is applied across the electrodes of a THUNDER device, the piezoceramic is geometrically allowed to ‘shrink’, reducing the internal compression. This causes the stainless steel substrate to flatten and the THUNDER to move downward. Conversely, when negative voltage is applied across the electrodes of a THUNDER device, the piezoceramic is electrically excited and geometrically ‘grows’ in size. Since it is bonded to the stainless steel substrate, the substrate is made to arch to accommodate the ceramic’s increased length. This causes THUNDER to move upward. [Figure

2-6c]

The THUNDER actuator used in the present work was the model TH 8-R, which may vibrate at a maximum displacement of about 2 mm within a frequency range up to 2 kHz in the absence of loading and may produce a force up to 67 N. [Figure 2-6(b)]. There are two mounting methods for the THUNDER actuator: simply supported mounting and cantilever mounting. [Figure 2-7]. Various measurements were done to check these two methods. It was found that the THUNDER actuator is easy to setup by using a simply supported mounting method, but the displacement achieved by using the simply supported mounting method was much less than that of the cantilever mounting method. Another key factor that needs to be considered is that the THUNDER actuator needs to be fixed at one end to make sure that the actuator will not move when placed in the flow. So in the present experiment, the THUNDER is arranged in the cantilever position.

The detail of the installation of the THUNDER actuator in the cantilever position is shown in Figure 2-7(b). The THUNDER actuators should be firmly clamped or fastened at one end by using the tabs made in the substrate material. Slots in the tabs are not mandatory but are provided for ease of mounting. As a rule of thumb, the aluminum top layer can be considered as the geometric limits of the piezoceramic. The extreme deflection capability of THUNDER may cause stress at the mounting point, so to be certain the THUNDER is fastened at least 0.015 to 0.025 inches away from the edge of the ceramic. The deflection of THUNDER is measured in the cantilevered beam mount by placing a laser beam on the far edge of the ceramic, not the edge of the bottom substrate.

2. The surface perturbation technique and experimental set-up

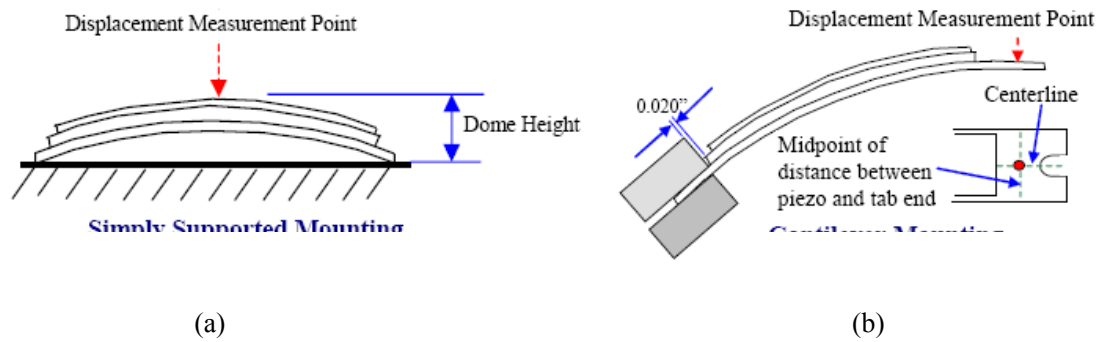


Figure 2-7 Mounting method of the THUNDER actuator. (a) Simply supported mounting and displacement measurements; (b) Cantilever mounting and displacement measurements. (Refer to: technique document of THUNDER actuators).

The characteristic of a single THUNDER actuator in the cantilever mounting position was measured by using a Polytec Series 3000 Dual Beam laser vibrometer. A signal generator generated various sinusoidal signals with different frequencies. These control signals were amplified by a PZT amplifier before they were applied to the THUNDER actuator. The results were shown in Figure 2-8, where it was found that the THUNDER had resonant frequencies at 55Hz and 380Hz. In the subsequent experiments, the vortex shedding frequency is smaller than 200Hz, so the vibration characteristic of the THUNDER actuator at first resonant frequency 55Hz will be used for the design of test model in Section 2.5.

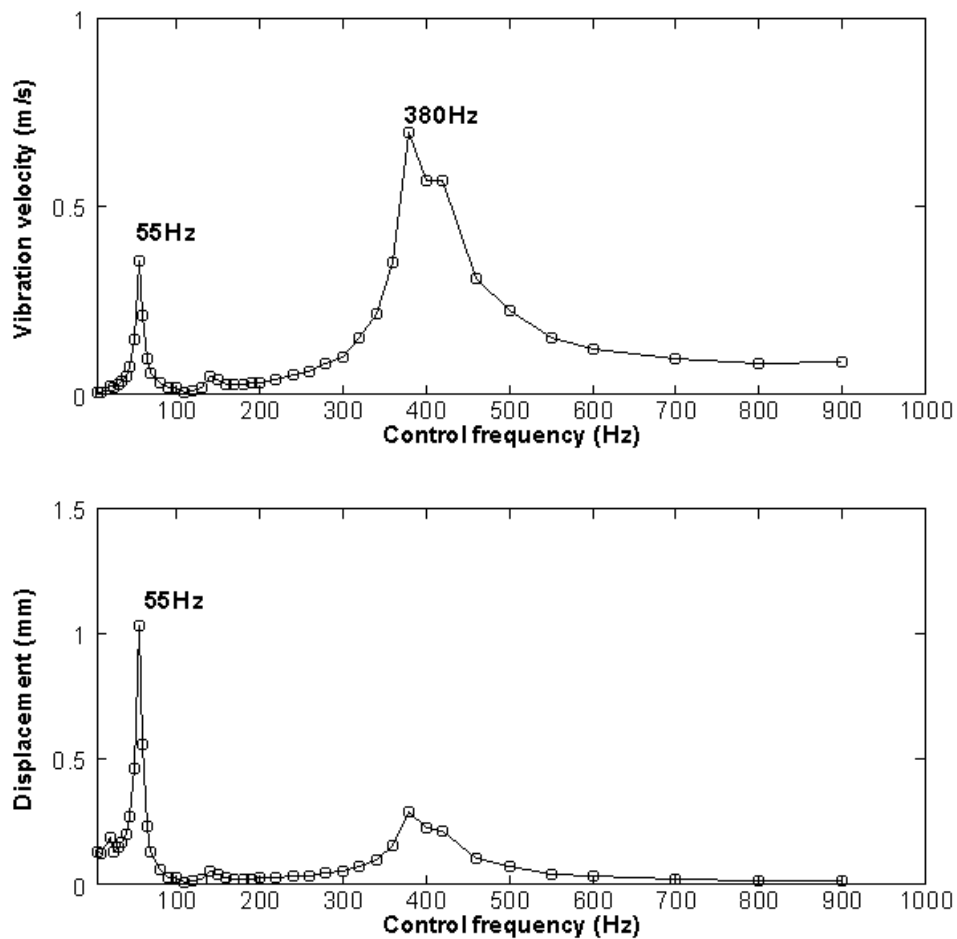


Figure 2-8 Vibration characteristic of the single THUNDER at various control frequencies. The control voltage is set to 140V: (a) Vibration velocity; (b) Displacement.

2.5 The designs of test models and downstream cavities

2.5.1 The perturbation module and its characteristic

In this section, a perturbation module was constructed aiming at generating a small local perturbation for control purposes. A small local perturbation can be generated by using a thin plastic plate which is attached to THUNDER actuators. The surface perturbation can be applied on the up surface, down surface or on both up and down surfaces of the perturbation module. For an ideal perturbation module, the flow field around the up and down surfaces of the test model should be the same for vortex shedding control effectiveness. In other words, the local surface perturbations on the up surface and the down surface should create similar flow behavior over the module.

Another point needs to be considered is that the thickness of the perturbation module used in the experiment was 11mm, it was very difficult to add perturbation on both up and down surfaces by using the THUNDER actuators due to the geometrical constraints. So in the present investigation, the perturbation was added only on the up surface of the perturbation module.

It should be noted that the small surface perturbation displacement d_p was relatively small compared to the thickness of the bluff body t . When the THUNDER actuators are installed using the cantilever mounting method, the maximum displacement measured at the displacement measurement point as Figure 2-7(b) is about 2mm. This displacement level was still consistent with the small perturbation requirement, relative to the thickness of the perturbation module.

Figure 2-9 shows the installation of THUNDER actuators by using the cantilever mounting method. The position of the free-end in the module was adjusted in the installation using an adjustment bolt. Such an adjustment can change the vibration characteristic of THUNDER actuators. The distance between the fixed bolt and the adjustment bolt was relatively small (about 2mm) for avoiding a major change on the vibration characteristic of THUNDER actuator. The fixed bolt and the adjustment bolt were attached to the support plate, whose thickness was chosen as 5mm. A 1.2mm vibration plate was connected to the free-end of actuators using a double-sided tape, with the overall thickness of plate and tape was about 3.0mm. In this configuration, the THUNDER actuator required a vertical space of about 3.0mm, so to allow it to vibrate freely. Thus a channel was cut in the support plate that was located below the position of the free-end of the THUNDER actuator.

2. The surface perturbation technique and experimental set-up

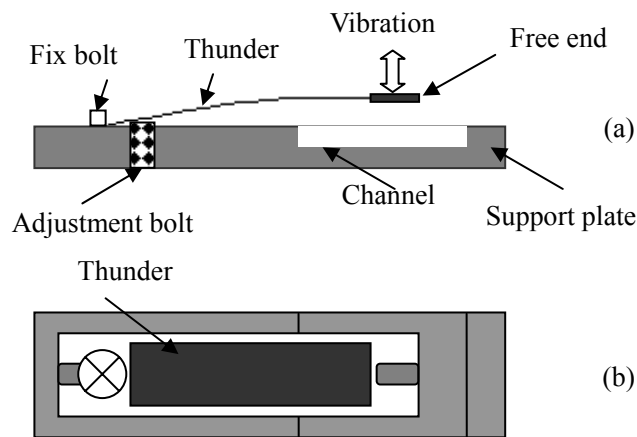


Figure 2-9 The installation of the THUNDER actuator by using cantilever mounting method (a) Side view; (b) Top view.

For investigating the mechanism of the surface perturbation in controlling vortex shedding, the generated surface perturbation motion by the module must be reasonably uniform. In order to satisfy this requirement, the placement of the THUNDER actuators needs to be considered carefully. There are two placements for the THUNDER actuators in the perturbation module, they can be simply classified as type P-A and type P-B in Figure 2-10. Comparing these two different placements, though in theory the motions of all points on the vibration plate in these two placements can be nearly the same, it is not easy to install the vibration plate in type P-B. In fact, during the testing, it was not possible to find a good way to install this type in the requirement way. So in the perturbation module, type P-A is used. In this type of placement, the installation of the vibration plate is very easy and repeatable for every installation. All the motions of the points on the vibration plate are nearly the same.

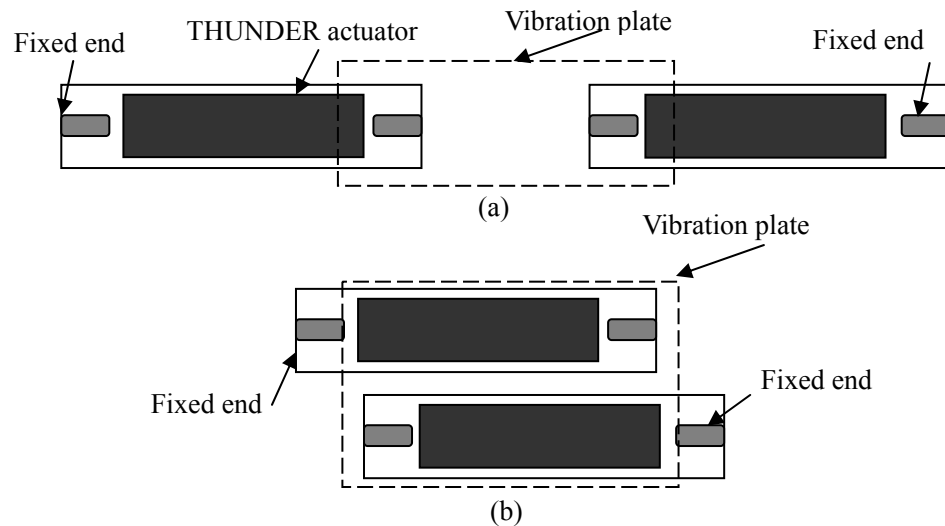


Figure 2-10 The placement of THUNDER actuators in the perturbation module. (a) Placement type P-A; (b) Placement type P-B

The connection between the vibration plates with THUNDER actuators is not rigid to allow the plate to freely vibrate. In the design, a flexible plastic ring covered the free-end of THUNDER actuator, the vibration plate was connected the flexible plastic ring by using a double-sided tape. This connection method only allowed the vibration plate to move in a tiny distance along THUNDER actuators as shown in Figure 2-11(a) for improving the performance of actuators.

The final configuration of the perturbation module is shown in Figure 2-11. The module's height $t = 11$ mm, and its width $c = 16$ mm. Two THUNDER actuators, each with a length of 63 mm and a width of 14 mm, were embedded in a slot of 240 mm long, 16mm wide and 7 mm deep on the top side of perturbation module. The actuators were installed in a cantilevered manner to create a maximum perturbation displacement in the transverse y -direction, and thus to achieve a better control performance for the same excitation condition. The actuators and the walls of the slot around the actuators were lubricated to minimize contact friction. A thin plastic plate with a thickness of 1.2 mm, mounted flush with the upper surface of the plate, was connected with the cantilevered end of the actuators using a double-sided tape. Two

adjustment bolts were used to adjust the position of the vibration plate. Driven by the actuators, the vibration plate oscillated to create a uniform transverse vibration on the y-direction of the plate surface. Figure 2-12 shows the picture of the perturbation module.

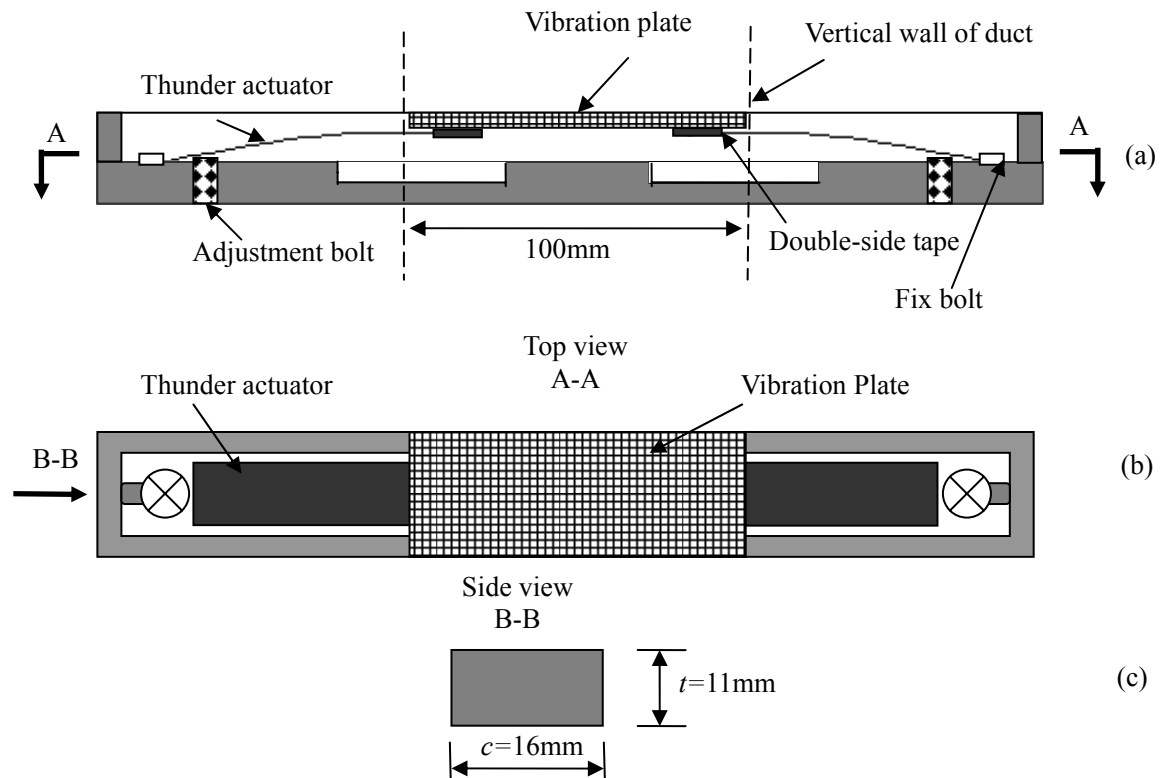


Figure 2-11 The perturbation module (a) Installation of the perturbation module; (b) Top view of the perturbation module; (c) Side view of the perturbation module.

The characteristic of perturbation module was measured by using a Polytec Series 3000 Dual Beam laser vibrometer at the center point on the vibration plate. A signal generator generated various sinusoidal signals with different frequencies, these control signals were amplified by a PZT amplifier before applied to the THUNDER actuators inside the test model. The results were shown in Figure 2-13. It was found that the vibration characteristic of the perturbation module was changed when compared with the vibration characteristic of the single THUNDER actuators. The resonance frequency was around 30Hz.

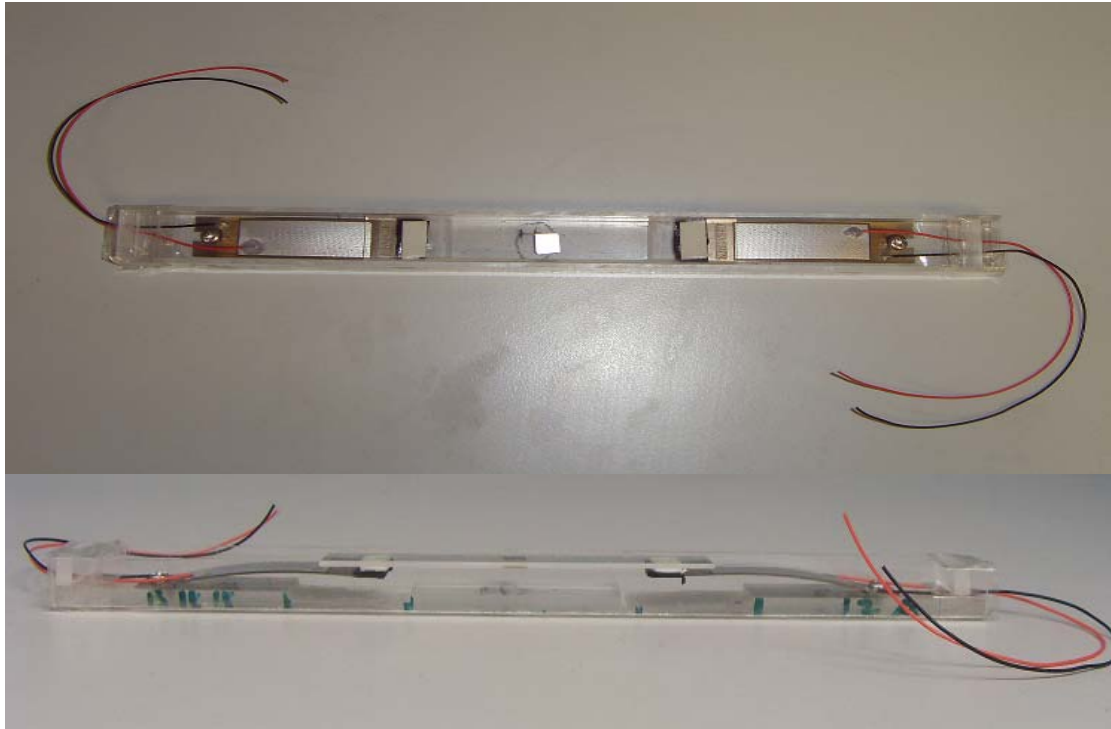


Figure 2-12 The photo of perturbation module

Two THUNDER actuators were used in the perturbation module and connected with each other by a double-sided tape with the vibration plate. This connection would change the vibration characteristic of the perturbation module. The vibration characteristic of the perturbation module at control frequency $f_p = 30\text{Hz}$ and control voltage $V_{rms} = 140$ volts are shown in Figure 2-14. Further, because the THUNDER actuator had maximum peak to peak voltage of $\pm 240\text{V}$ (root mean square voltage was about 168V), in the voltage of input signal was limited to this maximum voltage level.

2. The surface perturbation technique and experimental set-up

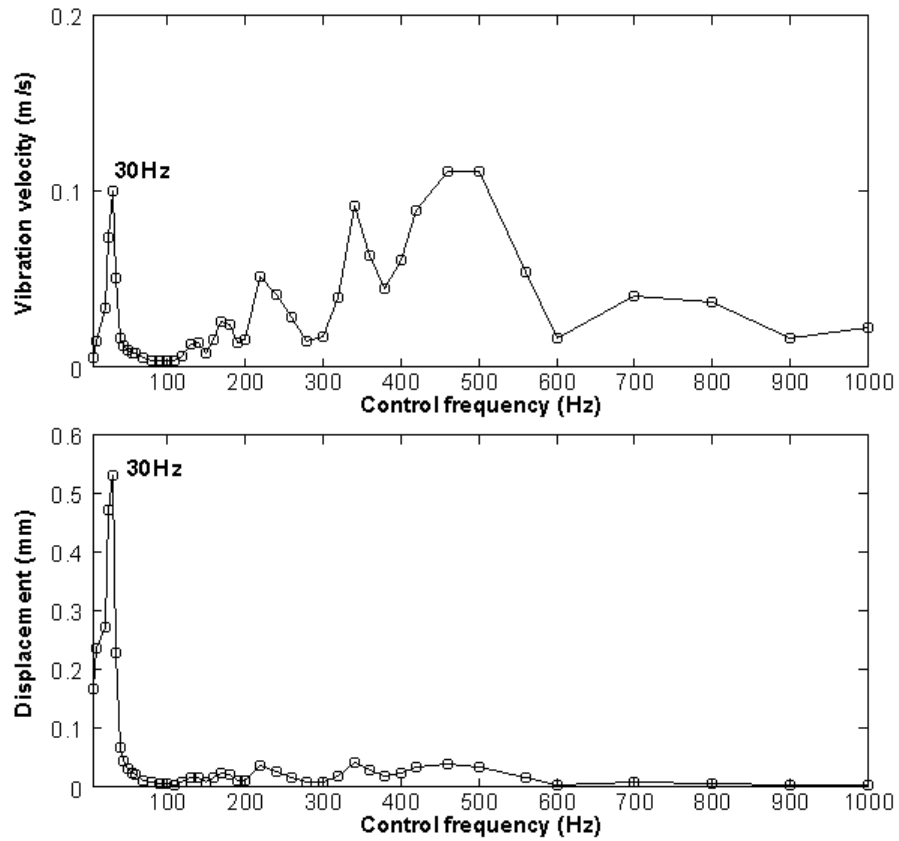


Figure 2-13 Vibration characteristic of the perturbation module at various control frequencies. The control voltage was set to 140V

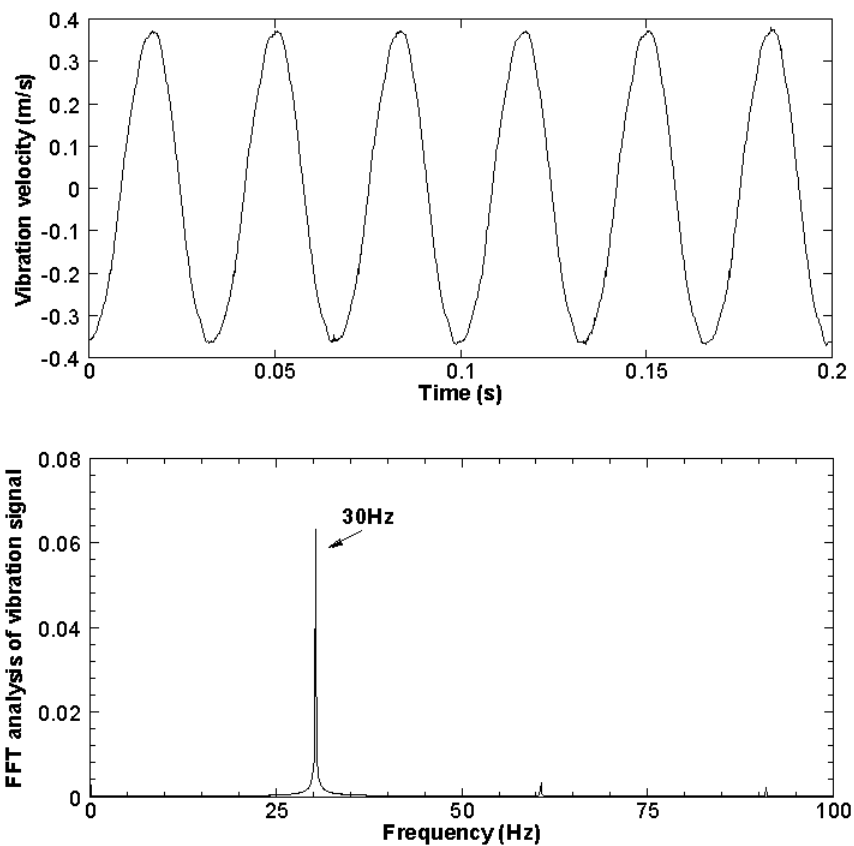


Figure 2-14 Characteristic of the perturbation module at $f_p = 30\text{Hz}$, $V_{rms} = 160\text{V}$ a) Time-domain; b) Frequency domain.

2.5.2 Test models

In this work, the ‘module’ was used to classify different parts of the test model. In the experiment, different test models were used, using a combination of different leading edges, trailing edges and test model’s dimensions. In other words, a perturbation module was used to combine with other modules to form different types of test models. By using this method, all test models have the same perturbation characteristic, which was beneficial for investigating the differences in control mechanism of different test models. Another advantage for using such modules in the test model is that the installation of the test model becomes easy and repeatable.

A complete test model contained the leading edge module, the perturbation module and the trailing edge module. Figure 2-15 shows different leading edge and trailing edge modules. In this experiment, only a square trailing edge was used in the test model. The thickness of all these modules were $t=11\text{mm}$, and the width of the semi-circular leading edge module was $t/2=5.5\text{mm}$. The width of the square leading edge module was 1.0mm and the width of square trailing edge module was 1.5mm .

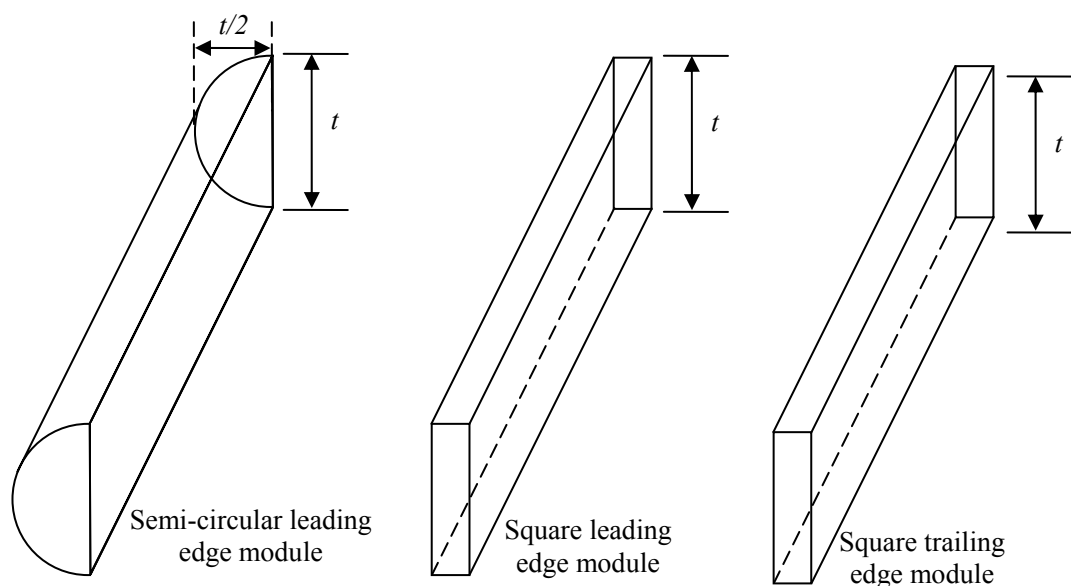


Figure 2-15 The leading edge and trailing edge modules.

These different modules were combined to construct a complete test model. Figure 2-16 shows the process of constructing a semi-circular leading edge test model. A semi-circular leading edge module, a perturbation module and a trailing edge module were combined together as a test model with dimensions of $t = 11$ mm and $c = 23$ mm. In a similar way, a square leading edge test model ($t = 11$ mm and $c = 18.5$ mm) was built as shown in Figure 2-17.

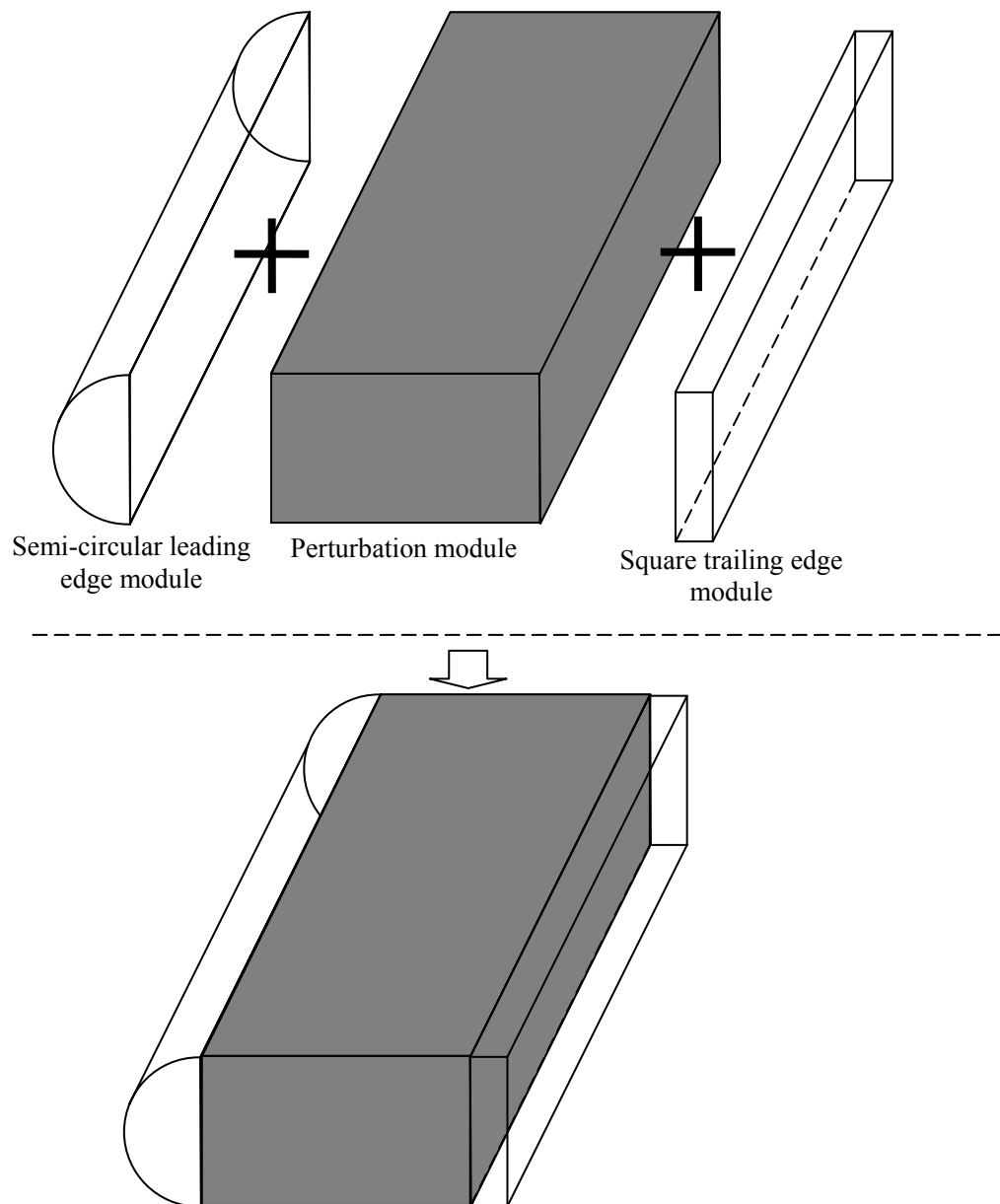


Figure 2-16 The process for combining semi-circular leading edge test model.

2. The surface perturbation technique and experimental set-up

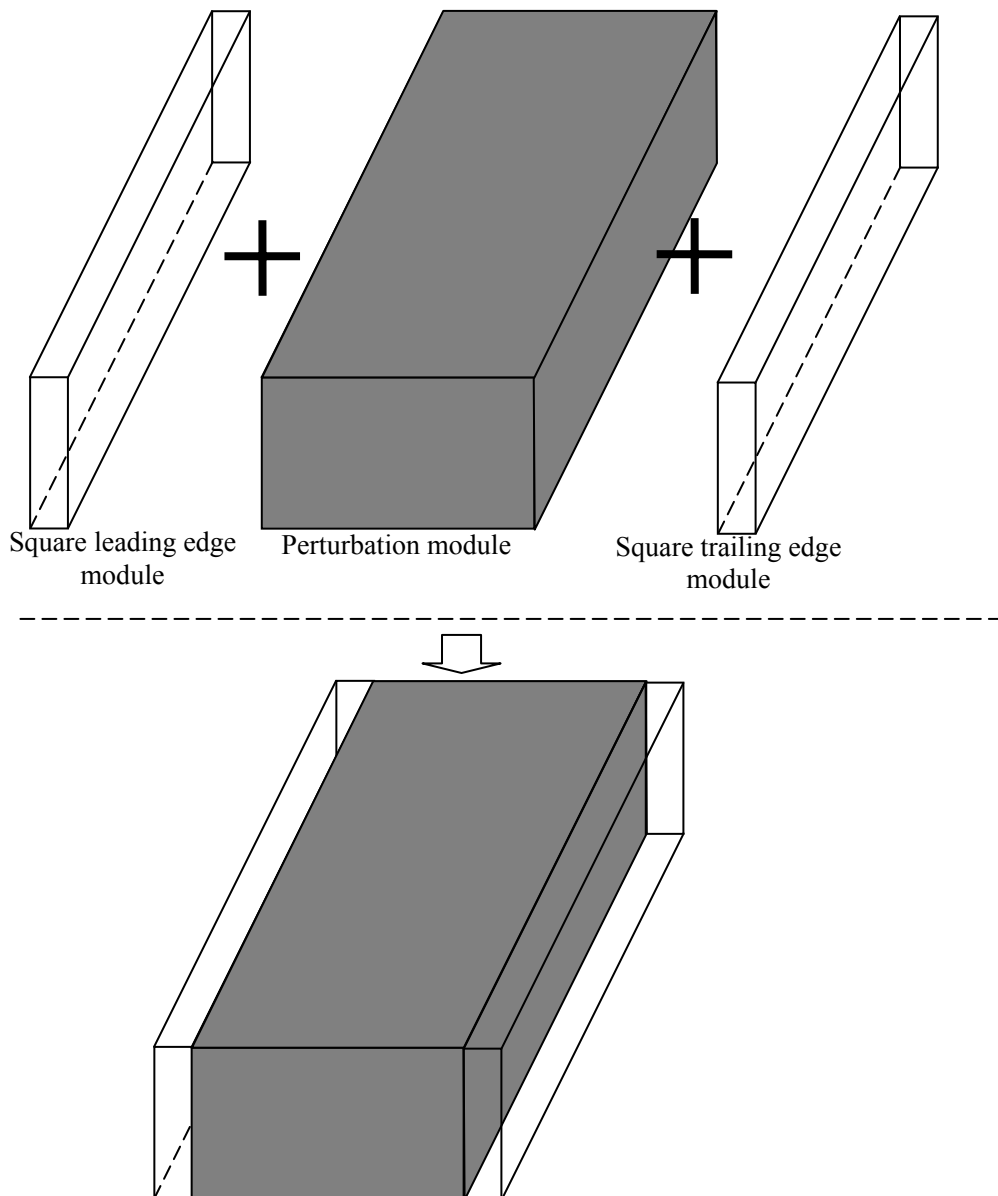


Figure 2-17 The process for combining square leading edge test model.

Although the present experiment is performed in an acoustic wind tunnel, the background noise inside the duct still exists and can affect the measurement. A flow velocity $U=8.2\text{m/s}$ was used in the experiment to achieve a certain vortex shedding frequency f_s , the sound pressure level (SPL) at the shedding frequency f_s was measured for various dimensions c of the bluff body, c is the width of the bluff body. For a square leading edge bluff body, the background noise was about 70 dB m when measured around the shedding frequency f_s in the duct. Figure 2-18(a) shows that

the strength of vortex shedding was strong enough to be distinguished from the background noise when $10\text{mm} \leq c \leq 30\text{mm}$, while the other dimensions were not suitable for measurement. For a semi-circular leading edge bluff body, the background noise was about 60 dB measured in the duct around the shedding frequency f_s . In this case, Figure 2-18(b) shows that the strength of vortex shedding was strong enough to be distinguished from the background noise when $20\text{mm} \leq c \leq 30\text{mm}$. Based on the observations, therefore, the length of the test model was chosen within $10\text{mm} \leq c \leq 30\text{mm}$ for a square leading edge bluff body and $20\text{mm} \leq c \leq 30\text{mm}$ for a semi-circular leading edge bluff body.

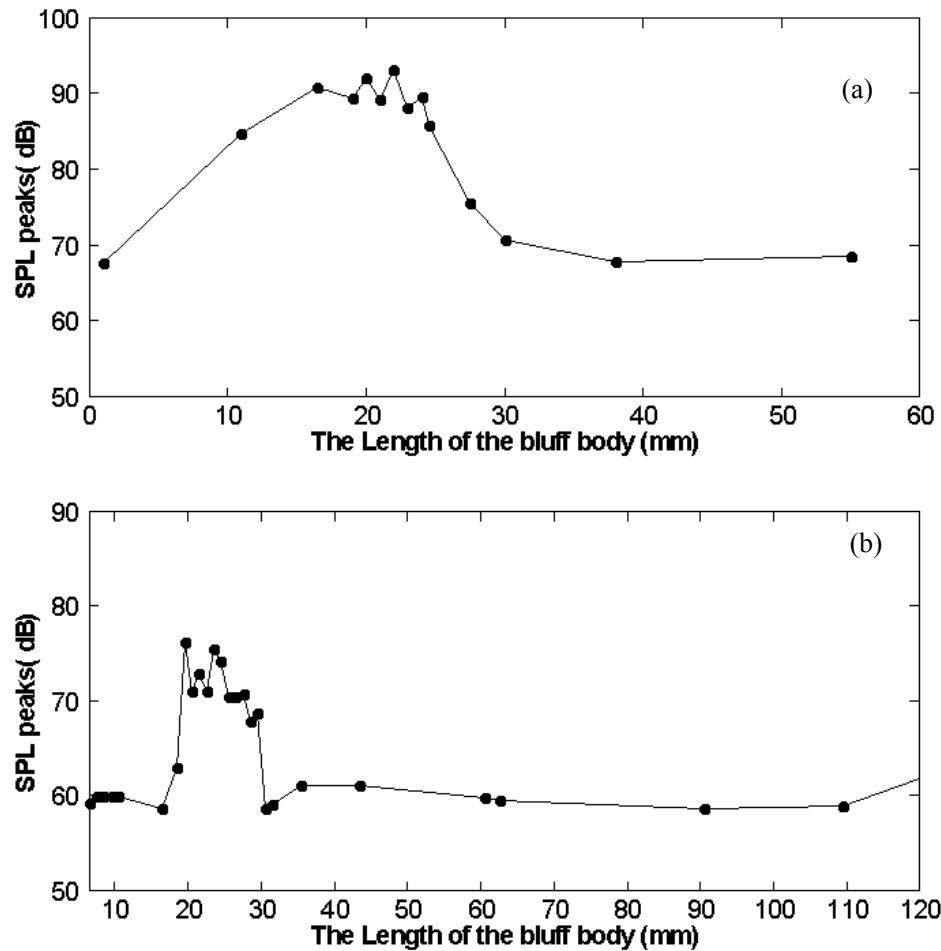


Figure 2-18 Peak values measured in the duct by microphone 1 at the shedding frequency f_s for different length of the bluff bodies, (a) Square leading edge; (b) Semi-circular leading edge.

Therefore, by considering the acoustic characteristic of bluff bodies with various lengths, various test models are designed as shown in Table 2-1.

Table 2-1 The list of test models used in experiment

Name	Leading edge type	t (mm)	c (mm)	Remarks
C-1	Semi-circular leading edge	11	23	
C-2	Semi-circular leading edge	11	39	
C-3-1	Semi-circular leading edge	11	23	The width of vibration plate is only 3mm and near the leading edge
C-3-2	Semi-circular leading edge	11	23	The width of vibration plate is only 3mm and near the trailing leading edge
S-1	Square leading edge	11	19	
S-2-1	Square leading edge	11	19	The width of vibration plate is only 3mm and near the leading edge
S-2-2	Square leading edge	11	19	The width of vibration plate is only 3mm and near the trailing leading edge

2.5.3 Downstream cavities

Downstream cavities were installed in the downstream of the test model in the duct. Two cavities were installed symmetrically as shown in Figure 2-3 which acted as side-branch acoustic resonators. In the experiment, the cavity had a square cross section, whose dimensions were described by the depth of cavity L ; the width of the cavity B in the stream-wise direction; and the width of the cavity H in the vertical direction relative to the stream-wise flow. The same value for the parameter $H=100\text{mm}$ was used as previously described. The other two parameters B and L were to be chosen based on the following considerations.

Figure 2-19 shows the main dimension in the room of the acoustic wind tunnel when duct and downstream cavities were installed in the work section of the wind tunnel. In the installation, a microphone was mounted on the bottom of the cavity CA. The depth of cavity CA was $L_{CA} \leq 1150\text{mm}$ and the depth of cavity CB was $L_{CB} \leq 780\text{mm}$. These dimension limitations needed to be considered for choosing the depth of cavities,

2. The surface perturbation technique and experimental set-up

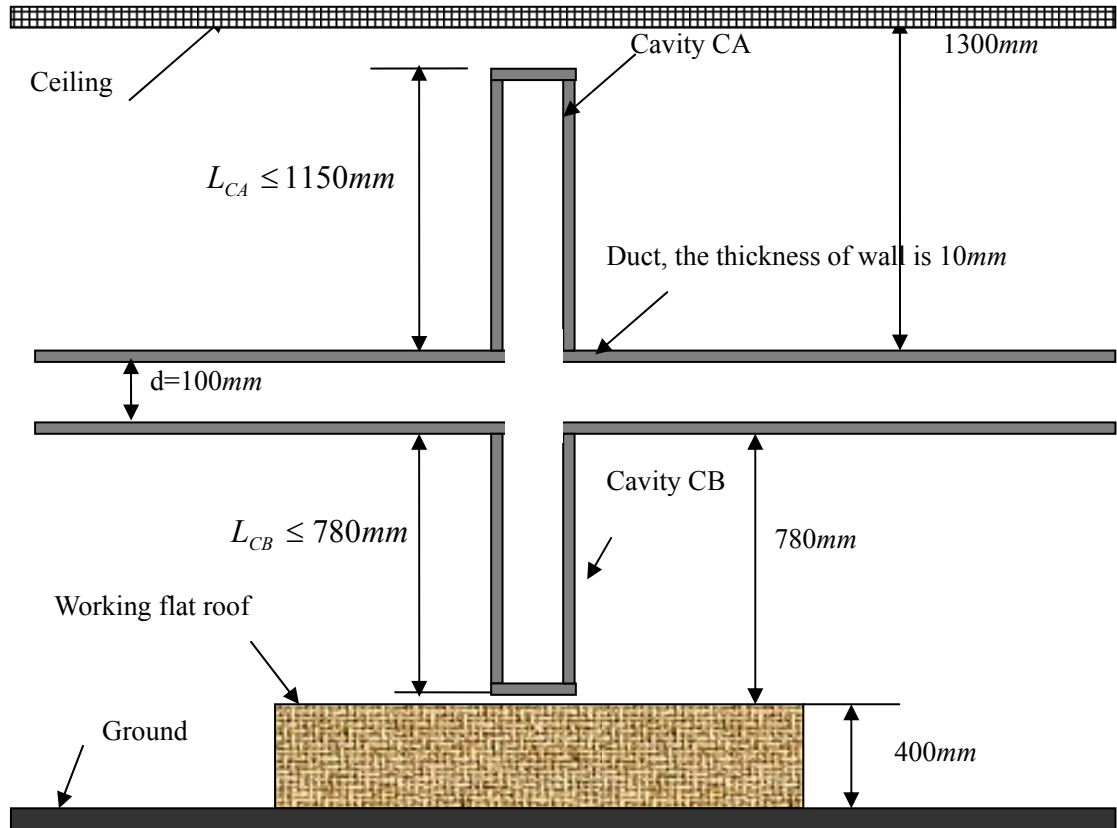


Figure 2-19 The dimension limitation in the room of acoustic wind tunnel

Ziada and Shine(1999) and Graf and Ziada(1992) demonstrated that the resonance frequencies of the coaxial side-branch modes can be accurately predicted based on the length between the ends of the side-branches and the speed of sound. The piping system uses a standard relationship used for long coaxial branches, the resonance frequency of the cavities f_a is:

$$f_a = \frac{C(2n-1)}{2L} \quad (2-7)$$

where L is the total length of the side-branches including the diameter of the main duct ($L_{CA} + L_{CB} + d$). Here, L_{CA} and L_{CB} are the depth of the cavities; d is the height of the duct; and n is the acoustic mode number. So the first acoustic resonance frequency of the cavity is

$$f_a^{(1)} = \frac{C}{2L} \quad (2-8)$$

If the first acoustic resonance frequency $f_a^{(1)}$ is known, then the depth of the cavities can be calculated by using the equation 2-8. In the experiment setup, $d=100\text{mm}$, $C=344\text{m/s}$. suppose that the desired resonance frequency is $f_a^{(1)}=160\text{ Hz}$, the depth of each cavity can be calculated as 487mm . If $f_a^{(1)}=80\text{Hz}$, the cavity configuration is $L_{CA} = 1150\text{mm}$ and $L_{CB} = 780\text{mm}$.

Another parameter to be considered is the width of the cavity B . If the width of cavity is too large, it will affect the flow field behind the test model, so it is better to select the width as small as possible. Various measurements were done to check the suitable width of cavity. In the measurements, two values were checked: $B=20\text{mm}$ and $B=70\text{mm}$. The results are shown in Figure 2-20, where it was found that the resonance at $f_a^{(1)}$ with $B=20\text{mm}$ was stronger than that of $B=70\text{mm}$. However, there was a ‘drop’ in the sound pressure level at shedding frequency f_s when $B=20\text{mm}$. This behavior did not exist for $B=70\text{mm}$. Because of this behavior, the width of the cavity could not be too small. Thus in the experiment, the width of the cavity was chosen to be $B=70\text{mm}$. Table 2-2 shows the list of the cavities that were used in the experiment.

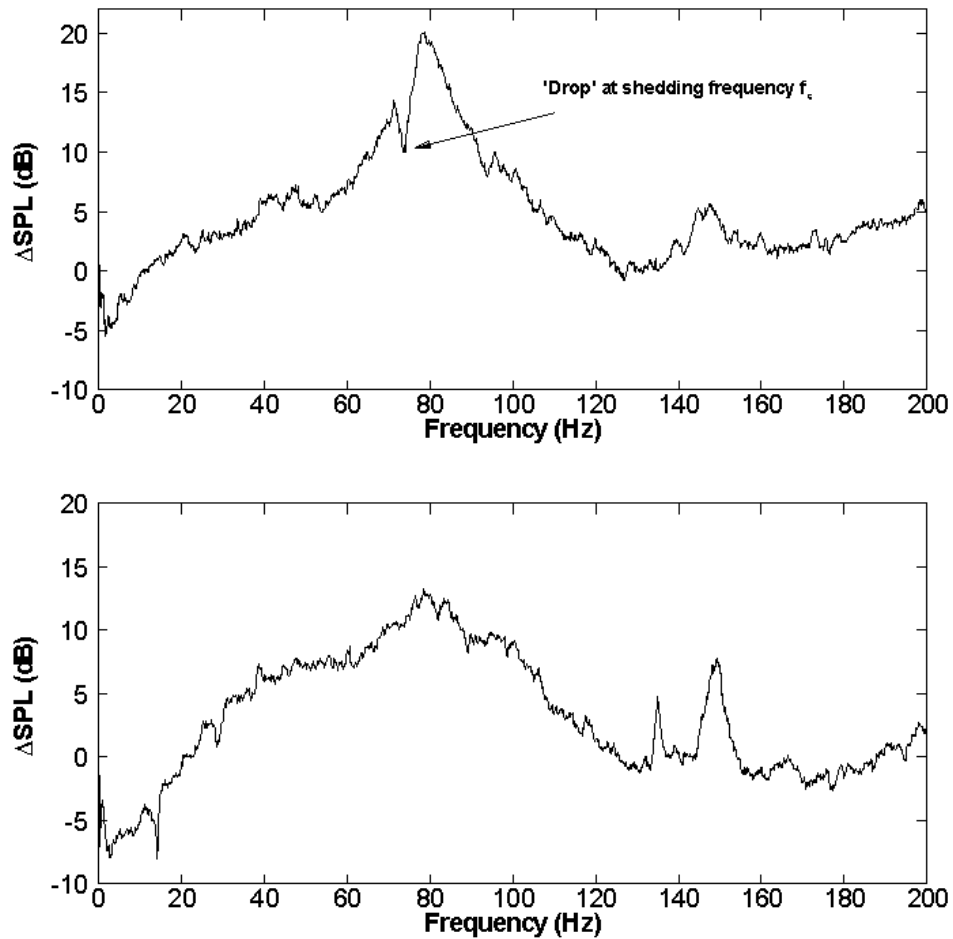


Figure 2-20 The characteristic of cavity at different width of cavity: (a) $B=20\text{mm}$; (b) $B=70\text{mm}$, $U = 8.2\text{m/s}$ and the shedding frequency of the bluff body installed in the duct is 78Hz .

Table 2-2 The list of downstream cavities

Name	Resonance frequency (Hz)	L_{CA} (mm)	L_{CB} (mm)	B (mm)
DC-1	160	487	487	70
DC-2	83	1150	780	70

2.6 Platform and control strategy

2.6.1 Measurement system

The measurement system used in the present study was shown in Figure 2-21. Two 1/2' condenser microphones (B&K 4189) were used to measure the fluctuating acoustic pressure. Microphone 1, referred to as Mic.1 hereafter, was flush-mounted with the top wall of the duct vertical to the trailing edge of the test model. Another microphone, Mic.2, was installed flush with the center of the top wall of the upper

2. The surface perturbation technique and experimental set-up

cavity [Figure 2-21]. To analyze the control effect on the flow field, two $5\ \mu\text{m}$ tungsten hot wires were deployed to measure the fluctuating flow velocity. One was located behind the test model, and the other one was located at $y=11\text{mm}$ and $x=0\text{mm}$, which was the vertical plane of the leading edge of the test model. In addition, the perturbation displacement produced by the THUNDER actuators was measured at the center of the vibration plate using a Polytec Series 3000 Dual Beam laser vibrometer.

2. The surface perturbation technique and experimental set-up

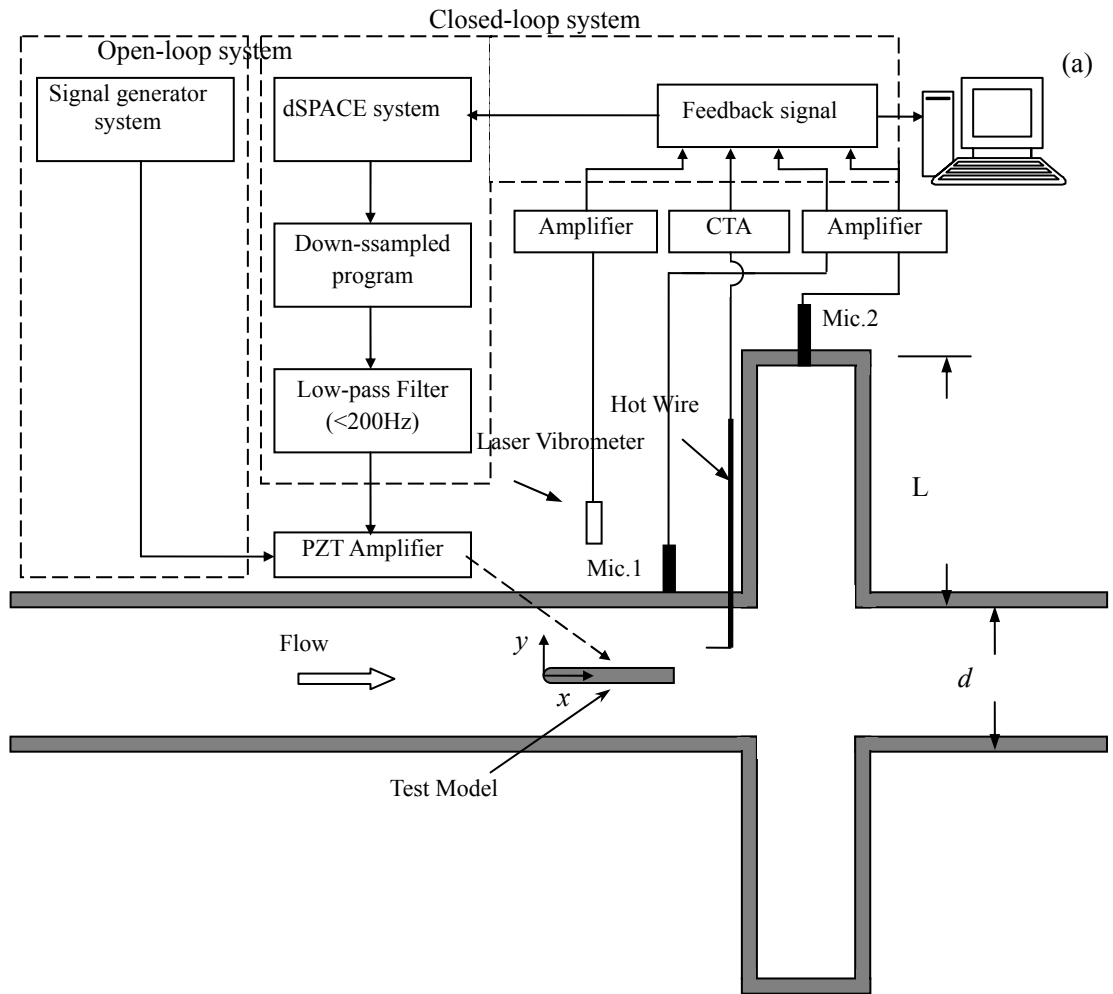


Figure 2-21 Sensing configurations, the control and measurement systems

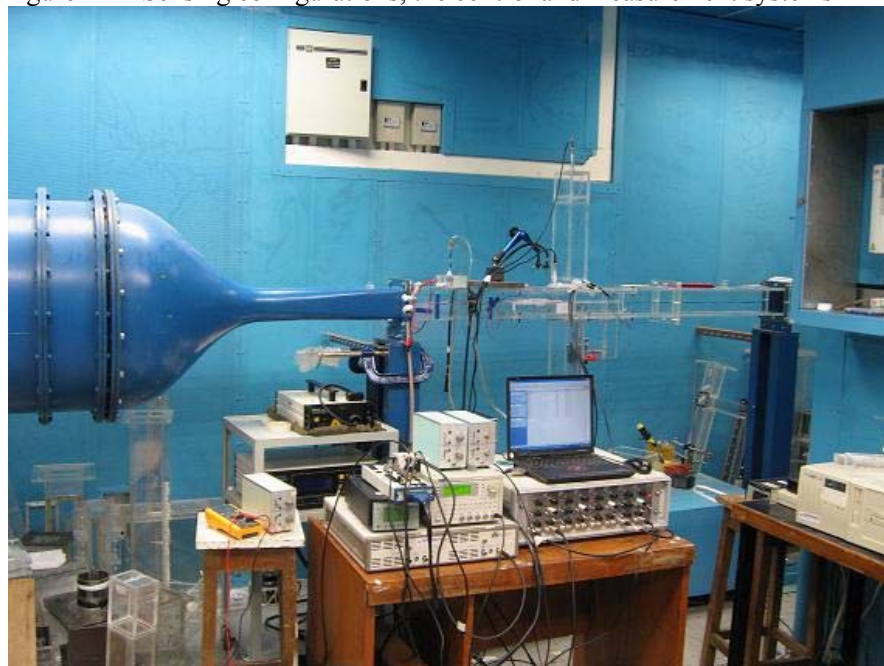


Figure 2-22 The experimental set-up system

All measurement signals were recorded using a real-time system rapid control prototyping and production code generation system, dSPACE. The data was measured at a sampling frequency of 6 kHz per channel. The duration of each record was about 11 s. A dual channel PZT amplifier (Trek PZD 700-2) was used to amplify the control signal before it was applied to the THUNDER actuators inside the test model. The experiment set-up is shown in Figure 2-22. The schemes of open-loop control and closed-loop control are shown in Figure 2-21, they will be described later.

2.6.2 dSPACE system and Simulink

The dSPACE system was used as the control platform in the experiment. It provided both software and hardware tools for implementing and testing real-time systems including advanced control systems, hardware-in-the-loop simulations and other high-end signal-processing applications.

dSPACE system, was especially designed for rapid prototyping of applications in the field of control engineering and digital signal processing. It could automatically generate codes for Simulink a model to test them in a real time process environment.

The Simulink used in the dSPACE system was a commercial tool for modeling, simulating and analyzing multi-domain dynamic systems. The primary interface of Simulink was a graphical block diagramming tool and a customizable set of block libraries. It offers a compact integration with the rest of the MATLAB environment and can either drive MATLAB or be scripted from it.

2.6.3 Open-loop and closed-loop control strategies

In the experiment, the THUNDER actuators in the test model can be activated in two different ways: 1) by a sinusoidal signal at a tunable frequency to form an open-loop control; and 2) by feedback signals acquired from system response to form

a closed-loop control. The detail of these two control strategies are introduced in the followings.

Open-loop control, which is also called non-feedback control, is a type of control which computes its input into a system using only the current state of the system. A characteristic of the open-loop control is that no feedback is used in this control to check whether the output has achieved the desired control results of the input control signal. Consequently, it cannot correct any errors that it could make. Open-loop control is useful where the relationship between input and the resultant state can be modeled by a mathematical formula. So the open-loop control is often used in simple systems because of its simplicity and low-cost, especially in the systems where the feedback is not critical. In the experiment, though it is not easy to model the vortex shedding by a simple formula, the open-loop can be used for initial investigation.

The aim of the experiment is to control the vortex shedding that is generated by the test model in the duct [Figure 2-21] and its acoustic resonance inside the downstream cavities. Figure 2-23 shows the open-loop control process in the experiment. In the open-loop control, the control signal is generated by a signal generator system, and then this signal is input to a PZT amplifier to amplify the signal before being applied to the THUNDER actuators in the test model. The THUNDER actuators generated the small local perturbation in the up surface of the test model.

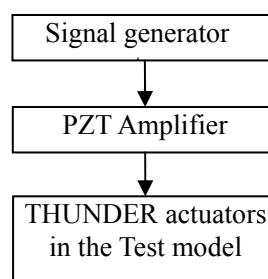


Figure 2-23 Open-loop control process

In the open-loop scheme, the harmonic actuation is independent of what is

occurring in the system. There is no possible direct adjustment on the control actuation. Thus, adding some feedback information from a number of sensors inside the duct or cavity may improve control performance because the control actuation will be influenced by the feedback response measured in the sensors. If these signals are adjusted properly, the generated control actuation may influence the flow field such that the resulting noise may be further reduced. So in order to avoid the problems of the open-loop control and improve the control performance, the feedback is introduced into the control system.

A closed-loop control system uses feedback to control states or outputs of a dynamical system. In the closed-loop control, the measured response of a physical system is compared with a desired response. The difference between these two responses initiates actions that will result in the actual response of the system to approach the desired response. This in turn drives the difference signal toward zero. Typically the difference signal is processed by another physical system, which is called a compensator, a controller, or a filter for real-time control system applications. A closed-loop system is able to regulate itself in the presence of disturbance or variations in its own characteristics. In this respect, a closed-loop system has a distinct advantage over an open-loop system.

In the experiment, control signal utilizes feedback signals acquired from the system, which may be from the hotwire, Mic.1 or Mic.2. In what follows, only cases using hotwire as feedback signal are discussed since the hotwire signal is generally more stable than the signals from microphones because the hotwire sensor is not significantly affected by the flow background noise that may be caused by the configuration of the experimental set-up. The signal is adjusted in simulink/dSPACE by using a down-sampled program before being applied to the PZT amplifier. The

detail of the down-sampled program is described in Chapter 4. The small local perturbation generated by the THUNDER actuators affected the vortex shedding in the duct and the change of the vortex shedding was measured using the hotwire. The signal was then used as feedback signals to the control system.

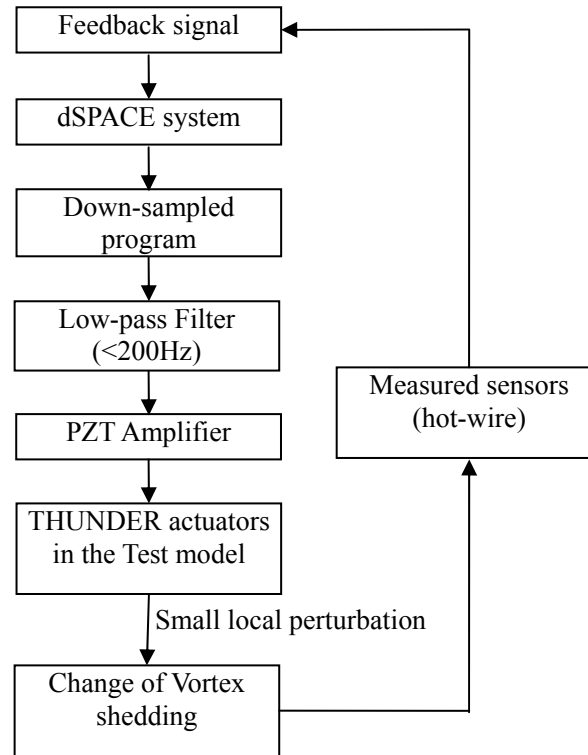


Figure 2-24 The closed-loop control process.

2.7 Flow characteristics

The characteristic of the flow in the duct was measured. A single boundary hot wire was used to measure the boundary layer at the position of $x=-275\text{mm}$. The boundary-layer thickness, δ , was used as a thickness beyond which the velocity was essentially the free-stream velocity U_∞ . The free-stream velocity is customarily defined as the distance from the wall to the point where $u(y) = 0.99U_\infty$. In the duct, the thickness of the boundary layer was about 4.0mm [Figure 2-25], and the uniform flow field was from $y=-46\text{mm}$ to $y=46\text{mm}$.

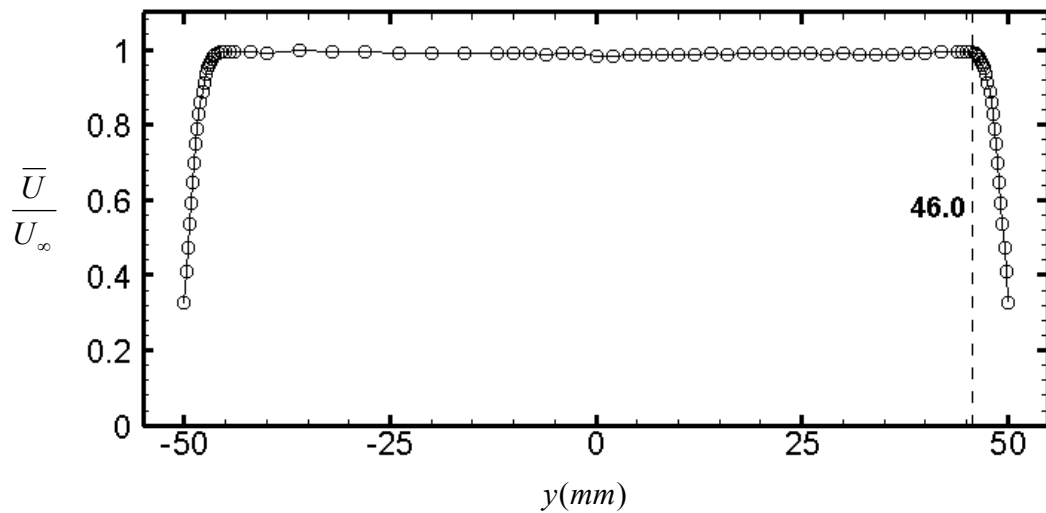


Figure 2-25 Velocity profile inside the duct, measured by a single boundary hot-wire probe at $x=-275\text{mm}$, $U_\infty = 8.2\text{m/s}$.

As an example, the C1 test model was installed in the duct. The x-wire probe was used to measure the flow velocities in x and y direction at the same time, and it was located at the position $x=34\text{ mm}$. The distribution of U and V are shown in Figure 2-26, where U and V is the mean velocity along x direction and y direction respectively. The vortex shedding was mainly in the range of -22mm to 22mm inside the duct, which was out of the range of boundary layer, so the results indicate that the vortex shedding in the duct was not affected by the boundary layer of the duct.

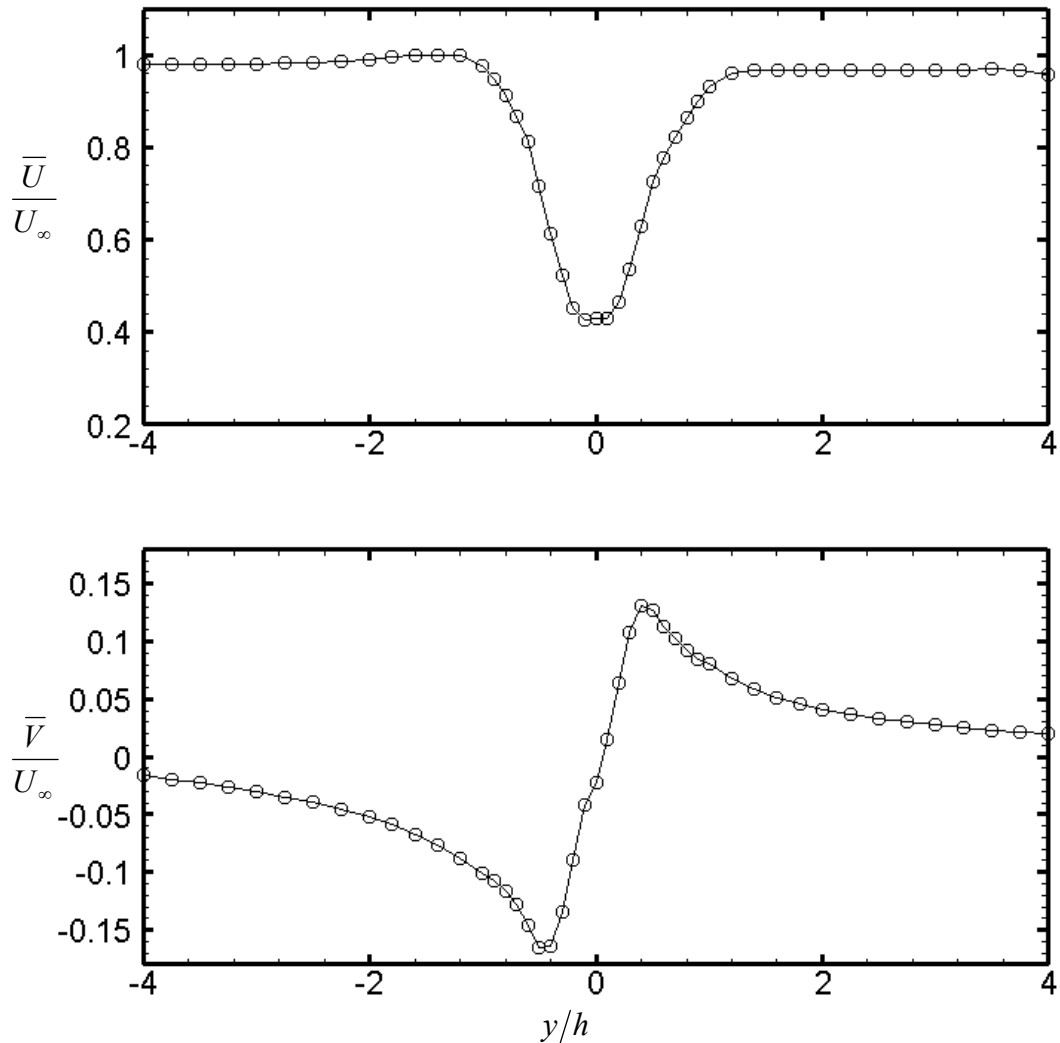


Figure 2-26 Flow distribution, measured at $x = 34\text{mm}$, C1 test model, $U_\infty = 8.2\text{m/s}$.

2.8 Conclusions

A low-order model for vortex shedding behind vibrating bluff body had been introduced. This simple model provides a simple explanation on the working principle of the surface perturbation technique for controlling the vortex shedding and its acoustic resonance in the downstream cavities. The technique, generating a controllable transverse motion of a structural surface using embedded piezo-ceramic actuators, aims at altering the fluid-structure interactions. Advanced piezo-ceramic THUNDER actuators were utilized since THUNDERs had a larger displacement and load capacity, smaller dimensions with more reliability, strength and flexibility

compared to those of other conventional actuators.

The design of test model and the downstream cavities were presented. The experimental setup, major experimental facilities and platform, as well as control strategy were explained in this chapter.

3. Active open-loop control of flow-induced acoustic resonance

3.1 Introduction

As the initial investigation, experiments were conducted using a surface perturbation technique with the open-loop control method. It was observed that the vortex-induced acoustic resonance could be effectively reduced after applying the surface perturbation technique. This was directly achieved not only from an impairment of the vortex shedding strength, but also from a shift in the shedding frequency created by the control action. The estimation of this frequency shift as well as its effect on the impairment acoustic resonance was experimentally assessed.

3.2 Optimal control parameters for open-loop control

The active open-loop control experiment was undertaken in the set-up shown in Figure 2-22. The test model C1 and downstream cavities DC-1 was used in the experiment. The process of implementing the surface perturbation by control signal implementation was shown in Figure 3-1. The signal generator system used was either the Model DS345 or the virtual signal generator in dSPACE system. Due to the high voltage requirement for the THUNDER actuators, A PZT amplifier (Trek PZD 700-2) was used to amplify the control signal to the THUNDER actuators inside the test model. The flow speed in the duct was set to 8.2m/s, which determined the vortex shedding frequency f_s at about 160Hz.

In the experiment, the primary focus was to investigate the vortex shedding phenomena, which had a tonal characteristics at vortex shedding frequency f_s . Therefore, the sinusoidal type signal was chosen as the control signal in the experiment. Let $u(t)$ to be the control signal implemented to the test model:

$$u(t) = A_p \sin(\omega t + \phi), \quad (3-1)$$

where A_p is the amplitude; $\omega = 2\pi f_p$ is the angular frequency; and ϕ is the phase.

In the present open-loop control, ϕ was set to zero:

$$u(t) = A_p \sin(2\pi f_p t). \quad (3-2)$$

After amplifying the control signal, this final control signal has the following form:

$$u(t) = V_p \sin(2\pi f_p t) \quad (3-3)$$

where V_p is the output voltage measured from the PZT amplifier. Here, V_p and f_p are critical control parameters that need to be optimized. From the principle of linear control, it can be argued that the effective control for such a system is when both vortex shedding and control actuation frequencies are similar $f_p = f_s$. However, in the present experiment, the test model's characteristic shown in Figure 2-13 indicates that the test model had the largest maximum displacement when the control frequency f_p was around 30Hz. The maximum displacement significantly deteriorated when the control actuation frequency was further away from 30Hz. particularly when it was around vortex shedding frequency $f_s \approx 160\text{Hz}$. In this case the displacement of the test model is extremely small and not sufficient to provide useful surface perturbation in the model. Because of this reason, $f_p = 30\text{Hz}$ was chosen for the control frequency.

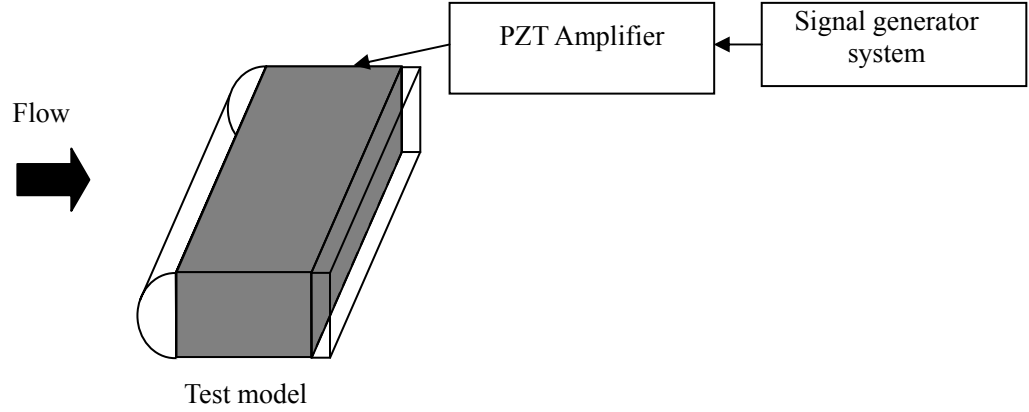


Figure 3-1 The surface perturbation process used in active open-loop control.

Various measurements were done to investigate another optimal control parameter V_p . Without control, the sound pressure level (SPL) at shedding frequency f_s measured in the duct was SPL_{m1} and inside the cavity was SPL_{m2} . With control, the sound pressure level (SPL) at shedding frequency f'_s measured in the duct was SPL'_{m1} and inside the cavity was SPL'_{m2} . The difference between the cases without control and with control could be used to analyze the control performance. Here,

$$\Delta SPL_{m1} = SPL_{m1} - SPL'_{m1}, \quad (3-4)$$

$$\Delta SPL_{m2} = SPL_{m2} - SPL'_{m2} \quad (3-5)$$

where ΔSPL_{m1} represented the SPL reduction in the duct and ΔSPL_{m2} represented the SPL reduction inside the cavity. The control frequency f_p was set to 30Hz and the control voltage V_p was varied from 0V to 160V. The results were shown in Figure 3-2. It was found that the SPL reduction linearly increased when the control voltage V_p increased. The best result was at the point $V_p = 160V$. So the optimal control parameters for the experiment were $f_p = 30\text{Hz}$ and $V_p = 160V$. Although in principle, the reduction could be increased as the displacement of the vibration

plate increased; there was a maximum voltage limitation for the THUNDER actuators. Therefore in the experiment, the maximum input voltage was set to 160V. Furthermore, when $V_p \geq 140V$, the SPL reductions in the duct and inside the cavity did not significantly vary. This indicates that a direct amplification of the plate displacement via open-loop control could not always achieve the same effect on the reduction of the SPLs both in the duct and inside the cavity. If one wants to improve the control performance, one needs to utilize other control method instead of a straightforward open-loop control. Furthermore, in Figure 3-2 the SPL reduction inside the cavity was larger than that in the duct because of the effect of downstream cavity resonance. The detail of this phenomenon will be investigated in Section 3.5.

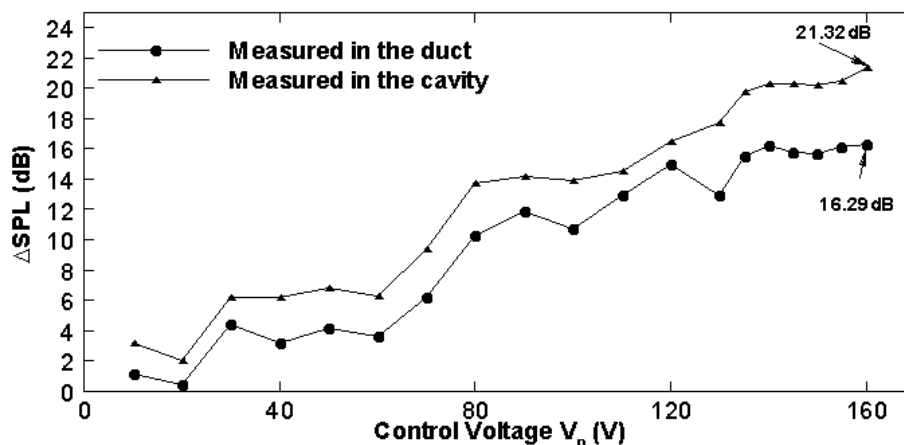


Figure 3-2 The control performance for different control voltages in open-loop control.

3.3 Control performance of open-loop control

The control performance of the test model in open-loop control was further evaluated in the sound field and flow field at $U=8.2\text{m/s}$ ($Re=5980$) at the shedding frequency $f_s = f'_a = 161.3\text{Hz}$. Figure 3-3 showed the variation of the SPLs at the two microphone positions, in time domain and their counterparts in frequency domain. The spectra in the frequency domain were obtained using FFT transform from the time domain signals with a frequency resolution of 0.1 Hz. The fine resolution was

needed for an accurate determination of the locations as well as the values of the resonance peak corresponding to the shedding frequency. It could be seen that, upon deployment of the control, the sound pressure inside both the duct and the cavity underwent immediate reductions to different extents in the time domain. SPL spectra showed that, with control, the SPL at Mic.1 decreases from 81.0dB to 64.7 dB (a reduction of 16.3dB) at the shedding frequency as shown in Figure 3-3(a). Meanwhile, the SPL measured by Mic.2 decreases from 97.1dB to 75.8 dB (a reduction of 21.3dB), as shown in Figure 3(b), which was larger than the reduction measured by Mic.1. This phenomenon would be investigated in detail in the next section. The third resonance frequency of the cavity f_a''' was also excited by the flow, as indicated by a sharp peak shown in Figure 3-3(b), this peak was also reduced by the control. Generally the control in the sound field was deemed to be effective. Furthermore, the vortex shedding frequency was shifted from 161.3Hz to 158.4Hz. The vortex shedding frequency shift phenomenon was one of interesting issues that arose from the investigation, which would be discussed in detail in Section 3.5. In addition, the surface perturbation used in the open-loop control did create some extra noise at 30Hz and the multiples of 30Hz. This however was moderate when compared with the noise generated by the vortex shedding, relatively far away from the targeted vortex shedding frequency. Therefore, in the present experiment, the extra noise generated by the perturbation was not included in the discussion.

3. Active open-loop control of flow-induced acoustic resonance

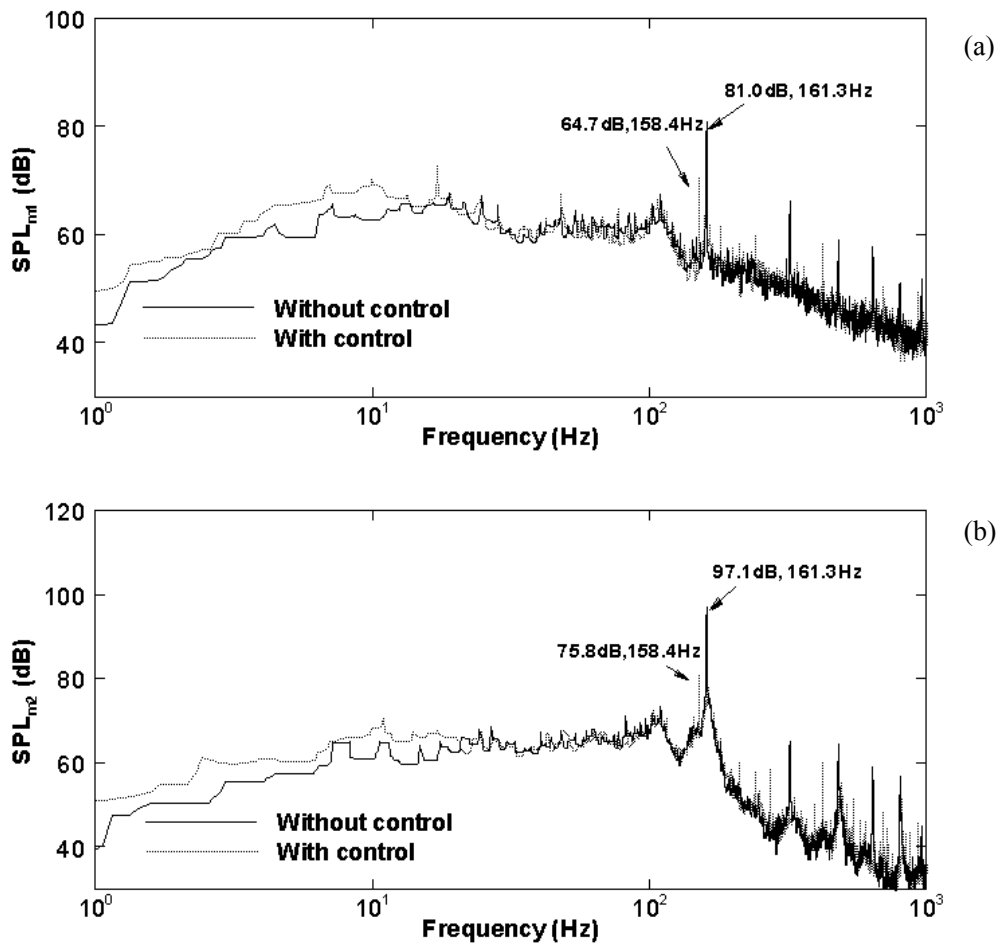


Figure 3-3 Control performance of open-loop control in sound field, flow speed is $U=8.2\text{m/s}$ ($Re=5980$). (a) SPL measured by Mic.1; (b) SPL measured by Mic.2.

The corresponding time-domain results for the control performance in sound field were shown in Figure 3-4. All the time-domain signals were filtered by a 5Hz-band around the shedding frequency. It showed that the measured signals of vortex shedding both in the duct and inside the cavity were obviously reduced after control. Due to the cavity resonance, the reduction inside the cavity was larger than that in the duct. In Figure 3-4(b) and Figure 3-4(d), one could find that the amplitude of the signal were decreased, but they fluctuated all the time, it was the 'Beat' phenomenon. It is interference between two signals of slightly different frequencies.

3. Active open-loop control of flow-induced acoustic resonance

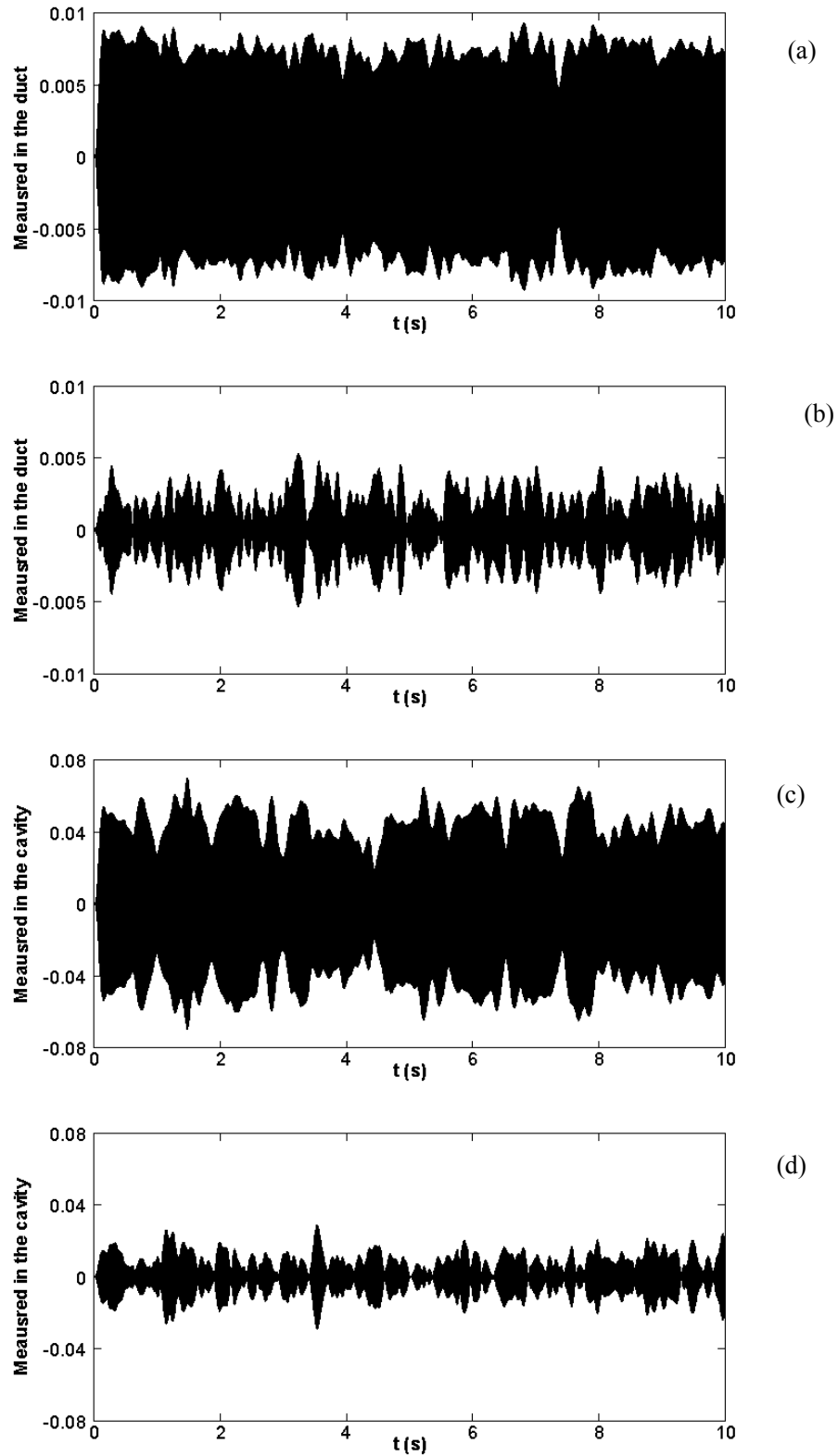


Figure 3-4 Time-domain results for the control performance in sound field, the signals are filtered by a 5Hz-band filter. (a) Without control: measured in the duct; (b) With control: measured in the duct; (c) Without control: measured inside the cavity; (d) With control: measured inside the cavity.

Figure 3-5 showed the corresponding changes in the flow field measured by the hot-wire 2 after the test model in terms of power spectra density E_u , located at $x =$

34mm and $y = 8.25\text{mm}$. It could be seen that Eu decreases from 4.1×10^{-3} to 6.2×10^{-4} (a reduction of about 85%). The result indicates that the open-loop control in the flow field was also effective; the perturbation on the up surface of the test model had damaged most part of the vortex shedding. The corresponding time domain signal was shown in Figure 3-6. It showed that the strong vortex shedding in flow field was damaged when with open-loop control.

The result for hot wire 1 which was located at the leading edge of the test model was similar with the result for hot wire 2, so the result for hot wire 1 was not shown.

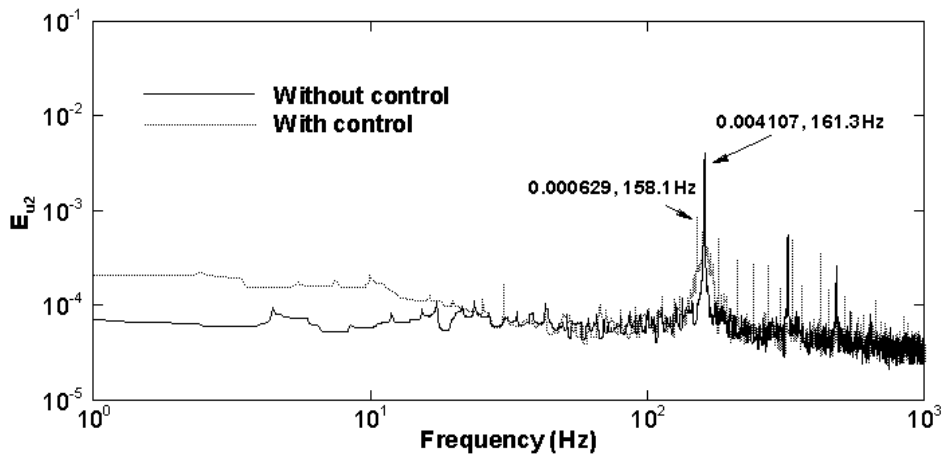


Figure 3-5 Control performance in flow field, flow speed is 8.2m/s ($Re=5980$). The hot wire 2 was located at $x = 34\text{mm}$ and $y = 8.25\text{mm}$.

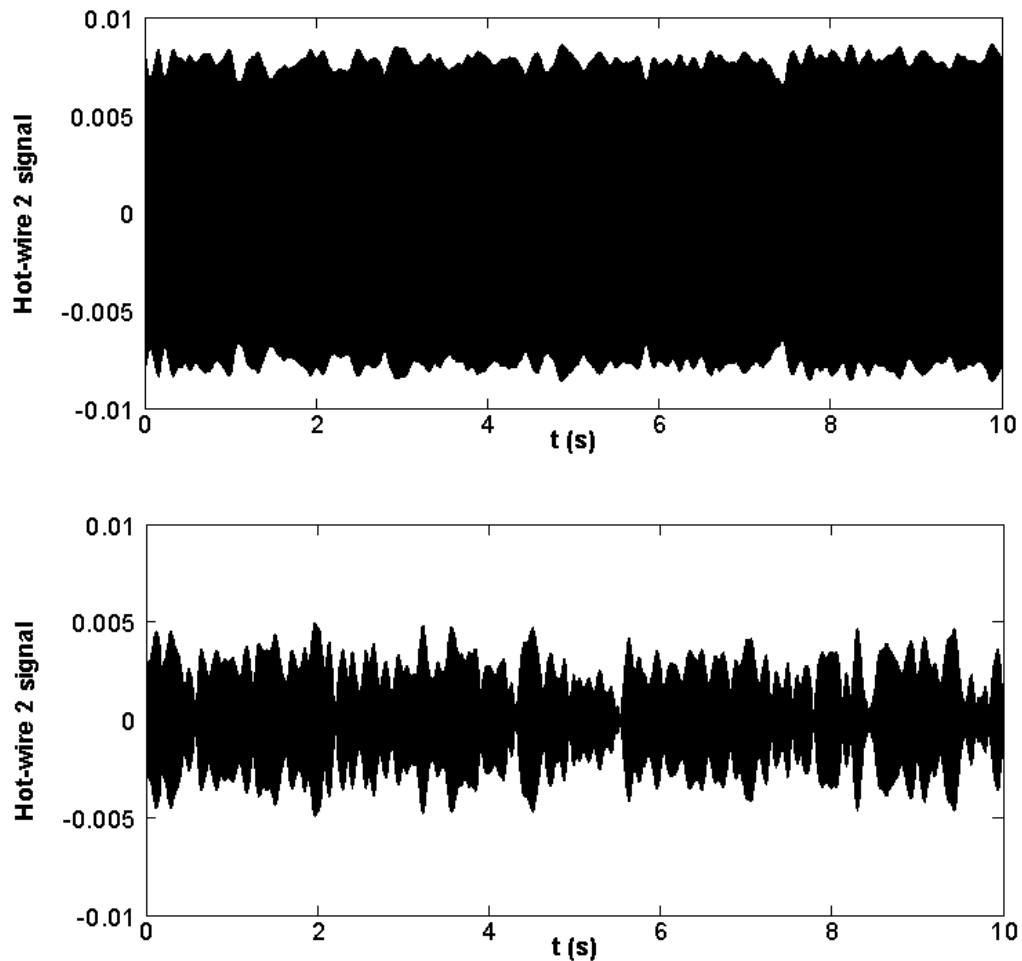


Figure 3-6 Time-domain results for the control performance in sound field, measured by hot-wire 2 located at $x = 34\text{mm}$ and $y = 8.25\text{mm}$. the signals are filtered by a 5Hz-band filter. (a) Without control; (b) With control.

3.4 Vortex strength abasement mechanism

When analyzing the control mechanism for control vortex shedding problem, the first task is to identify the characteristic of vortex shedding generation and the propagation path of the vortex shedding. The second task is to analyze how the vortex shedding can be affected by the control method.

3.4.1 The types of vortex shedding

Firstly, the types of vortex shedding around a semi-circular leading edge test model needed to be identified. In general, the vortex shedding could be classified into two types: Leading-edge vortex shedding (LEVS) and Trailing-edge vortex shedding

(TEVS). As mentioned in Chapter 1, around the short square leading edge bluff body, there was LEVS. LEVS and TEVS both existed for long square leading edge bluff body. When the leading edge was semi-circular, there was only TEVS.

Various measurements were performed to check the types of vortex shedding around a semi-circular leading edge test model. Hot-wire 1 was located at $x=0\text{mm}$ and $y=11\text{mm}$, hot-wire 2 was moved along the $y=11\text{mm}$ at different x positions. The spectral phase relationship $\phi_{u_1u_2}$ between hot-wire 1 and hot-wire 2 showed the vortex distribution along the $y=11\text{mm}$. The spectral phase $\phi_{u_1u_2}$ is defined by $\phi_{u_1u_2} (\equiv \tan^{-1}(Q_{u_1u_2} / Co_{u_1u_2}))$, where $Co_{u_1u_2}$ and $Q_{u_1u_2}$ are the cospectrum and quadrature spectrum of u_1 and u_2 , respectively. The cross-spectrum was computed from the Fast Fourier Transform of the correlation $\overline{u_1(t+\tau)u_2(t)}$. The results were shown in Figure 3-7. It was found that within the range of the surface of test model there was no clear vortex shedding, and behind the semi-circular leading edge test model, there was clear vortex shedding, so in the present test model, the type of vortex shedding was primarily TEVS. Furthermore, a simple measurement had been conducted to check the spectral phase $\phi_{u_1u_2}$ of the laminar boundary layer, it was found that for a laminar boundary layer, the spectral phase $\phi_{u_1u_2} = 0$. In Figure 3-7, the spectral phase $\phi_{u_1u_2} = 0$ from $x=0\text{mm}$ to $x=5.5\text{mm}$ and spectral phase $\phi_{u_1u_2} \neq 0$ from $x=5.5\text{mm}$ to $x=23\text{mm}$. The results imply that the laminar boundary layer had been changed within 5.5mm to 23mm, but it was not a vortex shedding. One could call it as redeveloped boundary layer. The redeveloped boundary layer acted as a key factor for the generation of the TEVS.

In addition, it was found that at the trailing edge the phase $\phi_{u_1u_2} = 0$, which indicated that TEVS had begun on this point. The TEVS was very clear along

$y=11\text{mm}$ and the length of one single vortex circle calculated by using the data in Figure 3-7 was about 38mm.

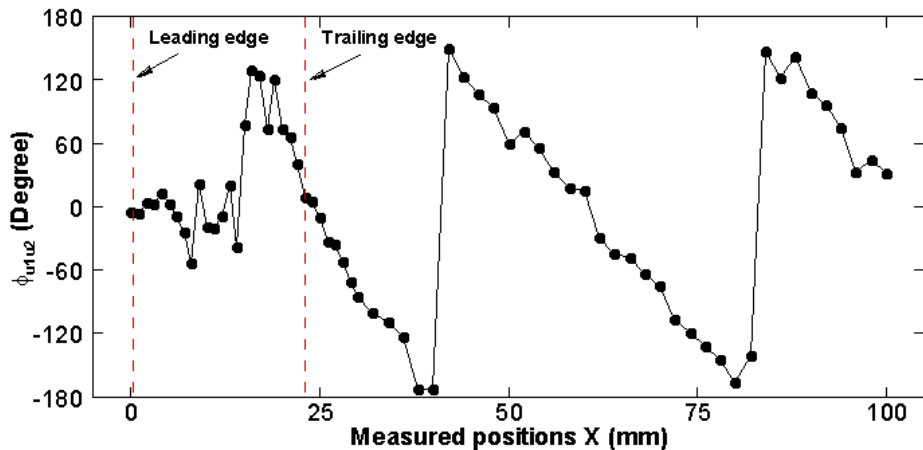


Figure 3-7 Phase relationship between hot-wire 1 and hot-wire 2 along $y=11\text{mm}$. Hot-wire 1 was located at $x=0\text{mm}$ and $y=11\text{mm}$, hot-wire 2 was move along the $y=11\text{mm}$ at different x positions.

3.4.2 Pressure disturbance mechanism

The low-order model for vortex shedding behind vibrating bluff body developed in Chapter 2 indicated that the vortex shedding behind the bluff body could be controlled by using external controllable vibration or perturbation. Furthermore, this model could be used to predict frequency shift phenomena. However, this model could not predict the exact change of both the frequency and strength of the vortex shedding under the surface perturbation because the model was only determine the qualitative relationship between two coupled oscillators. Section 3.3 described how the perturbation on the up surface of the test model did suppress the vortex shedding behind the test model. Although there were no exact mathematical models to explain the vortex strength abasement mechanism behind the vibrating bluff body, one could find a new way to explain the mechanism by the process of vortex shedding formation.

In general, a number of different local instabilities exist around elongated bluff

body or semi-circular leading edge bluff bodies when the flow past over them. The complexity of the flow around a bluff body is increased as a result of interaction between upstream and downstream flow structures and the interaction of flow structures and solid structures.

When the flow speed is above a critical Reynolds number, the instability in the wake is present in most bluff bodies. With long square leading edge bluff bodies and semi-circular leading bluff bodies, it is possible for the flow to separate at the leading edge and re-attach while shedding large-scale vortices at the trailing edge. A detailed investigation into the nature of this separated and re-attaching flow is found in Cherry et al. [110]. Two instabilities are involved: the Kelvin-Helmholtz instability that presents in the shear layer; and the instability that causes large-scale vortex shedding behind a bluff body. Experiments by Soria et al. [111] used long square leading edge bluff body to isolate any trailing edge effects. The separating and re-attaching flow was shown to be predominantly convectively unstable and receptive to a broad range of frequencies. The weak flapping of the shear layer without external perturbation could be the result of regions of local absolute instabilities. Another type of global instability occurs when a local convective instability interacts with a solid boundary downstream. Disturbances from the object downstream propagate upstream to complete a feedback loop. For a semi-circular leading edge bluff body, this phenomenon is observed when the shear layer from the leading edge is influenced by the trailing edge. This type of instability is similar to when jet or mixing layers impinge on some sharp edge downstream geometry of bluff bodies. The flow around square leading edge bluff body in the absence of any external forcing has been studied previously by Nakamura et al. [112-113]. The frequency of vortex shedding from the leading edge of the square leading edge is generally a single frequency. The instability

was thought to rely on the interaction of the leading-edge vortices with the trailing edge to generate a pressure pulse. This pressure pulse locks the leading-edge shedding and completes the feedback loop. The pressure pulse is relatively weak and therefore this locked response is restricted to low Reynolds numbers and only a limited range of chord-to-thickness ratios. It was described as impinging leading edge vortex (ILEV) instability since it can describes the process wherein leading edge vortices are shed, convected downstream and then interact with the trailing edge.

Hourigan[108] found that for short square leading edge bluff bodies, the leading edge shear layer can impinge directly on the trailing edge. For longer square leading edge bluff bodies, vortices are shed from the shear layer at the leading edge; these vortices convect along the plate and interact with the trailing edge. For semi-circular leading edge bluff body, it is the same characteristic as the long square leading edge bluff bodies. For bodies with streamlined trailing edges the leading-edge vortices generate a pressure pulse as they pass the trailing edge. However, for the bodies with bluff trailing edges as in the present case, the leading edge vortices or redeveloped shear layer interact with the shedding at the trailing edge. That is, trailing edge vortices can only form between the passing of leading edge vortices or redeveloped shear layer. The leading edge vortices punctuate the redeveloped boundary layer and restrict the phases at which trailing-edge shedding can occur. The pressure pulse from the vigorous trailing edge shedding then feeds back upstream and controls the leading edge shedding. The schematic of feedback loops of vortex shedding for semi-circular leading edge bluff body is shown in Figure 3-8. This process can be called as impinging leading edge vortex instability (ILEVI) and it consists of a combination of leading edge vortex shedding (LEVS) and trailing edge vortex shedding (TEVS).

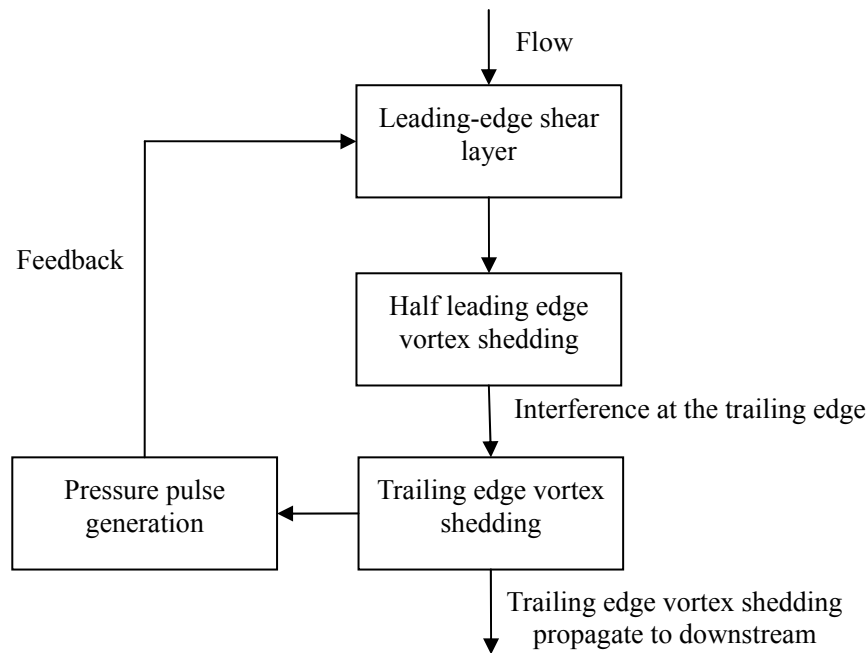


Figure 3-8 Schematic of feedback loops of vortex shedding for semi-circular leading edge bluff body.

In the present study, a surface perturbation was used on the up surface of semi-circular leading edge bluff body and obtained a reduction in vortex strength. The reduction can be explained when taking the ILEVI into account. In the process of feedback loops of vortex shedding for semi-circular leading edge bluff body, the pressure pulse is not very strong but it is a key factor for generating the next vortex shedding. In Figure 3-9, a semi-circular leading edge bluff body is placed in the flow stream. The flow is separated when it meets with the bluff body. Firstly, it generates leading edge shear layer which is a laminar layer. This shear layer will develop into redeveloped boundary layer on the surface of the bluff body. When redeveloped boundary layer passes the bluff trailing edge, it interacts with trailing edge and generates the TEVS. During the generation of the TEVS, it will also generate a pressure pulse and feedback to the leading edge shear layer to control the next vortex shedding. The surface perturbation technique is to generate a small local perturbation in the space between leading edge shear layer and trailing edge. This small local

perturbation has two effects on the flow around it. Firstly, it continuously changes the surface of the bluff body in sequence of time which disturbs the pressure pulse on the trailing edge to feedback to the exact corresponding point in the leading edge shear layer and then damage the generation of next vortex shedding. Secondly, the perturbation also generates a small velocity in the transverse of the surface which alters the flow structure around the surface of the bluff body. The alteration disturbs the leading edge shear layer to convect to the trailing edge and the pressure pulse to feedback the leading edge shear layer, which influences the generation of trailing edge vortex shedding. However, the surface perturbation disturbs the generation of the trailing edge vortex shedding, not prevent the generation of the trailing edge vortex shedding. So in the present experiment, the vortex shedding strength is reduced but not disappeared.

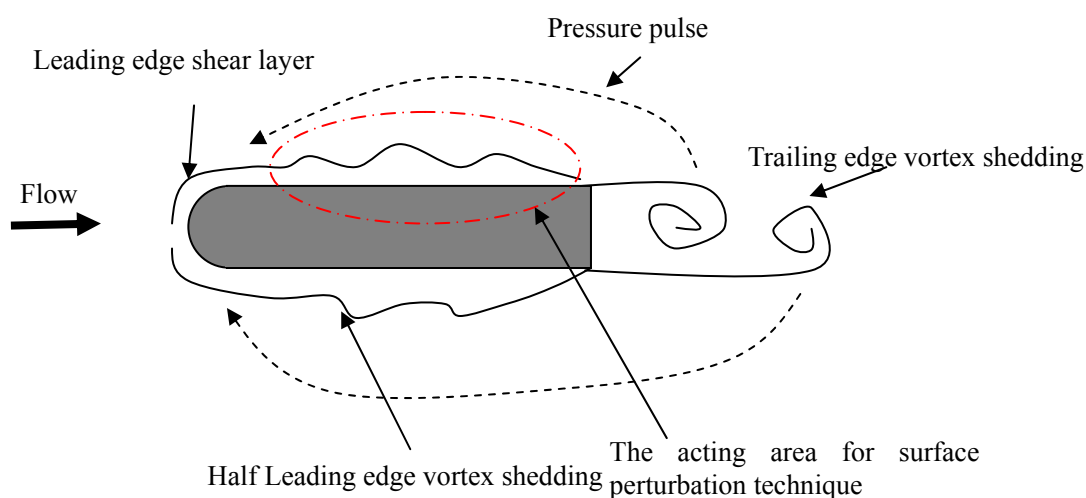


Figure 3-9 Illustration of pressure disturbance mechanism.

In conclusion, a mechanism which can be used to explained the abasement mechanism of vortex shedding strength when applying surface perturbation technique is developed and it is called 'Pressure disturbance mechanism'. However, the flow structure is very complex around the test model; it is not easy to build a mathematical model for this mechanism. Therefore, one can use this mechanism to explain the

physics of the control.

3.4.3 Shear layer shifts mechanism

In section 3.4.2, pressure disturbance mechanism was developed to explain the abatement of vortex strength. This mechanism is focus on disturbing the generation for the new vortex shedding in the leading shear layer. In this section, another way for investigating the control of the vortex shedding is discussed; this method is base on the trailing edge vortex shedding formation process and focus on the flow structure change around the trailing edge.

This trailing edge vortex shedding formation process, which was first presented by Gerrad [30] and further developed by Lucas and Turner [32], could be summarized in Figure 3-10,. In the model, two shear layers SL_1 and SL_2 alternately rolled up to form the vortices in the wake, the shear layer SL_1 created flow A , which entrained into the vortex V_1 ; Flow B from shear layer SL_2 caused detachment of V_1 ; the other flow C from shear layer SL_2 was induced back into the formation region, which was ready to initiate production of the next vortex V_2 . And the strength of the vortices would be determined by the relative magnitudes of flow A, B and C. Normally C should be maximum, A minimum, with B just sufficient to ensure effective detachment of the growing vortex.

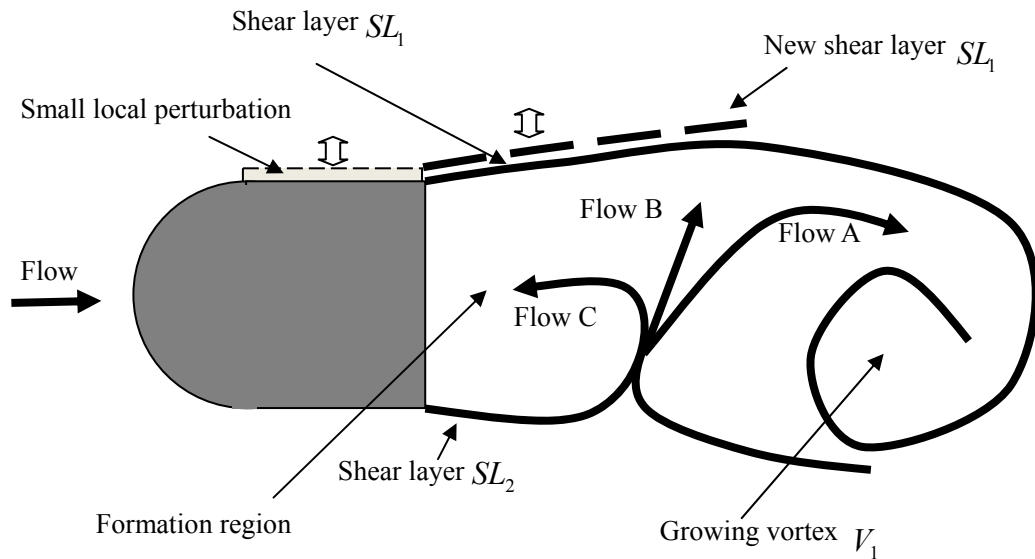


Figure 3-10 Motion of boundary layers during the trailing edge vortex formation process and the schematic for applying small local perturbation.

Two factors are centrally important in the trailing edge vortex shedding formation, (a) the shear layers should roll up to form vortices of sufficient strength; (b) the shear layers should interact closely with each other. If any one of these factors (or both of them) is disabled or disrupted, then, it would prevent proper roll up of shear layers and thus, the trailing edge vortex shedding phenomenon which would ultimately be suppressed.

At the absent of external perturbation, the distance of two shear layers is d_{SL} , the trailing edge vortex shedding is generated periodically. When small local perturbation is applied, the up surface of the vibration plate is vibrating on the transverse direction. The transverse velocity perturbation can weaken the strength of the shear layer SL_1 , causing the strength ‘disharmonic’ of shear layer SL_1 and shear layer SL_2 . This causes the relative magnitudes of flow A, B and C to change and subsequently weakens the strength of the trailing vortex shedding. The perturbation also changes the geometry of the up surface of the bluff body. The displacement along the transverse direction of the up surface of the bluff body is d_p , which varies based on

the applied control signal. Without the surface perturbation, there is no change in the up surface, $d_p = 0$, and the distance between two shear layers is d_{SL} . With the surface perturbation, the geometry of the up surface changes, $d_p \neq 0$ and the distance between two shear layers is now $d_{SL} + d'_p$, where d'_p is relative to the displacement of the vibration plate with $d'_p \leq d_p$. Therefore, the second factor in Gerrad [30] which is important for the generating of trailing edge vortex shedding cannot be satisfied. The distance between two shear layers changes all the time so the flow A, B and C cannot stay in a similar condition to that without control. Since the condition varies with time, the flow state may not be stable, which influences the generation of vortex shedding V_1 . In conclusion, the change of the distance between two shear layers can result in a significant reduction in the energy of trailing edge vortex shedding behind of the test model.

The small local perturbation shifts the shear layers and this shift weakens the flow A, B and C behind the test model and can determine the generation of the vortex shedding. When the generation of the vortex shedding is affected, the strength of the vortex shedding can be reduced. One could call it 'Shear layer shifts' mechanism' and the process is shown in Figure 3-11. This mechanism also indicates that there is a frequency shift phenomena due to the geometry change of the test model, which will be explained in the next section.

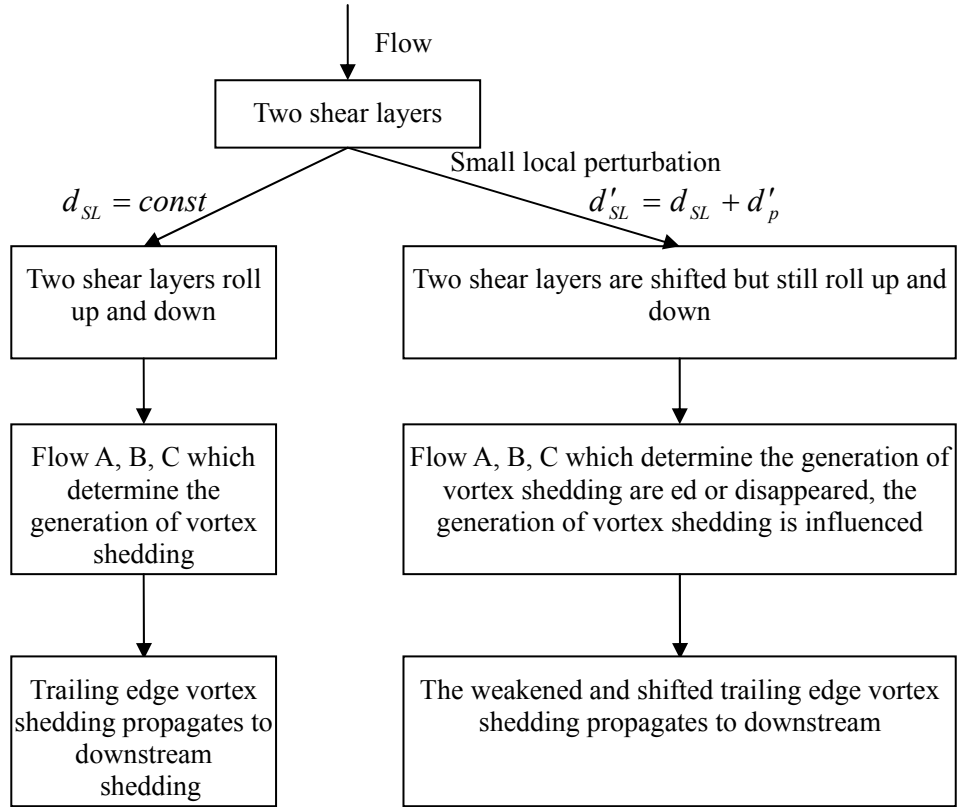


Figure 3-11 The shear layer shifts mechanism.

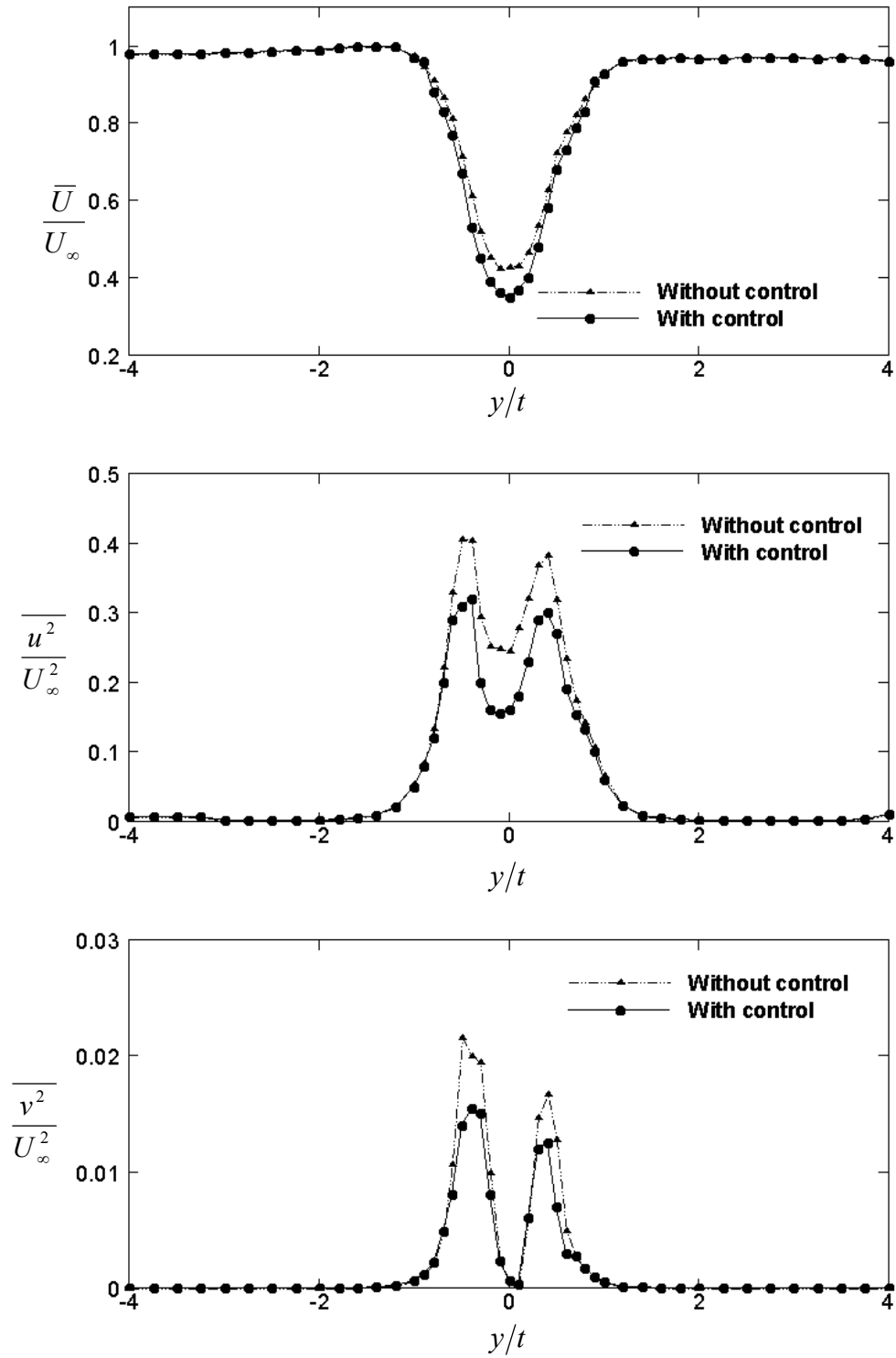
The occurrence of this mechanism in the experiment was investigated by measuring the flow distribution behind the test model. The test model was placed into the flow field. The root mean velocity values of $\overline{u^2}/U_\infty^2$ and $\overline{v^2}/U_\infty^2$ behind the test model were measured, where $\overline{u^2}/U_\infty^2$ and $\overline{v^2}/U_\infty^2$ were the x direction root mean velocity and y direction root mean velocity respectively of flow A, B or C [Gerrad [30]] The distributions at $x/h=1$ of these two values are shown by the solid s in Figure 3-12. After the application of the surface perturbation, $\overline{u^2}/U_\infty^2$ and $\overline{v^2}/U_\infty^2$ decreased by about 10%, imply that the strength of the generating vortex shedding had been weakened.

Based on the above analyses, the shear layer shifts mechanism for the abasement of vortex energy can be summed up as the followings. The vortex-induced acoustic resonance originates from the strong interaction of the coupled vortices shed from

trailing edge of the bluff body. The controlled surface perturbation disturbs the two shear layers, and thus weakens the strength of flow A, B and C, resulting in a clear disruption on the formation of the trailing edge vortices and creating a significant reduction in the vortex strength in the wake of the model. The whole process results in an effective impairment in the flow acoustic interaction and subsequently the vortex-induced acoustic resonance.

In conclusion, two mechanisms are developed for explaining the abatement of vortex shedding strength when open-loop control was implemented on the test model. Although these two models cannot predict the quantitative value of the vortex strength reduction, it can illuminate important factors that influence the development of the vortex shedding under the surface perturbation control. The disturbance pressure pulse mechanism might be a more proper way for explaining the control mechanism based on the physics of the control process. On the other hand, the shear layer shift mechanism is easy to understand and can be used to predict the shedding frequency shift as detailed in the next section.

3. Active open-loop control of flow-induced acoustic resonance



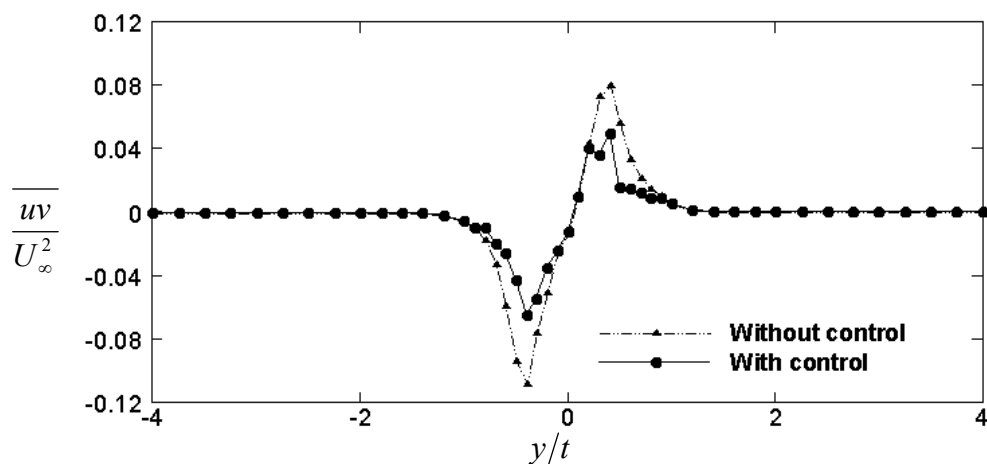


Figure 3-12 Cross-flow distribution of mean streamwise flow velocity and Reynolds stresses at x/t , open-loop control. (a) \bar{U}/U_∞ , (b) \bar{u}^2/U_∞^2 , (c) \bar{v}^2/U_∞^2 , (d) \bar{uv}/U_∞^2 . $U_\infty = 8.2\text{m/s}$.

3.5 Frequency shift phenomena

In Chapter 2, the low-order model has predicted that when an external surface control perturbation on the bluff body, the frequency of the vortex shedding behind the test model shifted to a lower or higher frequency, relative to the uncontrolled vortex shedding frequency. The frequency shift phenomenon was found in the present open-loop control results. In this section, the mechanism for the frequency shift will be analyzed.

In order to investigate the frequency shift in the open loop control, various measurements were done by using the open-loop system. When the perturbation displacement of the vibration plate was varied, the corresponding shedding frequency f_s was obtained from the Mic.1 measurements. The maximum displacement of the vibration plate d_{pm} was measured by a laser vibrometer at the center point of the vibration plastic plate. In the present study, when without control, the vortex shedding frequency was $f_s = 161.3\text{Hz}$. As Figure 3-13 shows that the shedding frequency f_s was generally reduced upon deployment of the control. With small perturbation amplitude of typically less than 0.4mm , the reduction is trivial of typically less than 1

Hz. With higher d_{pm} , the reduction in f_s became more appreciable. The optimum control configuration used in this paper ($f_p = 30\text{Hz}$ and $V_p = 160\text{V}$) corresponded to $d_{pm} = 0.83\text{mm}$, the shift in f_s could reach 2.84Hz . The effect of this frequency shift on the control performance will be assessed later.

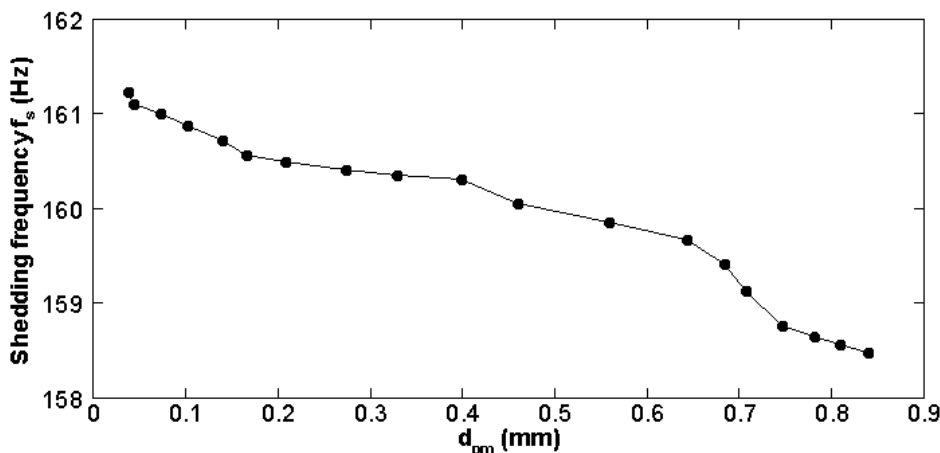


Figure 3-13 the shift of shedding frequency at various maximum displacement d_{pm} of the vibration plate, $f_p = 30\text{Hz}$, measured by Mic.1.

In Section 3-4, it was explained from the point of view of the shear layer shift mechanism that when a relatively small surface perturbation is applied, the thickness of the plate increases and the distance between two shear layers behind the test model will be changed as a consequence. The distance d_{SL} between two shear layers will determine the shedding frequency of the vortex shedding, which means that the shedding frequency will change with time when the time-varying surface perturbation control is implemented. This is the mechanism of the vortex shedding frequency shift. However, it is no easy to identify the exact distance between two shear layers. One can find another way to calculate the relationship between frequency shift and the perturbation displacement. In fact, the perturbation also changes the geometry of the up surface of the test model. As Figure 3-14 shows that when applying a small local perturbation in the open-loop control, the maximum displacement of the vibration

plate is d_{pm} ($d_{pm} \geq 0$). In this mechanism, one can consider that the reduction of the shedding frequency can be attributed to the geometry of the up surface of the test model generated by the surface perturbation technique. The shedding frequency f_s can be defined as follows,

$$f_s = S_t \frac{U}{t} \quad (3-6)$$

Where St is the Strouhal number, U is the flow velocity, and t is the thickness of the test model. In Equation 3-6, the shedding frequency can be calculated by using the Strouhal number S_t , flow velocity U and the thickness t of the test model. In the present case, the perturbation only generates small transverse velocity which cannot influence the flow velocity U . There is no direct evidence that the Strouhal number St will change when applying the surface perturbation technique. In fact, for a fixed experiment set-up and test model, the Strouhal number S_t is a constant value during the control period. So only the thickness of the test model can be considered to act as the key factor for the frequency shift. With control, the displacement of the vibration plate d_p varies with time with the maximum d_p value of d_{pm} as illustrated in Figure 3-13. Assuming \bar{d}_p represents the equivalent increase in the thickness of the vibration plate; the perturbed shedding frequency f_{sp} can be expressed as:

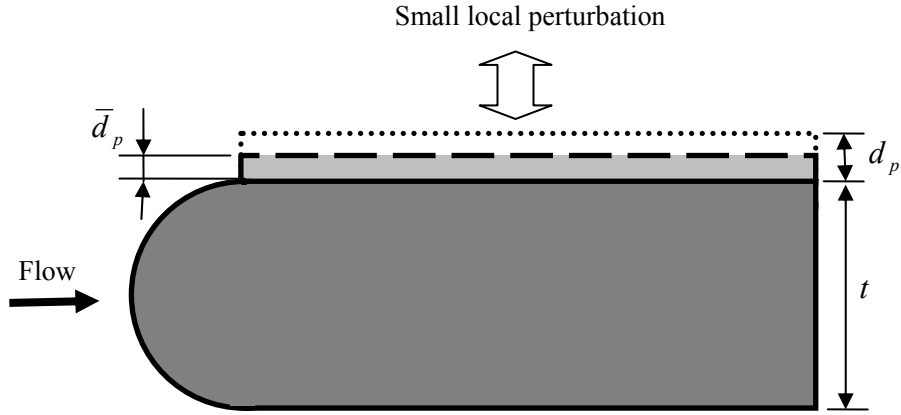


Figure 3-14 The schematic of effective displacement of the vibration plate

$$f_{sp} = \frac{S_t U}{t + \bar{d}_p} = \frac{S_t U}{t \left(1 + \frac{\bar{d}_p}{t} \right)} \quad (3-7)$$

Usually, $t \gg d_{pm} \geq \bar{d}_p$, therefore $\frac{\bar{d}_p}{t} \ll 1$ and

$$f_{sp} = \frac{S_t U}{t} \frac{1}{1 + \frac{\bar{d}_p}{t}} \approx \frac{S_t U}{t} \left(1 - \frac{\bar{d}_p}{t} \right) = f_{s0} \left(1 - \frac{\bar{d}_p}{t} \right) \quad (3-8)$$

where f_{s0} is the unperturbed vortex shedding frequency.

$$\Delta f_{sp} = f_{s0} - f_{sp} = \frac{\bar{d}_p}{t} f_{s0} \quad (3-9)$$

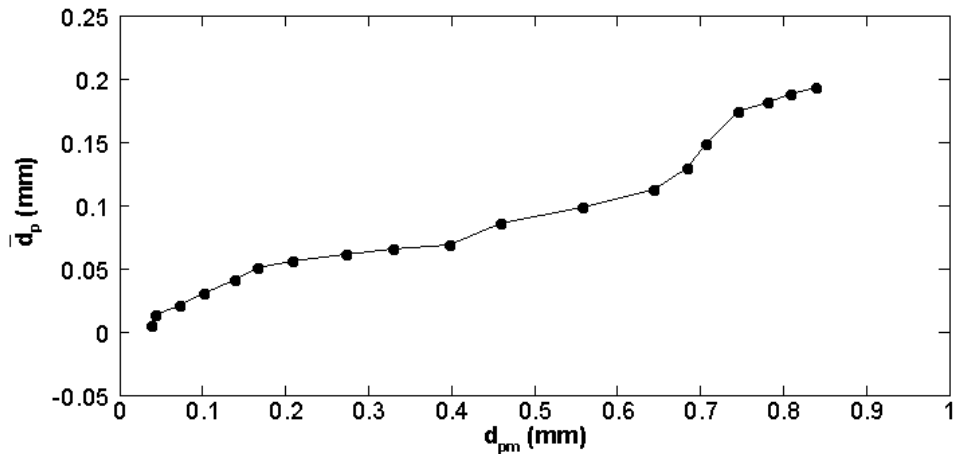
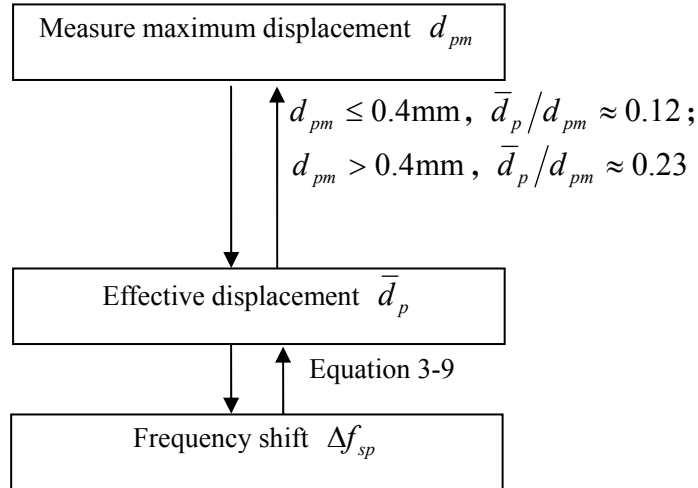


Figure 3-15 The effective perturbation displacement of the vibration plate, $f_p = 30\text{Hz}$.

Equation 3-9 shows that the reduction of Δf_{sp} is linearly related to \bar{d}_p , which

can be estimated by using the vortex shedding frequency shift data in Figure 3-13 and Equation 3-8. Figure 3-15 shows the variation of d_{pm} versus \bar{d}_p . In the low perturbation region (with small perturbation amplitude, typically $d_{pm} < 0.4\text{mm}$), \bar{d}_p/d_{pm} is roughly 12%, whilst for larger perturbation amplitude, \bar{d}_p/d_{pm} approached 23%. In the optimal configuration, the effective increase in the thickness of the vibration plate brought about by the perturbation is roughly $0.19/11 = 1.7\%$. This was shown to cause 2.84 Hz shift in f_s . So Equation 3-9 can be used to predict the shift of shedding frequency when using the surface perturbation technique.

In Equation 3-8, since in surface perturbation technique, $\bar{d}_p \geq 0$, it indicates that the when with perturbation, the vortex shedding frequency only shifts to low frequency. In Figure 3-15 shows that the value of \bar{d}_p/d_{pm} can be identified for the present test model and experiment set-up. When $d_{pm} \leq 0.4\text{mm}$, $\bar{d}_p/d_{pm} \approx 0.12$; when $d_{pm} > 0.4\text{mm}$, $\bar{d}_p/d_{pm} \approx 0.23$. A laser vibrometer was used to measure the maximum displacement d_{pm} at the centre point of vibration plate and calculate \bar{d}_p . Finally, the frequency shift Δf_{sp} was calculated by using the Equation 3-9. The overall process can be summarized as Figure 3-16. As a result, when the frequency shift Δf_{sp} is known, the maximum displacement of vibration plate on the surface of the test model can be predicted.

Figure 3-16 The prediction process of the frequency shift Δf_{sp} .

The frequency shift phenomena discussed in the section can draw the following conclusions:

- (1) A low-order model was developed in Chapter 2 which predicted the vortex shedding frequency shift when external vibration or perturbation was applied to the system. This prediction has been confirmed by the frequency shift phenomena explained in this section. Although the low-order model cannot predict the value of the frequency shift, the Equation 3-9 developed in this section can be used to calculate the exact value of the frequency shift.
- (2) In this section, the displacement of the vibration plate is considered to play the main role on shifting vortex shedding frequency. Physically, the vortex shedding frequency is determined by the distance between two shear layers around the test model. The shift of the vortex shedding indicates that the distance between two shear layers has been changed. On the other hand, the shift phenomenon has confirmed that the shear layer shifts mechanism developed in section 3.4.3 is consistent. The perturbation on the vibration plate shifts the shear layer around the up surface of the test model; this shift can change the vortex shedding

frequency. And its structure, resulting in the abatement of vortex shedding strength.

- (3) The frequency shift is very useful for controlling the acoustic resonance. The adjustable shift in the present experiment allows the system to control the vortex shedding frequency by shifting it away from the acoustic resonance in the system, leading to a further noise reduction inside the cavity. This part will be discussed in the next section.

3.6 Effects on downstream cavity resonance

Section 3.5 has shown that there is a shift in vortex shedding frequency when a surface perturbation is applied. Before discussing the effects of the shedding frequency shift on control performance, measurements were conducted to investigate the characteristics of the acoustic downstream cavity resonance.

3.6.1 The resonance of downstream cavities

Figure 2-22 shows how the test model was installed in a duct with a cross section of 100mm×100mm. The acoustic resonance of the straight duct itself is about 1700Hz, which is far away from shedding frequency of the test model in the experiment. Therefore the acoustics resonance of two downstream cavities can be used to check the effect of acoustics resonance. Downstream cavities DC-1 was used in the present experiment.

Using the above experiment configuration shown in Figure 2-22, and the test model is C1 and downstream cavities are DC-1. The sound pressure level spectra measured by the two microphones are compared in Figure 3-17 in terms of $\Delta SPL = SPL_{m2} - SPL_{m1}$, with SPL_{m2} and SPL_{m1} being the SPLs at Mic.2 and Mic.1, respectively. Figure 3-17 clearly shows three different regions in which ΔSPL shows

very different characteristics.

(1) Region A: In the low frequency range, ΔSPL totters around zero, indicating comparable SPLs in the duct and in the cavity. This suggests that the sound inside the duct is simply transported into the cavity. The flow noise inside the duct is within this region, since there is no effective way to avoid the influence of the flow noise, especially in the case of high flow speed, it is better to design the vortex shedding away this region.

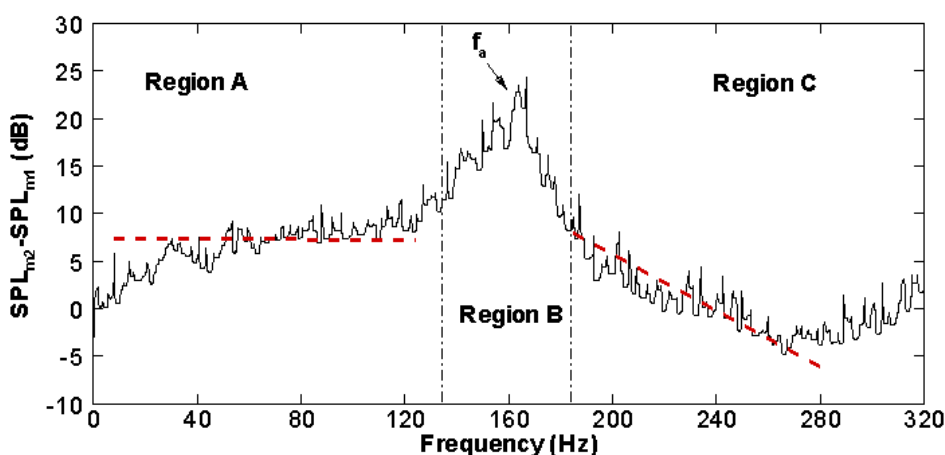


Figure 3-17 Downstream cavity resonance, $L = 487\text{mm}$, $d = 100\text{mm}$, $U = 8.2\text{m/s}$.

(2) Region B: In a region which is relatively close to cavity resonance frequency f_a , sound pressure level inside the cavity is obviously higher than that in the duct. This is a clear evidence that sound is amplified by the cavity resonance effect. As an example, at resonance $f = f_a$, the difference reached about 20dB. In order to show the effect of shift resonance, the vortex shedding frequency f_s is usually smaller than resonance frequency f_a . In the present open-loop control, when the vortex shedding frequency shift from 161.3Hz to 158.4Hz, there is 5.0dB extra reduction inside the cavity. This can be explained by the curve shown in Figure 3-17. When the vortex shedding frequency shift from 161.3Hz to 158.4Hz, the ΔSPL in Figure3-17 is decreased from 21.0dB to 16.8dB, the difference of these two points is 4.2dB, lower

than dB due to some unpredictable factor in the measurement system, it indicates that because the cavity acoustic resonance which contributes the extra reduction inside the cavity.

(3) Region C: Above the resonance region, ΔSPL decreases, indicating a weaker acoustic field inside the cavity compared with that in the duct. One plausible reason is that at higher frequencies, sound dissipations increase with the decrease of wave length. Therefore, sound becomes much weaker when reaching the Mic.2 position which is at the far end of the cavity.

3.6.2 Resonance bandwidth and acoustic resonance effect

In section 3.6.1, the characteristics of the acoustic cavity resonance has been identified. The resonance bandwidth is needed to be determined which is an important parameter for investigating the acoustical resonance effect. To this end, a series of tests were conducted to document the sound pressure level measured by Mic.1 and Mic.2 at shedding frequency f_s under various flow velocities before the control was deployed. The results are shown in Figure 3-18. The peak values of sound pressure level at f_s , measured by Mic.1, monotonously increase as the flow velocities increase. While the peak values of sound pressure level at f_s , measured by Mic.2, reaches a peak value of 97.1dB when $U = U_{cr} = 8.2\text{m/s}$ (i.e. $f_s = f_a = 161.3\text{Hz}$). Using the bandwidth definition corresponding to -3dB reduction, the band width of the resonance peak was determined as 3.4 Hz from 159.0Hz to 162.4Hz, corresponding to a flow velocity variation from 8.0m/s to 8.3m/s.

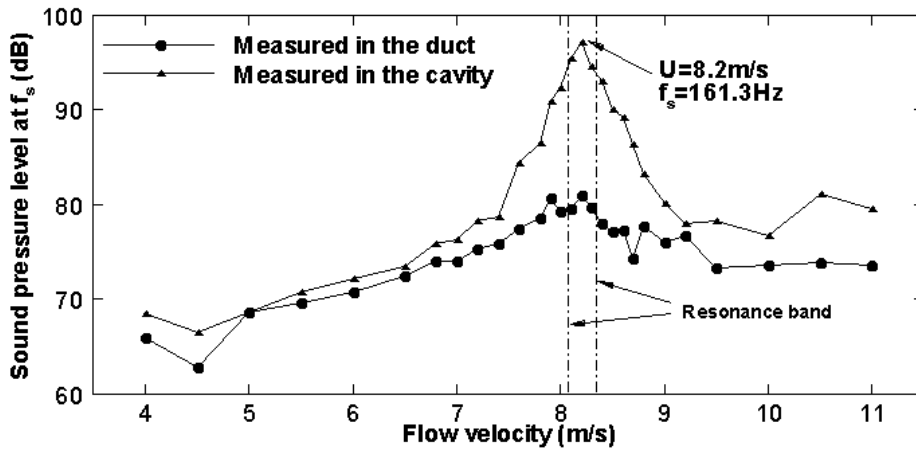


Figure 3-18 Sound pressure level at f_s at various flow velocities, without control.

Figure 3-19 shows the control effect on the previously defined ΔSPL at f_s at various flow velocities with $f_p = 30Hz$ and $V_p = 160$ volts. It can be seen that apart from resonance region, sound reductions in the duct and in the cavity are almost the same. This should be attributed to the weakened vortex strength, which has been extensively discussed in our previous section. Around cavity resonance, sound reduction inside the cavity exceeds that in the duct, by as much as 5.0dB. This can be attributed to the control-induced shift of the vortex shedding frequency. In fact, a 2.84Hz shift in f_s exceeds the half bandwidth of the cavity resonance, this alone should bring about more than 3dB reduction in the SPL.

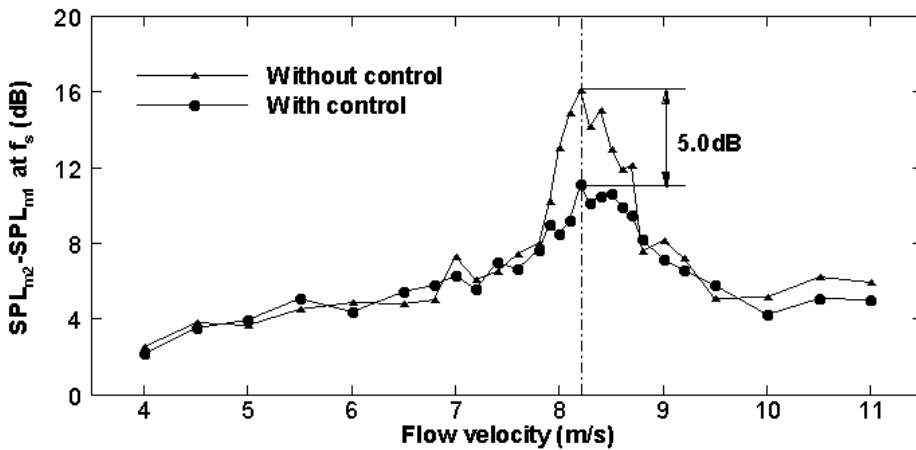


Figure 3-19 The control effect on $SPL_{m2} - SPL_{m1}$ at f_s at various flow velocities, $f_p = 30Hz$ and $V_p = 160$ V.

In conclusion, when applying surface perturbation technique on the test model, the perturbation increases the effective thickness of the plate. The increase of the effective thickness of the plate can shift the shedding frequency. The quantity of the shift can be estimated by Equation 3-9. If the shedding frequency shift that caused by the perturbation exceeds the resonance bandwidth of the acoustic cavity, the sound reduction inside the cavity is larger than that in the duct. In the present experiment, this phenomenon along gives a rise to a further sound pressure reduction of 5.0 dB inside the acoustic cavity. In a word, when vortex shedding occurs and its shedding frequency is close to the acoustic resonance of the cavity, the surface perturbation not only disturbs the two shear layers and thus weakens the strength of the vortex, but also shifts the shedding frequency, and then suppresses the acoustic resonance phenomenon.

3.7 Conclusions

The control of vortex-induced acoustic resonance by using an active open-loop control system has been experimentally investigated. The control results have shown that this method is an effectively control method for vortex-induced acoustic resonance problems. Generally, the present paper leads to the following conclusions.

(1) Using optimal control frequency f_p and control voltage V_p , the controller achieve the best performance by reducing the sound pressure level (SPL) at the first acoustic resonance by about 16.3 dB in the duct and 21.3dB in the cavity, respectively; Furthermore, the control performances are repeatable and reliable.

(2) During the generation of the TEVS, a pressure pulse is generated and feedback to the leading edge shear layer to control the subsequent vortex shedding. The surface perturbation technique in the present experiment is used to generate a

small local perturbation in the space between leading edge shear layer and trailing edge. This small local perturbation can disturb the pressure pulse on the trailing edge to feedback to the exact corresponding point in the leading edge shear layer and then alter the generation of next vortex shedding, leading to a reduction in the vortex shedding strength.

(3) The surface perturbation technique change the geometry of the up surface of the test model, it can shift the shear layer which attaches to the surface. The shift disturbs the two shear layers, and thus weakens the strength of flow A, B and C, which results in a clearly disturbance on the formation of the trailing edge vortices, leading to a significant reduction in the vortex strength in the wake of the model. This mechanism is called ‘shear layer shifts’ mechanism, which is also used to explain the vortex shedding frequency shift.

(4) There is a shift in the shedding frequency caused by the control action. A formula was derived to predict this frequency shift in the effective control region. It was shown that the perturbation brings about 1.7% increases in the effective height of the plate, resulting in a frequency shift of about 2.84 Hz that was confirmed by the experiment.

(5) It is found that when vortex shedding occurs at the case that its shedding frequency is close to the first acoustic resonance of the downstream cavity, the present surface perturbation not only weakens the strength of the vortex shedding, but also shifts the shedding frequency, and then suppresses the acoustic resonance phenomenon. In the present open-loop control, due to the downstream cavities resonance effect, there is a further sound pressure reduction of 5.0 dB inside the acoustic cavity.

So the surface perturbation technique is an effective and practical method for the

flow-induced vortex control, it can not only weakens the strength of the vortex, but also change the shedding frequency, and then suppresses the acoustic resonance phenomenon. However, the control signal in open-loop control is independent of what is occurring in the system. One can improve the control performance by involving more information in system response using closed-loop control to be investigated in the next Chapter.

4. Downsampling theory and implement in real time control system

4.1 Introduction

In Chapter 3, the control of vortex-induced acoustic resonance has been experimentally investigated by using an active open-loop control system. It is found that the open-loop control method is an effectively control method for vortex-induced acoustic resonance problems.

However, the control signals input into the test model are independent of what is occurring in the system, which does not allow adjusting the control signals according with the system response. Thus, adding some feedback information from a number of sensors inside the duct or cavity may be thought as a good way to improve control performance because the control actuation will be influenced by the feedback response measured by the sensors. The control system that uses feedback signals for controlling is called closed-loop control. If the feedback signal in the closed-loop control is adjusted properly, the generated control actuation may influence the flow field more such that the resulting noise may be further reduced. This consideration leads to the closed-loop control investigation.

At first, it seems to be a straightforward process to implement closed-loop control by using direct feedback signals from the sensors such as the hotwire. However, it is found from the investigation that there is a main difficulty of such control practice for our experiment configuration due to the characteristic of the test model used in the

present experiment which only generates larger displacement around 30Hz than that in high-frequency ($>100\text{Hz}$). Realizing the difficulty in using a high-frequency control signal in the closed-loop control system, a new signal analysis method which is called ‘downsampling’ is developed. In this method, the feedback signal at high frequency is down-sampled to a much lower frequency so that the test model can generate close to a maximum displacement. The detail of this signal analysis method and its implementation in real time control system will be described in this Chapter.

4.2 Limitations of the open-loop control

In Chapter 2, an open-loop control was successfully applied in the control of vortex-induced acoustic resonance. The control signal is $u(t) = V_p \sin(2\pi f_p t)$ in open-loop control, where V_p is the voltage that measured after the PZT amplifier and f_p is frequency of the control signal which is called control frequency. The optimal V_p and f_p was identified in Chapter 2 by conducting various measurements and the best performance in open-loop control was achieved at the optimal V_p and f_p . However, the signal of the open-loop control is independent with the system response, so there are some limitations for further improving the control performance.

Firstly, in the open-loop control, the sinusoidal type signal is chosen as the control signal based on the assumption that the measured signal around the shedding frequency f_s is primarily tonal. In fact, the measured signal around the shedding frequency f_s is relatively complex. The primary part of the signal is of a single frequency, but there also exists other signals with slightly different frequencies and magnitudes. In other words, it is a multi-tone signal. Therefore, a single-tone signal used in open-loop control may not be sufficient to capture the entire important

characteristics of the system response, particularly at frequencies around the vortex shedding frequency. Furthermore, the exact value of the vortex shedding frequency is practically not known since it varies according to the change in system dynamics. From the previous observation in open-loop control, the vortex shedding frequency is shifted to a low frequency and the shift slightly varies with time during control. These situations cannot be effectively accommodated in the open-loop control. The control performance can be improved if a more accurate signal, representative of the actual system response, is chosen as a reference to the control signal. In this case, the closed-loop control using feedback signals from the system provides a potentially better alternative to open-loop control. However, the challenge in this control method is in identifying the signals that are representative to the vortex shedding characteristics and in downsampling the signals so that they can be efficiently used for surface perturbation control.

Secondly, the maximum level of surface perturbation is fixed in the open-loop control. However, a larger perturbation does not necessarily correspond to a better control performance. To ensure that the surface perturbation achieve its performance objective in controlling the vortex shedding process, it is necessary to adjust the level of surface perturbation based on the system response. This method can be done using the closed-loop control, which is another potential improvement from the open-loop control system.

Finally, the surface perturbation generated using open-loop control does not have any time dependence on the system response. In other words, in the open-loop control, there is no phase relationship of its control signal with the system response. In general, the phase of the control signal is regarded as one of the key factors in control. In general, the control signal with different phases might result in different control

performances. In the open-loop control, the control actuation using the surface perturbation is applied at a random time relative to the system response. Therefore, the control performance may not be optimal because the surface perturbation is applied not necessarily at the best timing to optimally reduce the vortex shedding strength. Using the closed-loop control can alleviate this problem by applying the surface perturbation at a better timing to obtain an optimal control performance.

In conclusion, although the open-loop control could be successfully implemented in the previous study and good control performance has been achieved in the open-loop control, the open-loop control still has its own limitations. In order to achieve a better control performance, these limitations need be carefully considered. For this purpose, an active closed-loop control for flow-induced acoustic resonance is proposed in the present study. The initial preparations of the closed-loop control will be discussed in this Chapter.

4.3 Possibilities for applying closed-loop control strategy

In the closed-loop control system, the feedback signals can be obtained from hotwire, microphone and other sensors. Before the feedback signals are input into the test model, it can be dealt with different signal analysis processes. In this section, the possible ways for applying the closed-loop control strategy are discussed.

In general, the feedback signals can be used straightly in the closed-loop control, and then the system response can be feedback directly to the system again. In the present study, the main frequency of the feedback signal is around 160Hz. It means that the test model will work at this frequency when it is excited directly by the feedback signal. However, Figure 2-13 has shown that the test model used in the present study has a dominant frequency response at around 30 Hz, with a decreasing magnitude as the excitation frequency increases. The magnitude of control actuation

(displacement) is measured to be only 0.02mm at 160Hz, compared to the maximum displacement of 0.83mm at 30Hz. Such a small actuation of only 2.4% of the test model maximum capability at 160Hz is expected to lead to relatively poor control performance.

Realizing the difficulty in directly using a high-frequency control actuation in the present test model, one needs to find a new way for using the feedback signal in the closed-loop control. There are three parameters in the feedback signals: the amplitude, frequency and the phase. Due to the frequency response characteristic of the test model in the present study, the frequency of the feedback signal needs to around 30Hz which allows the test model to generate the maximum displacement when it is used as the control signal. However, one of the main challenges is to ensure the amplitude and phase of control signal can still be related to the original feedback signal when the signal is down-sampled from around 160Hz to around 30Hz.

A semi-closed-loop control was developed for an initial investigation. In this method, the type of the control signal was a sinusoidal function, where the control frequency was set to 30Hz, and the control voltage was fixed to a constant value. In this case, only the phase of the control signal was varied for control purposes. The sinusoidal cycle of the control signal was synchronized to start at the same phase relative to the phase of the primary feedback signal. After every cycle, the control signal was adjusted during control to ensure that it has the same initial phase relative to that of the corresponding feedback signal. This initial phase was varied for investigating the effect of phase information on control performance. Since the control signal uses the phase information from the feedback signals, it is called the semi-closed-loop control. This method can be easily realized in the control platform. However, it contains so fewer information of the feedback signal and cannot be

adjusted freely according to the system response.

Finally, a ‘downsampling’ concept was considered which involved two important factors. (1) The down-sampling of the frequency of original feedback signal to the optimal control actuation frequency of around 30Hz; (2) The corresponding frequency and phase relationship between original feedback signal and down-sampled control signal. In this method, the feedback signal at around 160Hz was down-sampled to a much lower frequency of around 30 Hz to ensure the test model can generate close to a maximum displacement. The detail of this proposed downsampling method will be explained in section 4.4.

The discussion in this section can be summarized in Figure 4-1. It shows the comparison of three different methods for applying closed-loop control. One can conclude that although it is not possible to use the feedback signal directly in the present study, a ‘downsampling’ concept which agrees with all the requirements in the present study can be used in the closed-loop control. Downsampling is a common concept in the signal processing that will be used for controlling the vortex shedding process using the surface perturbation method. In the next section, the detail of this concept will be described. The results of the control performance will be discussed in Chapter 5.

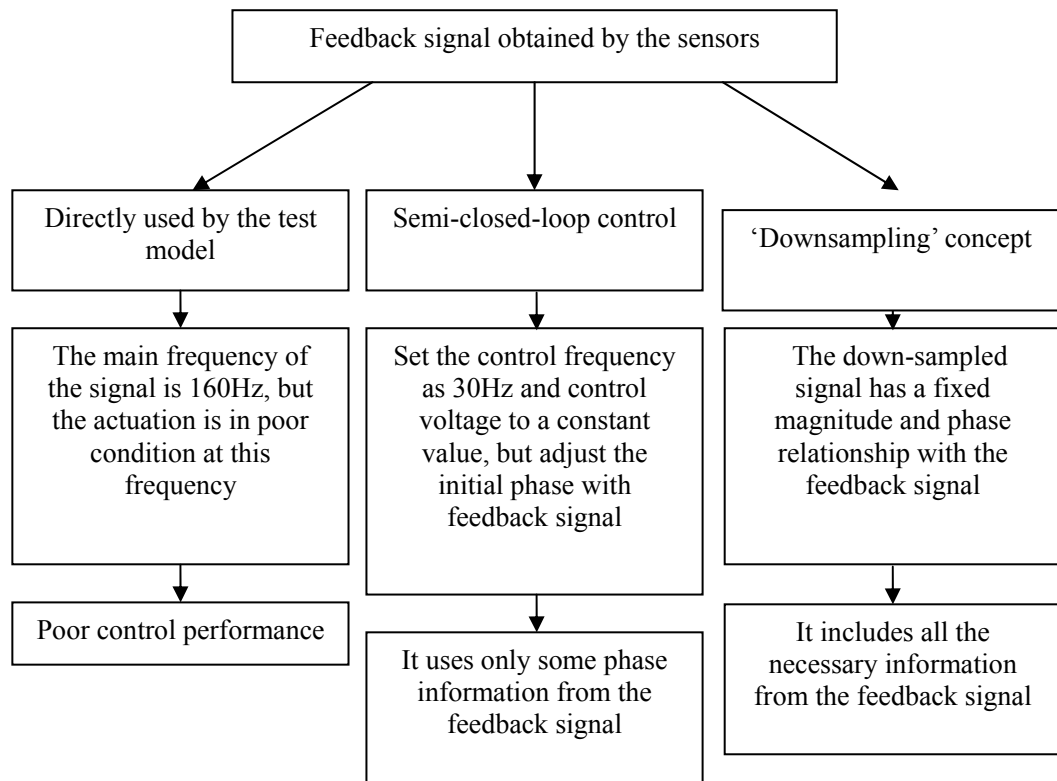


Figure 4-1 The possible methods for applying closed-loop control.

4.4 Downsampling theory and its implementation

In signal processing, downsampling (or ‘subsampling’) is the process of reducing the sampling rate (sample frequency) of a signal. This is usually done to reduce the data rate or the size of the data. In general, since downsampling reduces the sample frequency of the signal, one must be careful to make sure the Shannon-Nyquist sampling theorem criterion is maintained to avoid the aliasing problem. However, in the present study, the aliasing phenomenon which happens when the sampling theorem is not satisfied is utilized. The detail of this process will be discussed in this section.

4.4.1 Nyquist–Shannon sampling theorem and the aliasing phenomenon

The Nyquist–Shannon sampling theorem developed by Harry Nyquist and Claude

Shannon is a fundamental result in the field of information theory, especially in telecommunications and signal processing. Sampling is the process of converting a signal which is a function of continuous time into a numeric sequence which is a function of discrete time. The theorem can be stated as in the following [124]: If a signal $u(t)$ contains no frequencies higher than B_{NS} Hz, the spectrum of this signal $U(f)$ is shown in Figure 4-2, this signal $u(t)$ is completely determined by giving its ordinates at a series of points spaced $\frac{1}{2B_{NS}}$ seconds apart.

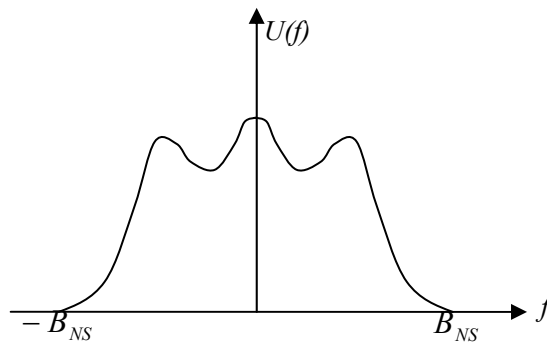


Figure 4-2 Spectrum of a band-limited signal as a function of frequency.

This theory can be further described by using the following equations. Let $u(t)$ represents a continuous-time signal and $U(f)$ is the continuous Fourier transform of this signal, it can be expressed:

$$U(f) = \int_{-\infty}^{\infty} u(t)e^{-i2\pi ft} dt \quad (4-1)$$

Here, the signal $u(t)$ is assumed to be band-limited to a one-sided baseband band-width B_{NS} , if $U(f) = 0$ for all $|f| > B$. Then the sufficient condition for exact re-constructability from samples at a uniform sampling rate f_{NS} is:

$$f_{NS} > 2B_{NS} \quad (4-2)$$

Where the quantity $2B_{NS}$ is called the Nyquist rate and is a property of the

band-limited signal, while $f_{NS}/2$ is called the Nyquist frequency and is a property of this sampling system. The time interval between successive samples is referred to as the sampling interval:

$$T = \frac{1}{f_{NS}} \quad (4-3)$$

and the samples of $u(t)$ are denoted by:

$$u[n] = u(nT) \quad (4-4)$$

where n is an integer. The sampling theorem leads to a procedure for reconstructing the original $u(t)$ from the samples and states sufficient conditions for such a reconstruction to be exact. The theorem describes two processes in signal processing: a sampling process, in which a continuous time signal is converted to a discrete time signal, and a reconstruction process, in which the original continuous signal is recovered from the discrete time signal. One can draw the following conclusions from this theorem.

(1) If the highest frequency B_{NS} in the original signal is known, the theorem gives the lower bound on the sampling frequency for which perfect reconstruction can be assured. This lower bound to the sampling frequency $2B_{NS}$ is called the Nyquist rate.

(2) If the sampling frequency is known, the theorem gives us an upper bound for frequency components $B_{NS} < f_{NS}/2$ of the signal to allow for perfect reconstruction. This upper bound is the Nyquist frequency.

A continuous time signal $u(t)$ can be converted to a discrete time signal $u(nT)$. However, the Poisson summation formula shows that the discrete samples $u(nT)$ of signal $u(t)$ are sufficient to create a periodic summation of function $U(f)$, it can be

expressed in the following [125],

$$U(f) = \sum_{k=-\infty}^{\infty} U(f - kf_{NS}) = T \sum_{n=-\infty}^{\infty} u(nT)e^{-i2\pi nTf} \quad (4-5)$$

The spectrum of Equation 4-5 is shown in Figure 4-3. It is found that there are several spectrums along the axis f . The spectrum which is shown in the solid line is the original spectrum and the other spectrums which are shown in dashed line are the image spectrums. In Figure 4-3, the spectrum is agree with the condition that $B_{NS} < f_{NS}/2$, so the original spectrum and the image spectrums do not overlap, there are independently with each other, so one can use a low pass filter to remove the images and leave the original spectrum, thus recovering the original signal from the samples $u(nT)$. It is the normal process for recovering the original signal.

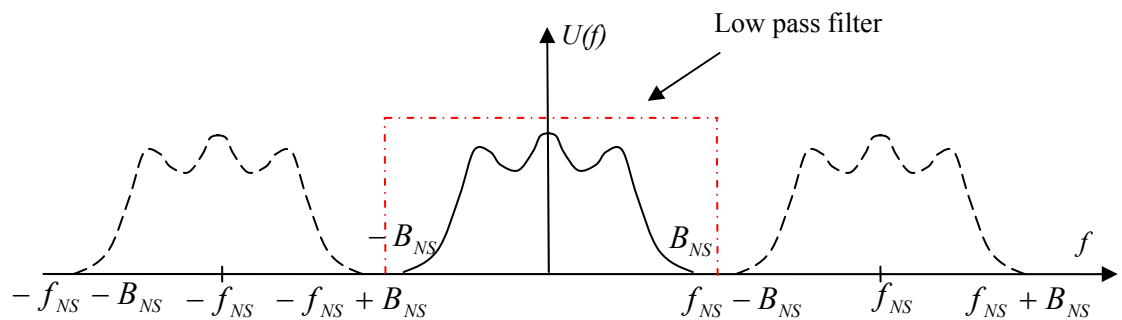


Figure 4-3 Spectrum of a properly sampled bandlimited signal (solid line) and images (dashed line) that do not overlap. A low-pass filter can remove the images and leave the original spectrum, thus recovering the original signal from the samples.

If the sampling condition is not satisfied, it is not possible to discern an unambiguous $U(f)$. In this case, any frequency component above $f_{NS}/2$ is indistinguishable from a lower-frequency component, which is called an aliasing phenomenon. Figure 4-4 described aliasing phenomenon. In the Figure 4-4, $B_{NS} > f_{NS}/2$, so sampled band-limited signal (solid line) $U(f)$ is overlap with the images(dashed line). These overlapping edges or ‘tails’ of the images can create a spectrum unlike the original. This spectrum cannot be reconstructed to the exact

original time domain signal. Because of this reason, the aliasing phenomenon needs to be avoided in the measurement. In this case, one can set high sample frequency f_{NS} to avoid this problem.

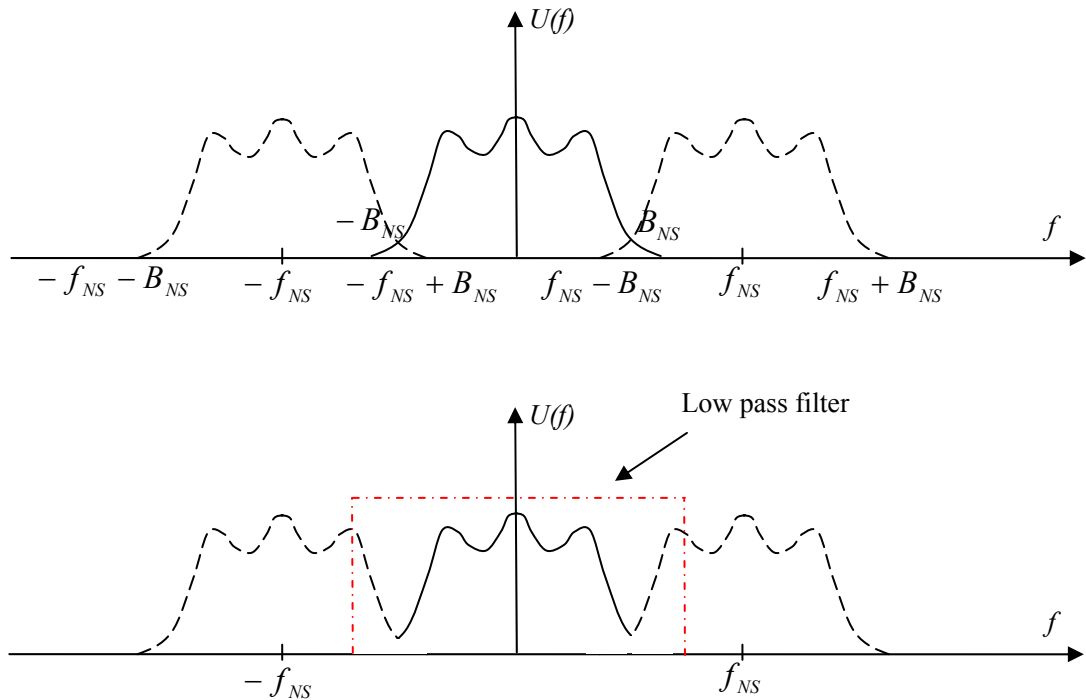


Figure 4-4 Spectrum of an insufficiently sampled band-limited signal (solid line) $U(f)$ is overlap with the images (dashed line).

In conclusion, Nyquist–Shannon sampling theorem is the basic theorem in signal processing. All the measurements need to satisfy this sampling theorem for obtaining completely original data. The aliasing phenomenon appears if the sampling condition is not satisfied. In general, the aliasing phenomenon needs to be avoided. However, one can find some useful properties from the aliasing phenomenon as described in the followings.

(1) Although the image spectrum is not the original spectrum of the signal, it can be made to completely overlap the original spectrum when shifted by a proper value along the frequency axis. This is of course can occur assuming that the aliasing problem is avoided by proper filtering. So the image spectrum can be regarded as the original spectrum which is shifted to other frequencies.

(2) The value of the sample frequency f_{NS} can determine the relative position between the original spectrum and image spectrum. One can use the sample frequency to shift the image spectrum to any position along the frequency axis.

(3) The overlap between the original spectrum and the image spectrum can create a spectrum that differs from the original spectrum. However, if the spectrum has the narrow-band characteristics, one can use proper band-pass filtering in reconstructing the signal to avoid the aliasing problem.

4.4.2 Downsampling theory

The purpose for the signal analysis is to down-sampled the frequency of the feedback signal from about 160Hz to about 30Hz while keeping as many as necessary frequency, magnitude and phase information that describe the system response. Based on the aliasing phenomenon, a new control method using the ‘Downsampling theory’ is developed to meet the control requirements. Since it is not possible to shift the original spectrum of a signal, but one can use a proper sample frequency f_{NS} to shift the image spectrum to the target low frequency and then use band-pass filtering to obtain a part of the image spectrum as the target spectrum. Because in the present study, the shifted image spectrum will overlap with original spectrum, it can be regarded as a type of aliasing phenomenon. The process can be described in Figure 4-5. A typical spectrum of the vortex shedding system is used in the illustration with its dominant response at the vortex shedding frequency. The band spectrums around the peaks are marked by S_n ($n = 1, 2, 3, 4 \dots$) in the Figure 4-5, the frequency band is BF .

In Figure 4-5, $U_n(f)$ (n is the integer number) is used for the definition of the spectrum, where $n = 0$ denotes the original spectrum $U_0(f)$ (Solid line in the

Figure 4-5). and $n \neq 0$ denotes the image spectrum. The position of the image spectrum is determined by the sampling frequency f_{NS} . $U_1(f)$ is the first image spectrum in the positive f axis, while $U_{-1}(f)$ is the first image spectrum in the negative f axis. The present study only focused on spectra $U_1(f)$ and $U_{-1}(f)$ (Dashed lines in the Figure 4-5). Only parts of the original spectrum which are defined as $U_{source}(f)$ (S_5 in the Figure 4-5) and $U_{source}(-f)$ (S_2 in the Figure 4-5) ($f \in [f_{source} - BF/2, f_{source} + BF/2]$) will be used in the measurement. Here f_{source} is a source frequency (it is the vortex shedding frequency in the present study) and BF is the frequency band of the band-pass filter. $U_{source}(f)$ and $U_{source}(-f)$ are the two mirror spectrum parts along the f axis with similar spectrum characteristic. The corresponding image spectra $U_{isource}(f)$ (S_4 and S_6 in the Figure 4-5) and $U_{isource}(-f)$ (S_1 and S_3 in the Figure 4-5). These four image spectra have been shifted by the sampling frequency f_{NS} , so

$$f \in ([f_{NS} + f_{source} - BF/2, f_{NS} + f_{source} + BF/2], [f_{NS} - f_{source} - BF/2, f_{NS} - f_{source} + BF/2]).$$

Here, f_{source} is a constant value for the present study, so one can choose a proper f_{NS} to move S_3 or S_4 to the target frequency f_{target} which is the target low frequency for investigation. If S_4 is moved to the target frequency f_{target} , then the relationship of f_{target} , f_{source} and f_{NS} can be expressed by:

$$f_{target} = f_{NS} - f_{source} \quad (4-6)$$

Another case is that if S_3 is moved to the target frequency f_{target} , then the relationship of f_{target} , f_{source} and f_{NS} can be expressed as the following:

$$f_{target} = f_{source} - f_{NS} \quad (4-7)$$

Because in the present study $f_{target} > 0$ and $f_{source} > 0$, so that f_{NS} in equation 4-6 is larger than that in equation 4-7. It is better to have larger f_{NS} in the program, In the present study, equation 4-6 was chosen for further investigation.

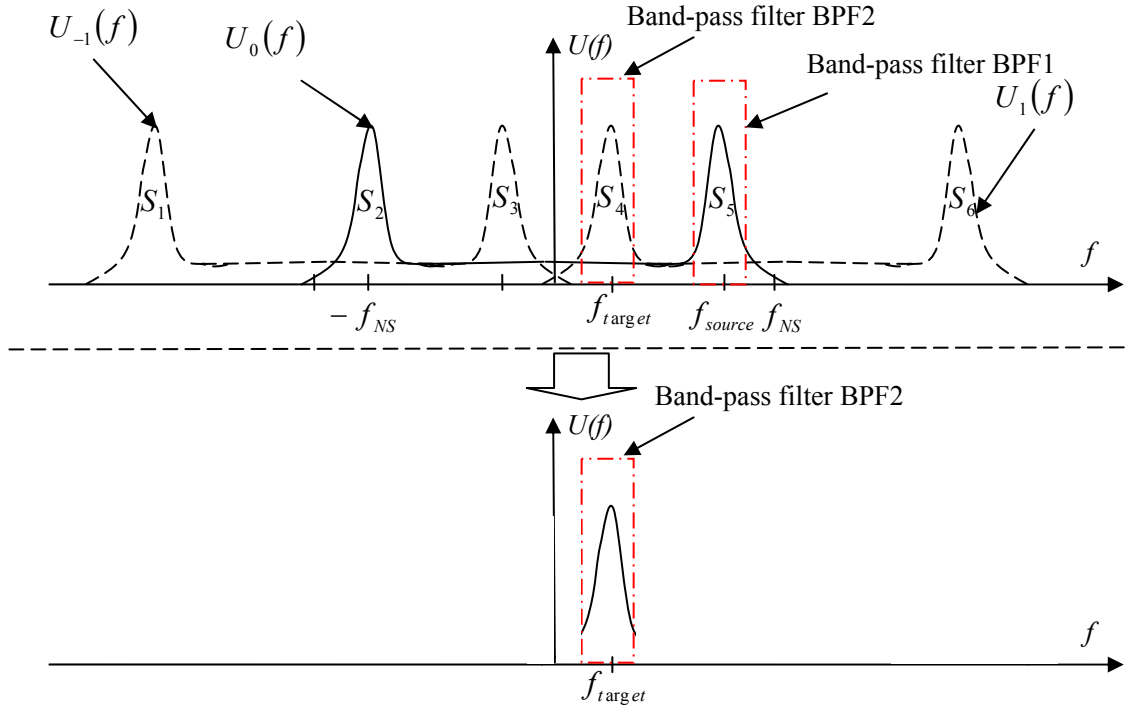


Figure 4-5 Schematic of the downsampling theory.

According to Equation 4-6, one of the spectra S_4 can be shifted to the target frequency. Furthermore, the corresponding relationship between S_5 and S_4 will be analyzed. S_5 is the original band spectrum, its mirror band spectrum is S_2 , the transform from band spectrum S_5 to band spectrum S_2 is a fix function which can be defined as R_{S_2} , in fact, band spectrum S_2 can be easily obtained by adding a minus sign in the front of band spectrum S_5 .

$$S_5 \xrightarrow{R_{S_2}} S_2 \quad (4-8)$$

$$R_{S_2} : U(f_{s_2}) = U(-f_{s_5}) \quad (4-9)$$

And the transform from band spectrum S_2 to band spectrum S_4 is defined as R_{24}

which is can be expressed as the following.

$$S_2 \xrightarrow{R_{24}} S_4 \quad (4-10)$$

$$R_{24} : U(f_{s_4}) = U(f_{s_2} + f_{NS}) \quad (4-11)$$

So the transform form band spectrum S_5 to S_4 can be expressed as the following,

$$S_5 \xrightarrow{R_{54}} S_4 \quad (4-12)$$

$$R_{54} : U(f_{s_4}) = U(f_{NS} - f_{s_5}) \quad (4-13)$$

Equation 4-13 indicates that there is a fix transform equation between band spectrum S_5 to band spectrum S_4 , so the characteristic of the band spectrum S_4 can be corresponded to the characteristic of the band spectrum S_5 .

Equation 4-6, 4-12 and 4-13 together can be used as the basis equation for the downsampling theory. In this theory, a high frequency spectrum $U_{source}(f)$ (S_5 in the Figure 4-5) ($f \in [f_{source} - BF/2, f_{source} + BF/2]$) can be down-sampled to a low frequency spectrum $U_{target}(f)$ (S_4 in the Figure 4-5) ($f \in [f_{target} - BF/2, f_{target} + BF/2]$) by using the Equation 4-6. And the relationship between $U_{target}(f)$ and $U_{source}(f)$ is identified by using Equation 4-12 and 4-13. Figure 4-5 also shows that after the down-sampled process, the target spectrum is obtained by using a band-pass filter to clear away the other spectrums. The target spectrum can be used to reconstruct the time-domain signal.

Figure 4-6 shows the typical process for applying the downsampling theory in signal processing. In the present study, $f_{source} = 160\text{Hz}$ and $f_{target} = 30\text{Hz}$. According to Equation 4-6, f_{NS} was chosen to be 190 Hz. So a 160Hz input signal would be down-sampled into a 30Hz signal. Similarly, a 159Hz input signal would be down-sampled into a 31Hz signal.

4. Downsampling theory and implement in real time control system

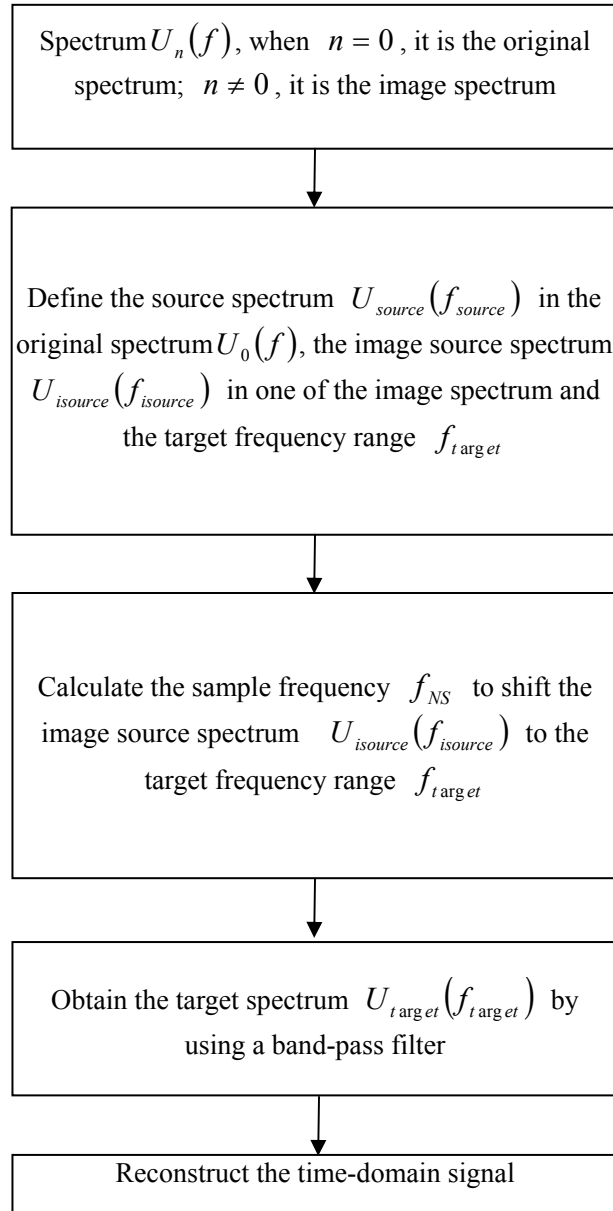


Figure 4-6 The typical process for applying the downsampling theory.

Additional, the possibility for the overlap between S_4 and S_5 also needs to be considered. In the present study, the spectrum around the vortex shedding frequency f_s is primarily narrow-band. Therefore, a $BF = 10\text{Hz}$ band-pass filtering around the vortex shedding frequency should be able to capture most primary spectral characteristics associated with the vortex shedding. In practice, there were still some spectral components from the original spectrum that overlap with the reconstructed target spectrum at the target frequency band. However, the spectral components at

these frequencies were considerably smaller than that of the target spectrum.

4.4.3 The implementation of downsampling theory

The process for applying the downsampling theory in the Simulink/dSPACE platform will be discussed in this section. Firstly, a sinusoidal signal generated by a Signal Generator in the Simulink was used instead of the feedback signal, and this signal was called the ‘original signal’. The characteristic of the original signal is shown in Figure 4-7. The frequency of the signal was 160Hz, and the sampling frequency was 5890Hz (5890Hz was calculated using the formula $190\text{Hz} \times 31$). Therefore only a tonal spectrum was found within 1Hz to 1000Hz in frequency domain. Since it was tonal, there was no need for any band-pass filtering to obtain the signal at around 160Hz.

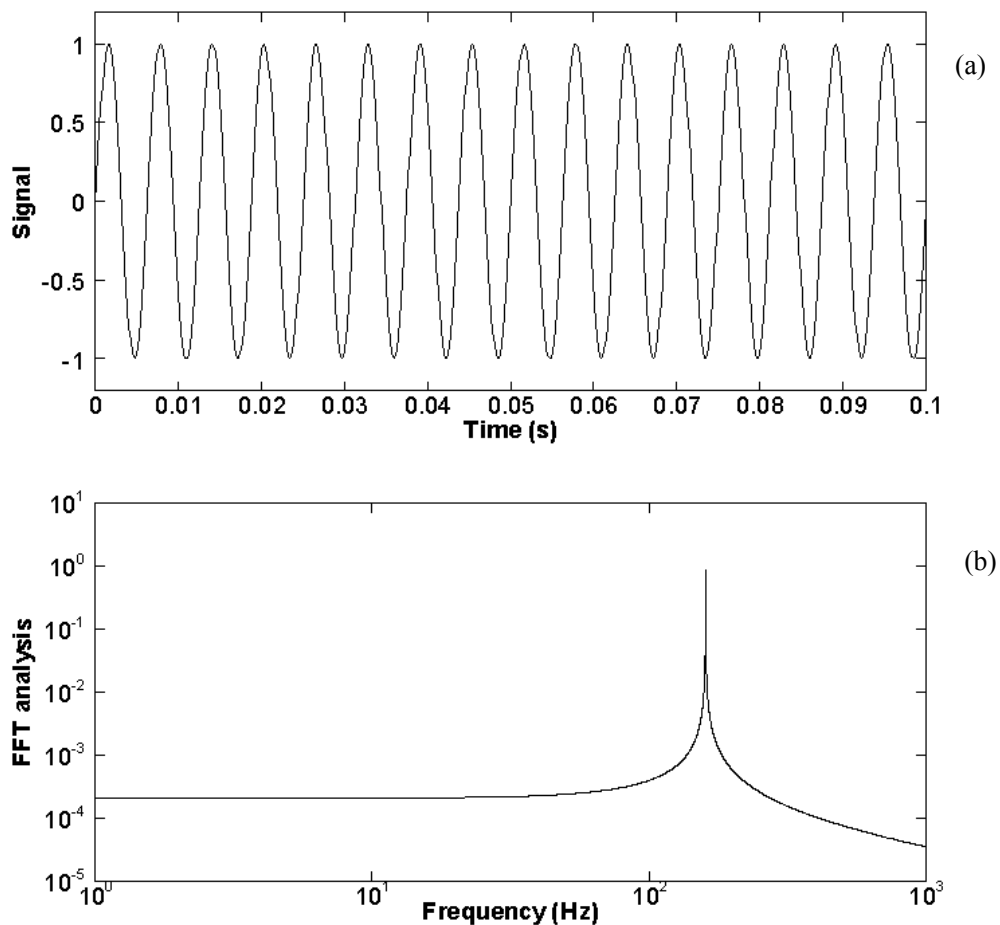


Figure 4-7 The characteristic of the original signal. (a) Time-domain; (b) Frequency-domain.

Secondly, based on the Equation 4-6, f_{NS} was chosen to be 190 Hz for the down-sampled signal. A Zero-Order Hold (ZOH) module in Simulink was used to change the data sampling from 5890Hz to 190Hz. The ZOH is one of commonly used practical signal reconstruction methods by a conventional digital-to-analog converter (DAC). It describes the effect of converting a discrete-time signal to a continuous-time signal by holding each sample value fixed over one sample interval. Thus ZOH could be used to reconstruct the present 160Hz original signal to a new low-frequency signal at 30Hz by using different sampling frequency f_{NS} . The result is shown in Figure 4-8, in which the signal after ZOH is called 'ZOH signal' in the present study. The frequency has now been shifted to 30Hz. However, the spectrum of reconstructed signal using the ZOH method consists of other peaks apart from the original peak. They are the peaks from the overlapped image spectra during the reconstruction. These peaks are useless so it was cleared using the filter.

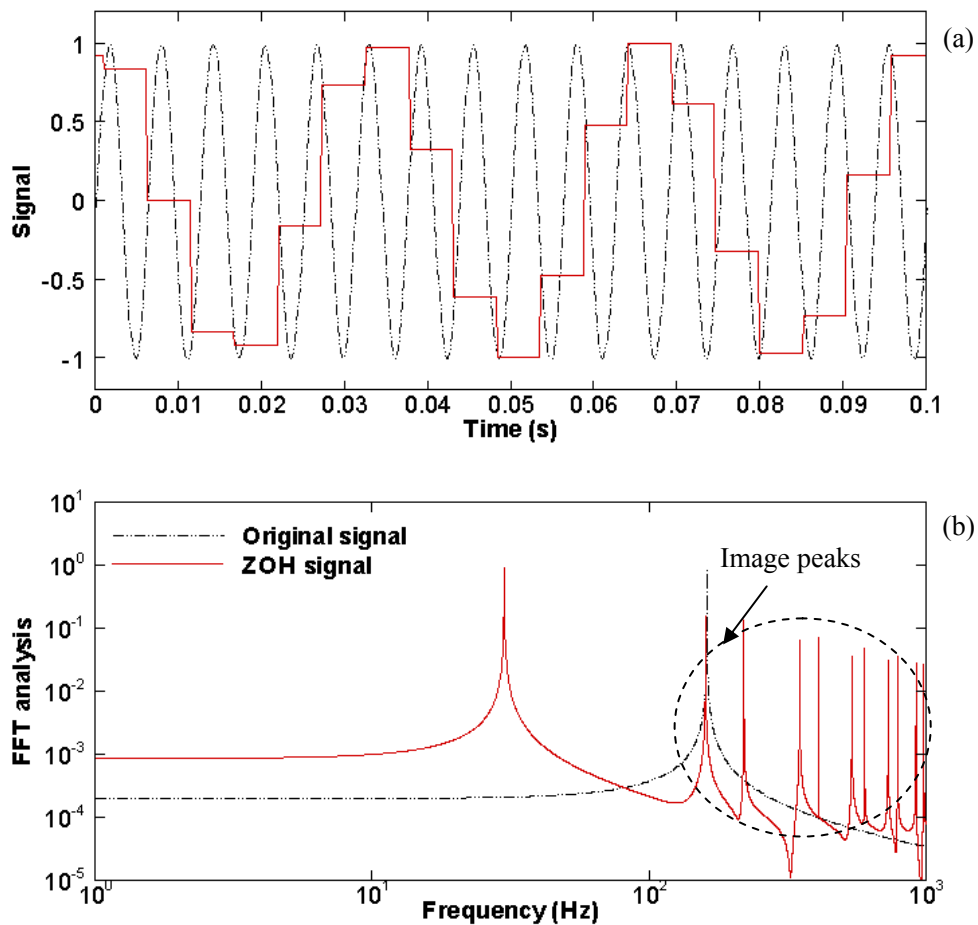


Figure 4-8 The comparison result by using Zero-Order Hold (ZOH) module to change the sample frequency of the signal. (a) Time-domain; (b) Frequency-domain.

Thirdly, after being down-sampled, the sampling frequency of the ZOH signal was 190Hz, with the time step of $\Delta t = 0.00526s$. However, the time step of the output signal needed to be the same as the original signal which was $\Delta t = 0.00017s$. A Rate Transition module was used to change the time step while keeping the characteristic of the ZOH signal. The output signal from the Rate Transition module was called ‘Transition signal’. The result is shown in Figure 4-9. In Figure 4-9(b) shows that though there are some small differences in frequency spectra between the original and reconstructed ones, all the peaks are mainly similar. In Figure 4-9(a), it is found that the Rate Transition module introduced a certain time-delay but with the same magnitude characteristic. It will cause the output signal to have a constant phase

difference relative to the original signal.

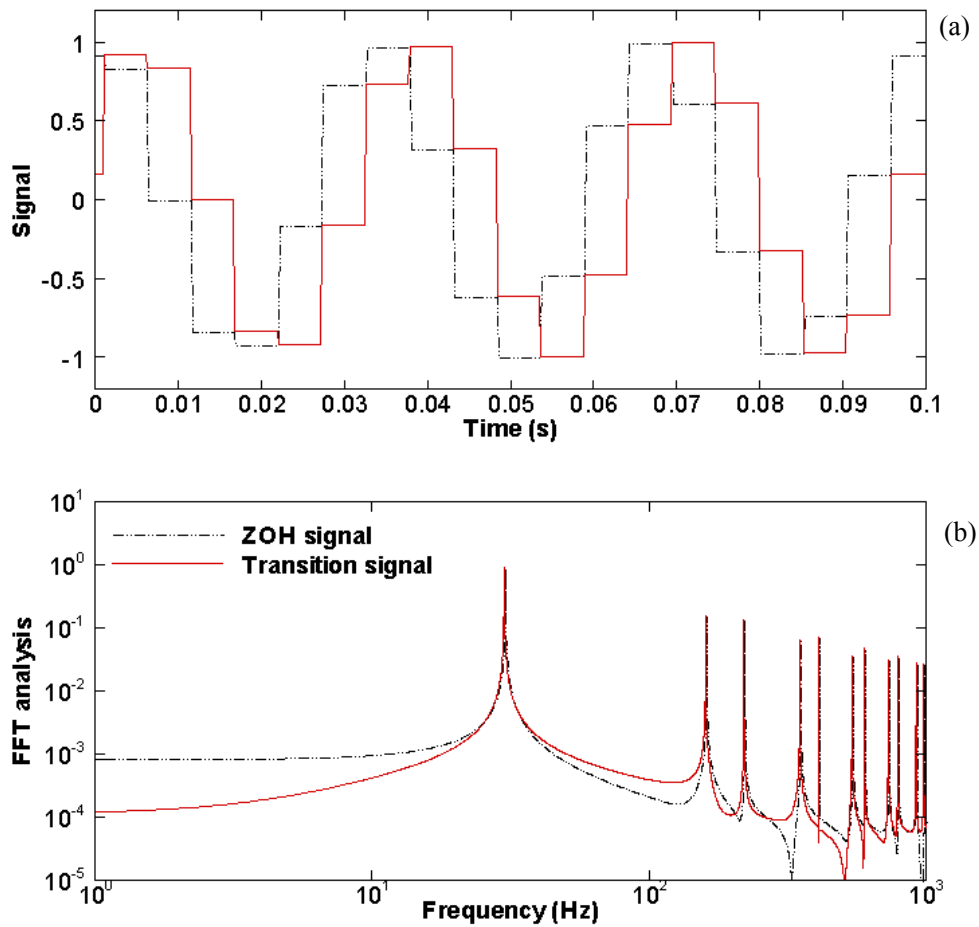


Figure 4-9 The results of using the Rate Transition module. (a) Time-domain; (b) Frequency-domain.

Finally, a band-pass filter was used to remove the image peaks of the reconstructed signal. A 2Hz-band-pass filter is used in the present study as shown in Figure 4-10. A down-sampled output signal was finally obtained at a frequency around 30Hz.

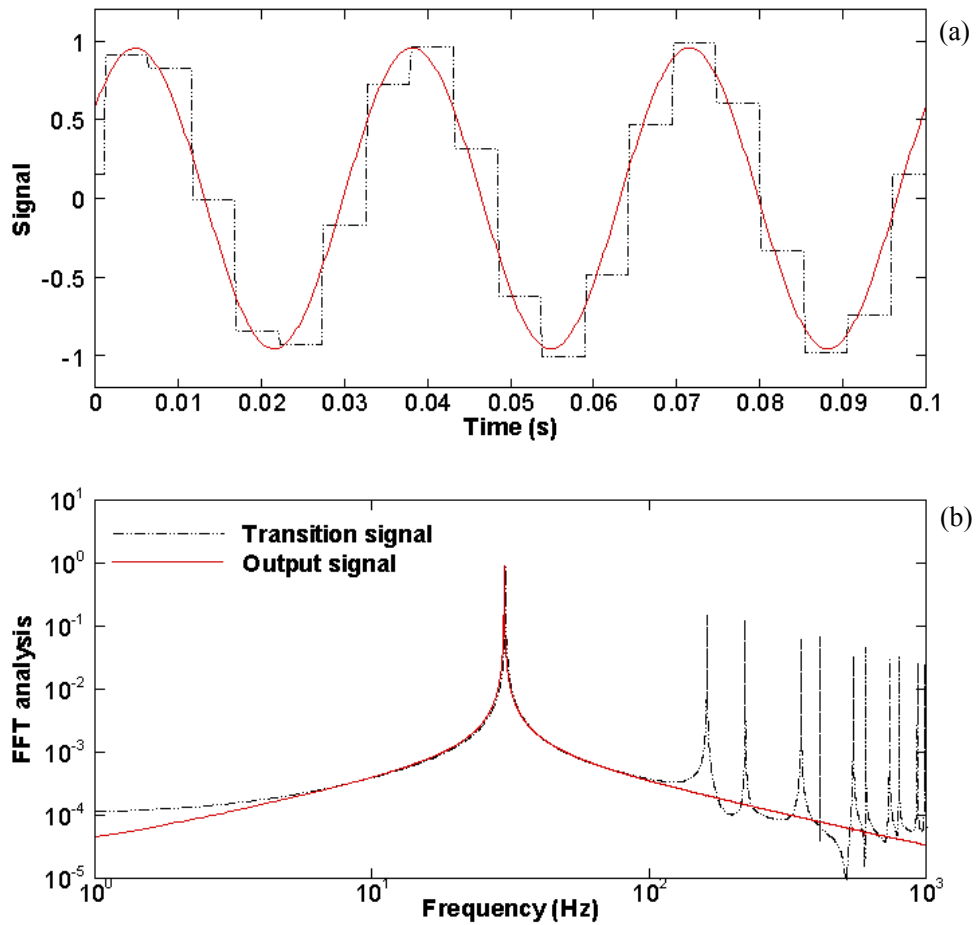


Figure 4-10 The comparison of transition signal with output signal. (a) Time-domain; (b) Frequency-domain.

The comparison between the output signal with the original signal is shown in Figure 4-11. From the figure, it is found that since the signal is a sinusoidal signal, the other image spectra of the original signal do not influence the output signal. In the real measurement system, one can use a band-pass filter to obtain a primarily tonal signal with a narrow-band spectrum.

4. Downsampling theory and implement in real time control system

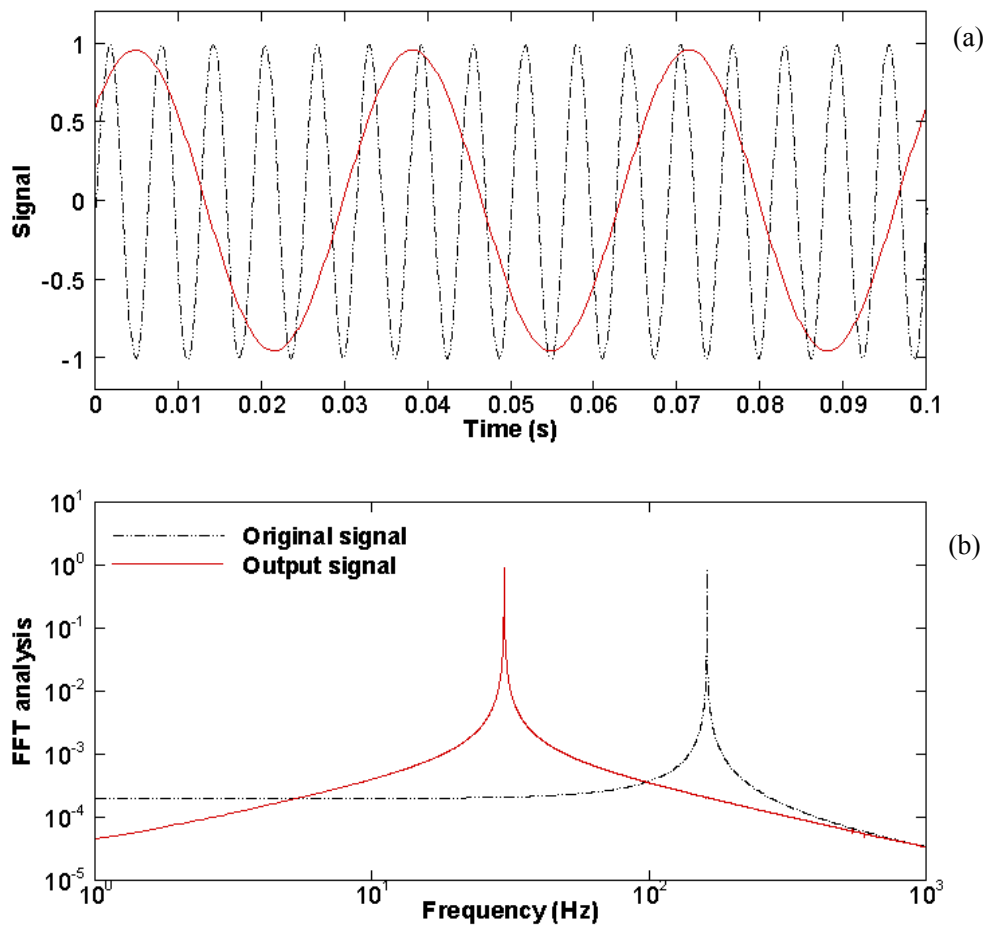


Figure 4-11 The comparison of the original signal with the output signal. (a) Time-domain; (b) Frequency-domain.

The down-sampling control program, implemented in Simulink/ dSPACE, is shown in Figure 4-12. Based on the downsampling theory, the original signal (feedback signal in the closed-loop control) can now be down-sampled in real time by using the ZOH module and Rate Transition module in Simulink/dSPACE. For control purposes, the original feedback signal can be downsampled to a lower frequency for closed-loop control.

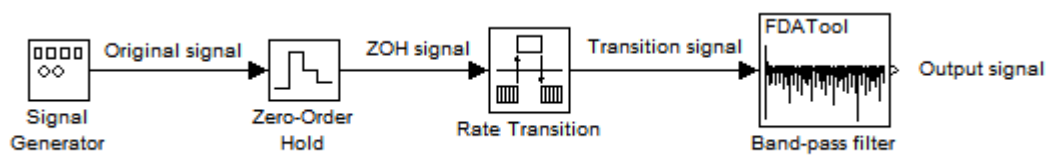


Figure 4-12 The downsampling algorithm for closed-loop control.

4.5 Conclusions

In order to further improve the control performance of the open-loop control, closed-loop control using a downsampling process was developed. Based on the analysis, a downsampling theory which utilizes the aliasing phenomenon and the Nyquist–Shannon sampling theorem has been developed to down-sample a high-frequency original signal (feedback signal) to a low-frequency output signal (modified feedback signal). The relationship between these two signals could be induced by using the aliasing phenomenon. The downsampling process was implemented in the Simulink/dSPACE platform by using the Zero-Order Hold, Rate Transition and Band-pass filter modules. It was concluded that the relationship between the feedback signal and the modified feedback signal could be identified by equations 4-6, 4-12 and 4-13 which guaranteed that the modified feedback signal contains all the necessary phase, frequency and magnitude information as that in the feedback signal. The test model can use the modified feedback signal to adjust its control properties according to the system response obtained from the feedback signal. The application of the downsampling program will be further discussed for the closed-loop control implementation in Chapter 5.

5. Closed-loop control for the flow-induced acoustic resonance

5.1 Introduction

In this chapter, the implementation of closed-loop control scheme was investigated in the view of achieving effective control of vortex-induced acoustic resonance.

In Chapter 4, the downsampling theory which utilizes the aliasing phenomenon and the Nyquist–Shannon sampling theorem is developed to down-sample a high-frequency original signal (feedback signal) to a low-frequency output signal (modified feedback signal). The relationship between these two signals can be induced by using the aliasing phenomenon. It is concluded that the relationship between these two signals could be identified by the Equation 4-6, 4-12 and 4-13 in Chapter 4 which guaranteed the modified feedback signal contains all the necessary phase, frequency and magnitude information involved in the feedback signal. The test model can now use the modified feedback signal to adjust its control properties according to the system response that come from the feedback signal. A downsampling program is developed in the Simulink/dSPACE platform in real time by using the Zero-Order Hold, Rate Transition and Band-pass filter modules base on the downsampling theory.

Using the downsampling theory and program developed in Chapter 4, a closed-loop control tests were carried out in this chapter. It was found that the flow-induced acoustic resonance was effectively reduced after applying the closed-loop control. The physical mechanism behind the control was experimentally investigated in the view of developing an optimal control strategy.

5.2 The signal processing in closed-loop control

The main difference between closed-loop and open-loop is that the feedback signal from the system response is used in the closed-loop control system. So in the closed-loop control, the signal processing is an important issue to be investigated. In this section, the process for dealing with the feedback signal before input into the test model is discussed.

5.2.1 The selection of the single feedback signal

In the closed-loop scheme, control signal utilizes feedback signals acquired from the system, which may be from the hot wire 1, hot wire 2, Mic.1 or Mic.2. Hot wire 1 is located at $x=0\text{mm}$, $y=11\text{mm}$ which is just above the leading edge of the test model; and hot wire 2 is located at $x=34\text{mm}$, $y=11\text{mm}$ which is within the area of strongest vortex shedding. There are several observations that can be made from this experiment.

Firstly, the comparison of the spectrum between the signal measured by hot wire 1 and measured by hot wire 2 is shown in Figure 5-1. It is found that these two spectrums are similar to each other except that the signal measured by hot wire 1 is much weaker than that measured by hot wire 2. It is better to use the strong signal in the closed-loop control since the signal-to-noise ratio will be higher. Therefore, the signal from hot wire 1 can be left out of consideration in this experiment.

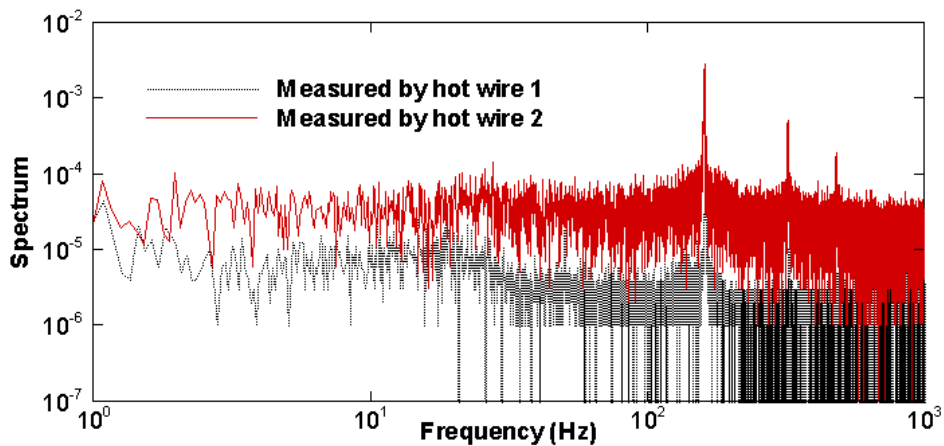


Figure 5-1 The comparison of the spectrum between the signal measured by hot wire 1 and measured by hot wire 2.

Secondly, the signal measured by Mic.1 is used to compare with the signal measured by hot wire 2. In Figure 5-2, it is found that the peak of the signal measured by Mic.1 at the shedding frequency is similar to the signal measured by hot wire 2. However, there are noises in the spectrum of the signal measured by Mic.1, especially in the low frequency region. In the present experiment set-up, these noises are mainly from flow noise. The microphone is sensitive to the flow noise, which cannot be directly detected by the hot wire. Therefore for closed loop control purposes, it is more useful to use the signal measured by hot wire 2 than the signal measured by Mic.1.

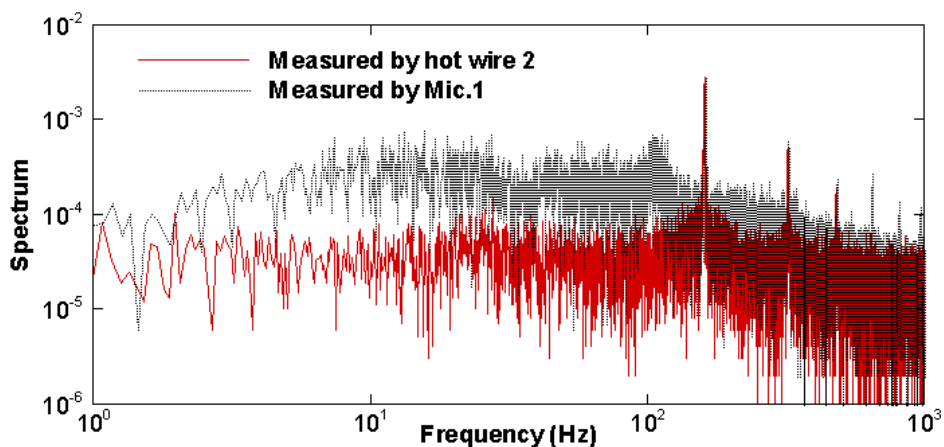


Figure 5-2 The comparison of the spectrum between the signal measured by hot wire 2 and measured by Mic.1

Thirdly, the spectrum of the signal measured by Mic.2 is shown in Figure 5-3. Due to the downstream cavity acoustic resonance, the peak at the shedding frequency f_s is amplified. Therefore, the signal-to-noise can be improved for the signal measured by Mic.2 around the vortex shedding frequency f_s . However, it was concluded that after applying control there was a vortex shedding frequency shift in Chapter 3. If the feedback signal is from the Mic.2, this frequency shift effect cannot be fully contained in the feedback signal.

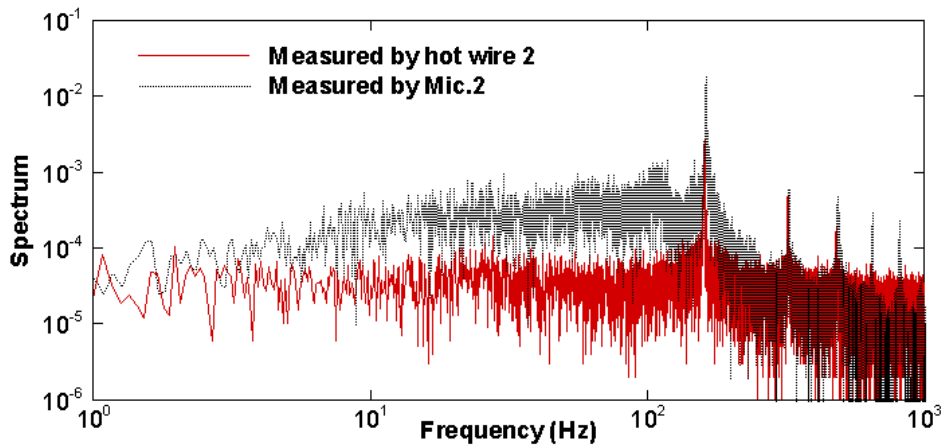


Figure 5-3 The comparison of the spectrum between the signal measured by hot wire 2 and measured by Mic.2

In conclusion, in the present study, only cases using hot wire 2 as feedback signal is discussed since the hot wire 2 signal is generally stronger than the signal measured by hot wire 1. The hotwire sensor is also more stable than the signals from microphones since it is not significantly affected by the flow background noise that may occur in the experiment.

5.2.2 The application of downsampling program in closed-loop control

The process of the application of the downsampling program in the closed-loop control is described in the following.

In the present study, the dominant vortex shedding is around 160Hz. Since the test model is placed in the flow stream inside the duct, there exist flow noise and background noise. The feedback signal measured by hot wire 2 is shown in Figure 5-4. In Figure 5-4 (a), it is found that the feedback signal has a considerable d.c. gain due to the electrical characteristic of the hot wire, and the signal contains much noise. Figure 5-4(b) shows the spectrum of this signal with a sharp peak around 160Hz. Therefore, a band-pass filter can be used to remove the extra noise from this feedback signal.

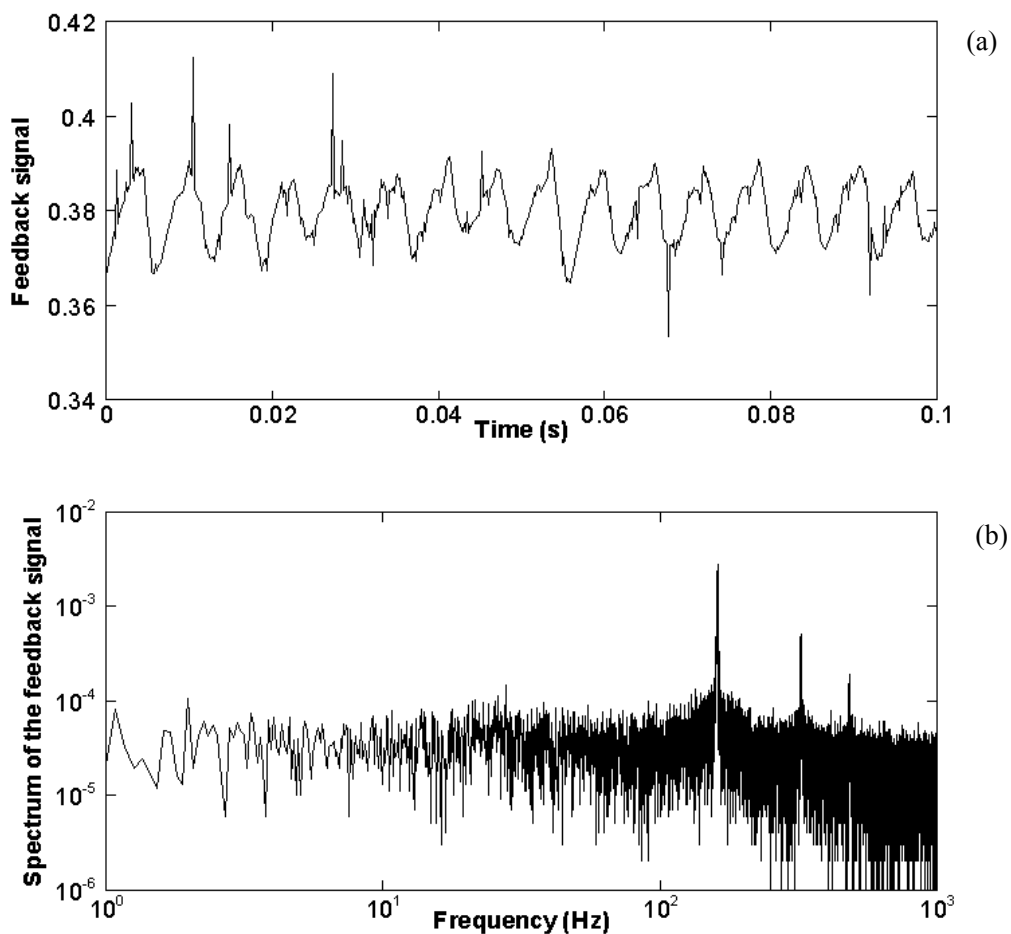


Figure 5-4 The feedback signal and its spectrum. (a) Time-domain; (b) Frequency-domain.

A 10Hz-band pass filter is used to filter the feedback signal. The filtered signal is called the 'original signal', which only contains the signal within 10Hz around the vortex shedding frequency. The filtered signal is shown in Figure 5-5. The main part of the original signal is the measured signal around the vortex shedding frequency; the

d.c. gain and extra noises have been removed. There is only one dominant peak in the spectrum, which satisfies the downsampling requirements. It should be noted that the original signal shown in Figure 5-5 is not a single-frequency signal. The signal generally consists of a combination of a number of sinusoidal signals at slightly different frequencies.

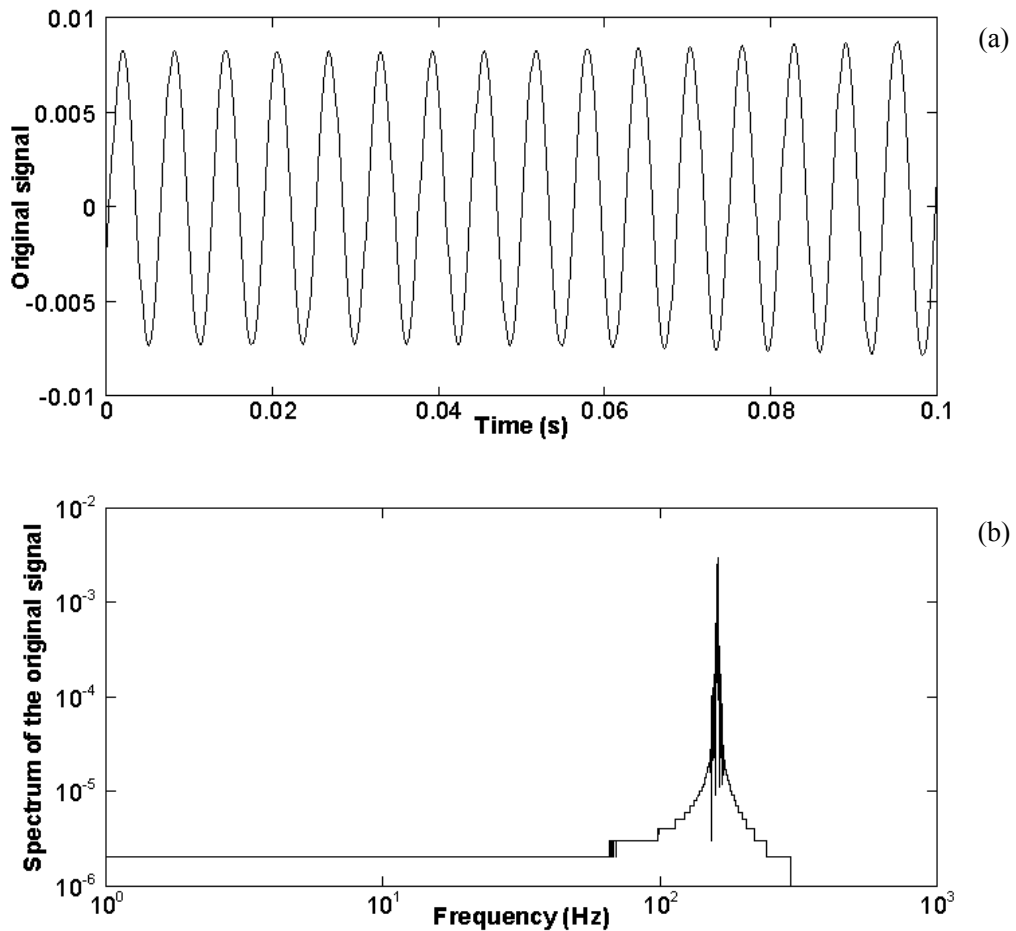


Figure 5-5 The original signal and its spectrum. (a) Time-domain; (b) Frequency-domain.

The downsampling control program which can be used in the present closed-loop study is developed. The schematic of this program is shown in Figure 5-6. In this processing, in order to obtain a pure original signal for the downsampling program, the feedback signal which obtained by the sensors is filtered by a band pass filter 1, and then the original signal can be down-sampled in real time by using the ZOH module and Rate Transition module in Simulink/dSPACE. The output signal after the

band-pass filter 2 is called ‘down-sampled signal’.

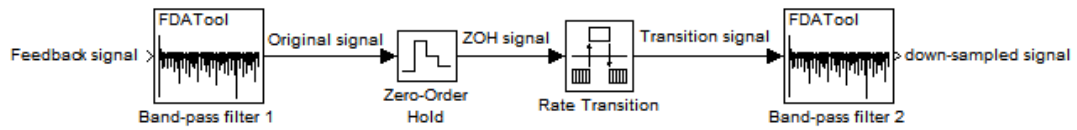


Figure 5-6 The downsampling algorithm for closed-loop control

5.2.3 The normalization program

A typical feedback signal obtained from hot wire 2 is shown in Figure 5-7. The mean amplitude of the feedback signal is about 0.009, as shown in Figure 5-7 (a). The feedback signal for the case with control is shown in Figure 5-7 (b). It can be observed that the signal strength has been reduced after the implementation of closed loop control. The mean value of the signal is approximately 0.003. The results indicate that the control action has damaged the vortex shedding, as also observed from the spectrum shown in Figure 5-8.

From the experiment, it is also observed that the amplitude of feedback signal is fluctuating during the control. In this case, the maximum amplitude is about 0.006, while the minimum amplitude is about 0.0005. This phenomenon can be classified as the ‘beat phenomenon’, which is the interference between two signals of slightly different frequencies. In the present study, the control action can shift the vortex shedding frequency, but the shift is also dependent on the amplitude of the input control signal. Therefore, signals with slightly varying frequencies can be generated during the control implementation creating the ‘beat phenomenon’.

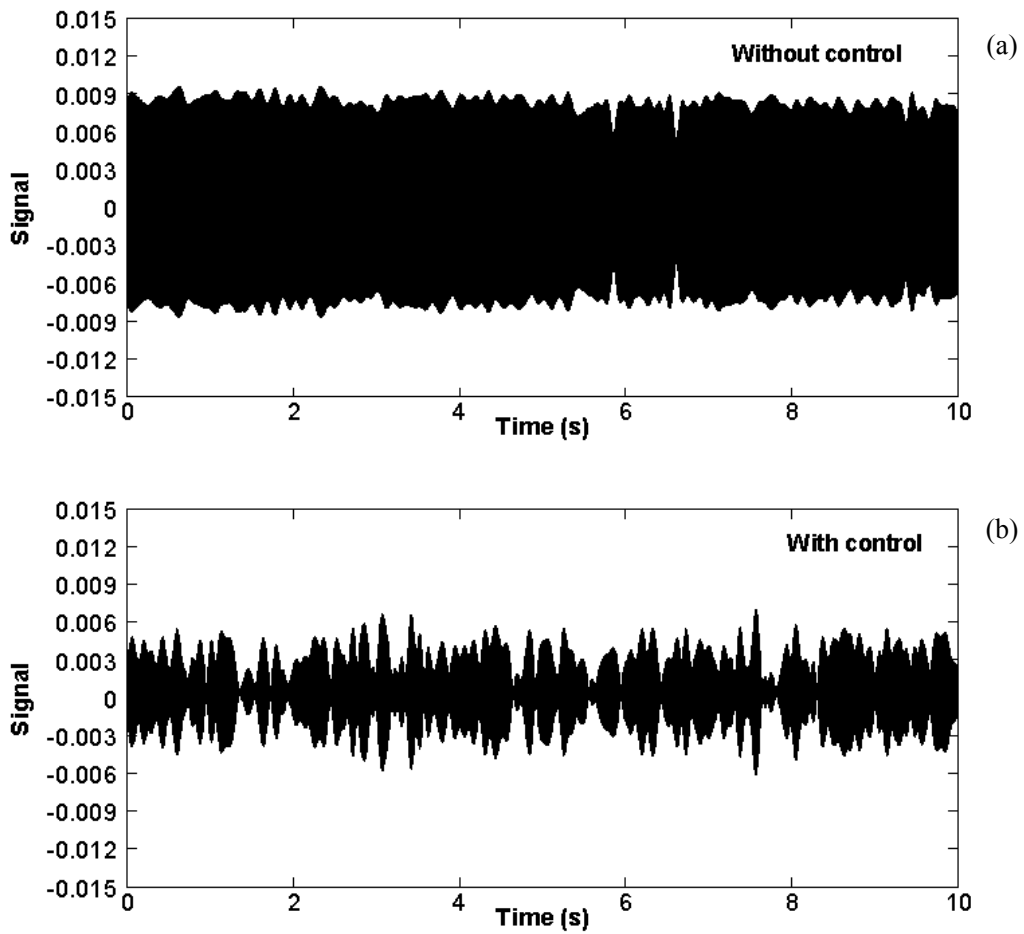


Figure 5-7 A typical feedback signal obtained from hot wire 2. (a) Without control; (b) With control, the control voltage is 150V which is measured before input into the test model.

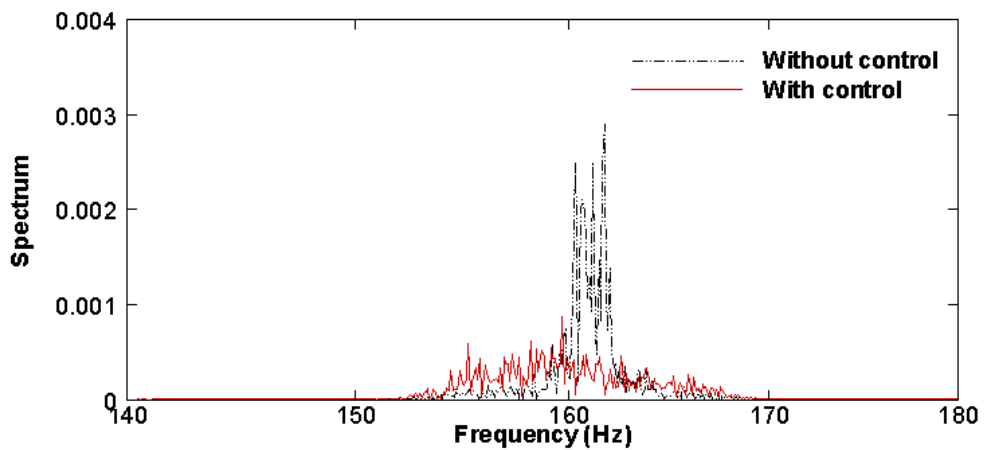


Figure 5-8 The spectrum of a typical feedback signal obtained from hot wire 2.

As shown in Figure 3-2 in Chapter 3, the input control maximum voltage was generally linear relative to the reduction of the strength of the vortex shedding. A fluctuating maximum control signal might result in a fluctuating control performance.

To achieve a consistent reduction in vortex shedding strength one needs to find a way to avoid the control signal that has a significant maximum amplitude variation. In the present study, a ‘Normalization’ program is developed to ensure that the maximum amplitude of control signal is reasonably constant during the control implementation.

In a standard process, the normalization program is used after the downsampling program by identifying the maximum amplitudes or peaks of the downsampled signal in real time. In the present study, the frequency of the dominant down-sampled signal is approximately $f_{ds} = 30\text{Hz}$. The peaks of the signal are estimated using the following approach. The 1/4 period of the signal can be calculated as

$$\frac{T_{ds}}{4} = \frac{1}{4f_{ds}} \approx 0.0333\text{s},$$

because the signal is expected to reach a peak within the 1/4

period from the zero-crossing point. In the present study, ‘Transport Delay’ and ‘Hit Crossing’ modules are used in the normalization program, the ‘Transport Delay’ is used to set a time delay for 1/4 periods and the ‘Hit Crossing’ is used to identify the point when the signal come across the zero axis. The process for the normalization is shown in the Figure 5-9. This process can ensure the signal can be normalized in real time. It should be noted that since the main frequency of the signal is changing, this approach may only be able to estimate the signal peak from every cycle. However, the estimation of signal peak has been observed to be sufficiently accurate and can be effectively used for control. It is relevant to point out that although the normalization process alters the magnitude of the feedback signal, it does not affect the phase of the feedback signal. Therefore, the normalized signal still contains sufficient information about the present system to be used in the closed-loop control.

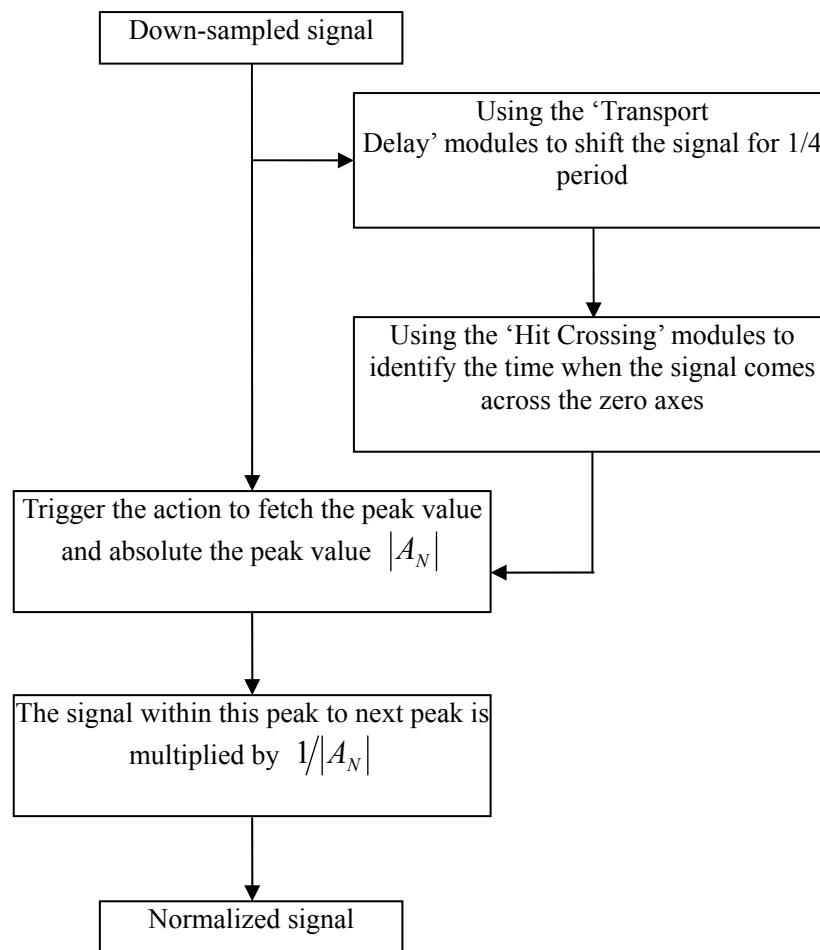


Figure 5-9 The process of normalization program

5.2.4 Modified PID controller

In general, the proportional–integral–derivative controller (PID controller) is widely used in the industrial control systems as a generic control loop feedback controller. A PID controller calculates an ‘error’ value as the difference between a measured process variable and a desired set-point. This controller attempts to minimize the error by adjusting the parameters of the control signal. In a standard PID controller, it involves three separate constant parameters, and is accordingly called three-term control: the proportional (P), the integral (I) and derivative (D) values. These values can be interpreted in terms of time: P depends on the present error, I on the accumulation of past errors, and D is a prediction of future errors, based on

current rate of change. The designed control action can be obtained by tuning the three parameters in the PID controller algorithm. However, the use of the PID algorithm for control does not guarantee optimal control of the system or system stability.

In the present study, initially the use of PID controller was investigated. However, our interest is to consider the effect of magnitude A and phase ϕ of the control signal on the control actuation. In general, the feedback signal has its own phase, defined as ϕ_0 . The phase ϕ is the initial angle between the feedback signal and the control signal. So tuning the phase ϕ is equal to adjusting the difference between the feedback signal and the control signal. The physics of the tuning will be discussed in the section 5.4.

In the PID controller, the changes in its parameters (P , I and D) do not correspond systematically to the changes in magnitude and phase of the controller, meaning that a full scale magnitude and phase investigation may not be easily performed. Therefore, this study considers a more direct feedback control whose magnitude and phase can be systematically adjusted so the impact of magnitude A and phase ϕ adjustment to control performance can be studied more closely. This type of controller is called ‘modified PID controller’, in which only two parameters magnitude A and phase ϕ are used. The optimal of the control can be obtained by tuning the magnitude A and phase ϕ . In fact, the magnitude of A in the modified PID controller is equal to the P parameter in PID controller. But phase ϕ is used to identify the optimal phase between the control signal with the feedback signal.

Therefore, the whole signal processing for the present study is developed. The process is shown in Figure 5-10. A high-frequency feedback signal is obtain from the system; it is down-sampled by using the downsampling program to a corresponding

low-frequency down-sampled signal which is suitable for the excitation of the test model. Since the ‘Beat’ phenomenon can affect the control performance, the down-sampled signal is normalized by using the normalization program to reduce the impact of the ‘Beat’ phenomenon to control performance. The normalized signal can then be input into the modified PID controller for controlling the vortex shedding.

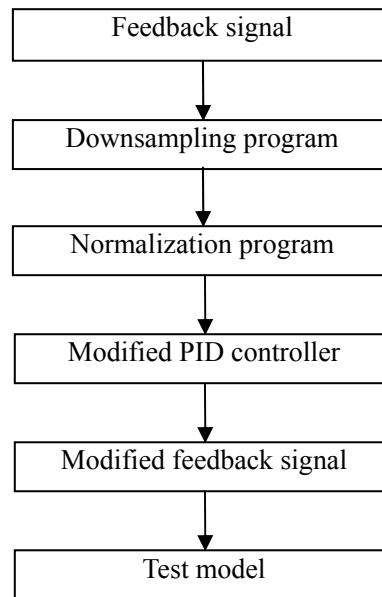


Figure 5-10 The process of signal processing.

5.3 Optimal control voltage and phase delay

The investigation for seeking optimal control voltage could be performed by varying the magnitude of modified feedback signal. This generated signal was then down-sampled to generate the output control voltage V_p for THUNDER actuation. The effect of varying the control voltage of the down-sampled feedback control on noise reduction was shown in Figure 5-11. Microphones in the duct and cavity both recorded the same general trend of increasing noise reduction as the control voltage was increased. The maximum magnitude was limited by the maximum voltage allowable for THUNDER actuator, which were about 160 V. For the present case, the best control voltage is $V_p = 155\text{V}$ when the control voltage was varied from 10V to

160V. The best noise reduction was 17.1dB in the duct, and 21.5dB inside the cavity.

In order to protect the THUNDER actuator in the test model, a limitation for the maximum control voltage needs to be imposed. A ‘Saturation’ module was used for this purpose. In the present closed-loop control, the feedback signal was dealt with the signal processing program which down-sampled and normalized the feedback signals. However, since the down-sampled signal was not a 30Hz tonal signal, the normalization program cannot fetch the exact peak in every cycle, so that the absolute value of some peaks of the normalized signal can exceed 1.0. In this case, these peaks will be cut off by the Saturation module so some of the feedback information is lost which is the reason why the control performance at 160V is not better than that at 155V.

Figure 5-12 shows the control performance when the phase delay of feedback signal was varied. The general trends of noise reduction measured by microphones in the cavity and duct were similar, indicating a consistent physical mechanism occurred in the system. The maximum performance occurred at the phase of approximately 288 degrees, in which the obtained noise reduction was 17.5 dB in the duct and 22.6 dB inside the cavity. Therefore, there was an optimal phase delay relative to the feedback signal that can be used in closed-loop control for obtaining an effective noise reduction in the cavity and duct. The mechanism for the optimal phase delay will be discussed in section 5.6.

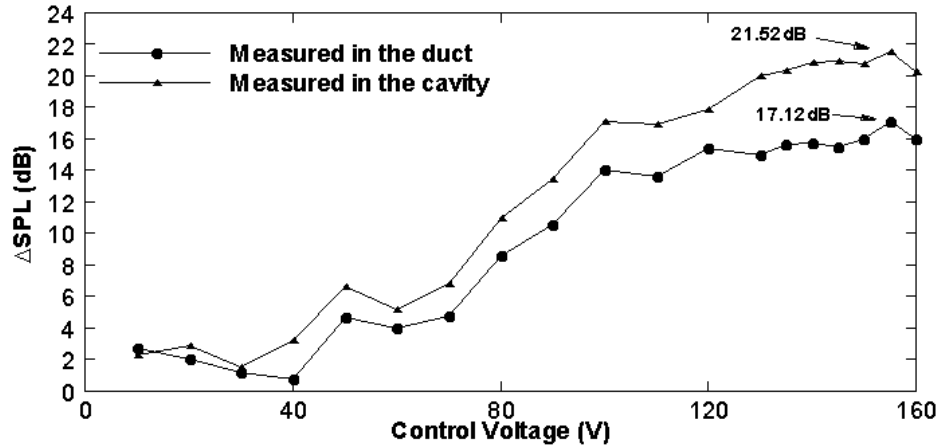


Figure 5-11 The control effect for different control voltages. The control signal was from hot wire 2 which was located at $x=35.5\text{mm}$, $y=11\text{mm}$.

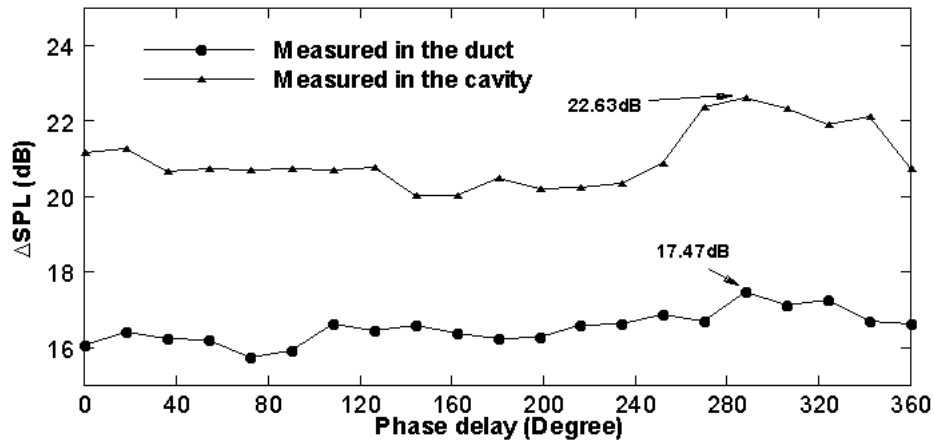


Figure 5-12. The closed-loop control performance for varying phases. The feedback signal was obtained from the hot-wire 2 located at $x=35.5\text{mm}$, $y=11\text{mm}$. the control voltage is 155V.

5.4 The control performance of closed-loop control

Using the optimal control voltage and phase delay, the best control performance was evaluated in terms of sound field and flow field. Figures 5-13 (a) and 5-13 (b) show the sound pressure spectra obtained from the Fast Fourier Transform (FFT) of time domain signals with a frequency resolution of 0.1 Hz. It can be seen that, upon deployment of active control, the sound pressures in the duct and the cavity underwent significant reductions. The Sound Pressure Level (SPL) spectra indicated that with control, the SPL in the duct decreased from 81.3dB to 63.8 dB (a reduction of 17.5 dB) at the vortex shedding frequency. Meanwhile, the SPL measured inside the cavity decreased from 97.8 dB to 75.1 dB (a reduction of 22.63 dB), which was

larger than the noise reduction measured in the duct. The experimental results showed that the active control in the sound field was effective.

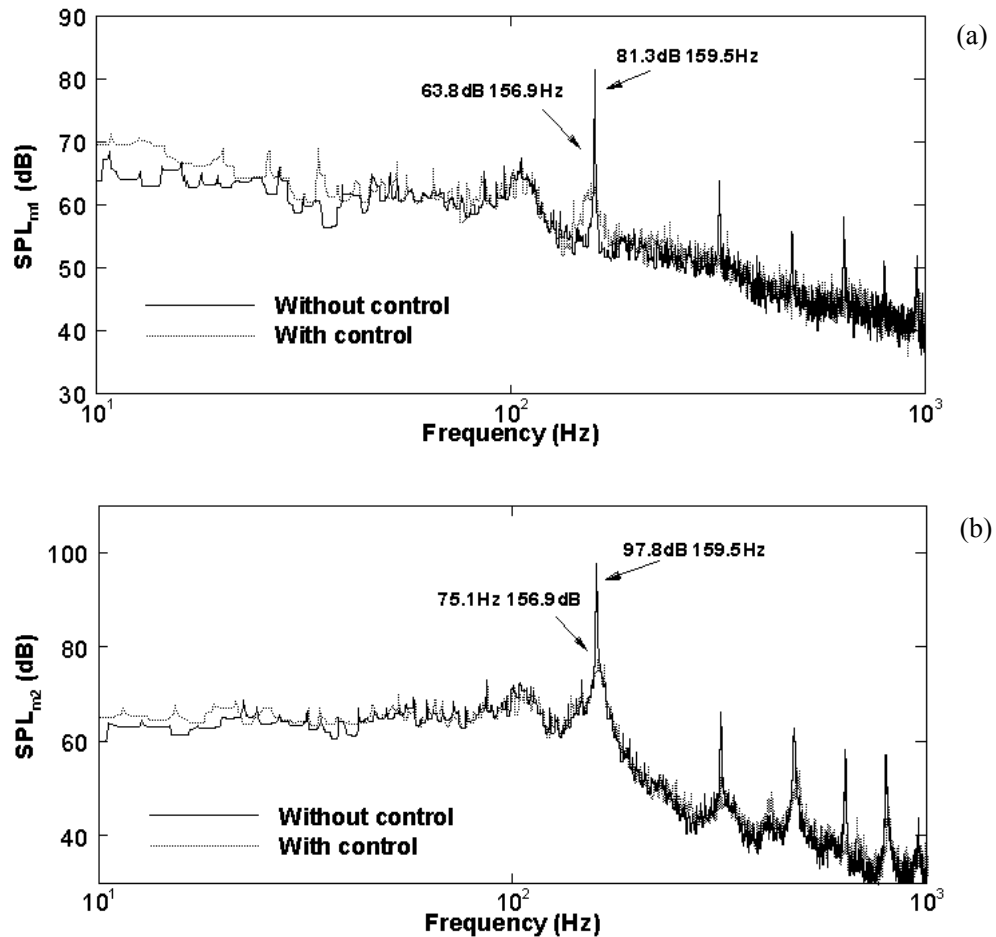


Figure 5-13 The best control performance in frequency-domain. (a) Measured in the duct; (b) Measured inside the cavity.

In the flow field, the control performance was investigated in terms of power spectra density of flow velocity E_u measured by two hot wires, located at $x=0$ mm, $y=11$ mm and $x=34$ mm, $y=11$ mm, as shown in Figures 5-14(a) and 5-14(b). From the figures, it can be seen that E_u has decreased from 3.1×10^{-4} to 4.4×10^{-5} (a reduction of about 86%) at hot-wire 1 and 4.2×10^{-3} to 7.2×10^{-4} (a reduction of about 83%) at hot-wire 2. The results show that the control in the flow field was also effective in reducing the flow velocity levels.

5. Closed-loop control for the flow-induced acoustic resonance

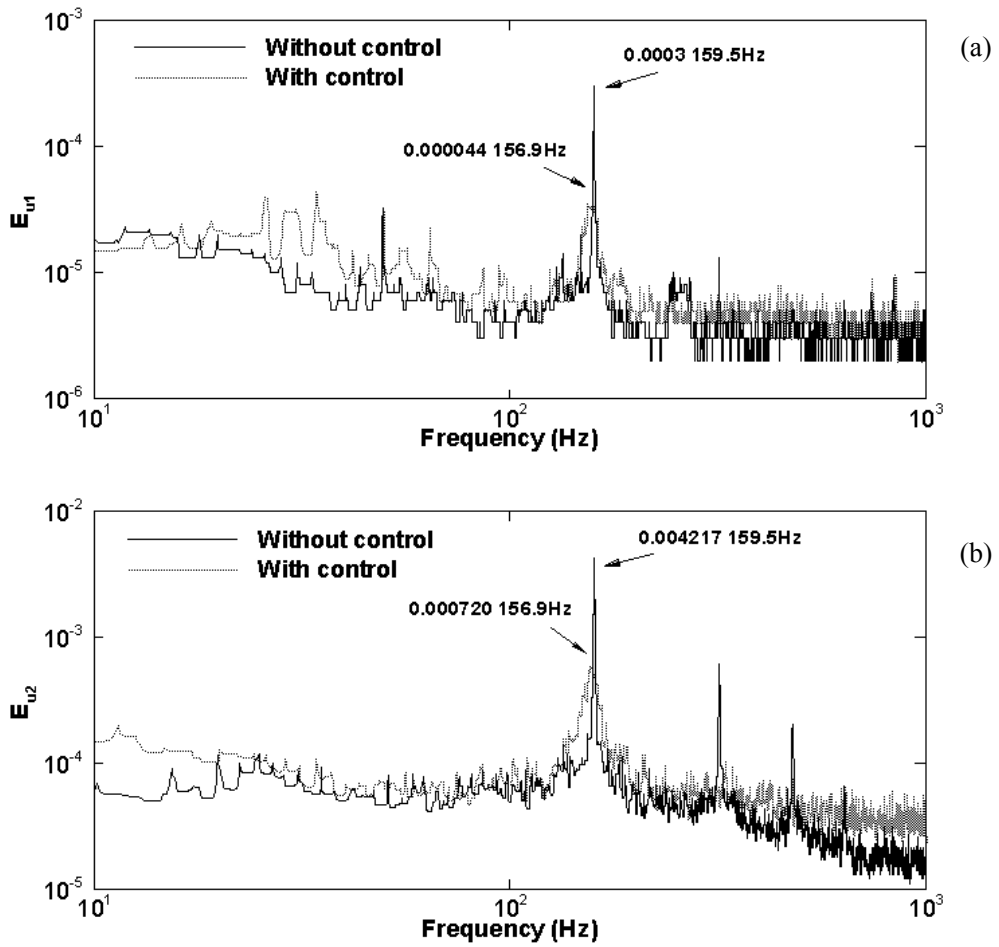


Figure 5-14 The best control performance in frequency-domain. (a) Measured by hot wire 1 at $x=0\text{mm}$, $y=11\text{mm}$; (b) Measured by hot-wire 2 at $x=34\text{mm}$; $y=11\text{mm}$;

5. Closed-loop control for the flow-induced acoustic resonance

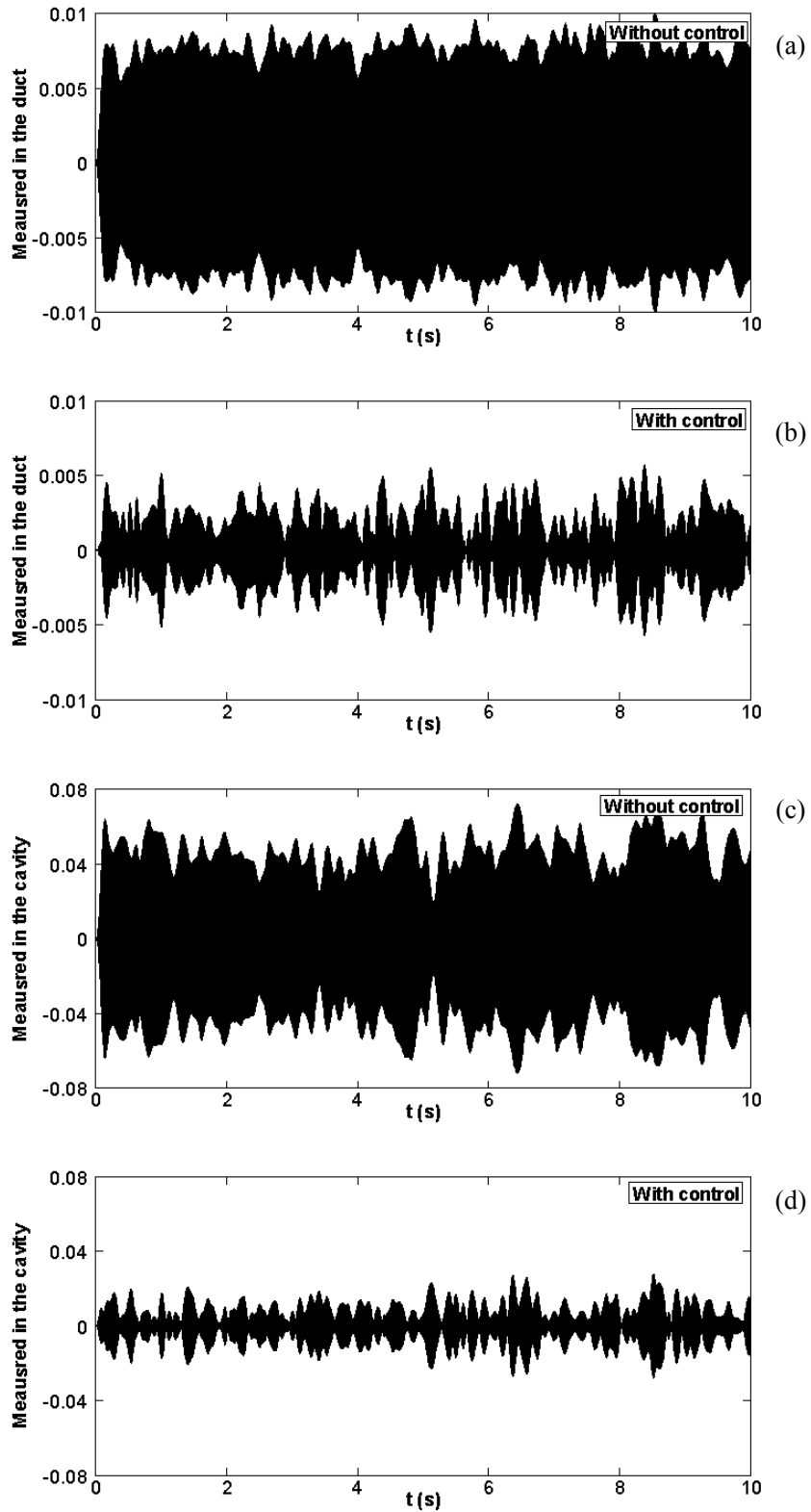


Figure 5-15. Time-domain results for the control performance in sound field; the signals are filtered by a 5Hz-band filter. a) Without control, measured in the duct; b) With control, measured in the duct; c) Without control, measured inside the cavity; d) With control, measured inside the cavity.

5. Closed-loop control for the flow-induced acoustic resonance

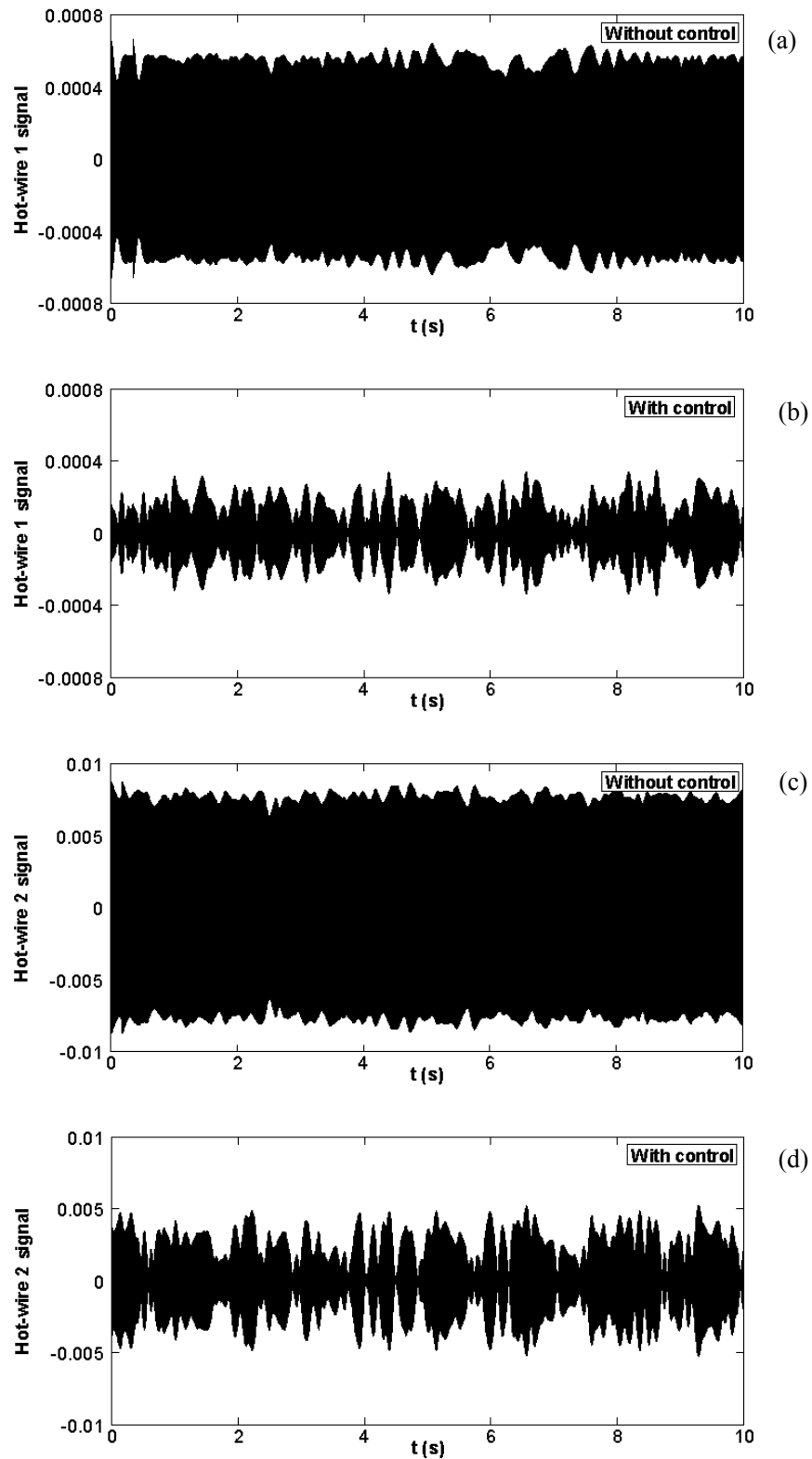


Figure 5-16. Time-domain results for the control performance in flow field; the signals are filtered by a 5Hz-band filter. a) Without control, measured by hot wire 1 at $x=0\text{mm}$, $y=11\text{mm}$; b) With control, measured by hot wire 1 at $x=0\text{mm}$, $y=11\text{mm}$; c) Without control, measured by hot wire 2 at $x=34\text{mm}$, $y=11\text{mm}$; d) With control, measured by hot wire 2 at $x=34\text{mm}$, $y=11\text{mm}$.

The control performance in time-domain was shown in Figures 5-15 and 5-16.

The signals were filtered by a 5-Hz band-pass filter around the vortex shedding frequency. Under control actuation, the noise and flow velocity reductions were clearly observed in all four sensors, indicating that the vortex shedding was disturbed by the control.

5.5 The analysis of fluid-sound interaction

The concept of spectral coherence and spectral phase were used to investigate the interaction of fluid and sound in the present experiment. The spectral coherence and spectral phase between two signals u_a and u_b can be calculated by [99]

$$Coh_{u_a u_b} = \frac{Co_{u_a u_b}^2 + Q_{u_a u_b}^2}{E_{u_a} E_{u_b}} \quad (5-1)$$

$$\phi_{u_a u_b} = \tan^{-1} \left(\frac{Q_{u_a u_b}}{Co_{u_a u_b}} \right) \quad (5-2)$$

where $Co_{u_a u_b}$ and $Q_{u_a u_b}$ are the cospectrum and quadrature spectrum of signal u_a and signal u_b , respectively. The cross-spectrum was computed from the Fast Fourier Transform of the correlation $\overline{u_a(t+\tau)u_b(t)}$. E_{u_a} and E_{u_b} are the energy of the signals. The control performance at the optimal configuration was investigated in this section.

Firstly, the interaction of flow between two different measured positions (hot-wire 1 & 2) was discussed. The result was shown in Figure 5-17. It was found that after applying control, the coherence was reduced from 0.475 to 0.215 (a reduction of 54.7%) at the vortex shedding frequency. This indicated that after applying control; the structure of vortex shedding was altered, resulting in the reduction of the coherence between two different measured positions on the up surface of the test model. Meanwhile, the spectral phase was increased from -127.5

degree to -80.7 degree (an increase of 46.8 degree) which indicated that the propagation speed of vortex shedding was slowed down between these two measured positions. This phenomenon was agreeable with the vortex shedding frequency shift phenomenon that was observed in the present experiment.

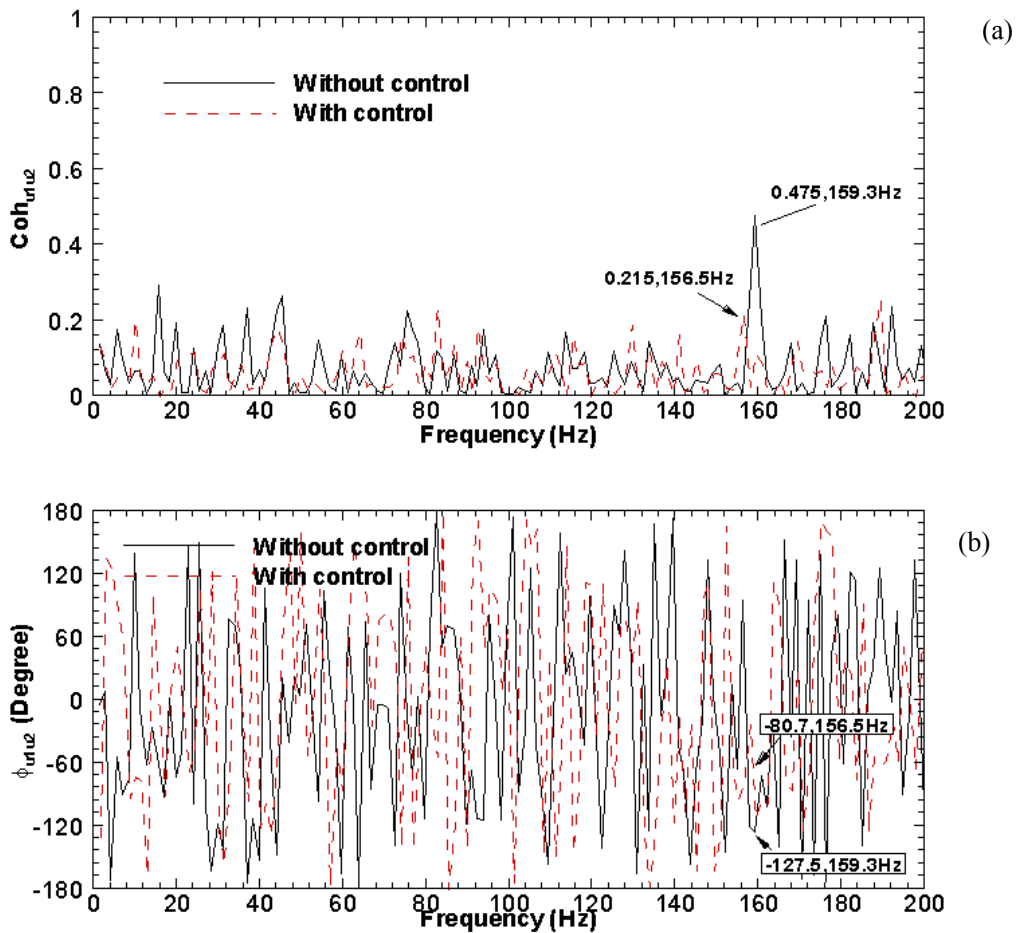


Figure 5-17 The spectral coherence and spectral phase at the vortex shedding frequency between u_1 and u_2 for closed-loop control. Here, u_1 was measured by hot-wire 1 which was located at $x=0$ mm, $y=11$ mm. u_2 was measured by hot-wire 2 which was located at $x=34$ mm, $y=11$ mm. The feedback signal was obtained from hot-wire 2 for closed-loop control. (a) Spectral coherence; (b) Spectral phase.

The spectral coherence and phase between the signals measured by two microphones were shown in Figure 5-18. The spectral coherence was decreased from 0.976 to 0.628 (a reduction of 36%) and the spectral phase was increased from -52.5 to -24.0 (a raise of 28.5 degrees). It indicated that the action of control had obviously affected the spectral coherence and phase between the signals measured by two

microphones.

Furthermore, it is found that when the certain frequency ranges of signals have a strong spectral coherence to each other. The corresponding spectral phase is nearly at the same value within these frequency ranges due to strong coherence between two signals. However, if there is no strong spectral coherence, the corresponding spectral phase fluctuates which can be observed in Figure 5-18. Therefore, if the vortex shedding is damaged, the stabilization range of corresponding spectral phase can be expected to decrease.

The spectral coherence and phase between the signal measured by Mic.1 and the signal measured by hot wire 2 were shown in Figure 5-19. It is found that the spectral coherence is decreased from 0.993 to 0.900 (a reduction of 9.3%) and spectral phase is changed from 30.5 to 50.8 (an increase of 20.3 degrees). The position of the hot wire 2 is almost near the position of the Mic.1 in the present experiment, so the spectral alteration was not large. Furthermore, it is found that there is no strong coherence from 20Hz to 120Hz which indicates that the hot wires are not sensitive with the background noise in the present experiment, in contrast to the microphones. That is one of the reasons why the signal measured by hot wire 2 is chosen as the feedback signal in the present experiment.

5. Closed-loop control for the flow-induced acoustic resonance

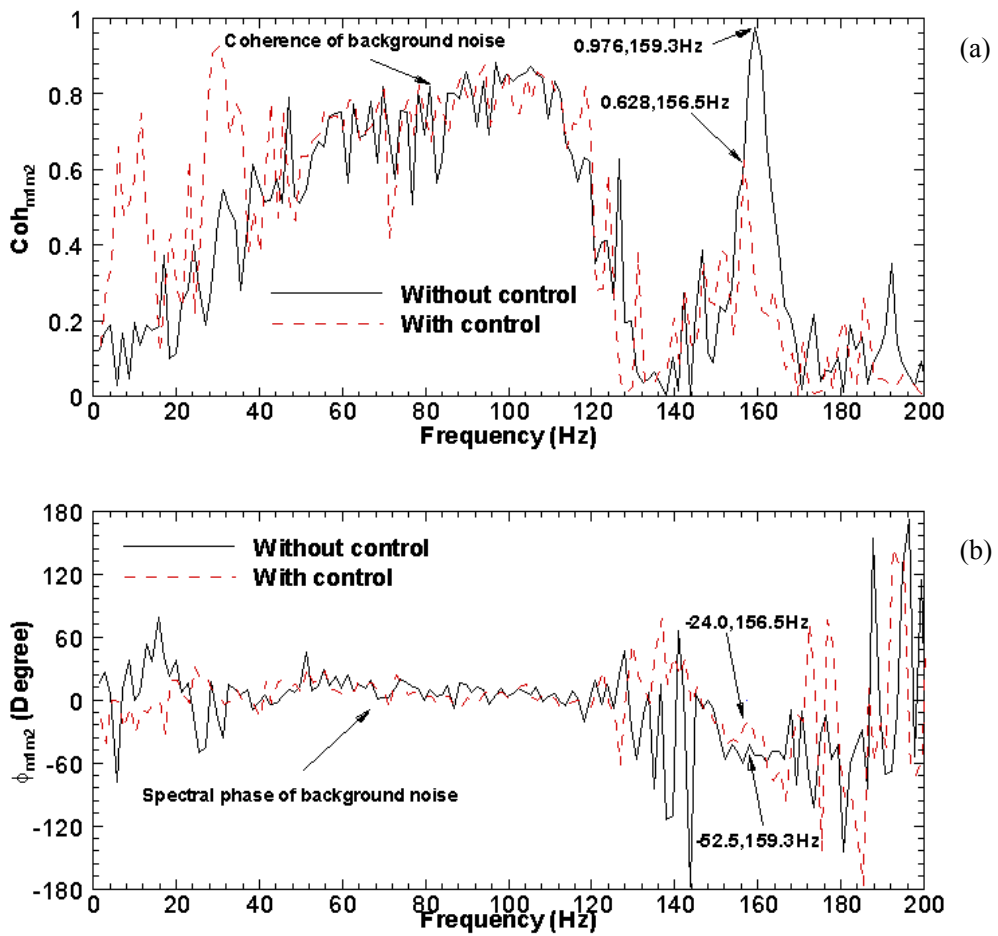


Figure 5-18 The spectral coherence and spectral phase at the vortex shedding frequency between m_1 and m_2 for closed-loop control. Here, m_1 was the sound pressure measured in the duct. m_2 was the sound pressure measured inside the cavity. The feedback signal was obtained from hot-wire 2 for closed-loop control.

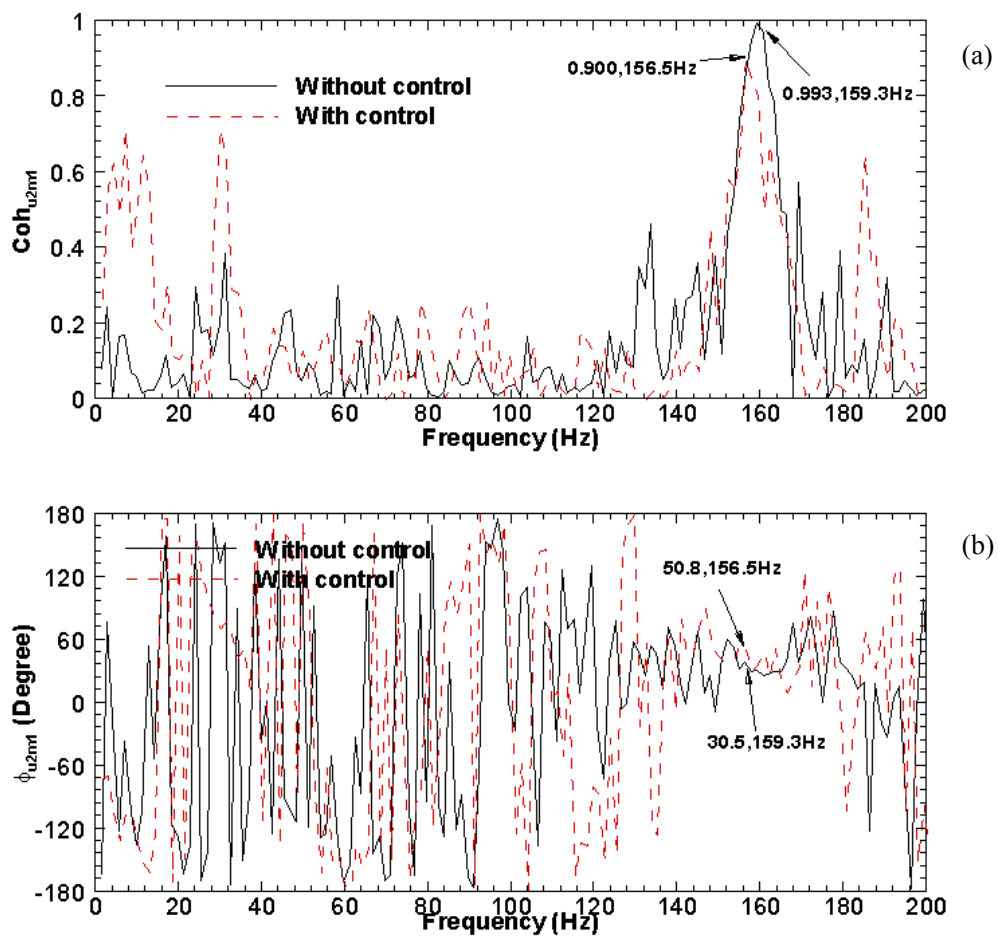


Figure 5-19 The spectral coherence and spectral phase at the vortex shedding frequency between m_1 and u_2 for closed-loop control. Here, m_1 was the sound pressure measured in the duct. u_2 was measured by hot-wire 2 which was located at $x=34\text{mm}$, $y=11\text{mm}$. The feedback signal was obtained from hot-wire 2 for closed-loop control.

The spectral coherence and phase between the signal measured by Mic.2 and the signal measured by hot wire 2 were shown in Figure 5-20. The spectral coherence is decreased from 0.974 to 0.529 (a reduction of 46%) and the spectral phase is increased from -22.3 to 27.3 (an increase of 49.6 degrees). The strong fluid-sound interaction of the signal measured by Mic.2 and signal measured by hot wire 2 was damaged by the closed-loop control action. Furthermore, since Mic.2 was installed inside the cavity, the alteration shown in the Figure 5-20 also represents that a strong fluid and resonance acoustic interaction that was influenced by the closed-loop control.

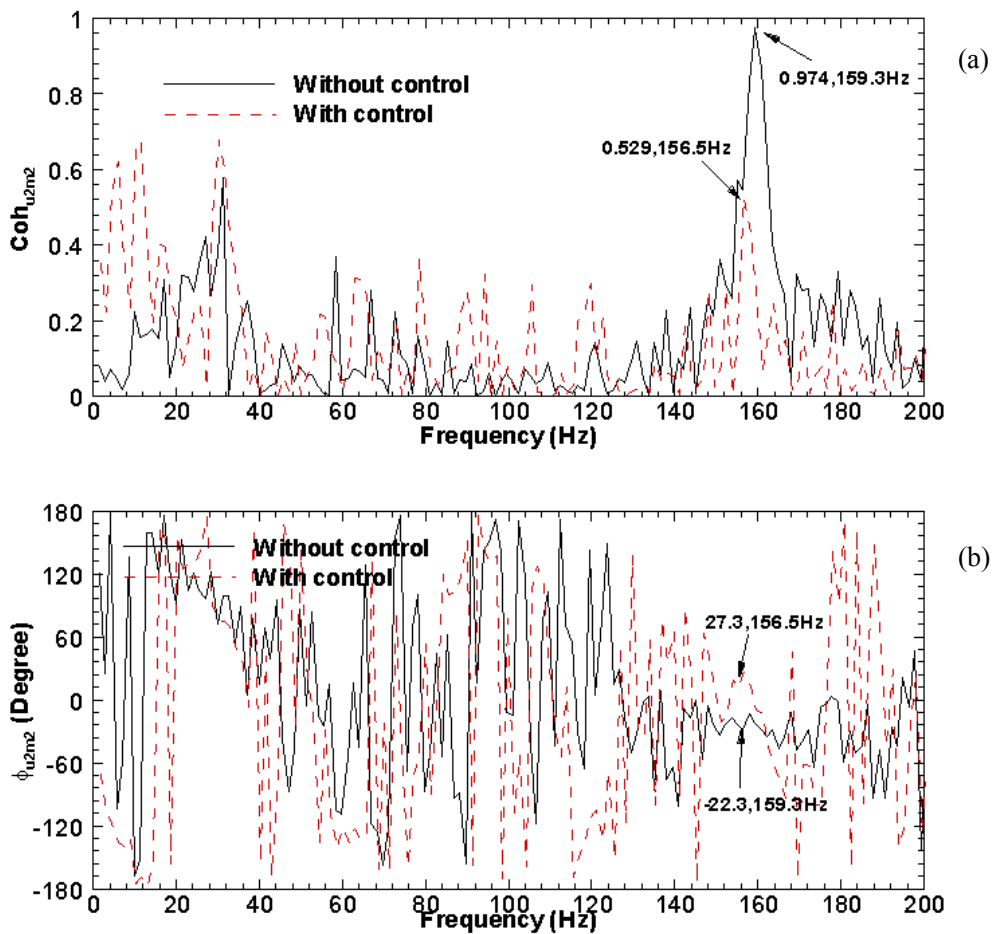


Figure 5-20 The spectral coherence and spectral phase at the vortex shedding frequency between m_2 and u_2 for closed-loop control. Here, m_2 was the sound pressure measured inside the cavity. U_2 was measured by hot-wire 2 which was located at $x=34\text{mm}$, $y=11\text{ mm}$. The feedback signal was obtained from hot-wire 2 for closed-loop control.

In conclusion, the spectral coherence of fluid and sound in the system was altered by the closed-loop control action. The spectral coherence at the vortex shedding decreased which indicates that control action of the closed-loop control has damaged the vortex shedding. The increase of the spectral phase shows that the vortex structure has been changed during the control action. The vortex shedding has been slowed down by the control action, which is agreeable with the vortex shedding frequency shift phenomena.

5.6 Vortex strength abatement mechanism for closed-loop control

The same trend of the noise reduction indicates that the vortex strength abatement mechanisms for the open-loop control which had been developed in Chapter 3 are also suitable to be used to explain the vortex strength abatement in the closed-loop control. The ‘Disturb pressure pulse mechanism’ and ‘Shear layer shifts mechanism’ can be used to explain the physical vortex strength reduction in the closed-loop control.

When comparing to the closed-loop control best results, the open-loop control achieved 1.3 dB less reduction at the optimal control voltage and phase delay. Such control results were as expected because the harmonic actuation on the open-loop control was independent of what was occurring in the system. In the closed-loop scheme, the control input was influenced by the feedback signal that reflected the system response. This control scheme allowed a better adjustment of surface perturbation of test model to disturb the generated vortices, resulting to weaker vortex shedding and acoustic resonance in the cavity.

In order to investigate the vortex shedding process over the test model, the spectral phase relationship between two flow velocity measurements along the up-surface of test model, u_1 and u_2 , was used. Here, u_1 was measured by hot-wire 1 which was located at leading edge, $x=0$ mm, $y=11$ mm, while u_2 was measured by hot-wire 2 which was moved along $y=11$ mm.

Figure 5-21 shows the spectral phase at the vortex shedding frequency for cases without control, with open-loop control and closed-loop control. The results show that when there was no control, each cycle of vortex shedding began at the trailing edge of test model. Between the leading edge and trailing edge, there was no clear vortex

shedding as indicated by no significant spectral phase shift over this region. In this case, the flow over the leading edge and trailing edge is roughly in-phase. The spectral phase for $0 \leq x \leq 5.5\text{mm}$ was relatively small, however the spectral phase shift began to increase significantly for $x > 5.5\text{mm}$. Such a spectral phase shift indicated that the flow structure over this region has started to change, leading to a full generation of vortex shedding at the trailing edge.

Under the control actuation of the test model, the surface perturbation was implemented in the range of $5.5\text{mm} < x < 25.5\text{mm}$. There was generally no dominant vortex shedding that dominated within this range. The boundary layer dominated the flow field in this range. Due to the complex nature of the boundary layer, the measured spectral phase shift was rather irregular. However, at the trailing edge, vortex shedding was fully developed and propagated downstream. From Figure 5-21, a clear trend of monotonically decreasing spectral phase shift was observed. In the majority of regions downstream the test model, the value of the spectral phase shift for controlled system was larger than that of the uncontrolled system. The increase of the spectral phase shift value might imply that more time was required for a vortex to travel from the trailing edge to the downstream of the test model. This is consistent with the phenomenon where the vortex shedding frequency was shifted to a lower frequency after control.

Further observation indicates that there was a generally larger spectral phase shift for system with closed-loop control than that of open-loop control, as can be seen in Figure 5-21. The result means that for the closed-loop control, the active surface perturbation has generated a more significant change to the vortex shedding structure than that of open-loop control. Therefore, the closed-loop control scheme could achieve more reduction in the vortex energy and induced noise in the duct and cavity,

compared to the open-loop control scheme. This is as expected since the closed-loop control utilizes feedback signals that contain the vortex information of the system, so an effective reduction of the vortex energy can be obtained. Thus, an optimal control strategy using the developed control technique could be used by optimally tuning the phase-delay term of the control actuation to create changes in vortex shedding structure, as observed by the spectral phase shift in the flow field.

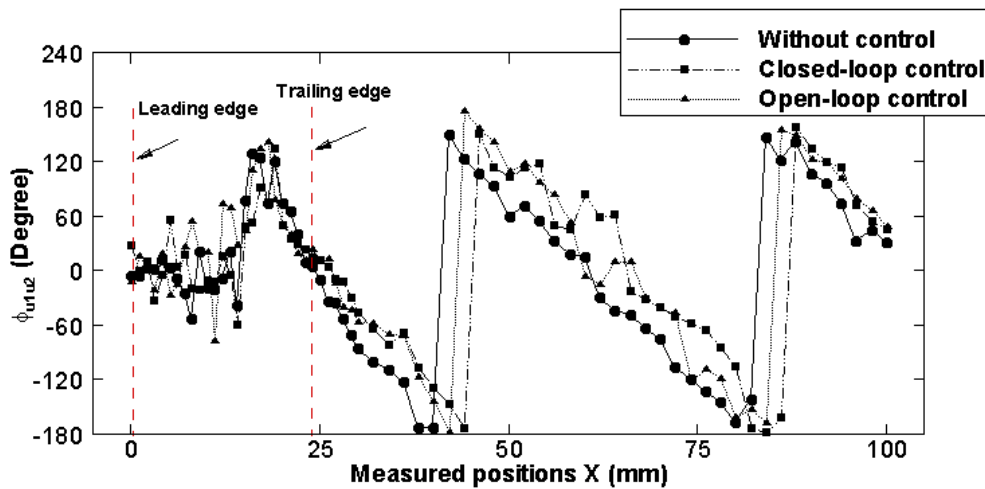


Figure 5-21. The spectral phase between u_1 and u_2 at the vortex shedding frequency. Here, u_1 was measured by hot-wire 1 which was located at $x=0$ mm, $y=11$ mm. u_2 was measured by hot-wire 2 which was moved along $y=11$ mm. The feedback signal was obtained from hot-wire 1 for closed-loop control.

5.7 Vortex shedding frequency shift in the closed-loop control

Chapter 3 had investigated the existence of vortex shedding frequency shift phenomenon that was observed in open-loop control results. It was found that when control actuation was activated, the vortex shedding frequency had been shifted away from the cavity resonant frequency, so that there was more noise reduction inside the cavity than that in the duct. In the present closed-loop control experiments, the phenomenon was also observed. The maximum displacement of the plastic plate d_{pm} was measured by a laser vibrometer at the center point of the plastic plate of test model. In the present measurement, the phase delay is set to zero, only various the control voltages.

Figure 5-22 indicates that when the perturbation displacement was increased, the vortex shedding frequency was shifted to a lower frequency. With a small displacement, typically less than 0.6mm, the frequency shift was trivial, typically less than 1 Hz. With a higher maximum displacement, however, more appreciable reduction in shedding frequency was observed. The maximum frequency shift was 2.6 Hz when the maximum displacement was at 0.91 mm. Chapter 3 had concluded that the reduction of the shedding frequency could be attributed to the effect of surface perturbation of test model, which could be regarded as a way to increase the effective thickness of test model. In this case, the vortex shedding frequency shift can be predicted by an equation which relates the frequency shift to the maximum effective thickness of test model, and consequently to the control voltage actuation. Therefore, the same physical mechanism exists on this frequency shift phenomenon due to surface perturbation of test model, independent of the control strategies.

In Chapter 3, it had concluded that the vortex frequency shift could be expressed as Equation 3-9.

$$\Delta f_{sp} = f_{s0} - f_{sp} = \frac{\bar{d}_p}{t} f_{s0} \quad (3-9)$$

It shows that the reduction of Δf_{sp} is linearly related to \bar{d}_p , which can be estimated by using the vortex shedding frequency shift data in Figure 5-22 and Equation 3-9.

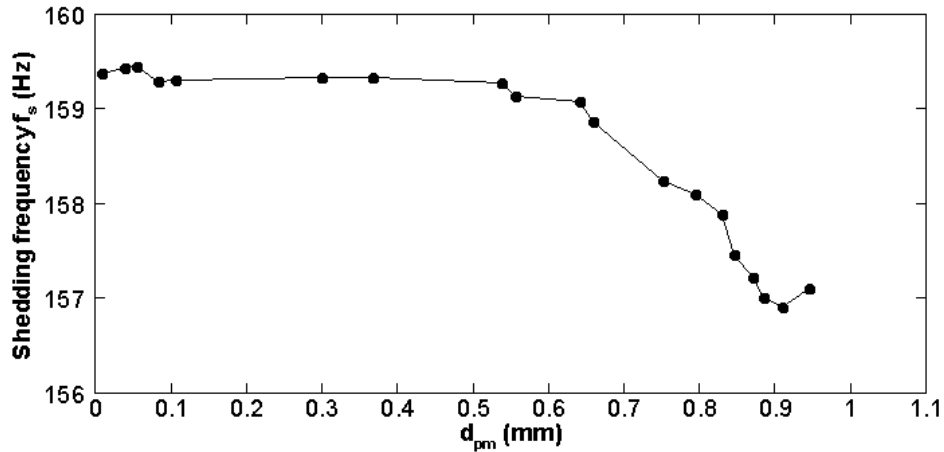


Figure 5-22 The shift in the vortex shedding frequency at various maximum displacements d_{pm} of the test model.

Figure 5-23 shows the variation of d_{pm} versus \bar{d}_p . In the low perturbation region (with small perturbation amplitude, typically $d_{pm} < 0.6\text{mm}$), \bar{d}_p/d_{pm} is roughly 3%, whilst for larger perturbation amplitude, \bar{d}_p/d_{pm} approaches 23%. In the optimal control voltage, the effective increase in the thickness of the vibration plate brought about by the perturbation is roughly $0.21/11 = 1.9\%$. This was shown to cause 2.6 Hz shift in f_s .

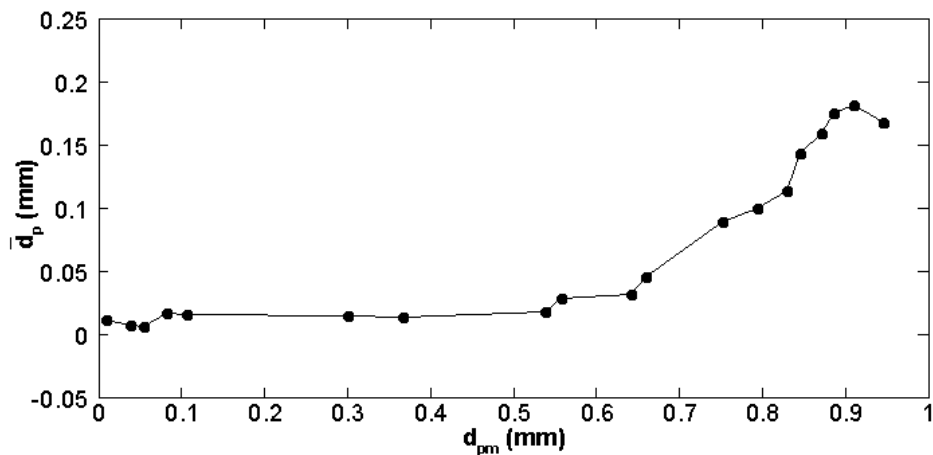


Figure 5-23 The effective perturbation displacement of the vibration plate.

It is found that the frequency shift is not obvious in the low perturbation region in the closed-loop control. In the open-loop control, the control signal is a pure 30Hz –signal. After applying control, extra noises generated by the test model was at 150Hz

and 180Hz, which are away from 160Hz, so The extra noise did not affect the results in the open-loop control. However in the closed-loop control, the frequency of the control signal was changing due to the system response, and it will generate an extra noise around the vortex shedding frequency f_s . This extra noise will mix with the measured signal and affect the identification of the frequency shift. Therefore, in the low perturbation region, the frequency shift is not obvious. In high perturbation region, the frequency shift is big enough to avoid the effect of extra noise influence.

5.8 Effects on cavity resonance in closed-loop control

Here, the resonance bandwidth is determined, which will be used as one of important parameters for investigating the acoustical resonance effect. To this end, a series of tests were conducted to document the sound pressure level measured by Mic.1 and Mic.2 at shedding frequency f_s under various flow velocities before the control was deployed at the optimal control voltage. The results are shown in Figure 5-24. The peak values of sound pressure level at f_s , measured by Mic.1, monotonously increase as the flow velocities increase. In contrast, the peak values of sound pressure level at f_s , measured by Mic.2, reaches a peak value of 97.8dB when $U = U_{cr} = 8.2\text{m/s}$ (i.e. $f_a \approx 160\text{Hz}$). Using the bandwidth definition corresponding to -3dB reduction, the band width of the resonance peak was determined as 3.4 Hz from 158Hz to 162Hz, corresponding to a flow velocity variation from 8.0m/s to 8.3m/s. Because the open-loop and closed-loop control was conducted in the same experiment setup, the results shown in Figure 5-26 are the same with the open-loop control except some small differences which come from measurement error.

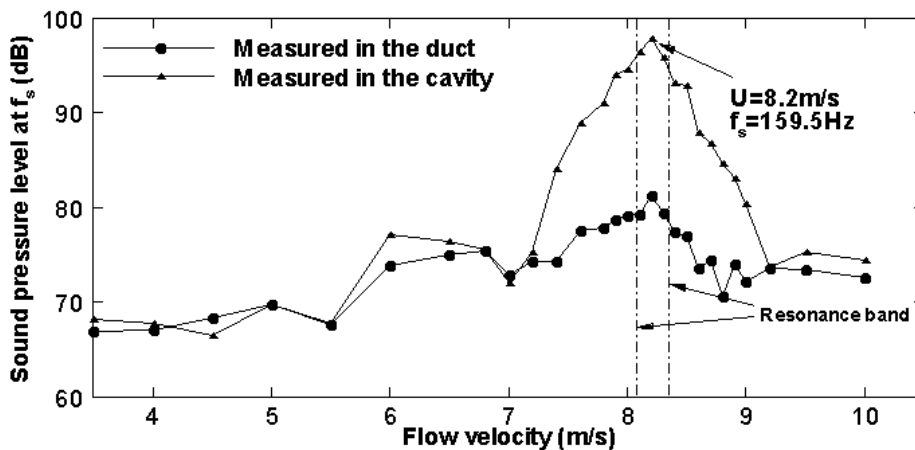


Figure 5-24 Sound pressure level at f_s at various flow velocities, without control.

Figure 5-25 shows the control effect on the previously defined ΔSPL at f_s at various flow velocities with optimal control voltage. It can be seen that apart from resonance region, sound reductions in the duct and in the cavity are almost the same. This should be attributed to the weakened vortex strength, which has been extensively discussed in our previous section. Around cavity resonance, sound reduction inside the cavity exceeds that in the duct, by as much as 4.4dB. This can be attributed to the control-induced shift of the vortex shedding frequency. In fact, a 2.6Hz shift in f_s exceeds the half bandwidth of the cavity resonance, this alone should bring about more than 3dB reduction in the SPL.

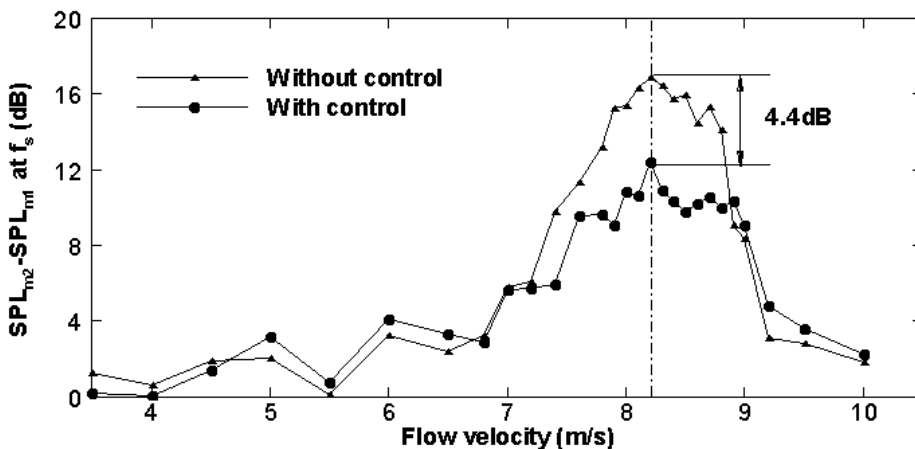


Figure 5-25 The control effect on $SPL_{m_2} - SPL_{m_1}$ at f_s at various flow velocities.

Therefore, when applying surface perturbation technique on the test model in the closed-loop control, the perturbation increases the effective thickness of the vibration plate. The increase of the effective thickness of the vibration plate can shift the vortex shedding frequency to a low value. The quantity of the shift can be estimated by Equation 3-9, which is the same as open-loop control. Furthermore, if the shedding frequency shift that caused by the perturbation exceeds the resonance bandwidth which is defined in the Figure 5-24 of the acoustic cavity, the sound reduction measured inside the cavity is larger than that in the duct. In the present experiment, this phenomenon along gives a rise to a further sound pressure reduction of 4.4 dB inside the acoustic cavity. In summary, when vortex shedding occurs and its shedding frequency is close to the acoustic resonance of the down-stream cavities, the surface perturbation of the test model excited by the modified feedback signal not only disturbs the two shear layers behind the test model and thus weakens the strength of the vortex shedding, but also shifts the vortex shedding frequency, and then suppresses the acoustic resonance phenomenon inside the down-stream cavities.

5.9 The combination of different feedback signals

In the present study, the feedback signal can be obtained from hot wire and microphone. The possibility to improve the control performance by using the combination of different feedback signals is an aspect worth considering. To that end, various measurements were conducted to check the control effect measured by Mic.1 for combination of different feedback signals. All the signals were directly combined together before implemented on the downsampling program. Since different feedback signals have different amplitude and phase, using a combination of different feedback signals may allow more information from the system to be used for control.

In the measurement, the signals measured by hot wire 1, hot wire 2, Mic.1 and

Mic.2 were represented respectively as Sh1, Sh2, Sm1 and Sm2. The control effect measured by Mic.1 for combination of different feedback signals was shown in Figure 5-26. It was found that control effect of the combination of different feedback signal were similar to that obtained using single feedback signal measured by hot wire 2. There was no obvious improvement by using the combination of different feedback signals.

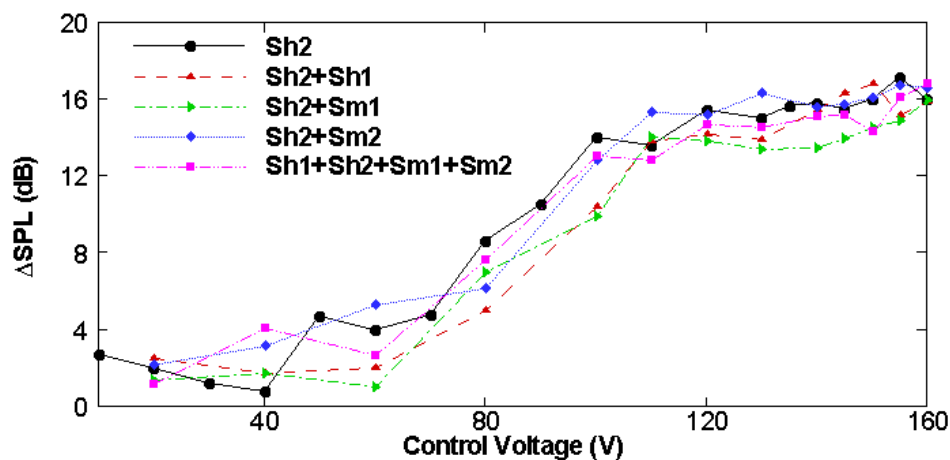


Figure 5-26 The control effect measured by Mic.1 for combination of different feedback signals.

Hot wire 1 and hot wire 2 were used to measure the vortex information in the flow field. Further, Mic.1 and Mic.2 were used to measure the vortex information in the sound field. There are no obvious improvements using multiple feedback signals because all the signals contained the same information of the mainly tonal vortex shedding response in the flow field.

5.10 Conclusions

The implementation of closed-loop control scheme was investigated in the view of achieving effective control of vortex-induced acoustic resonance in the system. The control signal in closed-loop control utilizes feedback signals acquired from the system, which may be from the hotwires and microphones. The hotwire signal is generally more stable than the signals from microphones because the hotwire sensor is

not significantly affected by the flow background noise that may be caused by the configuration of the experimental set-up. In the present experiment, the case of using hotwire as feedback signal was discussed.

A signal processing program was developed for closed-loop control. In this process, a high-frequency feedback signal obtained by hot wire 2 was down-sampled by using the downsampling program to a corresponding low-frequency down-sampled signal suitable for exciting the test model. Since the ‘Beat’ phenomenon could affect the control performance, the down-sampled signal was normalized by using the normalization program. The normalized signal was then input into the modified PID.

The control of flow-induced acoustic resonance by using active closed-loop control was then experimentally investigated. It was found that the noise contributed by the flow-induced acoustic resonance could be effectively minimized by the implementation of the proposed surface perturbation technique. The present study leads to the following conclusions:

- (1) The flow-induced acoustic resonance can be effectively reduced by the implementation of the developed closed-loop surface perturbation technique. At the optimum control voltage and control phase delay for the present experiment, there was a noise reduction of 17.5 dB in the duct and 22.6 dB inside the cavity.
- (2) The closed-loop control could achieve a better control performance than that of the open-loop control. In particular, the phase delay of control actuation could be optimally tuned so that the strength of vortex shedding energy could be minimized, leading to a better noise reduction in the duct and cavity. This process was evident from the spectral phase shift results for the case of closed-loop control, where the vortex traveling time has been delayed at downstream of the test model. Therefore, an optimal control strategy was proposed by utilizing an optimal phase-tuned

active surface perturbation to create sufficient changes in the vortex shedding structure, leading to an effective noise reduction in the system.

- (3) The vortex shedding frequency shift was also observed in the closed-loop control. It can take extra noise reduction inside the cavity than that in the duct due to the down-stream cavity resonance. The mechanism in the closed-loop control is consistent with the open-loop control and the same equation 3-9 can be used to predict the frequency shift. The frequency shift phenomenon in the closed-loop control can give a rise to a further sound pressure reduction of 4.4 dB inside the acoustic cavity. Therefore, when vortex shedding occurs and its shedding frequency is close to the acoustic resonance of the cavity, the surface perturbation not only disturbs the two shear layers and thus weakens the strength of the vortex, but also shifts the shedding frequency, and then suppresses the acoustic resonance phenomenon.

6. The investigation of control strategy

6.1 Introduction

The active control for a semi-circular leading edge test model has been investigated in Chapters 2 to 5. It was found that both active open-loop control and active closed-loop control could be used to control the flow-induced acoustic resonance. The surface perturbation technique could be successfully applied for controlling the vortex shedding generated downstream a semi-circular leading edge test model.

In practical engineering applications, various types of leading edge geometry can be used for a bluff body. However, they can be simply classified into two basic types: the square leading edge and the semi-circular leading edge. Other leading edge types can be regarded as a variation from these two basic types. It has been explained in Chapter 1 that when the flow past a bluff body, there are mainly two different vortex shedding types due to various leading edges: the leading edge vortex shedding (LEVS) and the trailing edge vortex shedding (TEVS). The corresponding control strategy will be discussed by taking into account the differences of these two types of vortex shedding.

In this Chapter, effective perturbation positions over the test model for both the square and semi-circular leading edges will be carefully investigated. The result of effective perturbation position will benefit the control strategy selection for various leading edge configurations. In Chapter 3, the ‘pressure disturbance mechanism’ was developed to explain the abatement mechanism of the surface perturbation technique for a semi-circular leading edge test model. This mechanism illustrated the physical control mechanism behind the surface perturbation technique.

Furthermore, it indicates a general control strategy for a semi-circular leading edge bluff body. In this mechanism, the pressure pulse, which is generated by the trailing edge vortex shedding along the surface of the test model, is one of the important factors for vortex shedding control. The existence and the directivity characteristic of this pressure pulse will be further investigated here.

Based on all these discussions, the optimal control strategy will be discussed and summarized for practical engineering applications.

6.2 Vortex types and their characteristic for various leading edges

Before discussing the control strategy for various leading edges of test model, one first needs to identify the vortex types for various leading edge of the test model.

In general, the vortex shedding can be classified into two types: the Leading-edge vortex shedding (LEVS) and the Trailing-edge vortex shedding (TEVS). As mentioned in Chapter 1, around a short square leading edge bluff body, there was only LEVS. LEVS and TEVS both existed for a long square leading edge bluff body. If the leading edge was semi-circular, there was only TEVS. In the present section, a short square leading edge test model and a short semi-circular leading edge test model were used to check the types of the vortex shedding.

6.2.1 Vortex type for semi-circular leading edge

Various measurements were performed to check the types of vortex shedding around a semi-circular leading edge test model, denoted as C-1 in Chapter 2, and a square leading edge, denoted as S-1 in Chapter 2. Hot-wire 1 was located at $x=0\text{mm}$ and $y=11\text{mm}$, while hot-wire 2 was moved along the $y=11\text{mm}$ at different x measured positions. The spectral phase relationship $\phi_{u_1 u_2}$ between hot-wire 1 and hot-wire 2

showed the vortex distribution along the $y=11\text{mm}$ in Figure 6-1 and Figure 6-4. The spectral phase $\phi_{u_1u_2}$ of the laminar boundary layer was first checked; it was found that for a laminar boundary layer, the spectral phase $\phi_{u_1u_2} = 0$. In Figure 6-1, the spectral phase $\phi_{u_1u_2} = 0$ from $x=0\text{mm}$ to $x=5.5\text{mm}$ and spectral phase $\phi_{u_1u_2} \neq 0$ from $x=5.5\text{mm}$ to $x=23\text{mm}$. The results implied that the laminar boundary layer had been changed from 5.5mm to 23mm, but it could be regarded as the redeveloped boundary layer. In Chapter 3, it had been concluded that the redeveloped boundary layer acted as a key factor for the generation of the TEVS.

Furthermore, the spectral phase between the point at the leading edge and the point at the trailing edge was close to zero, which implied that the TEVS started at the trailing edge. The range from leading edge to trailing edge can be defined as ‘Region T-A’, which is the ‘generation region’. And the range behind the test model can be defined as ‘Region T-B’ which is the vortex shedding region. Over the surface of test model ($0 < x < 23\text{mm}$) there was no vortex shedding, and behind the semi-circular leading edge test model, there was the periodic vortex shedding. In this case, the type of vortex shedding of the semi-circular leading edge test model was primarily TEVS.

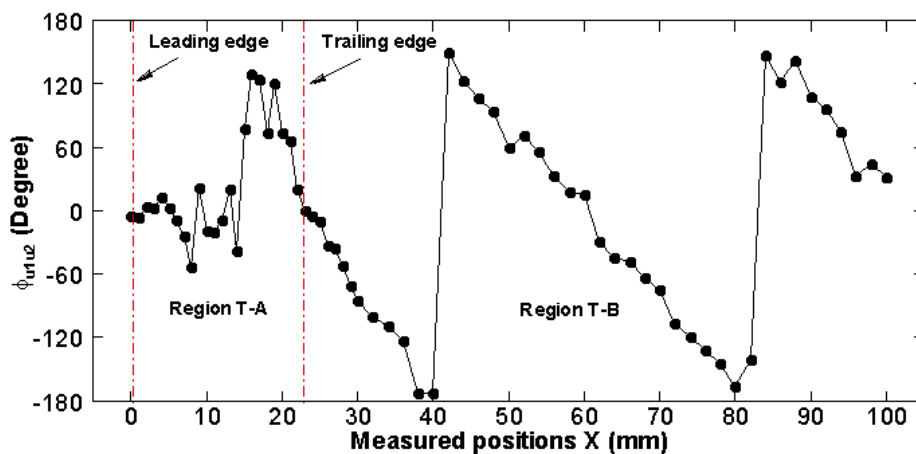


Figure 6-1 Phase relationship between hot-wire 1 and hot-wire 2 along $y=11\text{mm}$ for C-1 test model. Hot-wire 1 was located at $x=0\text{mm}$ and $y=11\text{mm}$, hot-wire 2 was move along the $y=11\text{mm}$ at different x positions.

The vortex shedding strength which can be expressed as the maximum magnitudes of the E_{u_2} measured by hot wire 2 along $y=11\text{mm}$ is shown in Figure 6-2. In region T-B, the maximum magnitudes of E_{u_2} increased from the trailing edge at $x=23\text{mm}$. The maximum vortex shedding strength $E_{u_2 \max}$ was about 0.004 at the measurement point $x=52\text{mm}$. In the region T-A, the maximum magnitudes of E_{u_2} were very small, which were only about 2.5% of $E_{u_2 \max}$ in the region from $x=0\text{mm}$ to $x=16\text{mm}$. From $x=17\text{mm}$ to $x=23\text{mm}$, the maximum magnitudes of E_{u_2} increased but they were only 10% of $E_{u_2 \max}$. Therefore, it can be concluded that in the region T-A there are no obvious vortex shedding. The small maximum magnitudes of E_{u_2} at the vortex shedding frequency in region T-A may be considered to come from the pressure pulse, which had been observed by Hourigan[123].

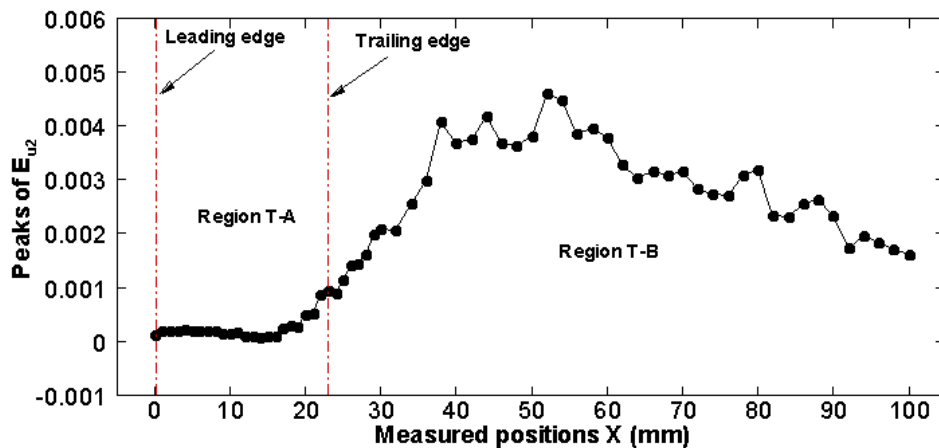


Figure 6-2 The strength of vortex shedding distribution along $y=11\text{mm}$ for C-1 test model. hot-wire 2 was moved along the $y=11\text{mm}$ at different x positions.

In conclusion, the vortex shedding around the semi-circular test model can be divided into two regions: Region T-A and Region T-B. Region T-A is the generation region for the TEVS, where there is no vortex shedding in this region. Small maximum magnitudes of E_{u_2} measured by hot wire 2 can be regarded as the pressure pulse. On the other hand, Region T-B is the vortex shedding region. The

vortex shedding was observed to start at the trailing edge. Furthermore, the strength of TEVS increases almost linearly after the trailing edge before reaching the maximum vortex strength.

6.2.2 Vortex type for the square leading edge

The square leading edge is another typical leading edge used in the engineering application. In the present study, a short square leading edge was chosen for investigation. As mentioned in Chapter 1, only LEVS exist for a short square leading edge bluff body. A diagram illustrating the vortex type for a short square leading edge test model and the measured points is shown in Figure 6-3. In the experiment, the hot wire could not be located very near to the surface of the test model for the sake of protecting the hot wire. Therefore, hot wire 1 was located just above the leading edge at $x=0\text{mm}$ and $y=11\text{mm}$. The hot wire 2 was moved along the dash dotted line as shown in Figure 6-3.

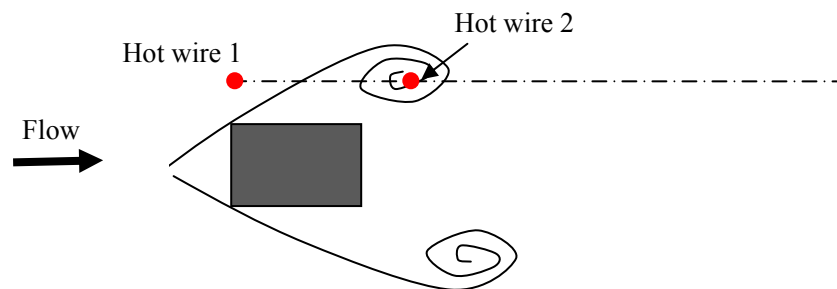


Figure 6-3 Diagram of the vortex type for short square leading edge test model and the measured points.

The spectral phase $\phi_{u_1 u_2}$ along $y=11\text{mm}$ is shown in Figure 6-4. It was found that the spectral phase was nearly zero over the front part of the test model ($0 \leq x \leq 12\text{mm}$). At $x = 13\text{mm}$, the spectral phase suddenly changed to 39 degrees with a tendency to decrease downstream the test model. The existence of a sudden change in spectral phase indicated that there was a vortex shedding occurring at $x \geq 13\text{mm}$. The sudden change can be explained by considering the measurement

points shown in Figure 6-3. For a square leading edge test model, the vortex shedding separated at the leading edge of the test model as illustrated in Figure 6-3. When the hot wire 2 was moved along the dash dot line in Figure 6-3, some of the measurement points were not within the range of the strong vortex shedding. Therefore when the hot wire 2 was moved at the range of $0 \leq x \leq 12\text{mm}$, the spectral phases $\phi_{u_1u_2}$ were near zero.

For a short square leading edge test model (S-1 in the present experiment), there are only LEVS which start at the leading edge of test model. Therefore there is no generation region for a square leading edge, and Regions L-A which is the region between the leading edge and the trailing edge and L-B which is the region behind the test model can be regarded as the vortex shedding region.

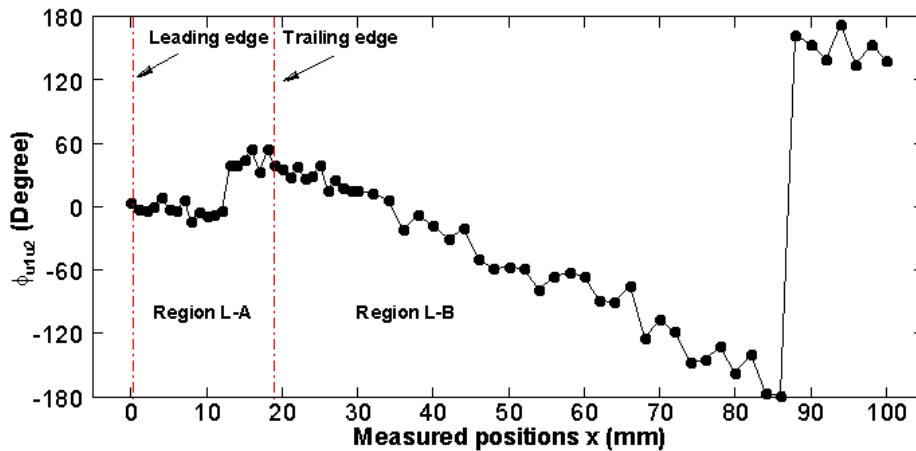


Figure 6-4 Phase relationship between hot-wire 1 and hot-wire 2 along $y=11\text{mm}$ for S-1 test model. Hot-wire 1 was located at $x=0\text{mm}$ and $y=11\text{mm}$, hot-wire 2 was move along the $y=11\text{mm}$ at different x positions.

The vortex shedding strength measured by hot wire 2 along $y=11\text{mm}$ was used to show the maximum magnitudes of E_{u_2} . The results were shown in Figure 6-5. It was found that the maximum magnitudes of E_{u_2} were small at the range $0 \leq x \leq 12\text{mm}$. When $x \geq 13\text{mm}$, the maximum magnitudes of E_{u_2} suddenly began to increase to a certain level as shown in the figure. This indicates that there was fully developed

vortex shedding for $x \geq 13\text{mm}$ and the vortex shedding was fully developed before the trailing edge.

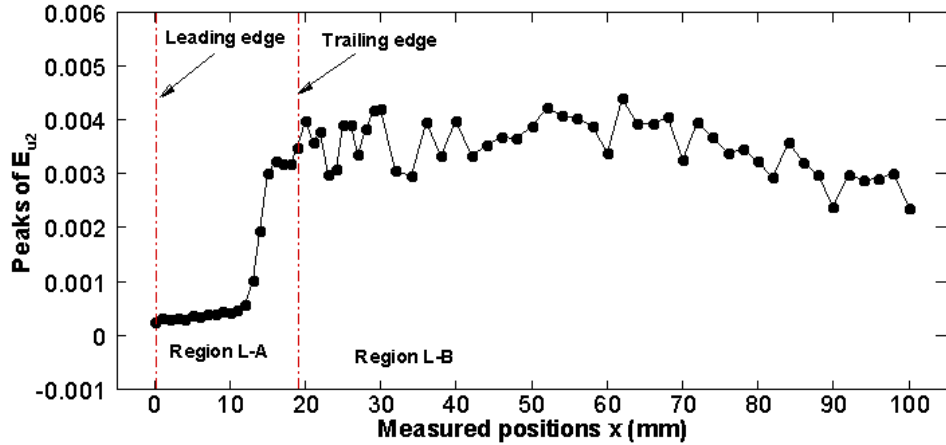


Figure 6-5 The strength of vortex shedding distribution along $y=11\text{mm}$ for S-1 test model. hot-wire 2 was moved along the $y=11\text{mm}$ at different x positions.

In conclusion, for a semi-circular leading edge there was only TEVS occurring in the system. The regions over the test model can be divided into generation region and the vortex shedding region, which have different flow characteristics. For a short square leading edge test model, there is only LEVS. The region around the test model is only the vortex shedding region. There is no generation region on the up surface of the test model, and the vortex shedding starts at the leading edge and then propagates downstream. Based on these observations, the optimal control strategy for test models with different leading edges can be investigated as follows.

6.3 Control performance of square leading edge test model

The semi-circular leading edge test model was used in Chapters 3 and 5. Before discussing the control strategy for various leading edges, the control performance of the square leading edge test model which contains the surface module was investigated. In this section, the test model S-1 and the downstream cavity DC-2 were used.

6.3.1 Optimal control parameters

Firstly, various measurements were conducted to investigate the optimal control voltage for the open loop control. The control frequency was set to $f_p = 30\text{Hz}$ and the result is shown in Figure 6-6. It was found that the optimal control voltage was 160V, and the best SPL reduction was 17.2dB inside the cavity and 14.9dB in the duct. Furthermore, it was found that the reduction was not obvious when $V_p \leq 120\text{V}$. However when $V_p > 120\text{V}$ the SPL reduction increased rapidly as control voltage increased. This phenomenon can be explained by the control mechanism which is different from the mechanisms for a semi-circular leading edge test model. The detail of this mechanism is described in Section 6.3.4.

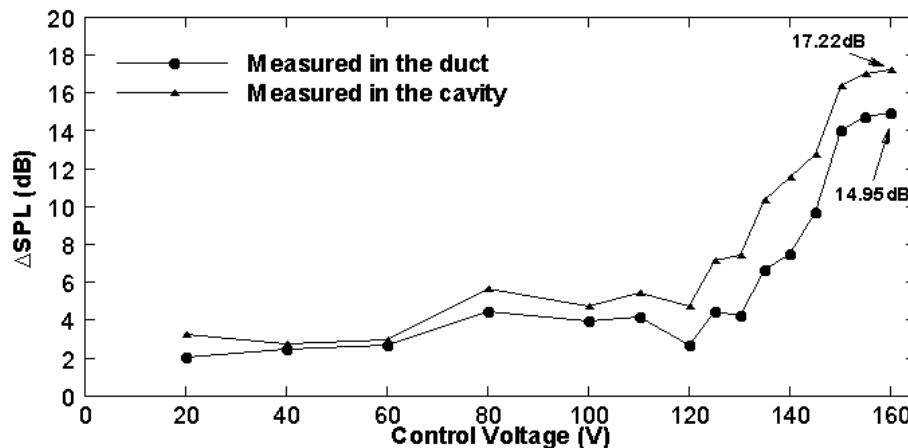


Figure 6-6 The control performance of different control voltages, open-loop control.

The determination for the optimal closed-loop control voltage could be performed by varying the magnitude of the modified feedback signal relative to the original feedback signal. The effect of varying the feedback control voltage of on noise reduction is shown in Figure 6-7. Microphones in the duct and cavity both recorded the same general trend of increasing noise reduction as the control voltage was increased. The maximum magnitude was limited by the maximum voltage allowable for THUNDER actuator, which were about 160V. The best control voltage was

$V_p = 155V$ when the control voltage was varied from 20V to 160V. The best noise reduction was 14.8dB in the duct, and 17.5dB inside the cavity.

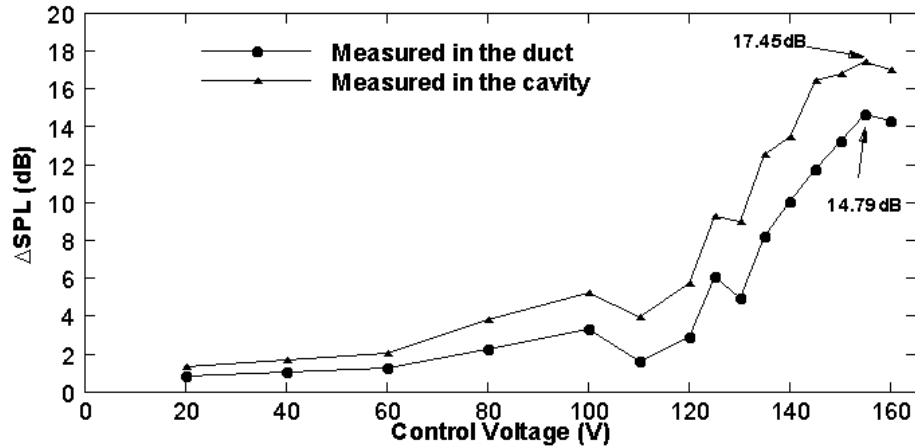


Figure 6-7 The control effect for different control voltages. The control signal was from hot wire 2 which was located at $x=30.0\text{mm}$, $y=11\text{mm}$.

Figure 6-8 shows the control performance when the phase delay of feedback signal was varied. The general trends of noise reduction measured by microphones in the cavity and duct were similar, indicating a consistent physical mechanism occurred in the system. The maximum performance occurred at the phase of approximately 288 degrees, in which the obtained noise reduction was 16.7 dB in the duct and 18.5dB inside the cavity. Therefore, there was an optimal phase delay relative to the feedback signal that could be used in closed-loop control for obtaining an effective noise reduction in the cavity and duct.

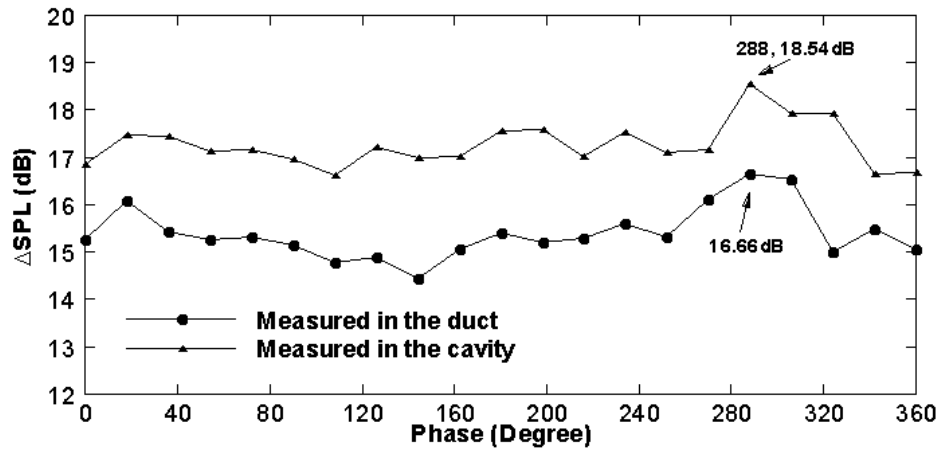


Figure 6-8. The closed-loop control performance for varying phases. The feedback signal was obtained from the hot-wire 2 located at $x=30.0\text{mm}$, $y=11\text{mm}$. the control voltage is 155V.

6.3.2 The control performance of closed-loop control

Using the optimal control voltage and phase delay, the best control performance of closed-loop control was evaluated in the sound field and flow field. Figures 6-9 (a) and 6-9 (b) show the sound pressure spectra obtained from the Fast Fourier Transform (FFT) of time domain signals with a frequency resolution of 0.1 Hz. It can be seen that, upon deployment of active control, the sound pressures in the duct and the cavity underwent significant reductions. The Sound Pressure Level (SPL) spectra indicated that with control, the SPL in the duct decreased from 92.2dB to 75.6 dB (a reduction of 16.6 dB) at the vortex shedding frequency. Meanwhile, the SPL measured inside the cavity decreased from 105.4 dB to 86.9 dB (a reduction of 18.5 dB), which was larger than the noise reduction measured in the duct. The experimental results showed that the active control in the sound field was effective.

6. The investigation of control strategy

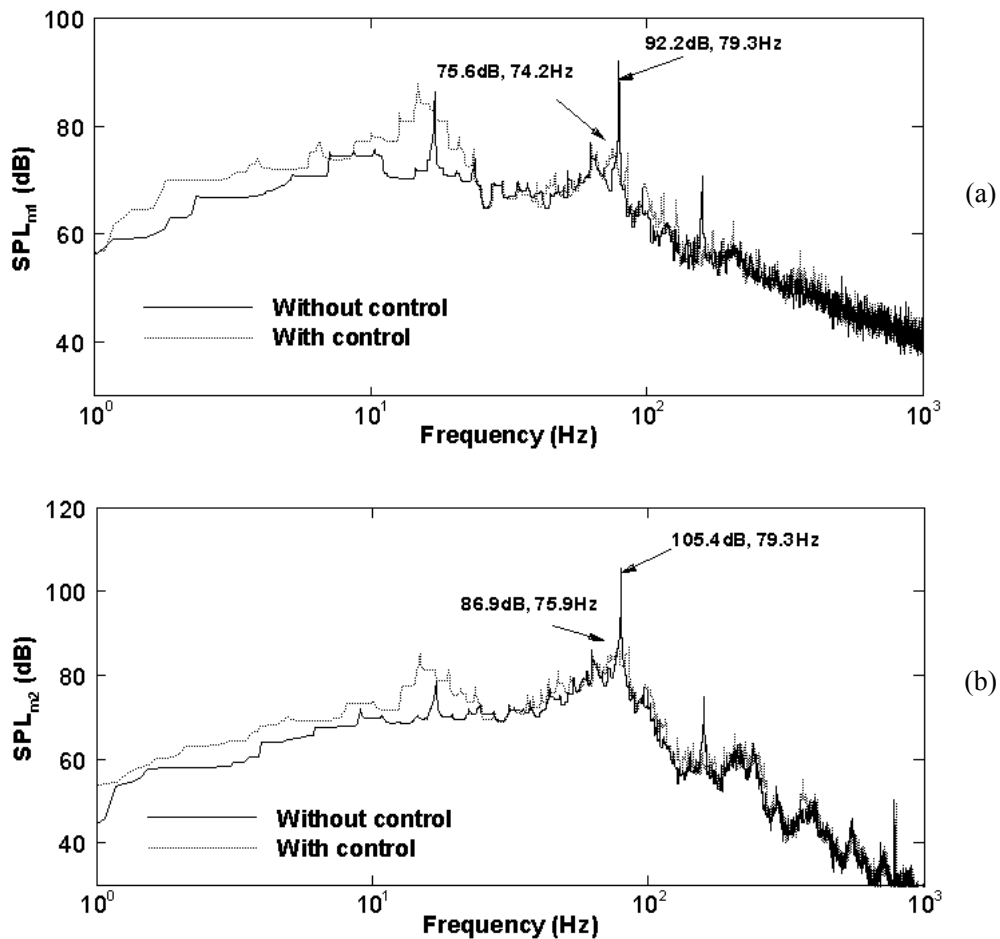


Figure 6-9 The best control performance in frequency-domain. (a) Measured in the duct; (b) Measured inside the cavity.

In the flow field, the control performance was investigated in terms of power spectra density of flow velocity Eu measured by two hot wires, located at $x=0$ mm, $y=11$ mm and $x=30$ mm, $y=11$ mm, as shown in Figures 6-10(a) and 6-10(b). From the figures, it can be seen that Eu has decreased from 1.7×10^{-3} to 2.7×10^{-4} (a reduction of about 84.3%) at hot-wire 1 and 2.2×10^{-2} to 2.9×10^{-3} (a reduction of about 87.1%) at hot-wire 2. The results show that the control in the flow field was also effective in reducing the flow velocity levels.

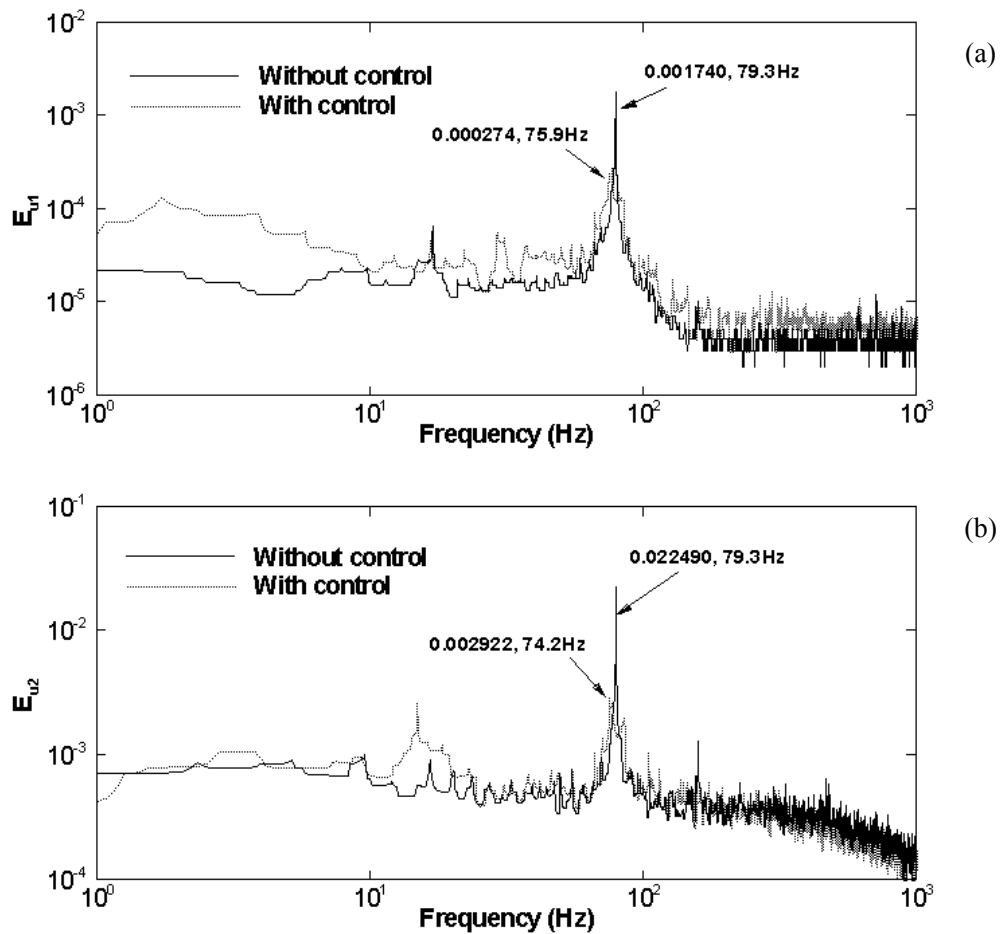


Figure 6-10 The best control performance in frequency-domain. (a) Measured by hot wire 1 at $x=0\text{mm}$, $y=11\text{mm}$; (b) Measured by hot-wire 2 at $x=30\text{mm}$; $y=11\text{mm}$.

The control performance in time-domain was shown in Figures 6-11 and 6-12. The signals were filtered by a 5-Hz band-pass filter around the vortex shedding frequency. Under control actuation, the noise and flow velocity reductions were clearly observed in all four sensors, indicating that the vortex shedding was disturbed by the control.

6. The investigation of control strategy

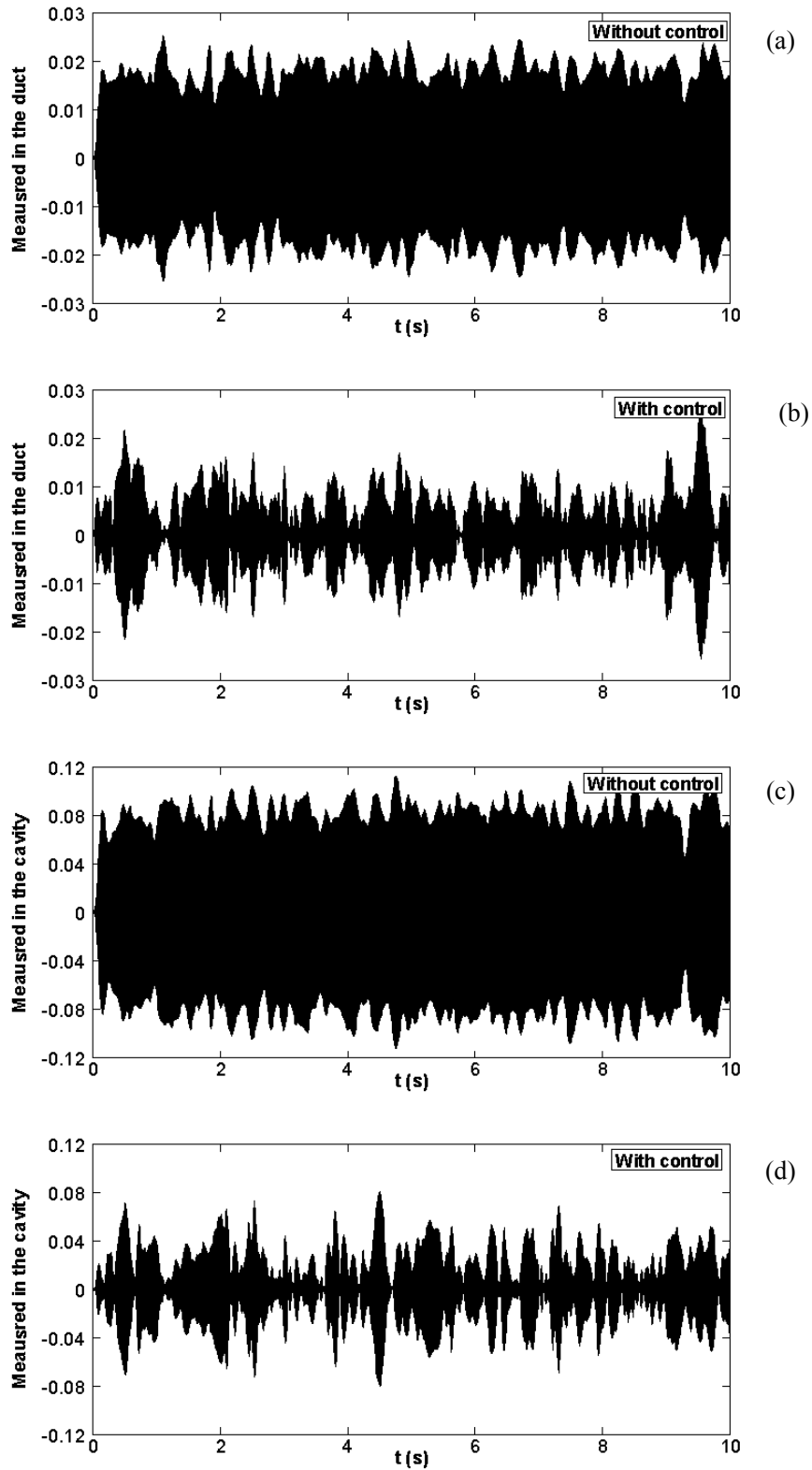


Figure 6-11. Time-domain results for the control performance in sound field; the signals are filtered by a 5Hz-band filter. a) Without control, measured in the duct; b) With control, measured in the duct; c) Without control, measured inside the cavity; d) With control, measured inside the cavity.

6. The investigation of control strategy

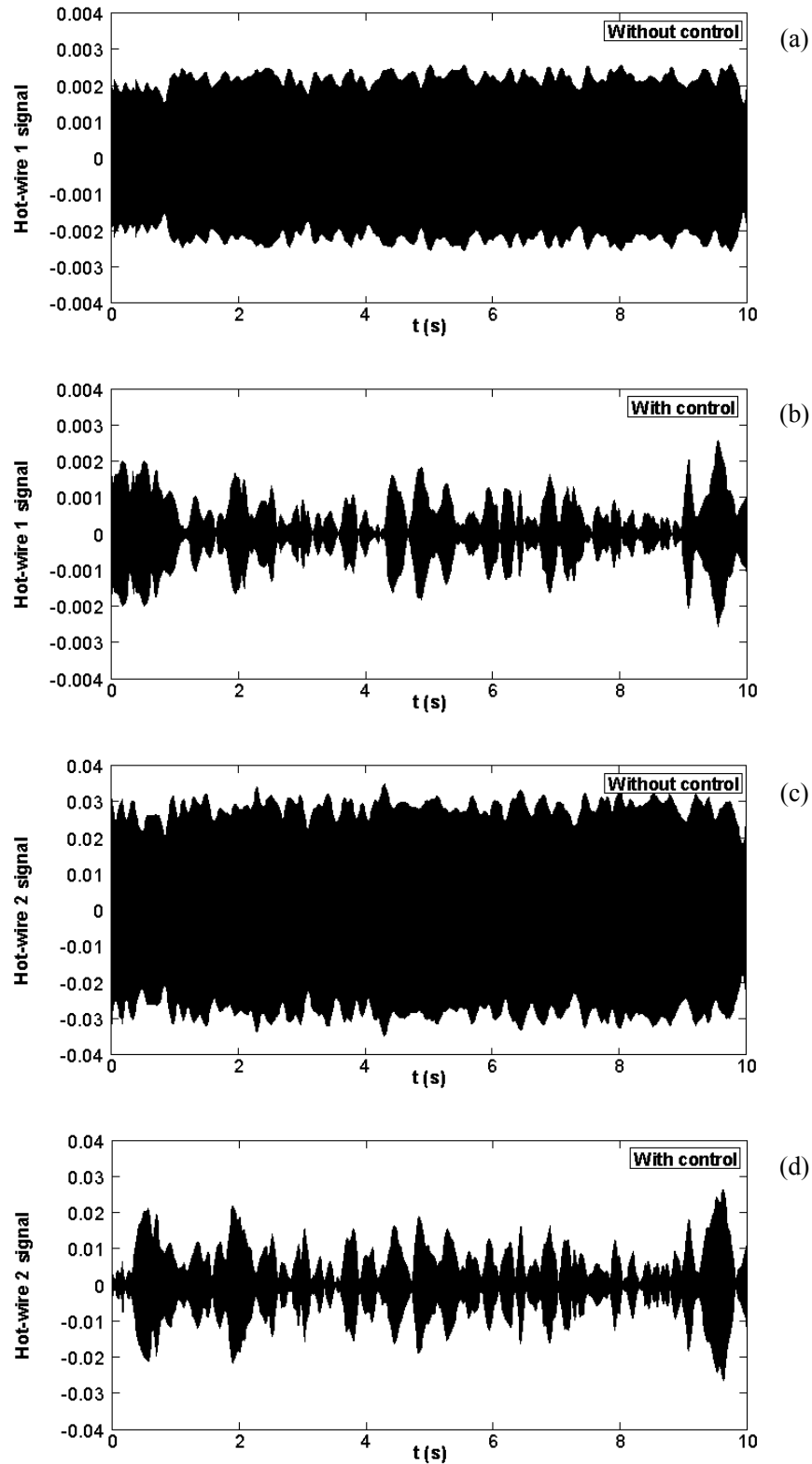


Figure 6-12. Time-domain results for the control performance in flow field; the signals are filtered by a 5Hz-band filter. a) Without control, measured by hot wire 1 at $x=0\text{mm}$, $y=11\text{mm}$; b) With control, measured by hot wire 1 at $x=0\text{mm}$, $y=11\text{mm}$; c) Without control, measured by hot wire 2 at $x=30\text{mm}$, $y=11\text{mm}$; d) With control, measured by hot wire 2 at $x=30\text{mm}$, $y=11\text{mm}$.

6.3.3 The frequency shift and its analysis

Similar frequency shift phenomenon has also been observed in the present study. Compared with semi-circular leading edge case, no significant differences were found. Therefore, the results were not shown in this section.

6.3.4 Vortex abatement mechanism for a square leading edge test model

In Chapter 3, two mechanisms were developed for explaining the abatement mechanism for a semi-circular leading edge test model. Since there is no generation region on the up surface of a square leading edge test model, these two mechanisms are not suitable for explaining the abatement mechanism for a square leading edge test model. From Figures 6-6 and 6-7, it was found that the reduction increased slowly when the perturbation was small. When the control voltage exceeded 120V ($d_{pm} = 0.78\text{mm}$), the reduction increased rapidly, which was different from the results of semi-circular leading edge test model. The results shown in Figure 6-13 indicate that displacement of the vibration plate linearly increased as the control voltage was increased during the measurements.

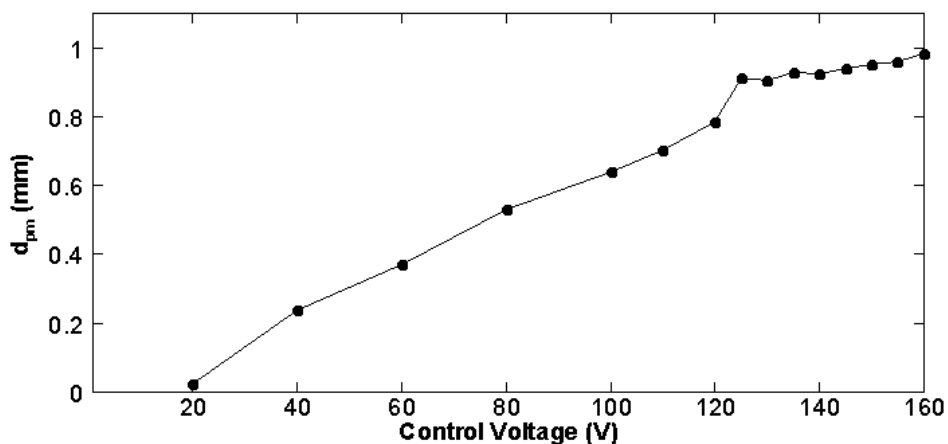


Figure 6-13 The maximum perturbation displacement of the vibration plate.

At low control voltages, the SPL reduction was relatively small, typically about

2dB, when control voltage is equal to 120V. This can be explained by a small level of vertical velocity perturbation generated by the vibration plate. The surface perturbation was not large enough to affect the fully developed vortex shedding.

Typical LEVS of a short square leading edge test model is shown in Figure 6-14. The path of the vortex shedding is shown in the figure. It shows that the vortex shedding was not attached to the surface of the test model. The path of it is some distance away from the surface of the test model. When the perturbation is small, the displacement is smaller than d_{pm1} , the vertical velocity generated by the vibration plate is small, and the influences on the LEVS is not notable. While the displacement of the vibration plate is larger than d_{pm1} , the vertical velocity generated by the vibration plate is strong enough to disturb the vortex shedding especially the initial part of the vortex shedding near the leading edge which can be more easily effected by the vibration plate, and then prevent the vortex shedding propagates to the downstream. Furthermore, the edge of the vibration plate can act as another separate point for shifted shedding frequency vortex shedding to some extent, all these actions disturb the normal propagation process of the LEVS and then result in a rapid increase of reduction measured in the duct and inside the cavity. This mechanism can be used to explain the strength abasement of LEVS for the square leading edge test model. In the present study, d_{pm1} is 0.78mm and it is about $\frac{0.78}{11} * 100\% = 7.0\%$ of the thickness of the test model.

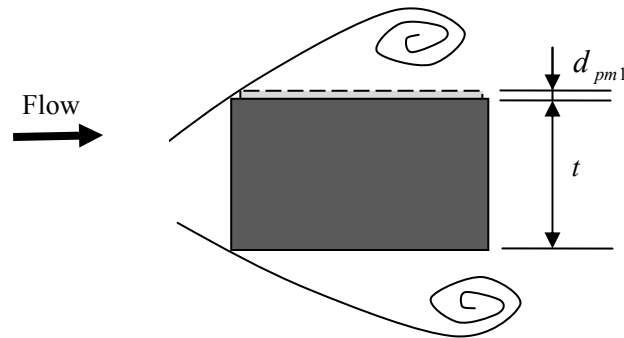


Figure 6-14 The illustration of the abasement mechanism for short square leading edge test model.

Therefore, the vortex strength abasement mechanism of vortex shedding was discussed based on the characteristic of LEVS for the short square leading edge test model. The control action was applied to the vortex shedding region of the square leading edge test model. The control mechanism was different from that for semi-circular leading edge test model. The path of the LEVS started from the leading edge and then propagated the downstream. When applying control on the test model, the vertical velocity generated by the vibration plate play a key role for the vortex strength reduction. However, the initial part of the vortex shedding is more easy to be effected when the displacement of the vibration plate exceed some value.

6.4 Effective perturbation position for various leading edges

The previous experiment utilized a vibration plate that almost covered the entire up surface of test model. In practice, only a part of the surface on the test model may be used for surface perturbation. So the effective surface perturbation positions for both the square and semi-circular leading edges need to be carefully investigated. Such an investigation will provide insights into how an optimal control strategy can be implemented for test models with different leading edges.

6.4.1 The semi-circular leading edge

The control strategy on the vortex generation region was investigated using the

semi-circular leading edge test model. The diagram of the test model is shown in Figure 6-15; a 3mm-vibration-plate was installed on the up surface of the test model which only covered 13% of the entire up surface area of test model. As mentioned in Chapter 1, the separation point for the semi-circular leading edge test model is at the apex of circular. As shown in Figure 6-15(a), the 3mm-vibration-plate was installed 6mm away from the leading edge (0.5mm away from the separation point), but 14mm away from the trailing edge which had been classified as C-3-1 in Chapter 2. In Figure 6-15(b), the 3mm-vibration-plate was installed 1mm away from the trailing edge but 19mm away from the leading edge (14.5mm away from the separation point) which had been classified as C-3-2 in Chapter 2. These two positions shown in Figure 6-15 are the two important positions in the vortex generation region which are related to the initial stability of shear layer and the generation of the TEVS. The results of investigating these two positions would help to understand the underlying control mechanism and the optimal surface perturbation position.

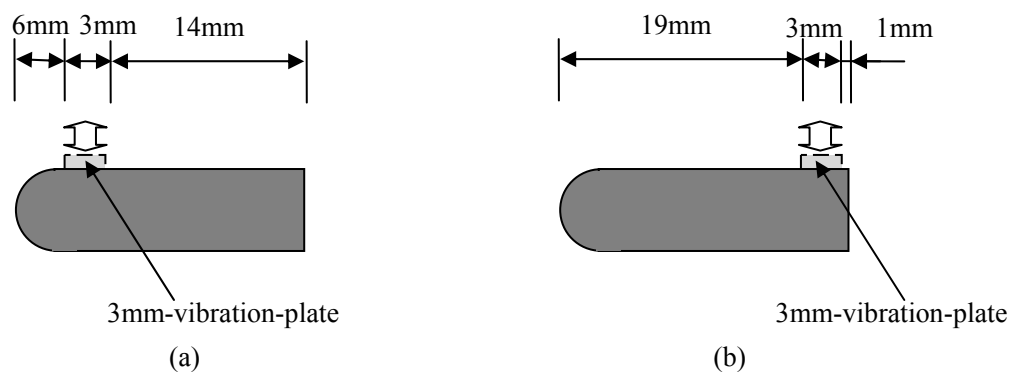


Figure 6-15 The sketch of the 3mm-vibration-plate semi-circular leading edge test model (a) C-3-1; (b) C-3-2.

Various measurements were conducted by using a sinusoidal signal at a frequency of $f_p = 30\text{Hz}$ using an open-loop control scheme. The reductions measured in the duct by increasing the control voltages are shown in Figure 6-16. It was found that the control action on these two positions were both effective in reducing the noise in the

duct. The best control performance of 10.0dB for the case of C-3-1 and 5.5dB for the case C-3-2 were achieved (The control performance of 16mm-vibration-plate shown in Chapter 3 was 16.29dB as measured in the duct). From the results, it is clear that the control performance for the case when the perturbation was near the leading edge is better than the case that the perturbation position was near the trailing edge.

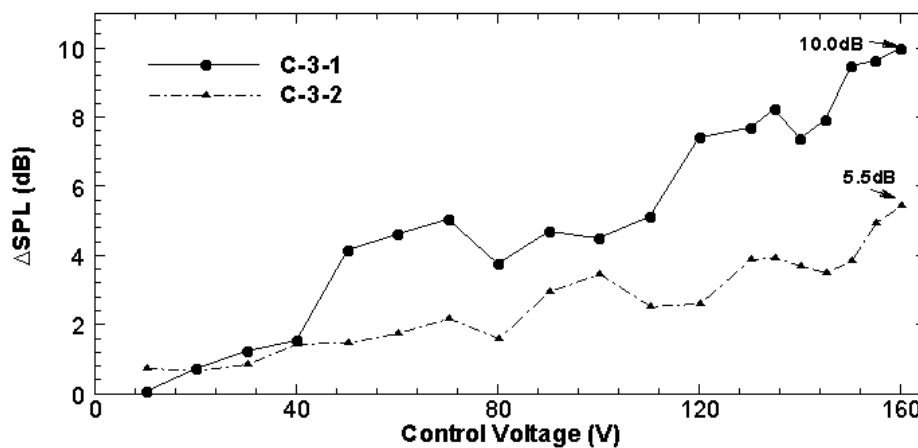


Figure 6-16 The control performance of different perturbation positions for semi-circular leading edge test model.

As described in Figure 6-2, it was found that in the vortex generation region for the semi-circular leading edge test model, although there was no fully developed vortex shedding, the pressure pulse was the key factor for the generation of the vortex shedding. It exists in this region and its strength increases when it goes away from the leading edge to the trailing edge which was shown in Figure 6-2, The averaged value of the maximum magnitudes of E_{u_2} from 6mm to 9mm was 1.9×10^{-4} for C-3-1 case and 5.3×10^{-4} from 19mm to 22mm for C-3-2 case. When applying the perturbation on the surface of the test model, the small perturbation generated by the vibration plate would disturb the pressure pulse on the surface of the test model in this vortex generation region. In general, the pressure pulse near the leading edge is still weak because the vortex is not fully developed. Thus, a smaller level of surface perturbation is already sufficient to disturb the pressure pulse that will further disturb

the development of vortex shedding downstream.

Therefore, it is beneficial to locate the surface perturbation near the semi circular leading edge. Although the surface perturbation only covered 13% of the up surface of test model, the configuration can be used to achieve 10dB SPL reduction in the duct. This is compared to 16.3dB SPL reduction achieved using the surface perturbation that covered 100% of the up surface.

In conclusion, when applying surface perturbation technique on a semi-circular leading edge test model, the control action should mainly occur within the vortex generation region for the TEVS. The optimal control strategy is to apply the surface perturbation on the weaker region for the pressure pulse, which is also the position near the leading edge of test model. In this position, an effective noise reduction can be achieved by using a relatively small surface perturbation with a low control voltage.

6.4.2 The square leading edge

The diagram of square leading edge test model is shown in Figure 6-17. A 3mm-vibration-plate was installed on the up surface of the test model which was only 16% of the whole surface. In Figure 6-17(a), the 3mm-vibration-plate was installed 1mm away from the leading edge, but 15mm away from the trailing edge, which had been classified as S-2-1 in Chapter 2. In Figure 6-17(b), the 3mm-vibration-plate was installed 1mm away from the trailing edge but 15mm away from the leading edge, which had been classified as S-2-2 in Chapter 2. Taking LEVS generated by the short square leading edge test model into account, these two perturbation positions were in the vortex shedding region for the square leading edge test model. The vibration plate in S-2-1 was near the path of LEVS so the applied perturbation could better influence the path for LEVS. The vibration plate in S-2-2 was some distance away from LEVS,

the influence of the surface perturbation brought on the vortex shedding was mainly due to the vertical velocity generated by the vibration plate.

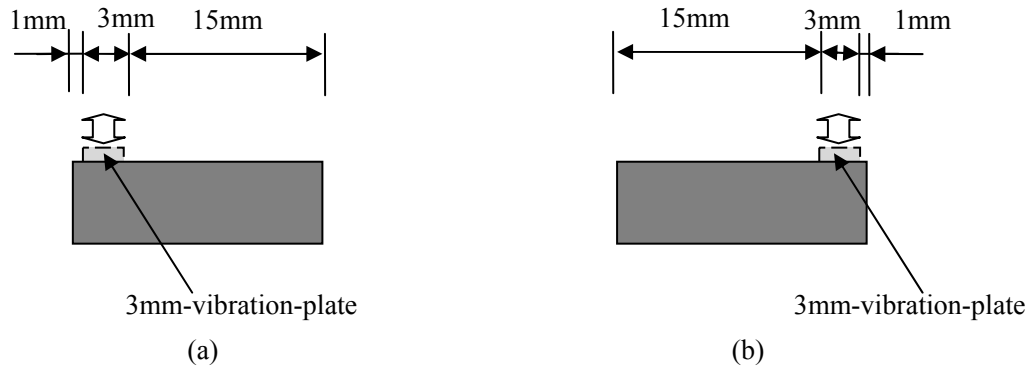


Figure 6-17 The sketch of the 3mm-vibration-plate square leading edge test model (a) S-2-1; (b) S-2-2.

Various measurements were conducted by using a sinusoidal signal with a frequency of $f_p = 30\text{Hz}$ in an open-loop control scheme. The reductions measured in the duct are shown in Figure 6-18 by varying control voltages. The best SPL reduction for S-2-1 was 12.0dB at $V_p = 160\text{V}$ and the corresponding SPL reduction for S-2-2 at $V_p = 160\text{V}$ was 1.2dB (A 16mm-vibration-plate was used in Section 6.3 and the best SPL reduction measured in the duct was 14.9dB). Therefore the control was only effective when the perturbation was applied near the leading edge of the test model.

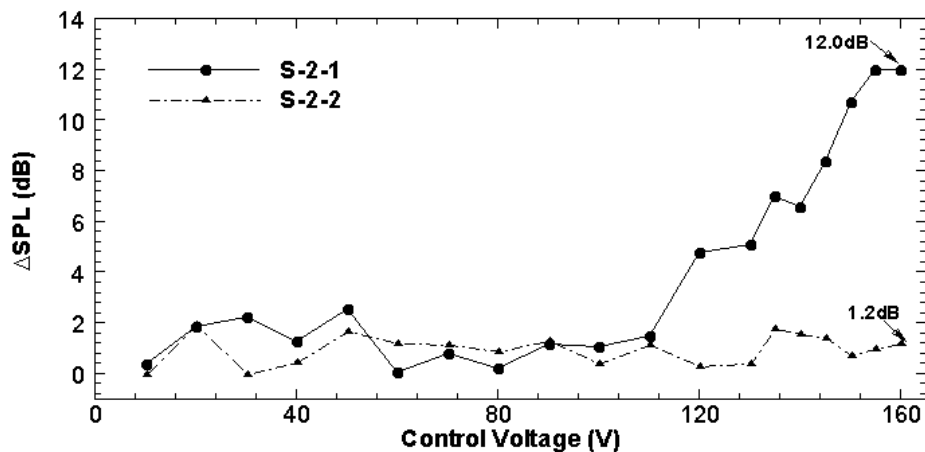


Figure 6-18 The control performance of different perturbation positions for square leading edge test model.

When the perturbation was applied near the trailing edge, the vortex shedding had already fully developed and stable at some distance away from the surface of the test model. The small surface perturbation generated by the vibration plate in the study could not directly affect the vortex shedding but influenced it via the vertical velocity generated by the vibration plate. The vertical velocity was much smaller than flow velocity contained in the vortex shedding, so the vertical velocity perturbation could only disturb the vortex shedding strength by a small amount.

When the surface perturbation technique was applied near the leading edge of the test model, the surface perturbation could better influence the path of LEVS. As it had been explained in Section 6.3.4, It is more easily to disturb the vortex shedding when the vibration plate is near the propagation path of the vortex shedding. Therefore, the effective position for the square leading edge is the perturbation arranged near the leading edge so that the perturbation can directly truncate the path of LEVS. In the present case, the vibration plate could better influence the vortex shedding when control voltage was larger than 110V. Using only 16% of the vibration surface, such a control configuration could achieve a 12dB SPL reduction measured in the duct, in contrast to a 14.9dB SPL reduction using 100% of vibration surface.

In conclusion, when applying the surface perturbation technique on the square leading edge test model, the control action is mainly within the vortex shedding region for LEVS. The optimal control strategy is to apply the perturbation near the path of the LEVS which is also the position near the leading edge of the test model. In this position, an effective vortex strength and noise reduction can be achieved.

In summary, although the effective perturbation positions for semi-circular and square leading edges are both located near the leading edge of the test models, the control strategies are completely different due to the different vortex characteristics of

these two leading edges. For a semi-circular leading edge test model, the control action of the surface perturbation mainly takes effect in the vortex generation region. Although the surface perturbation can be located anywhere within this region, the optimal control strategy is to arrange the perturbation at the position near the leading edge where the pressure pulse is smallest. This way, an effective vortex strength and noise reduction can be achieved simply by using a narrow vibration plate and a low control voltage.

In contrast, for a square leading edge test model, the control action of the surface perturbation is mainly in the vortex shedding region. The vertical velocity is relatively small compared with the strength of the vortex shedding. So it can only obtain a small amount of reduction measured in the duct. The optimal control strategy is to arrange the vibration plate near the path of LEVS and then the surface perturbation can better disturb the path of LEVS for achieving vortex strength abatement. This control strategy can also be applied in the vortex shedding region of the semi-circular leading edge test model. Other leading edge types can be regarded as the combination of the basic semi-circular and square leading edges, therefore the control strategies can be the combination of these two control strategies.

6.5 The verification of pressure pulse

Hourigan[115] found that for semi-circular leading edge bluff bodies, the pressure pulse played a key factor for the generation of the vortex shedding and it existed between the leading edge and the trailing edge. It has the characteristic of directivity, and since the pressure pulse is acting as an information carrier for the vortex shedding generation, it has the same frequency as the vortex shedding. The pressure pulse is very important for the optimal control strategy of the semi-circular leading edge test model. However, there are three things need to be identified. (1) The existence of the

pressure pulse between the leading edge and the trailing edge; (2) The corresponding relationship between the pressure pulse with trailing edge vortex shedding, without control and with control. Based on these two aspects, the characteristic of the pressure pulse and its function in the control mechanism needs to be discussed. (3) The characteristic of the pressure pulse which can benefit the control.

6.5.1 The existence of the pressure pulse

For the semi-circular leading edge test model, there is no vortex shedding in the generation region between the leading edge and the trailing edge. The TEVS behind the trailing edge cannot propagate to the upstream. Therefore, the flow measurement in the vortex generation region can provide a way to identify the existence of pressure pulse in this region.

Measurements were done to identify the pressure pulse in flow field. The maximum magnitudes of E_{u_2} at the vortex shedding frequency f_s measured by hot wire 2 between the leading edge and trailing edge are shown in Figure 6-19. It can be seen that between the leading edge and trailing edge, the maximum magnitudes of $E_{u_2} > 0$ at the vortex shedding frequency. As mentioned in Chapter 1, there was no vortex shedding between the leading edge and the trailing edge. Therefore, the maximum magnitudes of E_{u_2} at the vortex shedding frequency f_s shown in Figure 6-19 could only be caused by the pressure pulse between the leading edge and trailing edge. From 0mm to 16mm, the value of maximum magnitude of E_{u_2} was about 0.0002, while for $x > 16$ mm, the magnitude increased rapidly to 0.001, although it was still much smaller than the maximum magnitude of E_{u_2} measured in the strongest vortex shedding region. When open-loop control was implemented, the maximum magnitude of E_{u_2} decreased significantly as shown in Figure 6-19. The results

indicates that the small local surface perturbation could reduce the pressure pulse on the up surface of the test model and then influence the vortex shedding generation, which is the principle of the ‘pressure disturbance mechanism’.

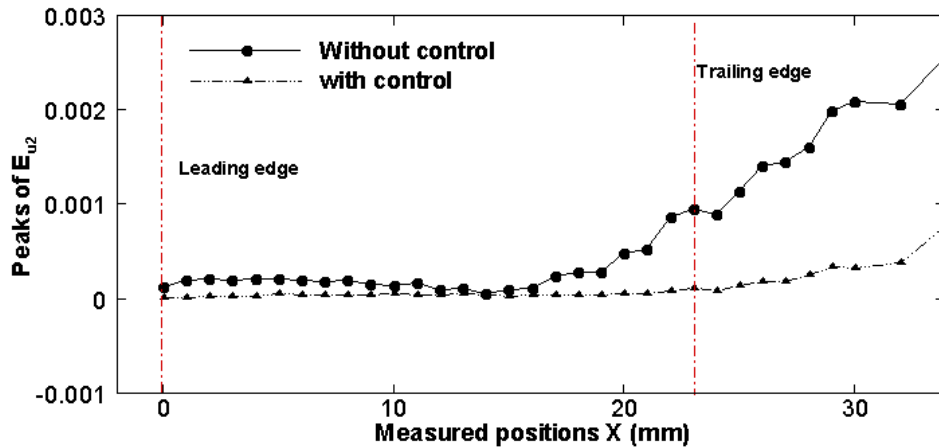


Figure 6-19 The maximum magnitudes of E_{u_2} measured by hot wire 2 between the leading edge and trailing edge.

In this study, the surface perturbation was applied between the leading edge and the trailing edge with the aim to reduce the pressure pulse over the up surface of test model. After control, the maximum magnitudes of E_{u_2} measured over the test model and downstream its trailing edge has both decreased. The results indicate that the pressure pulse in the vortex generation region may have a direct relationship with the vortex shedding downstream the trailing edge. Thus, when the pressure pulse is damaged, the corresponding vortex shedding will be damaged too. The pressure pulse plays a key factor for the generation of TEVS and the pressure pulse is relatively small compared with the vortex shedding as observed from the experiment. Therefore, the development of optimal control strategy for the semi-circular leading edge test model can be focused on the vortex generation region which contains the pressure pulse.

6.5.2 The directivity characteristic of the pressure pulse

The pressure pulse acts as information containers between the shear layer in the leading edge and the TEVS behind the trailing edge, so that the directivity of the pressure pulse is one of the important characteristics which ensure the information can be exactly sent and received. The pressure pulse can be measured by the hot wire; it is not the pure sound pressure. However, it can be regarded as a velocity pulse along the up surface of test model and the frequency of this pulse is around the vortex shedding frequency, which is far away from the background flow noise in the present system.

The general equation for sound pressure of vortex shedding which comes the downstream vortex shedding region can be expressed as $S(\omega t + \phi_1)$ which has the characteristic of no-directivity and can propagated in all directions in the duct. The general equation of pressure pulse can be expressed as $U_p(\omega t + \phi_2)$. It is assumed that the pressure pulse has the characteristic of directivity from the trailing edge to the leading edge or from the leading edge to the trailing edge. The sound pressure generated by the vortex shedding at the same measured position in the duct can be regarded as the same. By using these characteristics and assumption, a ‘modified two microphones method’ can be used to identify the directivity of the pressure pulse and its change during the control action.

The sketch of the ‘modified two microphones method’ is shown in Figure 6-20. Two microphones, Mic.3 and Mic.4, were used to measure the pressure (sound pressure and the pressure pulse in flow field) which were installed in the wall of the duct and just within the range of the leading edge and trailing edge. Two tubes, Tube A and Tube B, were used to guide in the pressure at the measured point around the test model. Tube A, is an L-tube and the nozzle of the tube parallels with the assumed direction of pressure pulse which is pointing from the trailing edge to the leading edge

of the test model. It can measure most parts of the pressure pulse. If Tube B is a straight tube and the nozzle of the tube is vertical with the assumed direction of pressure pulse, the tube can only measure a small level of pressure pulse. The position of the nozzles for both tube A and tube B are at the same distance away from leading edge to ensure they can obtain the same sound pressure of vortex shedding.

In tube A, the measured signal can be expressed as

$$f_A(t) = S(\omega t + \phi_1) + \eta_1 U_p(\omega t + \phi_2) \quad (6-1)$$

In tube B, the measured signal can be expressed as

$$f_B(t) = S(\omega t + \phi_1) + \eta_2 U_p(\omega t + \phi_2) \quad (6-2)$$

In general, there are two possibilities for the value of η_1 and η_2 . If the pressure pulse does not have directivity characteristic, $\eta_1 \approx \eta_2$; If the pressure pulse has directivity characteristic, $\eta_1 \approx 1 \gg \eta_2 \approx 0$. When applying control action, the pressure pulse and vortex shedding are reduced, and the remain pressure is about $\varepsilon\%$ of the original strength. The strength reduction measured in tube A and tube B can be expressed as

$$\Delta f_A(t) = (1 - \varepsilon)S(\omega t + \phi_1) + (1 - \varepsilon)\eta_1 U_p(\omega t + \phi_2) \quad (6-3)$$

$$\Delta f_B(t) = (1 - \varepsilon)S(\omega t + \phi_1) + (1 - \varepsilon)\eta_2 U_p(\omega t + \phi_2) \quad (6-4)$$

$$\Delta f(t) = \Delta f_A(t) - \Delta f_B(t) = (1 - \varepsilon)(\eta_1 - \eta_2)U_p(\omega t + \phi_2) \quad (6-5)$$

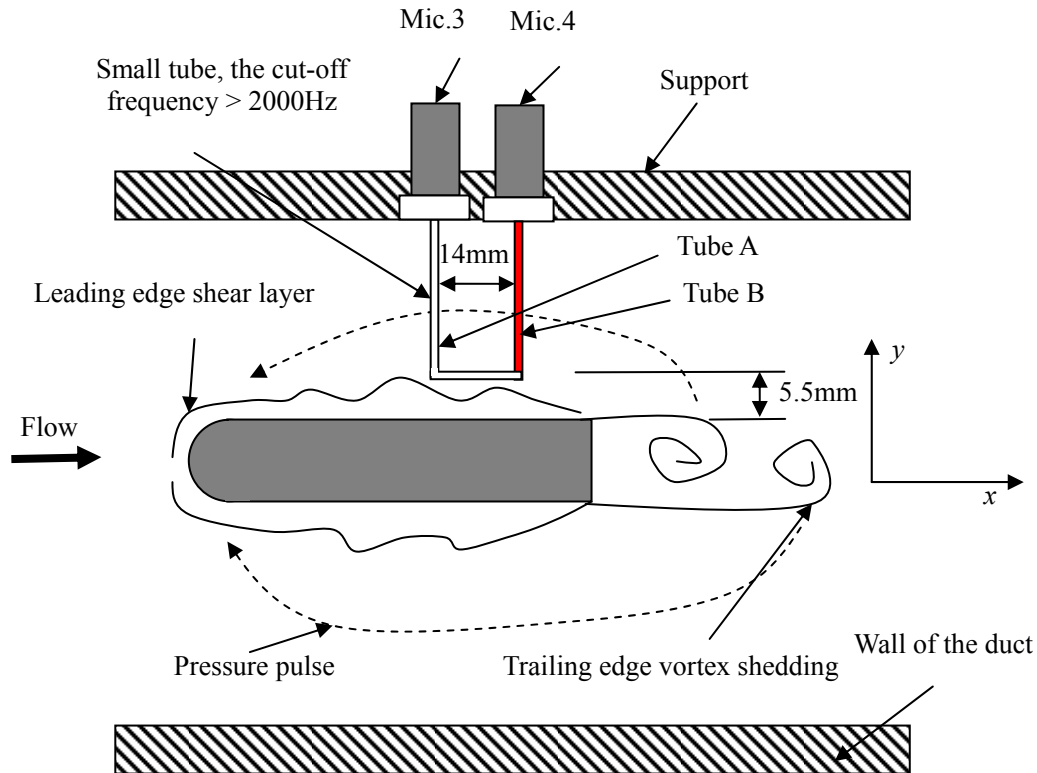


Figure 6-20 The sketch of the ‘modified two microphones method’, tube A is used to measure the pressure pulse from the trailing edge to leading edge.

If there is no directivity characteristic for the pressure pulse, then $\eta_1 \approx \eta_2$, $\Delta f(t) \approx 0$. It indicates that the reductions measured in tube A and tube B are almost the same. If the pressure pulse has directivity characteristic, $\eta_1 \approx 1 \gg \eta_2 \approx 0$, $\Delta f(t) \approx (1 - \varepsilon)U_p(\omega t + \phi_2) > 0$. This indicates that there is more reduction measured in the tube A than that in tube B. Based on these analysis, it is possible to identify the directivity characteristic of the pressure pulse.

Various measurements were conducted by using the system shown in Figure 6-20. The results are shown in Figure 6-21. It was found that the reduction measured in the tube A was larger than that measured in the tube B when $V_p > 70V$. The reduction of vortex shedding strength was 15.7dB when $V_p = 160V$, as measured in tube B in an open-loop control scheme. Further, there was another 2.5dB reduction of the pressure pulse measured in the tube A. It indicates the pressure pulse has directivity

characteristic.

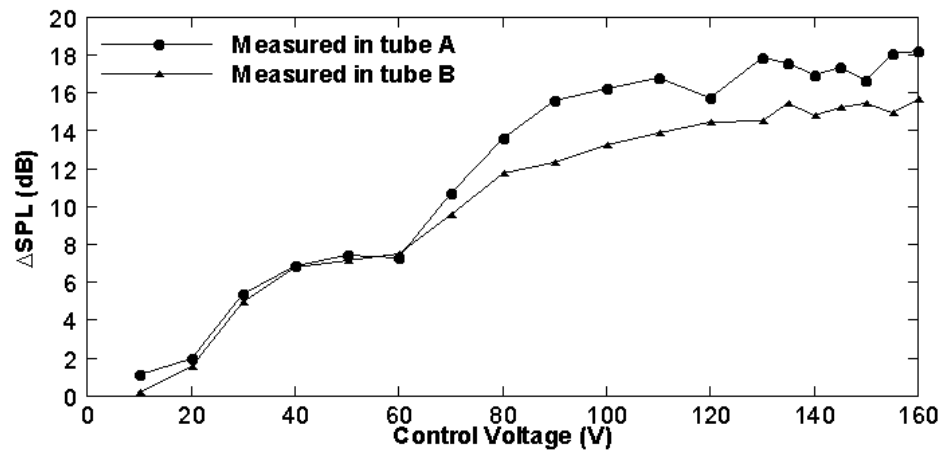


Figure 6-21 The comparison of the reduction between tube A and tube B. tube A is used to measure the pressure pulse from the trailing edge to leading edge.

Directivity characteristic is one of the important characteristic of the pressure pulse, it play an important role in the generation of the vortex shedding. In the control strategy scheme, this characteristic is also a very important issue to be investigated. The TEVS are generated periodically by the assistance of the pressure pulse, and the pressure pulse has directivity characteristic which has been identified. When applying the surface perturbation on the surface of the test model, the disturbance and the weak pressure pulse are one part of the control mechanism. Another part of the control mechanism is that the vertical velocity disturbance can change the direction of the pressure pulse and then influence the generation of the vortex shedding as illustrated in Figure 6-22. This is the primary reason why it is relatively easy to apply the surface perturbation technique in the vortex generation region to influence the vortex shedding process.

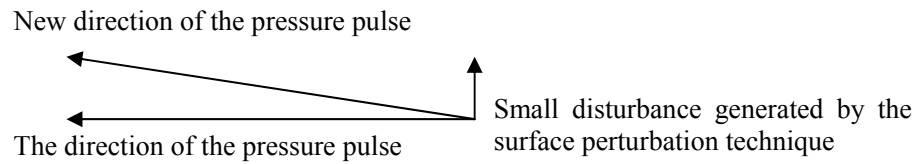


Figure 6-22 The sketch for changing the direction of the pressure pulse.

Furthermore, the direction of the perturbation should be vertical relative to the direction of pressure pulse to ensure an effective control performance.

6.6 The implementation of control strategy

Based on the investigations described in this chapter, the control strategy for semi-circular and square leading edges can be summarized as follows.

Firstly, one needs to identify the vortex shedding types for the bluff body depending on its leading edge type. There are generally two typical types of vortex shedding: LEVS and TEVS. In general, there exists the vortex generation region and vortex shedding region for TEVS. In the vortex generation region, there is only the pressure pulse which is the key factor for generation of the TEVS. In this case, the pressure pulse is relatively weak and it has exhibits strong directivity. Therefore, it is better to place the surface perturbation in the vortex generation region for effective control. In the case of LEVS, Vortex shedding starts at the leading edge of the bluff body, so there is only the vortex shedding region and no vortex generation region. Since the vortex shedding can be relatively strong and the vertical velocity generated by the vibration plate may not be sufficiently large to influence the vortex shedding, the optimal control strategy is to apply the perturbation near the path of the vortex shedding. This way, the truncation of the path for vortex shedding can decrease the strength of the vortex shedding.

Secondly, one also needs to identify the installation position and the area of the

vibration plate for generating the surface perturbation. In general, the area of vibration plate should be as large as possible for the semi-circular leading edge test model, and it should be installed in the vortex generation region. This way, the surface perturbation can effectively affect the pressure pulse in this region, which can lead to more significant reduction of vortex shedding strength. For a square leading edge test model, it is not necessarily to use a large perturbation area, since a small area of vibration plate should be enough to bring the perturbation effect on the LEVS.

Thirdly, due to the directivity characteristic of the pressure pulse in the generation region, the direction of the perturbation should be vertical relative to the direction of the pressure pulse.

6.7 Conclusions

A general control strategy to control the vortex shedding using the surface perturbation technique has been proposed. Two basic leading edge geometries for bluff bodies were investigated in this Chapter. It was found that the vortex shedding types were the main factor for considering the control strategy. Based on the characteristics of these two vortex shedding types, the perturbation position and its control mechanism were studied.

7. Conclusions

7.1 General conclusions

Active control of flow-induced acoustic resonance has been experimentally investigated by using a novel surface perturbation technique. The whole work underwent five parts:

1) Based on a low-order model for the vortex shedding behind a vibrating bluff body, the novel surface perturbation technique, developed by Cheng *et al* [97], was used and interpreted to actively control vortex shedding and flow-induced acoustic resonance. This novel technique was primarily used to generate a controllable transverse motion on a structural surface using embedded piezo-ceramic actuators to alter the fluid-structure interaction for suppressing the vortex shedding and the corresponding acoustical resonance. Various test models for implementing this novel surface perturbation technique were designed. The experimental setup, major experimental facilities and platform, as well as the control strategy were developed for intensive investigation.

2) Open-loop control tests were first carried out. Control results had shown that this method was an effective control method for vortex-induced acoustic resonance problems. It was also found that the control strategy could not only weaken the strength of the vortex, but also changed the shedding frequency, which subsequently suppressed the acoustic resonance phenomenon.

3) Due to the difficulties in using a high-frequency control signal to excite the THUNDER actuators, a downsampling theory, which utilized the aliasing phenomenon and the Nyquist–Shannon sampling theorem, have been developed to down-sample a high-frequency original signal (feedback signal) to a low-frequency

output signal (the modified feedback signal). The downsampling process was implemented in the Simulink/dSPACE platform by using the Zero-Order Hold, Rate Transition and Band-pass filter modules. The modified feedback signal was supposed to contain all the necessary phase, frequency and magnitude information for effective control, as those in the feedback signal. The results indicate that effective control of high-frequency vortex-induced acoustic resonance problems can be achieved by using a low-frequency surface perturbation.

4) To further improve the control performance, a closed-loop control scheme was implemented in view of achieving better control of vortex-induced acoustic resonance in the system. The control signal in closed-loop control utilized feedback signals from hot wire sensors, which were down-sampled to a suitable low-frequency signal for test model excitation. Closed-loop tests were performed and the results were compared to those of the open-loop tests.

5) Various leading edges were investigated for seeking a general control strategy for controlling vortex shedding in engineering applications. Two types of vortex shedding, LEVS and TEVS were elaborated. Based on the characteristic of these two vortex types, the perturbation position and its mechanism, the perturbation direction and the analysis were carefully studied, leading to a general control strategy.

The present work leads to the following conclusions.

1) The surface perturbation technique was utilized to control the vortex shedding and its associated acoustic resonance for a semi-circular leading edge test model in the open-loop control scheme. Using the open-loop control scheme, the sound pressure level (SPL) at the acoustic resonance can be reduced by about 16.3 dB in the duct and 21.3dB in the cavity. It was found that the control performances were repeatable and reliable.

2) The abatement of the vortex shedding strength during the control can be contributed by two mechanisms: ‘the pressure disturbance mechanism’ and ‘the shear layer shifts mechanism’. During the generation of the TEVS, a pressure pulse was generated and feedback to the leading edge shear layer to influence the formation of the next vortex shedding. The surface perturbation technique generates a small local perturbation in the space between leading edge shear layer and trailing edge. This small local perturbation disturbs the pressure pulse on the trailing edge, which is feed-backed to the leading edge shear layer. This pressure pulse alters the generation of next vortex shedding that can lead to a reduction in the vortex shedding strength. Furthermore, the surface perturbation technique changes the geometry of the up surface of test model and shifts the shear layer which is attached to the surface. The shift disturbs the shear layers around the test model, and thus weakens the strength of vortex shedding behind the test model. This situation results in a clear disturbance on the formation of the trailing edge vortices, leading to a significant reduction in the vortex strength in the wake of the model.

3) The frequency shift phenomenon and its effect on the suppressing acoustical resonance were revealed. In the open-loop control scheme, a shift in the shedding frequency is caused by the control action. A formula was derived to predict this frequency shift in the effective control region. It was shown that the applied perturbation brings about 1.7% increases in the effective height of the control plate, resulting in a frequency shift of about 2.84 Hz that was confirmed by the experiment. If the shedding frequency shift exceeded the resonance bandwidth of the downstream acoustic cavity, the sound reduction inside the cavity would be larger than that in the duct. This phenomenon along gave a rise to a further sound pressure reduction of 5 dB inside the acoustic cavity. The same phenomenon was also observed in the

closed-loop control. This frequency-shift mechanism assists the control process in achieving a larger noise reduction level inside the cavity than that in the duct due to the down-stream cavity resonance. The mechanism in the closed-loop control is consistent with the open-loop control. The frequency shift phenomenon in the closed-loop control can give a rise to a further sound pressure reduction of 4.4 dB inside the acoustic cavity.

4) For a semi-circular leading edge test model, closed-loop tests demonstrated the effectiveness of the proposed control technique. At the optimum control voltage and control phase delay, a noise reduction of 17.5dB in the duct and 22.6dB inside the cavity was obtained. It was observed that the closed-loop control could achieve a better control performance than that of the open-loop control. In particular, the phase delay of control actuation could be optimally tuned so that the strength of vortex shedding energy could be minimized effectively, leading to a satisfactory noise reduction in the duct and cavity. This process was evident from the spectral phase shift results for the case of closed-loop control, where the vortex traveling time has been delayed at downstream of the test model. Therefore, an optimal control strategy was proposed by utilizing an optimal phase-tuned active surface perturbation to create sufficient changes in the vortex shedding structure, leading to an effective noise reduction in the system.

5) The developed surface perturbation technique can also be applied to a square leading edge test model using both open-loop and closed-loop control schemes. Under the application of control, the SPL in the duct decreased from 92.2dB to 75.6dB (a reduction of 16.6dB) at the vortex shedding frequency. Meanwhile, the SPL measured inside the cavity decreased from 105.4dB to 86.9dB (a reduction of 18.5dB). For the square leading edge model, it was found that its control mechanism was different

from that of the semi-circular leading edge test model. The path of the LEVS started from the leading edge and then propagated downstream. After the deployment of the control, the vertical velocity generated by the vibration plate played the key role in the vortex strength reduction. More significant reductions can be achieved when the velocity disturbance was near the propagation path of the vortex shedding.

6) Control strategies for two primary leading edge geometries have been proposed. For the semi-circular leading edge test model, the surface perturbation mainly takes effect in the generation region, although perturbing on any surface within this region can lead to reduction when applying control. The optimal control strategy is to arrange the perturbation at the position where the pressure pulse was the smallest. This way, the target noise reduction can be achieved by using perturbation within a relatively small area at a low control voltage. For the square leading edge test model, the control action of the surface perturbation mainly exists in the vortex shedding region. It was observed that the vertical velocity generated by the perturbation was relatively small when compared with the strength of the vortex shedding. The optimal control strategy requires arranging the vibration plate near the propagation path of the LEVS for achieving sufficient vortex strength abatement. Furthermore, the process for choosing the optimal control strategy has been proposed in this work. In general, the area of vibration plate should be as large as possible for the semi-circular leading edge test model, to be installed in the vortex generation region. The perturbation can affect a stronger pressure pulse in this region so to lead to more reduction of vortex shedding strength. For the square leading edge test model, it is not necessarily to use a large perturbation area to bring the perturbation effect on the LEVS.

7) The existence of the pressure pulse for the semi-circular leading edge test

model has been confirmed. This was identified by using hot wires to measure the energy distribution at vortex shedding frequency along the up surface of test model. The directivity of the pressure pulse was studied by using a modified two microphone method and it was found that the pressure pulse had strong directivity characteristics. A small disturbance generated by the surface perturbation can change the direction of the pressure pulse and then influence the generation the vortex shedding.

7.2 Recommendations

The following areas are worthy investigating in the future:

1) In the present work, the investigation was only focused on two typical leading edges. For other type of leading edge, a combination of control mechanism for both semi-circular and square leading edges can be intuitively used. However, further investigation can be done by applying the surface perturbation to models with more complex leading edges, such as airfoil and polygon leading edges that can generate complex vortex behavior. The optimal control strategy for these configurations can then be investigated.

2) The present work focused on the active control mechanism for controlling the vortex shedding and acoustic resonance processes. The fluid-sound-structure interaction during the control still needs to be further investigated with the help of more accurate mathematical models which can allow a better understanding of the physical mechanism.

3) Due to the vibration characteristic of the THUNDER actuators, the present work down-sampled the control frequency to low frequency. However, it can be beneficial to utilize other actuators with better dynamic properties which hopefully can provide more freedom during the investigation.

4) When the flow passes the semi-circular leading edge test model, there exist shear layers on the surface of the test model. A small surface perturbation does have influence on this shear layers. Further study can be done to investigate the control mechanism of these shear layers and to extend the application of the perturbation technique to boundary layers control.

8. Reference

- [1] Bishop, R. E. D. & Hassan, A. Y. 1964 The lift and drag forces on a circular cylinder in a flowing fluid. *Proceeding of the Royal Society Series A, London*, 277, 51-75.
- [2] Tanida, Y., Okajima, A. & Watanabe, Y. 1973 Stability of a circular cylinder oscillating in a uniform flow or in a wake. *Journal of Fluid Mechanics*, 61, 769-784
- [3] Griffin, O. M. & Ramberg, S. E. 1975 On vortex strength and drag in bluff-body wakes . *Journal of Fluid Mechanics*, 69, 721-728
- [4] Davies, M. E. 1976 A comparison of the wake structure of a stationary and oscillating bluff body, using a conditional average technique. *Journal of Fluid Mechanics*, 75, 209-231
- [5] Sarpkaya, T. 1979 Vortex-induced oscillations- A selected review. *Journal of Applied Mechanics*, 46, 241-258
- [6] Bearman, P. W. 1984 Vortex shedding from oscillating bluff bodies. *Annual Review of Fluid Mechanics*, 16, 195-222
- [7] Ongoren, A.& Rockwell, D. 1988 Flow structure from an oscillating cylinder. Part I, Mechanisms of phase shift and recovery in the near wake. *Journal of Fluid Mechanics*, 191, 197-223
- [8] Williamson, C. H. K & Roshko, A, 1988 Vortex formation in the wake of an oscillating cylinder, *Journal of Fluids and Structures*, 2, 355-381
- [9] Roshko A., Perspectives on bluff body aerodynamics, *J. Wind Eng. Ind. Aerod.* 49 (1993) 79–100.
- [10] Roshko A., On the drag and shedding frequency of two-dimensional bluff bodies, NACA TN 3169, 1954.

- [11] Monkewitz P.A., Wake control, in: Eckelmann H. et al. (Eds.), Bluff-Body Wakes, Dynamics and Instabilities, IUTAM Symp., Göttingen, Germany, Springer, Berlin, 1992.
- [12] Schumm M., Berger E., Monkewitz P.A., Self-excited oscillations in the wake of two-dimensional bluff bodies and their control, *J. Fluid Mech.* 271 (1994) 17–53.
- [13] Roussopoulos K., Monkewitz P.A., Nonlinear modelling of vortex shedding control in cylinder wakes, *Physica D* 97 (1996) 264–273.
- [14] Ware, A. G. & Shah, V. N. 1988 Age-related degradation of boiling water-reactor vessel internals. *Nuclear Engineering and Design*, 133, 49-62
- [15] Yamane, T. & Orita, T. 1994 Relationship of pressure wave velocity to self-excited oscillation of collapsible-tube flow. *JSME international Journal Series A - Solid Mechanics and Material Engineering*, 37, 71-78
- [16] Guerout, F.M. & Fisher, N. J. 1999 Steam generator fretting-wear damage: A summary of recent findings, *Journal of Pressure Vessel Technology-Transactions of the ASME*, 121, 304-310
- [17] Pettigrew, M. J. & Taylor, C. E. 2003 Vibration analysis of shell-and-tube heat exchangers: an overview- Part I: Flow, damping, fluid elastic instability. *Journal of Fluids and structures*, 18, 469-483
- [18] Naudascher, E&Rockwell, D . 1994, Flow-induced vibration—An engineering guide .Rotterdam : A . A . Balkema .
- [19] Naudascher, E&Wang,Y, 1993 Flow-induced vibrations of prismatic bodies and grids of prisms . *Journal of Fluids and Structures* 7 , 341 – 373 .
- [20] Acheson, D.J., Elementary Fluid Dynamics, Oxford applied mathematics and computing science series, 1995
- [21] Douglas, J.F., Gasiorek, J.M., Swaffield, J.A., Fluid mechanics, Longman, 1995

- [22] M. M. Zdravkovich, Different modes of vortex shedding: an overview, *Journal of Fluids and Structures*, Vol. 10 (1996), pp. 427-437
- [23] Strouhal, V.C., On a particular way of tone generation (German), *Annalen der Physikund Chemie*, Vol. 5, 1878, pp. 216-251
- [24] Parkinson, G.V., Phenomena and modelling of flow-induced vibrations of bluff bodies, *Aerospace Science*, Vol. 16 (1989), pp. 169-224
- [25] Parkinson, G.V., Mathematical models of flow induced vibrations of bluff bodies, in: *Flow-Induced Structural Vibrations*, Naudascher (ed.), Springer, 1974
- [26] Deniz, S., T. Staubli, Oscillating rectangular and octagonal profiles: interaction of leading- and trailing-edge vortex formation, *Journal of Fluids and Structures*, Vol. 11 (1997), pp. 3-31
- [27] Matsumoto, M., Vortex shedding of bluff bodies: a review, *Journal of Fluids and Structures*, Vol. 13 (1999), pp. 791-811
- [28] Deniz, S., T. Staubli, Oscillating rectangular and octagonal profiles: modelling of fluid forces, *Journal of Fluids and Structures*, Vol. 12 (1998), pp. 859-882
- [29] Deniz, S., T. Staubli, Oscillating rectangular and octagonal profiles: interaction of leading- and trailing-edge vortex formation, *Journal of Fluids and Structures*, Vol. 11 (1997), pp. 3-31
- [30] Gerrard, J. H, 1966, The mechanics of the formation region of vortices behind bluff bodies, *J, Fluid Mech*, 25, 401-413
- [31] Abernathy, F. H., Kronauer, R.E. 1962, The formation of vortex streets. *J. Fluid Mech.* 13, 1-20
- [32] J.T. Turner, C.O. Popiel, D.I. Robinson, Evolution of an improved vortex generator, *Flow. Meas. Instrum.* 4 (4) (1993) 249–258.
- [33] J.P. Bentley , J.W. Mudd, Vortex shedding mechanisms in single and dual bluff

bodies, *Flow Measurement and Instrumentation* 14 (2003) 23–31.

[34] G.K.Batchelor,1970. An introduction to fluid dynamics. Cambridge University Press

[35] P.W.Bearman, 1984, vortex shedding from oscillating bluff bodies. *Ann, Rev. Fluid mMech*, 16, 195 -222

[36] A. Roshko. 1954, On the drag and shedding frequency of two-dimensional bluff bodies . NACA, Technical note 3169

[37] M.F.Unal and D. Rockwell, 1988a, on vortex formation from a cylinder. Part 1, The initial instability. *J. Fluid Mech*, 190, 491-512

[38] M.F.Unal and D. Rockwell, 1988b, on vortex formation from a cylinder. Part 2, Control by splitter-plate interference. *J. Fluid Mech*, 190, 513-529

[39] J.K. Eaton and J.P. Johnston, 1982, Low frequency unsteadiness of a reattaching turbulent shear layer, Springer, 162-170

[40] R. Parker and M. C. Welsh, ‘Effects of sound on flow separation from blunt flat plates,’ *Int. J. Heat and Fluid Flow* 4, 113-127 (1983).

[41] Bearman P.W. and Trueman D.M., An investigation of the flow around rectangular cylinders. *Aero. Q.*, 23, 1972, 229-237.

[42] A.M. Blazewicz, M.K. Bull and R.M. Kelso, ‘Characteristics of flow regimes for single plates of rectangular cross-section’, 16th Australasian Fluid Mechanics, Conference Crown Plaza, Gold Coast, Australia 2-7 December 2007

[43] Kiya M. and Sasaki K., Structure of a turbulent separation bubble. *J. Fluid Mech.*, 137, 1983, 83-113.

[44] M.J. Lighthill, 1952, On sound generated automatically Proc, Roy. Soc. (London) A212,564-587

[45] M.J. Lighthill, 1954, I- General theory; II-Turbulence as a source of sound. Proc,

Roy. Soc. (London) A222,1-32

[46] N.Curle,1955, The influence of solide boundaries on aerodynamic sound. Proc. Roy.Soc (London) A231, 505-514

[47] B.Etkin,G.K.Korbacher and R.T. Keefe.1957, Acoustic radiation from a stationary cylinder in a fluid stream(Aeolian Tones). *J.Acoust.Soc. Am.* 29(1),30-36

[48] Nakamura Y., Ohya Y. and Tsuruta H., Experiments on Vortex Shedding from Flat Plates with Square Leadingand Trailing Edges, *J. Fluid Mech.*, 222, 1991, 437–447.

[49] Naudascher E. and Wang Y., Flow-Induced Vibration of Prismatic Bodies and Grids of Prisms, *J. Fluid Struct.*, 7, 1993, 341–373.

[50] Nakayama R., Nakamura Y., Ohya Y. and Ozono S., A Numerical Study of the Flow around Flat Plates at low Reynolds Numbers, *J. Wind Eng. Ind. Aerodyn.*, 46 & 47, 1993, 255–264.

[51] Ohya Y., Nakamura Y., Ozono S., Tsuruta H. and Nakayama R., A Numerical Study of Vortex Shedding from Flat Plates with Square Leading and Trailing Edges, *J. Fluid Mech.*, 236, 1992, 445–460.

[52] Hourigan K., Thompson M.C. and Tan B.T., Selfsustained Oscillations in Flows around Long Blunt Plates, *J. Fluids Struct.*, 15 (3/4), 2001, 387–398.

[53] Parker R., Resonant Effects in Wake Shedding from Parallel Plates: Some Experimental Observations, *J. Sound Vib.*, 4, 1966, 62–72.

[54] Welsh & Gibson, Interaction of Induced Sound with Flow Past a Square Leading Edged Plate in a Duct, *J. Sound Vib.*, 67(4), 1979, 501–511.

[55] Welsh M.C., Stokes A.N. and Parker R. Flow-Resonant Sound Interaction in a Duct Containing a Plate, Part I: Semi-circular Leading Edge, *J. Sound Vib.*, 95(3), 1984, 305–323.

- [56] Stokes A.N. and Welsh M.C., Sound Interaction in a Duct Containing a Plate, Part II: Square Leading Edge, *J. Sound Vib.*, 104(1), 1986, 55–73.
- [57] A. Mohany and S. Ziada, ‘Flow-excited acoustic resonance of two tandem cylinders in cross-flow,’ *J. Fluids Struct.* 21, 103-119 (2005).
- [58] Strouhal, V. (1878) ijber eine besondere Art der Tonerregung, *Annalen der Phys J. und Chemie.* 5. 216.
- [59] Howe, MS. (1975) Contributions to the theory of aerodynamic sound, with application to excess Jet noise and the theory of the flute, *J. Fluid Mech.* 71. 625-613.
- [60] M. Mathias, A.N. Stokes, K. Hourigan and M.C. Welsh, Low-level flow-induced acoustic resonances in ducts, *Fluid Dynamics Research* 3 (1988) 353-356
- [61] Blevins, R.D., Bressler, M.M., 1993. Experiments on acoustic resonance in heat exchanger tube bundles. *Journal of Sound and Vibration* 164, 503–533.
- [62] Oengooren, A., Ziada, S., 1998. An in-depth study of vortex shedding, acoustic resonance and turbulent forces in normal triangle tube arrays. *Journal of Fluids and Structures* 12, 717–758.
- [63] Parker, R., Pryce, D.C., 1974. Wake excited resonances in an annular cascade: an experimental investigation. *Journal of Sound and Vibration* 37, 247–261.
- [64] Ziada, S., Oengooren, A., Vogel, H., 2002. Acoustic resonance in the inlet scroll of a turbo-compressor. *Journal of Fluids and Structures* 16, 361–373.
- [65] Ziada, S., Shine, S., 1999. Strouhal numbers of flow-excited acoustic resonance of closed side branches. *Journal of Fluids and Structures* 13, 127–142.
- [66] Graf, R., Ziada, S., 1992. Flow induced acoustic resonance in closed side branches: an experimental determination of the excitation source. In: *Proceedings of the Third International Symposium on Flow-Induced Vibration and Noise*, vol.7, ASMEWAM, Anaheim, pp.63–80.

- [67] L. Cattafesta, D. Williams, C. Rowley and F. Alvi, 'Review of active control of flow-induced cavity resonance,' AIAA 2003-3567 (2003).
- [68] Gad-el-Hak M. 2000. Flow Control: Passive, Active and Reactive Flow Management. Cambridge, UK: Cambridge Univ. Press
- [69] Shih WCL, Wang C, Coles D, Roshko A. 1993. Experiments on flow past rough circular cylinders at large Reynolds numbers. *J. Wind Eng. Ind. Aerodyn.* 49:351–68
- [70] Bearman PW, Harvey JK. 1993. Control of circular cylinder flow by the use of dimples. *AIAA J.* 31:1753–56
- [71] Choi J, Jeon W-P, Choi H. 2006a. Mechanism of drag reduction by dimples on a sphere. *Phys. Fluids* 18:041702
- [72] Lee S, Kim H. 1997. The effect of surface protrusions on the near wake of a circular cylinder. *J. Wind Eng. Ind. Aerodyn.* 69–71:351–61
- [73] Lim H, Lee S. 2002. Flow control of circular cylinders with longitudinal grooved surfaces. *AIAA J.* 10:2027–36
- [74] Anderson E, Szewczyk A. 1997. Effects of a splitter plate on the near wake of a circular cylinder in 2 and 3-dimensional flow configurations. *Exp. Fluids* 23:161–74
- [75] Dalton C, Xu Y, Owen JC. 2001. The suppression of lift on a circular cylinder due to vortex shedding at moderate Reynolds numbers. *J. Fluids Struct.* 15:617–28
- [76] Baek S, Sung HJ. 1998. Numerical simulation of the flow behind a rotary oscillating circular cylinder. *Phys. Fluids* 10:869–76
- [77] Choi S, Choi H, Kang S. 2002. Characteristics of flow over a rotationally oscillating cylinder at low Reynolds number. *Phys. Fluids* 14:2767–77
- [78] Cetiner O, Rockwell D. 2001. Streamwise oscillations of a cylinder in a steady current. Part 1: locked-on states of vortex formation and loading. *J. Fluid Mech.* 427:1–28

- [79] Blackburn H, Henderson R. 1999. A study of two-dimensional flow past an oscillating cylinder. *J. Fluid Mech.* 385:255–86
- [80] Carberry J, Sheridan J, Rockwell D. 2003. Controlled oscillations of a cylinder: a new wake state. *J. Fluids Struct.* 17:337–43
- [81] Konstantinidis E, Balabani S, Yianneskis M. 2005. The timing of vortex shedding in a cylinder wake imposed by periodic inflow perturbations. *J. Fluid Mech.* 543:45–55
- [82] Artana G, Sosa R, Moreau E, Touchard G. 2003. Control of the near-wake flow around a circular cylinder with electrohydrodynamic actuators. *Exp. Fluids* 35:580–88
- [83] Arcas D, Redekopp L. 2004. Aspects of wake vortex control through base blowing/suction. *Phys. Fluids* 16:452–56
- [84] Fujisawa N, Takeda G, Ike N. 2004. Phase-averaged characteristics of flow around a circular cylinder under acoustic excitation control. *J. Fluids Struct.* 19:159–70
- [85] Kim J, Choi H. 2005. Distributed forcing of flow over a circular cylinder. *Phys. Fluids* 17:033103
- [86] Amitay M, Smith BL, Glezer A. 1998. Aerodynamic flow control using synthetic jet technology. 36th AIAA Aerosp. Sci. Meet., Reno, Nev., AIAA Pap. No. 98–0208
- [87] R. L. Sarno and M. E. Franke, ‘Suppression of flow-induced pressure oscillations in cavities,’ *J. Aircr.* 31, 90-96 (1994).
- [88] Berger E. 1967. Suppression of vortex shedding and turbulence behind oscillating cylinders. *Phys. Fluids* 10:S191–93
- [89] Ffowes Williams J, Zhao B. 1989. The active control of vortex shedding. *J. Fluids Struct.* 3:115–22
- [90] Park DS, Ladd DM, Hendricks EW. 1994. Feedback control of von Kármán

vortex shedding behind a circular cylinder at low Reynolds numbers. *Phys. Fluids* 6:2390–405

[91] X. Y. Huang and D. S. Weaver, ‘On the active control of shear layer oscillations across a cavity in the presence of pipeline acoustic resonance,’ *J. Fluids Struct.* 5, 207-219 (1991).

[92] L. N. Cattafesta III, S. Garg, M. Choudhari and F. Li, ‘Active control of flow-induced cavity resonance,’ AIAA-97-1804 (1997).

[93] L. N. Cattafesta III, S. Garg and D. Shukla, ‘The development of piezoelectric actuators for active flow control,’ AIAA J. 39, 1562-1568 (2001).

[94] L. N. Cattafesta III, J. Mathew and A. Kurdila, ‘Modeling and design of piezoelectric actuators for fluid flow control,’ SAE 2000 Tran. J. Aero. 109, 1088-1095 (2001).

[95] H. Kook, L. Mongeau and M. A. Franchek, ‘Active control of pressure fluctuations due to flow over Helmholtz resonators,’ *J. Sound Vib.* 255, 61-76 (2002).

[96] S. Ziada, H. Ng and C. E. Blake, ‘Flow excited resonance of a confined shallow cavity in low Mach number flow and its control,’ *J. Fluids Struct.* 18, 79-92 (2003).

[97] L. Cheng, Y. Zhou and M. M. Zhang, ‘Perturbed interaction between vortex shedding and induced vibration,’ *J. Fluids Struct.* 17, 887-901 (2003).

[98] J. P. Marouzé and L. Cheng, ‘A Feasibility Study of Active Vibration Isolation THUNDER Actuators,’ *Smart Materials and Structures* 11, 854-862 (2002).

[99] Zhang Ming Ming, ‘Open- and close-loop control of flow-structure interaction on square cylinders in a cross flow’, chapter 3, 43-58, PhD thesis, Department of mechanical engineering, The Hong Kong polytechnic university

[100] M. M. Zhang, L. Cheng and Y. Zhou, ‘Closed-loop-controlled vortex shedding from a flexibly supported square cylinder under different schemes,’ *Phy. Fluids* 16,

1439-1448 (2004).

[101] M. M. Zhang, L. Cheng and Y. Zhou, 'Closed-loop-controlled vortex shedding from a flexibly supported square cylinder under different schemes,' *Euro. J. of Mechanics BFluids* 23, 189-197 (2004).

[102] M. M. Zhang, L. Cheng and Y. Zhou, 'Control of vortex-induced non-resonance vibration using piezo-ceramic actuators embedded in a structure,' *Smart Mater. Struct.* 14, 1217-1226 (2005).

[103] L. Cheng, Y. Zhou and M. M. Zhang, 'Controlled vortex-induced vibration on a fixsupported flexible cylinder in crossflow,' *J. Sound Vib.* 292, 279-299 (2006).

[104] M. M. Zhang, L. Cheng and Y. Zhou, 'Closed-loop controlled vortex-airfoil interactions,' *Phys. Fluid* 18, 046102 (2006).

[105] M. M. Zhang, L. Cheng and Y. Zhou, 'Control of post-stall airfoil aerodynamics based on surface perturbation,' *AIAA J.* 46, 2510-2519 (2008).

[106] M.M. Zhang, L. Cheng and Y. Zhou, 'Asynchronous Control of Vortex-induced Acoustic Cavity Resonance Using Imbedded Piezo-electric Actuators ,' *J. Acoust. Soc Am.* ,2009, Jul, 126(1):36-45.

[107] D. Arthurs and S. Ziada, 'Flow-excited acoustic resonances of coaxial side-branches in an annular duct,' *J. Fluids and Structures*,25, 42–59 (2009)

[108] H. Hourigan, M. C. Thompson and B. T. Tan, 'Self-sustained oscillations in flows around long blunt plates,' *J. Fluids Struct.* 15, 387-398 (2001).

[109] R. Mills, J. Sheridan and K. Hourigan, 'Particle image velocimetry and visualization of natural and forced flow around rectangular cylinders,' *J. Fluid Mech.* 478, 299-323 (2003).

[110] Cherry, N. J, Hillier, R.&Latour,M. E.M. P. 1984 Unsteady measurements in a separated and reattaching flow. *Journal of Fluid Mechanics* 144, 13-46.

- [110] Soria, J., Sheridan, J. & Wu, J. 1993 'Spatial evolution of the separated shear layer from a square leading-edge plate.' *Journal of Wind Engineering and Industrial Aerodynamics* 49, 237-246.
- [112] Nakamura, Y. 1996. 'Vortex shedding from bluff bodies with splitter plates.' *Journal of Fluids and Structures* 10, 147-158.
- [113] Nakamura, Y., Ohya, Y. & Tsuruta, H. 1991. 'Experiments on vortex shedding from flat plates with square leading and trailing edges'. *Journal of Fluid Mechanics* 222, 437-447.